Model-based quantitative scanning transmission electron microscopy for measuring dynamic structural changes at the atomic scale

Annelies De wael

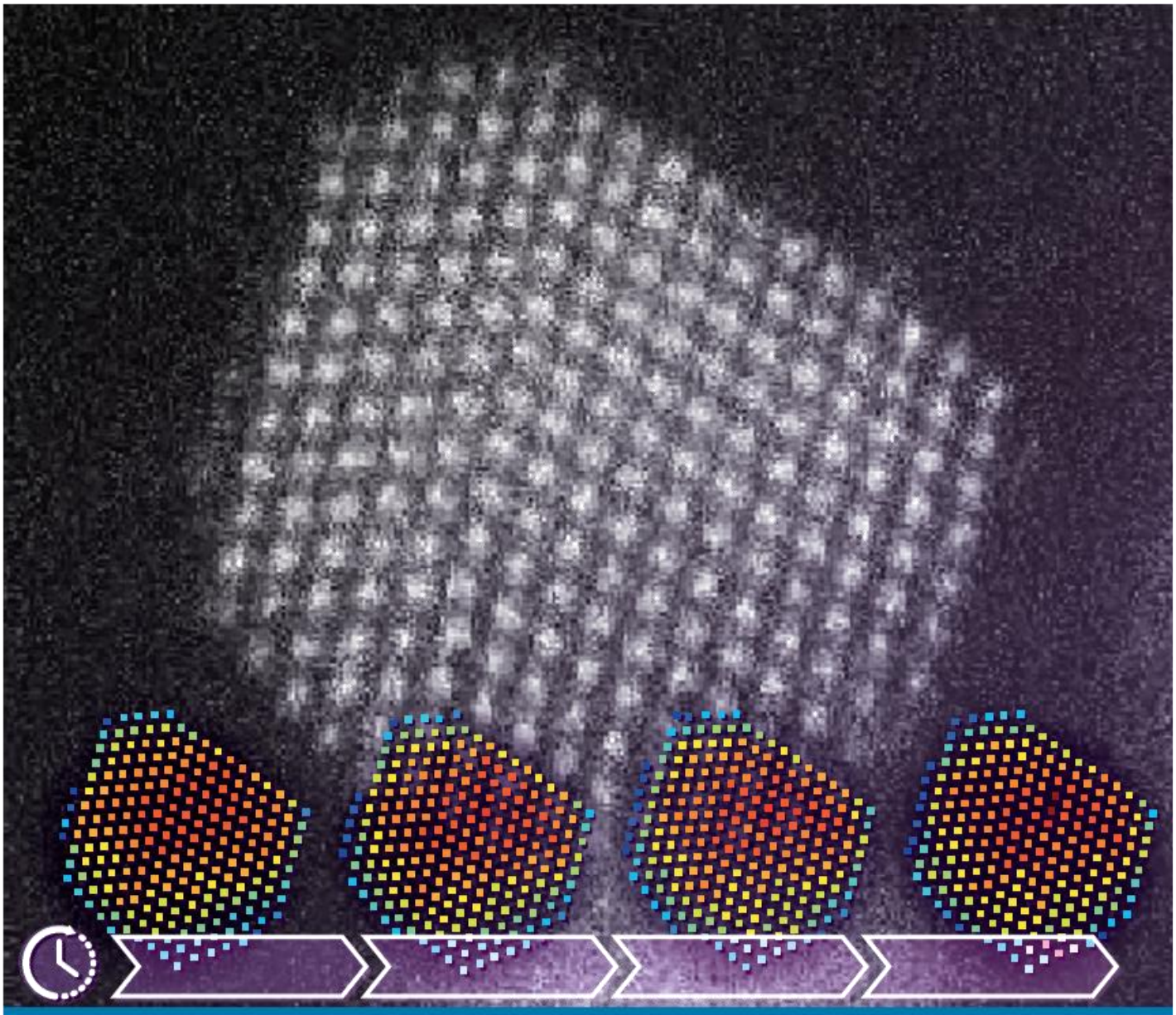

Promotoren **prof. dr. Sandra Van Aert | dr. Annick De Backer**

Proefschrift voorgedragen tot het behalen van de graad van doctor in de wetenschappen: fysica
Faculteit Wetenschappen | Antwerpen, 2021

Universiteit Antwerpen

Universiteit Antwerpen

Departement Fysica
Faculteit Wetenschappen

Model-based quantitative scanning transmission electron microscopy for measuring dynamic structural changes at the atomic scale

Modelgebaseerde kwantitatieve raster transmissie elektronenmicroscopie voor het meten van dynamische structuurveranderingen op atomaire schaal

Proefschrift voorgelegd tot het behalen van de graad van
Doctor in de Wetenschappen: Fysica
aan de Universiteit Antwerpen, te verdedigen door

Annelies De wael

Promotoren:
prof. dr. Sandra Van Aert
dr. Annick De Backer

Antwerpen, 2021

Doctoral Committee

Chairman
prof. dr. Pierre Van Mechelen, University of Antwerp - Belgium

Promotors
prof. dr. Sandra Van Aert, University of Antwerp - Belgium
dr. Annick De Backer, University of Antwerp - Belgium

Members
prof. dr. Scott Findlay, Monash University - Australia
dr. Rolf Erni, Empa - Switzerland
prof. dr. Christel Faes, University of Hasselt - Belgium
prof. dr. Milorad Milosevic, University of Antwerp - Belgium

This research was financially supported by the Research Foundation Flanders

Contact Information
Annelies De wael
University of Antwerp - Department of Physics
EMAT - Electron Microscopy for Materials Science
Groenenborgerlaan 171
B-2020 Antwerp
Belgium
annelies.dewael@uantwerpen.be

The more you know,
the more you know you don't know.

♫ Tower of Power, 1997 ♫

Samenvatting

Nanomaterialen kunnen uiterst interessante eigenschappen vertonen voor een verscheidenheid aan veelbelovende toepassingen, gaande van zonnecrème tot batterijen voor elektrische auto's. Een nanometer is een miljard keer kleiner dan een meter. Op deze schaal kunnen de materiaaleigenschappen volledig verschillen van bulkmaterialen op grotere schaal. Bovendien hangen de eigenschappen van nanomaterialen sterk af van hun exacte grootte en vorm. Kleine verschillen in de posities van de atomen, in de grootte-orde van een picometer (nog eens duizend maal kleiner dan een nanometer), kunnen de fysische eigenschappen al drastisch beïnvloeden. Daarom is een betrouwbare kwantificering van de atomaire structuur van kritisch belang om de evolutie naar materiaalontwerp mogelijk te maken en inzicht te verwerven in de relatie tussen de fysische eigenschappen en de structuur van nanomaterialen. Daarnaast kan de atomaire structuur van nanomaterialen ook veranderen in de loop van de tijd ten gevolge van verschillende fysische processen. *Het onderzoek dat in deze thesis gepresenteerd wordt, maakt het mogelijk om de dynamische structuurveranderingen van nanomaterialen betrouwbaar te kwantificeren op atomaire schaal door gebruik te maken van transmissie elektronenmicroscopie (TEM).*

Een ideale beeldvormingstechniek voor kwantificering van nanomaterialen is elektronenmicroscopie, meer bepaald in de zogenaamde ringvormige donkerveld raster transmissie elektronenmicroscopie (ADF STEM) beeldvormingsmodus. In kristallijne nanomaterialen zijn de atomen georganiseerd in atoomkolommen. Door dergelijke nanomaterialen te oriënteren langs een zone-as, met de atoomkolommen parallel aan de kijkrichting, kunnen beelden opgenomen worden met atomaire resolutie. De driedimensionale (3D) atomaire structuur van het nanomateriaal wordt dan geprojecteerd in die tweedimensionale (2D) beelden. Om informatie over de ontbrekende derde dimensie te bekomen, is een kwantitatieve analyse noodzakelijk. De intensiteit van atomaire resolutie ADF STEM beelden is gepiekt op de posities van de atoomkolommen en gevoelig aan de chemische samenstelling en dikte van het nanomateriaal. Een ADF STEM beeld is dus meer dan een bovenaanzicht van de atoomkolommen. Atoomkolommen met meer atomen zullen namelijk intenser zijn in het ADF STEM beeld. Dit maakt ADF STEM beelden zeer bruikbaar voor het tellen van het aantal atomen in de atoomkolommen van kristallijne nanomaterialen. De telresultaten kunnen dan op hun beurt gebruikt worden om de 3D atomaire structuur te reconstrueren, met behulp van een zogenaamde structuurrelaxatie. Daarom worden in deze thesis kwantitatieve methoden ontwikkeld voor het tellen van het aantal atomen in elke atoomkolom van monoatomaire nanokristallijn materialen.

Het startpunt is de kwantificering van de ADF STEM beeldintensiteiten met behulp van een parametrisch model dat eerder in het domein van de kwantitatieve electronenmicroscopie geïntroduceerd werd. Dit model bestaat uit een superpositie van 2D Gaussfuncties en maakt het mogelijk om de posities van de atoomkolommen in het beeld te schatten, alsook de zogenaamde verstrooiingsdoorsnede voor elke atoomkolom. De verstrooiingsdoorsnede van een atoomkolom komt overeen met de totale intensiteit aan verstrooide elektronen van de atoomkolom naar de detector en is rechtstreeks gerelateerd aan het type en aantal atomen in de atoomkolom. Voor een monoatomair kristallijn nanomateriaal neemt de verstrooiingsdoorsnede monotoon

toe wanneer het aantal atomen in de atoomkolom toeneemt. Daarom is het parametrische model voor de kwantificering van ADF STEM beeldintensiteiten een erkende aanpak in de kwantitatieve elektronenmicroscopie.

Wanneer het nanomateriaal echter gekanteld is, zodat de atoomkolommen niet langer perfect evenwijdig met de kijkrichting georiënteerd zijn, worden de ADF STEM beeldintensiteiten van de atoomkolommen uitgesmeerd. Bovendien neemt de verstrooiingsdoorsnede van een atoomkolom af ten gevolge van een dergelijke tilt van het nanomateriaal, wat tot telfouten kan leiden. Daarom onderzoek ik in deze thesis een nieuw parametrisch model, met elliptische in plaats van symmetrische Gaussische pieken. Dit elliptisch model blijkt inderdaad kwalitatief een betere beschrijving voor de beeldintensiteiten dan het symmetrisch model. Met behulp van een simulatiestudie voor een platinum nanokristal wordt het echter duidelijk dat de fysische parameters van de atomaire structuur, zoals de positie en verstrooiingsdoorsnede van de atoomkolommen, niet nauwkeuriger geschat worden. De extra inspanning voor het schatten van het meer gecompliceerde elliptisch model is dus niet nodig. Mijn aanbeveling is daarom om het bestaande symmetrisch parametrisch model voor de kwantificering van ADF STEM beeldintensiteiten ook te gebruiken in geval van een kleine hoeveelheid specimen tilt.

Er bestaan reeds twee verschillende manieren om atomen te tellen gebruikmakend van de verstrooiingsdoorsneden geschat op basis van een ADF STEM beeld: op basis van beeldsimulaties en op basis van statistische parameterschattingtheorie. De beeldsimulatie-gebaseerde methode vergelijkt de geschatte verstrooiingsdoorsneden uit het experiment rechtstreeks met verstrooiingsdoorsneden die bepaald worden uit beeldsimulaties voor verschillende diktes. De statistiek-gebaseerde methode schat het aantal atomen in elke atoomkolom daarentegen door de set van geschatte verstrooiingsdoorsneden uit het experimenteel beeld te ontbinden in verschillende componenten die elk overeenstemmen met een verzameling atoomkolommen met hetzelfde aantal atomen. Beide methoden werden succesvol toegepast voor de analyse van ADF STEM beelden opgenomen met een hoge elektronendosis. Veel interessante nanomaterialen worden beschadigd echter onder invloed van de intense elektronenbundel. Om ongewenste schade en structuurverandering te vermijden, moet de elektronendosis voor dergelijke stralingsgevoelige nanomaterialen verlaagd worden. Vergelijkbaar met een gedimde lichtbron bij een lichtmicroscoop, zorgt een lage elektronendosis in de elektronenmicroscoop ook voor ruis in de beelden. Dit is uitdagend voor een betrouwbare kwantificering, en daarom zijn geavanceerde kwantitatieve methoden nodig die goed presteren bij een lage signaal-ruis verhouding. Daarom introduceer ik in deze thesis een zogenaamde hybride statistiek-simulaties gebaseerde methode voor het tellen van atomen. Deze methode verwerkt voorkennis uit beeldsimulaties rechtstreeks in het statistisch kader van de statistiek-gebaseerde telmethode. Door de nauw verweven combinatie van statistische parameterschattingstheorie en beeldsimulaties is deze telmethode robuuster en kunnen atomen geteld worden bij een lagere elektronendosis. Een hoge dosis ADF STEM beeld van een stabiele gouden nanorod wordt gebruikt om de telresultaten van de hybride methode te valideren. Verder worden gesimuleerde beelden van een platinum nanodeeltje gebruikt om aan te tonen dat betrouwbaar tellen van atomen zelfs mogelijk is voor getilte nanomaterialen, dankzij de parametrische relatie die de voorkennis uit beeldsimulaties in het statistisch model verwerkt. De verbeterde robuustheid voor een lage signaal-ruis verhouding wordt gedemonstreerd aan de hand van een experimenteel en een gesimuleerd ADF STEM beeld van een klein katalytisch platinum nanodeeltje, waarvoor betrouwbaar tellen van het aantal atomen voorheen niet mogelijk was. De hybride methode opent zo mogelijkheden voor de kwantitatieve analyse van werkelijk stralingsgevoelige nanomaterialen.

Om de betrouwbare kwantificering van dynamische structuurveranderingen van nanomaterialen op atomaire schaal mogelijk te maken, wordt de telmethode uitgebreid van één beeld naar

een tijdreeks. Daartoe introduceer ik het zogenaamde hidden Markov model in het domein van de elektronenmicroscopie. Dankzij de optimale eigenschappen voor het modelleren en analyseren van tijdreeksen, werden hidden Markov modellen in andere wetenschapsdomeinen eerder al succesvol toegepast, bijvoorbeeld voor spraakherkenning en uitlijning van sequenties van aminozuren in eiwitten. Het hidden Markov model stelt ons inderdaad in staat om op basis van een tijdreeks het aantal atomen in elke atoomkolom in elk beeld beter te tellen dan met de hybride telmethode, die weliswaar ontworpen werd voor de analyse van een enkel beeld. Zo wordt het hidden Markov model gebruikt om de veranderingen in de morfologie van een katalytisch platinum nanodeeltje, die veroorzaakt werden door de bestraling met de elektronenbundel, te kwantificeren op basis van een experimentele tijdreeks van ADF STEM beelden.
Een belangrijke parameter van het hidden Markov model, die zorgt voor de verbeterde telprestaties, is de zogenaamde transitiekans. Deze parameter wordt gebruikt om expliciet de mogelijkheid tot veranderingen in de atomaire structuur tijdens de tijdreeks te modelleren. De transitiekans geeft weer hoeveel kans een atoomkolom met een zekere dikte heeft om één of meerdere atomen te verliezen of bij te krijgen gedurende de tijdreeks. Op basis van de geschatte transitiekans kan de globale kans op structuurveranderingen voor het nanomateriaal tijdens de tijdreeks gekwantificeerd worden. Dit kan gebruikt worden om een dosisonafhankelijke werkzame doorsnede te kwantificeren op basis van het experiment. Wanneer de structuurveranderingen veroorzaakt worden door oppervlaktediffusie, kan deze werkzame doorsnede zelfs gebruikt worden om de drempelenergie voor oppervlaktediffusie te schatten uit het experiment. De drempelenergie die op deze manier geschat wordt voor een experimentele tijdreeks van een wigvormig platinum nanomateriaal komt goed overeen met de eerder berekende theoretische waarde voor dit type materiaal. Dit bevestigt dat het hidden Markov model de dynamische structuurveranderingen op atomaire schaal betrouwbaar kwantificeert.
Het hidden Markov model voor het tellen van atomen kan ook toegepast worden op *in situ* experimenten. Zo werden beelden opgenomen van een katalytisch gouden nanodeeltje bij een verhoogde temperatuur in de elektronenmicroscoop. Het aantal atomen geteld door het hidden Markov model wordt gecombineerd met moleculaire dynamica om de veranderingen in de 3D atomaire structuur in functie van de tijd te karakteriseren. Tenslotte wordt nog een simulatiestudie uitgevoerd om aan te tonen wat de mogelijkheden zijn van het hidden Markov model voor de betrouwbare kwantificering van de atomaire structuur in geval van variabele omgevingscondities zoals een geleidelijk aan toenemende temperatuur of een afwisselende gasstroom.
Kortom, het hidden Markov model voor het tellen van atomen is veelbelovend voor het onthullen en kwantificeren van de atomaire structuur wanneer deze verandert in de tijd, bijvoorbeeld via oppervlaktediffusie, door dosis gerelateerde effecten of tijdens *in situ* experimenten.

De *take-home* boodschap van deze thesis is dat ik statistische modellen heb gebruikt om de veranderingen in de structuur van een nanomateriaal op atomaire schaal betrouwbaar te kwantificeren in functie van de tijd. Ik heb dit gerealiseerd door methodes te ontwikkelen waarmee ik het aantal atomen “achter elkaar” kan tellen in elke atoomkolom van een nanomateriaal, en dit op basis van beelden opgenomen met een elektronenmicroscoop. Een belangrijk verschil met telmethodes voor de analyse van een enkel beeld is het schatten van de kans dat een atoomkolom atomen zal verliezen of bijkrijgen van het ene naar het andere beeld in de tijdreeks. Deze kwantitatieve methode kan het ontrafelen van de tijdsafhankelijke structuur-eigenschappen relatie van een nanomateriaal mogelijk maken, wat uiteindelijk kan leiden tot efficiënter design en productie van nanomaterialen voor innovatieve toepassingen.

Summary

Nanomaterials can exhibit highly interesting properties for a variety of promising applications, ranging from sunscreen to batteries in electrical cars. A nanometer is a billion times shorter than a meter. At this scale, a material's properties can be radically different as compared to bulk materials at larger scales. Furthermore, the properties of nanomaterials are strongly size and shape dependent. Small differences in the atomic positions, of the order of a picometer (yet a thousand times smaller than a nanometer), can already drastically change physical properties. Therefore, a reliable quantification of the atomic structure is of crucial importance in order to evolve towards materials design and to understand the structure-properties relationship of nanomaterials. Additionally, the atomic structure of nanomaterials can change over time, as a result of various physical processes. *The research presented in this thesis enables the reliable quantification of dynamic structural changes of nanomaterials at the atomic scale using transmission electron microscopy (TEM).*

An ideal imaging technique for quantification of nanomaterials is electron microscopy, specifically an imaging mode called annular dark field scanning transmission electron microscopy (ADF STEM). In crystalline nanomaterials, the atoms are organised in atomic columns. Atomic resolution images can be achieved by orienting the nanomaterial in a main zone axis orientation, such that the atomic columns are parallel to the viewing direction. In the two-dimensional (2D) images of the nanomaterial, the three-dimensional (3D) atomic structure is projected. In order to retrieve information from the missing third dimension, quantitative analysis of the images is necessary. The intensities of atomic resolution ADF STEM images are peaked at the atomic column positions. Interestingly, the intensities are also sensitive to the chemical content of the nanomaterial and are thickness dependent. Therefore, an ADF STEM image is more than a "top view" of the atomic columns. Atomic columns that contain more atoms will appear brighter in the ADF STEM images. ADF STEM images can therefore be used to count the number of atoms in each atomic column of a monatomic crystalline nanomaterial. These counting results can be used to reconstruct the 3D atomic structure using a so-called structural relaxation method. Therefore, the quantitative methods developed in this thesis mainly focus on counting the number of atoms in each atomic column of monatomic nanocrystalline materials.

As a starting point, the ADF STEM image intensities are quantified using a parametric imaging model that has been introduced in the field of quantitative STEM, prior to this thesis. This model consists of superimposed 2D Gaussian functions, and provides estimates for the positions of the atomic columns in the image and for the so-called scattering cross sections. The scattering cross section of an atomic column corresponds to the total intensity scattered from the atomic column towards the detector. This is directly related to the type and number of atoms in the atomic column. In case of a monatomic crystalline nanomaterial, the scattering cross sections increase monotonically with the number of atoms in the atomic column, making them particularly suitable for atom-counting. Therefore, the use of the parametric imaging model for the quantification of ADF STEM image intensities has become a recognised approach in quantitative electron microscopy.

However, when the nanomaterial is tilted, such that the atoms in the atomic columns are no longer oriented parallel to the viewing direction, an elongation of the intensity of the atomic columns in the ADF STEM images is observed. Furthermore, such sample tilt leads to a decrease of the scattering cross section for an atomic column, which may lead to errors during atom-counting. Therefore, in this thesis, I investigate a novel parametric model with elliptical rather than symmetrical Gaussian peaks. Qualitatively, this elliptical model indeed seems to be a better description for the image intensities as compared to the symmetrical model. However, a simulations study of a platinum nanocrystal reveals that the accuracy of the estimated physical parameters related to the atomic structure, such as the atomic column positions and the scattering cross sections, does not significantly improve as compared to the existing model. Therefore, it is not worth the extra effort required to fit the more complicated elliptical model. I recommend the use of the existing symmetrical parametric imaging model for the quantification of ADF STEM images, even in the presence of small amounts of sample tilt.

Two approaches for atom-counting using the scattering cross sections estimated from an ADF STEM image have been developed prior to the research presented in this thesis, based either on image simulations or on statistical parameter estimation theory. In the image simulations-based approach, counting results are obtained by directly comparing the scattering cross sections estimated from the experimental image to scattering cross sections obtained from image simulations at different thicknesses. The statistics-based method on the other hand estimates the number of atoms in each atomic column by decomposing the set of scattering cross sections estimated from the experimental image in different components corresponding to sets of atomic columns with the same number of atoms. Both methods have been applied successfully to the analysis of ADF STEM images with a high electron dose. However, many interesting nanomaterials easily damage when the incident electron beam intensity is too high. In order to avoid unwanted changes to the atomic structure under investigation, the electron dose needs to be reduced for such beam-sensitive nanomaterials. Comparable to the use of a dimmed light source in light microscopy, imaging using a low electron dose in electron microscopy results in more noisy images. This poses a challenge for reliable quantification, and requires advanced quantitative methods with a performance that can cope with a low signal-to-noise ratio. To this purpose, I introduce a so-called hybrid statistics-simulations based method for atom-counting in this thesis. In this method, prior knowledge from image simulations is directly incorporated into the statistical framework of the statistics-based atom-counting procedure. As a result of this interwoven combination of statistical parameter estimation theory and image simulations, the atom-counting procedure becomes more robust and atom-counting can be performed reliably at lower electron doses. A high dose ADF STEM image of a stable gold nanorod is used to validate the counting results obtained by the hybrid method. Furthermore, simulated images of a platinum nanoparticle are used to demonstrate how the parametric relationship used to include the prior knowledge from image simulations even allows reliable atom-counting in the presence of sample tilt. The improved robustness to a low signal-to-noise ratio is demonstrated using an experimental and simulated ADF STEM image of a small catalytic platinum-iridium nanoparticle for which reliable atom-counting from a single image could not be achieved before. The hybrid method opens up possibilities for the quantitative analysis of truly beam-sensitive nanomaterials.

In order to enable the reliable quantification of dynamic structural changes of nanomaterials at the atomic scale, the atom-counting procedure is extended from a single ADF STEM image to a time series of ADF STEM images. To this purpose, I introduce the so-called hidden Markov model in the field of electron microscopy. Hidden Markov models are successfully used in other fields of science for applications such as speech recognition and sequence alignment of

protein structures, owing to their optimal properties for modelling and analysing time series data. Indeed, using this hidden Markov model to perform time series atom-counting allows us to significantly surpass the performance of the hybrid method, which was developed for single frame analysis. In this manner, beam-induced changes in the morphology of a catalyst platinum nanoparticle could be quantified from an experimental time series of ADF STEM images.
A key parameter of the hidden Markov model that gives rise to this major improvement in the atom-counting performance is the so-called transition probability. This parameter is used to explicitly include the possibility of structural changes during the time series in the model. The transition probability represents the probability that an atomic column with a given thickness gains or loses one or more atoms from one frame to the next during the time series. Using the estimated transition probability, the probability of structural changes for the nanomaterial throughout the time series can be quantified. This can be used to estimate a dose independent measure, called the cross section (not to be confused with the previously mentioned scattering cross section), from the experiment. When the structural changes are caused by surface diffusion, this cross section can even be used to estimate the threshold energy for surface diffusion from the experiment. The threshold energy estimated in this manner from an experimental time series of a platinum wedge-shaped nanomaterial is in close agreement with theoretical calculations previously performed for this type of material. This confirms that the hidden Markov model can be used to reliably characterise dynamic structural changes at the atomic scale.
The hidden Markov model for atom-counting can also be applied to *in situ* experiments. For example, a catalytic gold nanoparticle was imaged at a constant elevated temperature inside the microscope. The counting results obtained using the hidden Markov model are combined with molecular dynamics relaxation in order to quantify the changes in the 3D atomic structure over time. Finally, a simulations study is used to demonstrate the possibilities of the hidden Markov model for a reliable quantification of the atomic structure in variable environmental conditions such as a gradually increasing temperature or an alternating gas flow.
In summary, the hidden Markov model for atom-counting is promising for revealing and quantifying the atomic structure when it evolves over time, for example, via surface diffusion, due to beam effects or during *in situ* experiments.

The *take-home message* from this thesis is that I have used statistical models to reliably quantify the changes in the structure of a nanomaterial at the atomic scale as a function of time. I could realise this by developing methods to count the number of atoms "behind" each other in the atomic columns of the nanomaterial from electron microscopy images. An important difference with single frame counting procedures is that the probability for atomic columns to lose or gain atoms from one frame to the next during the time series is estimated. This quantitative method opens up new possibilities for unravelling the time dependent structure-properties relation of a nanomaterial, which can ultimately lead to the more efficient design and production of nanomaterials with innovative applications.

Contents

1 General introduction

1.1 The relevance of nanomaterials

The goal of the research discussed in this thesis is to develop methods for the reliable characterisation of nanomaterials. Since academia is largely funded by government funding (read: tax payer's money), we start this introduction by explicitly stepping down from the ivory tower we're sometimes accused of living in [Berebichez 2019]. In this part we will therefore discuss the relevance of nanomaterials, not only for scientists, but for every single one of us. Over the last decades, nanotechnology and nanomaterials have become buzzwords. Most people have heard of nanoparticles, although not always with a positive connotation. Generalisations across different samples of particles composed of what is nominally the same material can lead to unjustifiable fear in the public opinion about all nanomaterials [Berube 2008]. Nanomaterials can exhibit highly interesting properties for a variation of promising applications. Therefore, the reliable study of nanomaterials is highly relevant. This brings us to the following question: what are nanomaterials exactly? Nanomaterials are materials with at least one dimension in the nanometer (nm) range, usually up to 100 nm, although there is still some debate about whether the physical dimensions are sufficient to define nanomaterials [Williams 2007]. A nanometer is a billion times smaller than a meter. As a comparison, a human hair has a diameter of approximately one micrometer (μm) - a million times smaller than a meter, as shown schematically in Figure 1.1. The infamous coronavirus has a diameter of 60-140 nm [Zhu 2020].

Nowadays, nanomaterials are being used in an increasing number of applications. Recently, the Belgian news was buzzing with concerns about the mouth masks that were freely distributed by the federal government [De Maeseneer 2021]. Those masks had an antimicrobial silver and titanium dioxide nanocoating. Silver nanoparticles are shown to have a higher efficiency as an antimicrobial agent as compared to bulk silver [Wilkinson 2011]. However, research using electron microscopy of the masks revealed that the nanoparticles are not only inside the fibers of the mask, but also on top [Sciensano 2021]. Upon inhalation, nanoparticles can have potentially harming effects in the human body, depending on their structural characteristics [Schmid 2016, Hadrup 2020]. A reliable characterisation during the production of the nanomaterials for such applications is therefore crucial.

Another application of nanomaterials in everyday life is sunscreen with titanium dioxide and

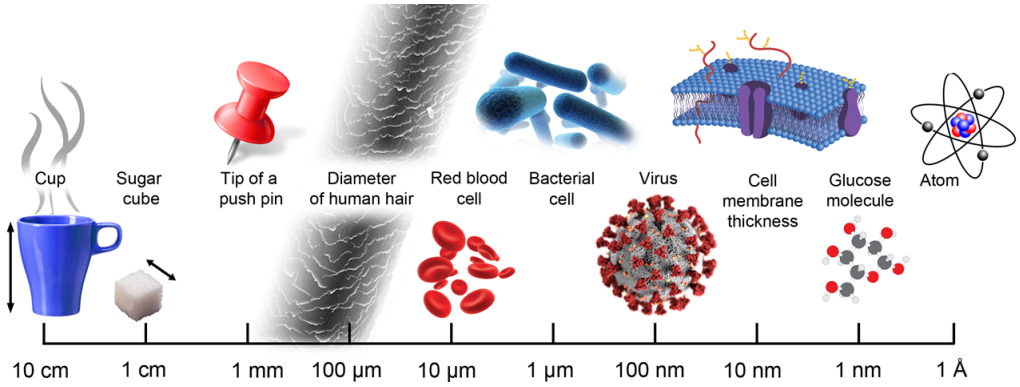

Figure 1.1: *Length scale of daily life objects down to the size range of nanomaterials. Figure adapted from [Claes 2018].*

zinc oxide nanoparticles. These nanoparticles are used in the emulsion because they provide an efficient absorption of ultraviolet (UV) light, while maintaining transparency [Lu 2018]. Industrial and technological applications include batteries and catalysts. For example in hydrogen fuel cells, catalysts are used to facilitate the electrochemical reaction [Coralli 2019]. Nanoparticles are highly interesting for catalysis because of the high surface area to volume ratio [Chen 2020]. However, the size of the nanoparticles used as catalysts has a crucial impact on the degradation of the catalyst [Sandbeck 2020]. Furthermore, nanomaterials are essential for the design of next generation lithium batteries in order to make them smaller, lighter and more powerful, for applications such as smartphones and electric cars [Lu 2016, Manthiram 2017].

Small differences in the atomic positions, of the order of a picometer (pm, 1000 times smaller than a nanometer), can drastically change the properties of a nanomaterial [Kisielowski 2001, Van Dyck 2012]. For example, such small changes in the interatomic distances can turn an insulator into a conductor [Locquet 1998], or can cause embrittlement, leading to fracture of the nanomaterial [Muller 1999, Wade 2016]. Furthermore, catalytic properties of a nanomaterial can even depend on single atoms [Thomas 2015, Egerton 2018]. When a single atom can make or break the desired properties of a nanomaterial, a reliable characterisation of the nanomaterials is essential, in order to evolve towards materials design. Materials science ultimately aims at understanding how the synthesis of a material influences its structure, and thus the material's properties and performance. Knowledge of the interrelationships among a material's properties, performance, processing and structure allows us to evolve from experimental observation, theoretical understanding and description of existing materials towards theoretical predictions and the actual production of new materials [Olson 2000, Yang 2012].

1.2 The relevance of statistical models

In order to achieve a reliable characterisation of nanomaterials, statistical models have been developed for the analysis of the properties such as atomic positions with the required precision [den Dekker 2005, Van Aert 2005, Van Aert 2009]. In this thesis, statistical model-based parameter estimation will therefore be applied in order to characterise the atomic structure of nanomaterials based on a dataset acquired using an electron microscope. The acquisition of this dataset is discussed in the next section. First, we consider the relevance of statistical modelling in order to interpret a given dataset in a more general context. The use of statistical models to characterise an experimental dataset is widely used in various fields of science.

When we talk about statistics - perhaps after thinking this was a topic you did not like in high school - some of the things that might come to mind are your chances to win the lottery, the average age and age distribution of the citizens in your city or the number of goals and assists made by your favourite football team. These are examples of chance theory and descriptive statistics. Often, descriptive statistics are sufficient to describe the average responses. While this can already provide insights in population distributions, modelling the distribution allows to go one step further. An example of statistical modelling that has recently become very tangible to the general public is the modelling of the evolution of the current pandemic. Modelling of the evolution of the number of hospitalisations and new infections can be used to model and even predict the effect of various health measures [Abrams 2021]. In order to make predictions, here the model components were constructed in a stochastic manner, to account for the inherent uncertainties in the number of infections as time progresses. An important advantage of statistical modelling is that the precision and accuracy can be quantified. As such, experiment design can be used to determine the optimal experimental conditions. In this manner, for example, the optimal experimental setup for quantification of the transmission between subjects in a pharmaceutical dose-response study could be determined [Price 2018].

An interesting model for the analysis of time dependent data such as the detection of epidemics [Rath 2003, Watkins 2009] is the so-called hidden Markov model. An often used dummy example to demonstrate this model is represented in Figure 1.2. The story goes as follows. Suppose that you are residing in an underground facility with no direct connection to the outside. The only way to know whether it is sunny, cloudy or rainy outside is to see whether external visitors bring an umbrella or not. The state of the weather is hidden, and the observations only contain indirect information on the state of that day. Through the analysis of a time series of observed data using a hidden Markov model, the hidden state sequence, in this case the sequence of the weather state, can be retrieved. The hidden Markov model indeed has real applications for weather forecasting [Khadr 2016, Joshi 2017], and can be found in many more scientific applications. Examples are application to gene sequencing [Eddy 2004], speech recognition [Gales 2007] and robotics [Kúlic 2008].

The arrows in Figure 1.2 represent probabilities, and as such, the hidden Markov model can be written as a parametric model, for which the parameters need to be estimated. Statistical parameter estimation deals with the estimation of the model parameters based on the dataset. Different types of estimators can be constructed to obtain an estimate for the model parameters. An important estimator often used to accurately and precisely estimate model parameters is the so-called maximum likelihood estimator. Applications of this type of parameter estimation can be found in various fields of science. For example, maximum likelihood estimation has

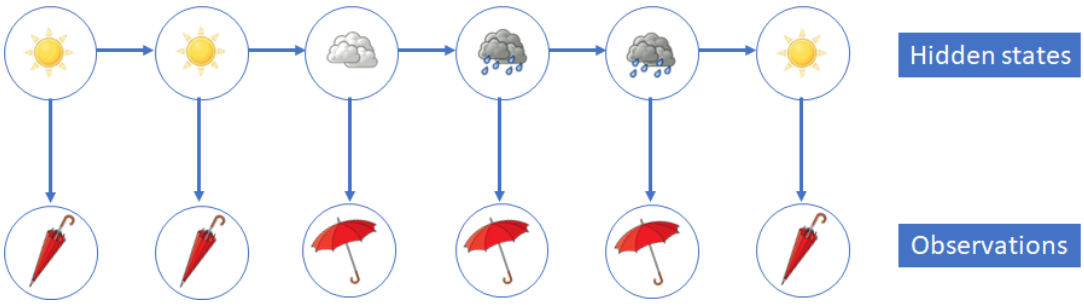

Figure 1.2: *Dummy example of a hidden Markov model used to model the hypothetical situation where the state of the weather (sunny, cloudy or rainy) can only be observed indirectly via an open or closed umbrella.*

been applied in survey research to estimate the proportions of yes and no answers to survey questions, surpassing the effect of subjects that refuse to answer or they may provide a socially desirable answer [Cruyff 2016]. In health sciences, the maximum likelihood estimator is often applied to structural equation modelling [Beran 2010], used for example to understand the relation between the size of newborns and the systolic blood pressure of these children at a later age [Dahly 2009].
In this thesis, nanomaterials will be studied using model-based statistical parameter estimation. Therefore, in the remainder of this introductory chapter, we illustrate how we can observe nanomaterials and how the observations can be quantified and related to the atomic structure of the nanomaterial.

1.3 "Looking" at nanomaterials

Because of the small size, we cannot simply look at a nanomaterial. Even magnifications achieved by a regular light microscope are not sufficient. A light microscope has a resolution limited to the order of 100 nm, owing to the relatively large wavelength of optical light (400-700 nm) [Heintzmann 2006]. Although superresolution provides a way to circumvent the diffraction limit [Heintzmann 2009], probing nanomaterials using a smaller wavelength enables a more precise study of the atomic structure. Possible candidates are X-rays, neutrons and electrons, with wavelengths that are up to a factor 100000 smaller [Cullity 1978, Howard 1994, Henderson 1995]. Alternatively, scanning tunnelling and atomic force microscopy provide information about the local surface structure without the need for lenses and beam irradiation, with atomic resolution [Wiesendanger 1994, Gross 2010]. X-ray and neutron diffraction techniques do not only provide information about the surface but about the inside of the material as well, albeit averaged structure information [Zanchet 2000]. Diffraction techniques are therefore very useful for the analysis of periodic materials, such as crystals, whereas they do not suffice for the analysis of nanomaterials which are usually aperiodic. An excellent technique to study nanostructures that provides non-averaged information about the entire material is atomic resolution transmission electron microscopy (TEM) because of the strong interaction of electrons with small volumes of matter [Henderson 1995]. A TEM instrument can be operated in imaging or diffraction mode. Electron diffraction allows the collection of data from smaller samples as compared to X-ray diffraction, even down to single crystals using electron diffraction tomography, at lower electron doses as compared to imaging modes of the TEM [Palatinus 2017, Gemmi 2019]. Imaging modes of the TEM on the other hand provide direct structure information. In convential TEM, a parallel electron beam is used to illuminate the sample, whereas in scanning transmission electron microscopy (STEM), the electron beam is focussed onto the sample and scanned in a two-dimensional (2D) raster pattern. The accelerated electrons used in the TEM interact with the interior of the nanomaterial and contain information about the positions and types of the atoms. When the scattered electrons are collected using an annular detector, the imaging mode is referred to as annular dark field (ADF) STEM. Interestingly, ADF STEM image intensities are sensitive to the chemical content of the nanomaterial and are thickness dependent [Nellist 2000].
High-technology developments in the lens design have greatly improved the image resolution [Haider 1998]. Nowadays, state-of-the-art instruments are available with a resolution of the order of 50 pm [Erni 2009, Takayanagi 2011, Akashi 2015]. For most atom types, this exceeds the point where the electrostatic potential of the atoms is the limiting factor [Van Dyck 2003]. This makes (S)TEM a particularly suitable technique for the study of nanomaterials. In addition, detectors behave more and more like ideal quantum detectors [Ruskin 2013], mak-

ing the microscope itself less restricting. Therefore, the quality of experimental images is mainly set by the unavoidable presence of electron counting noise and environmental disturbances [Jones 2013, Jones 2015].

1.4 Quantitative electron microscopy of nanomaterials

Looking at nanomaterials is one thing. However, in order to evolve towards new materials design and to understand physical properties of nanomaterials of different sizes and shapes, a quantitative interpretation of the images is required. As discussed earlier, the properties of a nanomaterial are strongly size dependent. As a validation for the production process, the distribution of the minimal external particle diameter can be quantified from low magnification TEM images [Verleysen 2019]. Many physical properties of nanomaterials, however, are determined by the local atomic structure. Therefore, in the field of atomic resolution electron microscopy, quantitative methods are becoming increasingly important for a reliable structure determination of a nanomaterial in three dimensions (3D). In order to study the atomic structure, numbers need to be extracted from the electron microscopy images, which ultimately allow one to quantify the positions and types of the atoms present in the nanomaterial. Therefore, quantitative electron microscopy is an essential tool in the characterisation of nanomaterials. Quantitative electron microscopy implies that images are treated as datasets, rather than assessed visually, in order to extract physical quantities such as size, positions of the atoms, thickness and type of atoms with high accuracy and precision. In this section, we discuss quantitative electron microscopy in general. A more detailed discussion on the concepts used to perform quantitative STEM in this thesis is given in Chapter 2.

Quantitative electron microscopy can be performed through comparison of the experimental image intensities to image simulations or by using statistical model-based techniques. When experimental image intensities are directly compared to image simulations on a pixel-by-pixel basis, an accurate and precise knowledge of all microscope parameters such as detector efficiency and aberrations is crucial [LeBeau 2008b, Dwyer 2012]. Furthermore, image intensities from the experimental electron microscopy image should first be put on an absolute scale. In TEM, quantification through comparison with image simulations is hampered by the so-called Stobbs factor, an often reported scaling problem between the simulated and experimental image contrast [Hÿtch 1994]. A lot of research has been invested to explain the origins of this discrepancy and achieve TEM image simulations on an absolute scale [Thust 2009, Van Dyck 2011, Forbes 2011, Krause 2013]. Alternatively to the comparison with image simulations, the so-called exit wave can be used to quantify the atomic structure from TEM images [Wang 2010, De Backer 2011, Wang 2012a]. The exit wave is the complex wave function of the electron as it exits the specimen at the bottom surface. This wave function contains information on the specimen, but upon detection of the coherent TEM image intensity, the phase information is lost. Therefore, the phase should be reconstructed, using focal series reconstruction, off-axis holography, or using a phase plate [Allen 2004, Erni 2010, Van Dyck 2010, Linck 2012]. For ADF STEM, the scaling problem between simulations and experimental images does not exist. Moreover, there is no phase problem, as this is an incoherent imaging technique. Furthermore, the robustness to microscope aberrations as well as the sensitivity to thickness improves significantly when the total intensity scattered from each atomic column is used as a measure for quantification, rather than the individual pixels or the peak intensities [E 2013, Martinez 2014a, Martinez 2018]. This integrated intensity is the so-called scattering cross section and can be quantified by integrating the intensities in a Voronoi cell around the atomic column positions [E 2013]. Alternatively, a parametric imaging model consisting of a super-

position of 2D Gaussian peaks can be fitted to the image intensities [Van Aert 2009]. The scattering cross sections are then quantified by the volumes under the 2D Gaussian peaks. The scattering cross sections have been used to determine the composition of nanomaterials [Van Aert 2009, Boschker 2011, Huijben 2013, Martinez 2014b], and to count the number of atoms in each atomic column of monatomic [LeBeau 2010, Van Aert 2011, Van Aert 2013, De Backer 2013, Jones 2014, De Backer 2015b, De Backer 2015a, De wael 2017] and mixed element [van den Bos 2016, van den Bos 2019] nanomaterials. Furthermore, the parametric imaging model provides precise estimates for the atomic column positions with a precision that surpasses the spatial resolution limit of the electron microscope [den Dekker 2005, Van Aert 2005]. When the electron dose is low, it becomes more challenging to correctly identify all atomic columns present in the STEM image. In such case, the maximum *a posteriori* (MAP) probability rule can be used to reliably detect each atomic column [Fatermans 2018, Fatermans 2019].

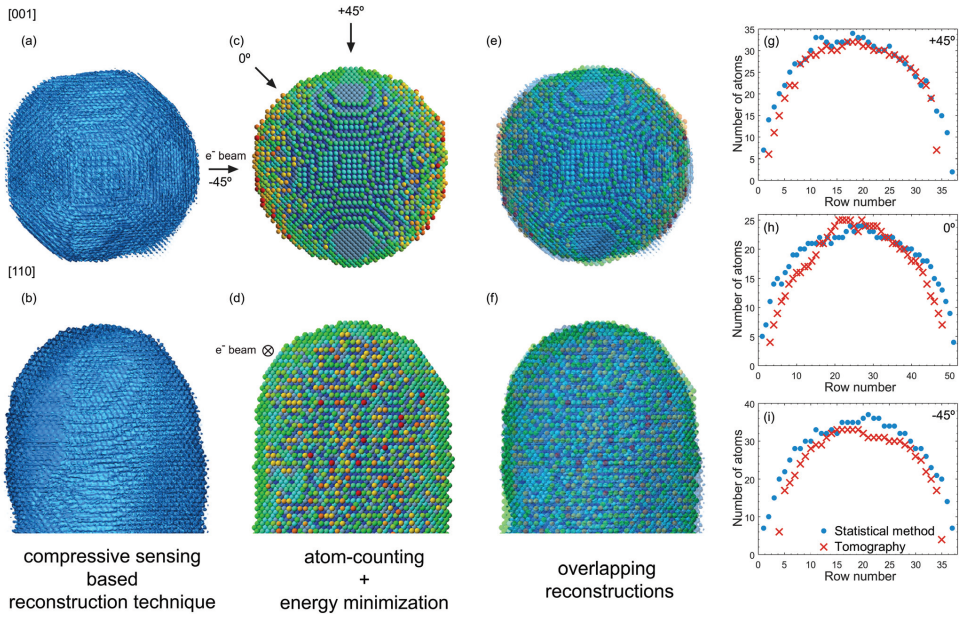

Figure 1.3: *Comparison of the 3D reconstructions based on atom-counting with energy minimisation and those obtained by atomic resolution tomography. Figure reproduced from [De Backer 2017].*

Images of nanomaterials provide 2D information about the 3D nanomaterials. However, in order to relate the properties to the atomic structure and evolve from materials science to materials design, a precise and accurate knowledge of the atomic structure in 3 dimensions is required. Electron tomography was designed to image nanomaterials in 3 dimensions. Over recent years, this has even evolved to atomic resolution electron tomography [Bals 2014]. Recently, the reconstruction of the 3D atomic structure of highly disordered nanomaterials was achieved [Yang 2021]. The main drawback of electron tomography is the long acquisition time for acquiring a tilt series, which is of the order of an hour, although fast acquisition schemes have been developed [Vanrompay 2018]. Many interesting nanomaterials are not stable enough to survive electron beam irradiation for such a long period [Meyer 2014, Egerton 2019]. In structural biology, damage due to beam irradiation is avoided by using cryo electron microscopy to reconstruct biological assemblies in 3D using so-called single particle analysis. Here, several images of different particles - presumed identical - are aligned and averaged [Frank 2006, Agard 2014, Rosenthal 2016]. In order to study only one nanoparticle, this cannot be applied. Therefore, retrieving the 3D atomic structure information from a few view-

ing directions or even from a single image is very promising in order to shorten acquisition times, to prevent beam damage, and avoid practical issues concerned with controlled tilting of a nanoparticle. Different approaches have been suggested, such as discrete tomography [Van Aert 2011, Bals 2011], iterative refinement by comparison on an absolute scale to image simulations [Jia 2014] and the combination of atom-counting with a structure relaxation [Bals 2012, Jones 2014, Geuchies 2016, De Backer 2017, Peters 2017, Altantzis 2019]. Recently, in [De Backer 2017], the 3D atomic structure obtained by relaxation of 2D counting results from a single viewing direction was validated using 3D atomic structure from atomic resolution electron tomography, as shown in Figure 1.3. From this work, it is clear that atom-counting from 2D images is a reliable approach to obtain 3D structural information, especially from nanostructures without voids which are roughly symmetrical along the electron beam in the electron microscope. Therefore, the methods for (2D) atom-counting developed in this thesis open up opportunities for the reliable quantification of the 3D atomic structure from low dose images and from time series of STEM images.

1.5 Quantification of dynamic structural changes

Many interesting phenomena are related to dynamic[†] behaviour of nanomaterials. A reliable quantification of crystal growth and nucleation, for example, plays a critical role in many physical and biological phenomena [Zhou 2019]. Depending on their size, the dynamics of nanoparticles can be very different [Batson 2008]. Atoms that lie on the surface facets of a catalyst nanoparticle can diffuse as a function of time, leading to dynamic changes in the active sites of the catalyst [Somorjai 1975, Tian 2007, Wang 2012b]. Furthermore, transformation between energetically excited configurations of small clusters [Bals 2012] or in situ studies of transformations of catalytic nanoparticles [Cao 2018] can give valuable insights in the properties. Nanomaterials in an electron microscope are exposed to the electron beam. Therefore, in many cases, beam-induced effects may occur during the experiment. Averaging all frames of a time series can therefore lead to a misinterpretation of the atomic structure [Peter 2017].

Different time-resolving techniques exist for the study of nanomaterials with very high temporal resolution, up to the order of femtoseconds (1 fs = 10^{-15} s). In ultrafast electron diffraction and microscopy, for example, packets of electrons are created using femtosecond pulses to stroboscopically illuminate the specimen [Barwick 2008]. In dynamic transmission electron microscopy (DTEM), nanosecond pulses with higher current density are used to form the image [Armstrong 2007, Browning 2012]. Using ultrafast X-ray imaging, intermediate states and mechanistic pathways that the molecules pass through as they transform can be studied owing to the very high temporal resolution [Chapman 2011, Lindenberg 2017]. A drawback of these techniques, however, is the limited spatial resolution [LaGrange 2012].

For many processes, however, (sub-)second temporal resolution can be sufficient, making it possible to achieve a higher spatial resolution in order to obtain local structural information at atomic resolution [Kotakoski 2014, Han 2015, Liu 2019]. In such cases, TEM or STEM images are acquired sequentially. In this manner, atomic scale dopant diffusion has been studied as a function of time [Ishikawa 2014]. By lowering the electron dose and dose rate, reversible atom displacements could be captured at video rates [Kisielowski 2013].

Despite the advantages of the STEM imaging mode, the high beam currents used in STEM imaging make the technique less suitable for the study of beam-sensitive nanostructures. Fur-

[†]Note that the term "dynamic" is often used in a different context to imply the presence of multiple scattering in thick samples [Glaeser 1993]. Here, the term dynamic changes is used to refer to changes as a function of time.

thermore, small beam-sensitive nanoparticles are very sensitive and will exhibit small amounts of sample tilt [Li 2008, Altantzis 2019]. In order to minimise radiation damage, the electron dose, i.e. the number of incident electrons used to record an electron microscopy image per unit of area in the material, should be reduced [Buban 2010, Egerton 2019]. Comparable to the use of a dimmed light source in light microscopy, imaging using a low electron dose in electron microscopy will result in more noisy images. This poses a challenge for reliable quantification, and requires advanced quantitative methods with a performance that can overcome a low signal-to-noise ratio. Alternative scan strategies have been developed to reduce the electron dose and the sensitivity to sample drift during acquisition [Béché 2016, Prabhakara 2020]. Furthermore, fast scanning approaches have been developed in STEM [Mittelberger 2018, Ishikawa 2020, Mullarkey 2020] that enable to achieve high temporal resolution and spatial resolution at the same time, through the acquisition of a time series. This introduces additional noise originating from the scanning. In order to overcome this limitation, rigid and non-rigid registration can be performed on the time series [Jones 2013, Yankovich 2014, Jones 2015]. Recently, a convolutional neural network was even developed to perform additional reconstruction of STEM images to compensate for different types of (scan) distortions [Altantzis 2019]. In this manner, STEM becomes a suitable instrument for the quantification of dynamic structural changes at the atomic scale, even at low electron doses and high scanning speeds. As mentioned earlier, hidden Markov models are highly useful for the reliable analysis of sequential data. Therefore, in this thesis, I introduce this model in the field of electron microscopy, in order to reliably quantify atomic scale dynamic structural changes from sequential STEM images.

1.6 Thesis outline

The goal of the research presented in this thesis is to use statistical parameter estimation theory and image simulations to obtain accurate and precise information on the atomic structural changes of nanomaterials as a function of time using annular dark field scanning transmission electron microscopy.

In Chapter 2, an introduction to the specific concepts of quantitative scanning transmission electron microscopy (STEM) used throughout this thesis is given. The principles of STEM image formation and simulation are briefly discussed and the principles of statistical parameter estimation theory are introduced. Next, a parametric imaging model for the quantification of STEM image intensities, and two currently existing approaches for atom-counting, based either on comparison to image simulations or on statistical parameter estimation theory, are discussed. In Chapter 3, an alternative parametric imaging model using elliptical rather than symmetrical peaks is investigated in order to quantify STEM image intensities in the presence of sample tilt. In Chapter 4, a hybrid statistics-simulations based approach for atom-counting is proposed to overcome limitations for small nanoparticles and for low electron doses of the current state-of-the-art atom-counting procedures. A validation using simulations and an experimental gold nanorod is performed, and the possibilities of this new method for atom-counting from lower dose acquisitions are demonstrated using experimental and simulated images of a small platinum/iridium nanoparticle. In Chapter 5, a novel methodology is presented to measure dynamic structural changes from a STEM time series at the atomic scale by performing reliable atom-counting as a function of time. This method is based on the so-called hidden Markov model and explicitly aims at an accurate and precise quantification of the changes, without misinterpreting noise fluctuations. The performance is demonstrated using simulations and by means of a comparison to the hybrid atom-counting methodology, which was not specifically designed

for time series analysis. An interesting parameter of the hidden Markov model that allows for improved atom-counting reliability from time series is the so-called transition probability. In Chapter 6, this transition probability is related to physical probabilities and cross sections for structural changes. Furthermore, the hidden Markov model for atom-counting from time series is applied to various experimental examples and the effect of variable environmental conditions causing structural changes is considered. Finally, in Chapter 7, general conclusions are drawn and future perspectives are discussed.

2

Introduction to quantitative scanning transmission electron microscopy

2.1 The scope of this chapter

Quantitative electron microscopy refers to the image processing of electron microscopy images in order to extract quantitative information about the material's structure and composition, whereas in qualitative electron microscopy the images are interpreted visually, without extracting any numerical data. In order to predict properties of materials using ab initio calculations, positions of the atoms need to be known with a high precision, in the picometer range [Kisielowski 2001, Van Dyck 2012]. Therefore, the quantitative interpretation of high resolution electron microscopy images of nanomaterials is an essential step towards materials design. In the field of atomic resolution electron microscopy, quantitative methods are becoming increasingly important for a reliable structure determination of a nanomaterial in three dimensions (3D) [Galindo 2007,De Backer 2016,Wang 2016,Nord 2017,de la Peña 2017,Madsen 2018]. In this chapter, the concepts of quantitative STEM that will be used throughout the remainder of this thesis are introduced.

Different approaches for the quantitative interpretation of scanning transmission electron microscopy (STEM) images exist. Either the image intensities are directly compared to image simulations, or an approach based on statistical parameter estimation theory can be followed. When experimental image intensities are directly compared to image simulations on a pixel-by-pixel basis, an accurate and precise knowledge of all microscope parameters such as detector efficiency and aberrations is crucial [LeBeau 2008b, Dwyer 2012]. The robustness to microscope aberrations as well as the sensitivity to thickness improves significantly when the total intensity scattered from each atomic column is used as a measure for quantification, rather than the individual pixels or the peak intensities [E 2013,Martinez 2014a,Martinez 2018]. This integrated intensity is the so-called scattering cross section and can be quantified reliably by fitting a parametric imaging model consisting of a superposition of Gaussian peaks to the image intensities [Van Aert 2009]. These scattering cross sections are highly suitable for atom-counting from monatomic nanomaterials, owing to their monotonic increase with increasing atomic column thickness. At present, two procedures for atom-counting exist. The first method is based on a direct comparison of the experimental scattering cross sections to scattering cross sec-

tions determined from image simulations [LeBeau 2010, Jones 2014]. The second method on the other hand uses considers the unavoidable presence of noise, and therefore uses statistical parameter estimation theory to determine the most likely number of atoms corresponding to each atomic column based on the set of scattering cross sections estimated from the experiment [Van Aert 2011, Van Aert 2013, De Backer 2013].

In Section 2.2, we will introduce the principle of STEM and describe the imaging mode that will be used throughout this thesis. Electron microscopy image simulations are briefly introduced in Section 2.3. The goal of this section is not to provide the full theory of image simulations for electron microscopy, but rather to discuss some practical considerations. Then, in Section 2.4, statistical parameter estimation theory for STEM images is introduced. We discuss the accuracy and precision of estimated parameters, and introduce the concepts Fisher information and Cramér-Rao lower bound (CRLB). This measure will be used to assess the precision of the parameter estimation of the methods introduced in the Chapters 4 and 5. Next, in Section 2.5, the parametric imaging model for the quantification of STEM image intensities is introduced for nanomaterials aligned in zone axis orientation. In Sections 2.6 and 2.7, we describe how the scattering cross sections can be used for atom-counting, respectively by using image simulations, or by using statistical parameter estimation theory. The advantages and limitations of these atom-counting approaches are illustrated. Finally, general conclusions on quantitative STEM are summarised in Section 2.8.

2.2 Annular dark field scanning transmission electron microscopy (ADF STEM)

In a STEM, schematically shown in Figure 2.1, the electron beam is focused into a fine probe, which is scanned across the sample in a two-dimensional (2D) raster. For each probe position, the electrons scattered towards the detector are integrated to determine the image intensity. An image of the sample is formed, displaying the integrated scattered intensities at the different probe positions. Different imaging modes exist for a STEM, depending on the type of signal that is collected, and the detector geometry. In annular dark field (ADF) STEM, the inner angle of the annular detector (β_1 in Figure 2.1) exceeds the probe convergence angle (α in Figure 2.1). Depending on the detector inner angle, imaging modes are called low angle (LA, $2\alpha > \beta_1 > \alpha$), medium angle (MA, $3\alpha > \beta_1 > 2\alpha$) or high angle (HA, $\beta_1 > 3\alpha$) ADF STEM respectively [Hovden 2012]. Alternatively, in annular bright field (ABF) STEM, the detector inner and outer angle are smaller than the probe convergence angle [Okunishi 2009, Findlay 2009]. In bright field (BF) STEM, the detector collects the central transmitted beam, resulting in a coherent image [De Graef 2003].
In the detector plane, a coherent convergent beam electron diffraction (CBED) pattern is formed. The intensity of one pixel in the ADF STEM image is determined by summing the CBED pattern over the area of the annular detector. Alternatively, the entire CBED pattern can nowadays be acquired on a pixelated detector, allowing to save a 2D image at each probe position, resulting in four-dimensional (4D) STEM [Yang 2015, Ophus 2019]. From such a 4D STEM dataset, it is then also possible to create 2D ADF STEM images with desired angular ranges [Fang 2019]. The contrast in the ADF STEM images arises from the overlap regions between the diffracted discs in the CBED pattern. The size of the hole in the annular detector largely determines the nature of the intensity in the final image. The higher the inner collection angle of the detector, the more incoherent the signal. As a result, the intensities

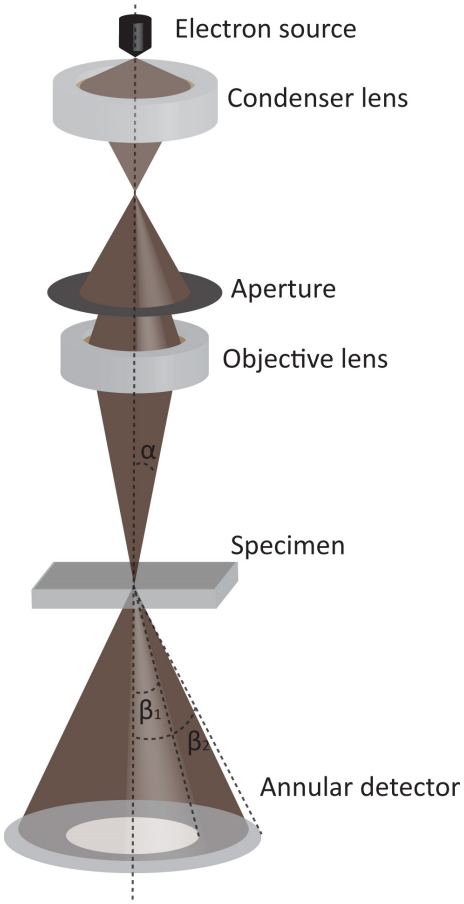

Figure 2.1: *Schematic representation of the image formation in the scanning transmission electron microscope (STEM) [Van Aert 2016].*

can be modelled as the convolution of a point spread function of the microscope and an object function determined by the projected potential of the atomic structure in the case of thin specimens [Nellist 2000]. In ADF STEM, both elastic and thermal diffuse (inelastic) scattered electrons reach the annular detector. At high enough scattering angle, diffraction contrast does not contribute, and the scattering can be described using Rutherford scattering, leading to Z-contrast [De Graef 2003]. Importantly, at high angles, thermal diffuse scattering (TDS) also plays a significant role in the image intensity. TDS arises from the thermal vibrations of the atoms in the crystal around their equilibrium positions. The small displacements of the atoms from their equilibrium position slightly destroys the translational symmetry, resulting in diffuse intensity in between the Bragg reflections. TDS contributes to the incoherent nature of the ADF STEM image [Pennycook 2011].
As an additional benefit of the STEM for the quantitative study of nanomaterials, simultaneous to the acquisition of an ADF STEM image, a second annular detector - or even a pixelated detector - can be used, for example to obtain an ABF image, which is useful for imaging light elements [Okunishi 2009, Findlay 2009, Lozano 2018, Fatermans 2020]. Furthermore, it is possible to simultaneously perform electron energy loss spectroscopy (EELS) or energy-dispersive X-ray (EDX) spectroscopy. This can aid chemical mapping of the atoms present in the nanomaterials [Dwyer 2013].
Owing to the incoherent nature of the ADF STEM images, intensities in ADF STEM images increase with increasing number of atoms in an atomic column [Anderson 1997]. This makes this

imaging mode particularly suitable for quantitative analysis of nanomaterials through atom-counting. Importantly, the total intensity scattered from an atomic column with two atoms does not simply equal twice the intensity scattered from a single atom, due to the so-called channelling effect [Loane 1988, Van Dyck 1996]. Traditionally, high angle annular dark field (HAADF) STEM is used to for the quantification of the atomic structure through atom-counting. However, optimal experiment design has shown that the HAADF STEM regime is not necessarily optimal for atom-counting. In order to extract the most precise counting results using the same electron dose, optimal imaging modes for quantification - rather than for visual interpretation - should be derived, balancing the detector collection area against the coherence of the image intensity [De Backer 2015a].
In the remainder of this thesis, model-based quantification of ADF STEM images will be used to characterise nanomaterials. Both image simulations and a statistical framework will be used for this quantification. These techniques are the topic of the remainder of this chapter.

2.3 Image simulations

In this section, we will briefly introduce image simulations for scanning transmission electron microscopy. The aim of this section is to describe the main principles, and discuss some practical aspects of setting up simulations correctly in order to obtain physically relevant images. Image simulations can serve as a reference for comparison of experimental electron microscopy images, and can as such help to perform quantitative STEM. To this purpose, the different parameters of the microscope used to acquire experimental images need to be reproduced. Equally important, but often overlooked, is the set-up of several simulation parameters to ensure realistic results. The aim of this section is not to reproduce the theory of image simulations, but to stress a few important aspects of image simulations to perform quantitative STEM. A full quantum mechanical derivation and detailed description of image simulations can be found in [Kirkland 2010].
Different approaches for advanced image simulations have been implemented for different modes of electron microscopy. Two main approaches exist for the calculation of the interaction of the electrons with thick specimens, using Bloch waves [Allen 2003, Findlay 2003, Kirkland 2010, Yamazaki 2013] or using the so-called multislice method [Cowley 1959, Bollig 1996, Ishizuka 2002, Croitoru 2006, Kirkland 2010, Dwyer 2010, Lobato 2015, Lobato 2016]. Recently, those two approaches have also been combined, in order to improve the speed, at the expense of a small loss in accuracy [Ophus 2017]. For thin specimens, the interaction of the electron probe with the specimen can be described by a multiplication of the electron probe with a transmission function depending on the specimen potential. For thick specimens, the multislice approach most accurately describes the electron-specimen interaction. In this approach, the sample is divided in several thin slices, as illustrated in Figure 2.2. In each slice, a transmission function is calculated and multiplied with the wave function. The resulting wave function after the slice is then propagated through free space to the next slice. The slice thickness should be chosen small enough, or coinciding with the lattice periodicity perpendicular to the slicing direction [Kirkland 2010].
Thermal vibrations of the atoms can be included in the image simulations using an absorptive potential [Ishizuka 2002, Allen 2003], the frozen phonon model [Loane 1991, Muller 2001, Koch 2002, Rosenauer 2007, Rosenauer 2008], or the more rigorous but equivalent quantum excitation of phonons based on a full quantum mechanical treatment [Van Dyck 2009, Forbes 2010, Allen 2015]. In the absorptive potential approach, the thermal vibrations of the atoms in the specimen are described by a damping factor that causes the intensity of diffracted

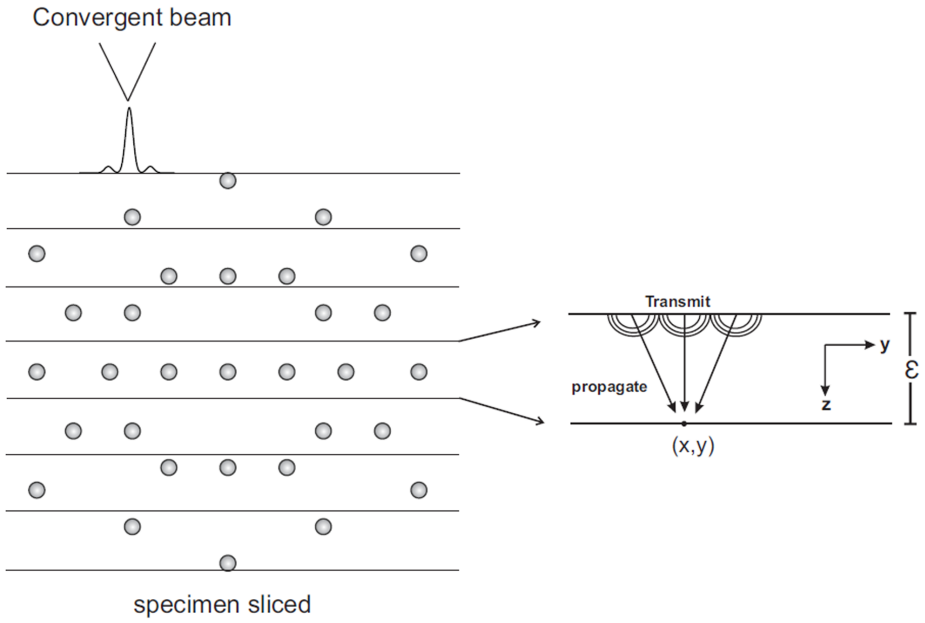

Figure 2.2: *Schematic representation of the multislice method [Alania 2017].*

beams to decrease, in order to account for the electrons that did not follow Bragg scattering. The frozen phonon model, on the other hand, models the thermal vibrations of the atoms in the specimen using many frozen phonon configurations. Each electron "sees" a different configuration, since the time the electron is inside the specimen and can interact with it is much smaller as compared to the period of thermal vibrations [De Graef 2003, Van Dyck 2009]. In each different configuration, the atoms are displaced compared to their crystalline positions according to a Debye-Waller factor [Gao 1999]. This material parameter can be obtained for example from molecular dynamics simulations, and is often assumed homogeneous for the whole specimen, although small variations on the image intensities can arise from inhomogeneous thermal vibration [Aveyard 2014]. This method is more time consuming as compared to the absorptive potential, since several multislice calculations are performed for different configurations of the atoms in the specimen, and averaged - after detection - to yield the final image [Van Dyck 2011]. The frozen phonon approach has been shown to be the most complete approach, as it is equivalent to a full quantum mechanical treatment if sufficient frozen phonon configurations are used [Van Dyck 2009]. Agreement with the absorptive potential is reached at certain detector angles and atom types [Findlay 2003, Rosenauer 2007, Alania 2018]. In this thesis, the image simulations have been performed using the MULTEM software package, which implements multislice calculations and the frozen phonon model [Lobato 2015, Lobato 2016].

Image simulations are performed using experimental parameters such as the acceleration voltage, probe convergence angle, aberrations of the incident electron beam and detector geometry as an input. The experimental set-up is matched accurately in order for the simulations to agree with the experiment [Findlay 2013, Martinez 2015, Jones 2016]. During the image simulations, the electron probe wave function is defined such that the integrated intensity of the incident electrons is equal to unity [Kirkland 2010]. As such, simulated image intensities are expressed as fractions of the incident electron dose. In order to use the image simulations for comparison with experimental images, both types of images therefore need to be put on an absolute scale, by taking into account the detector sensitivity [LeBeau 2008b, Rosenauer 2009, Martinez 2015, Krause 2016]. After image simulation, source size is included as a convolution

with an effective source size, typically taken as a Gaussian [Kirkland 2010].
In order to perform quantitative ADF STEM using simulated images, not only the specimen and microscope parameters should be carefully reproduced. Simulation-specific parameters such as simulation box size and potential sampling, both in real and reciprocal space, are also essential in order to obtain reliable image simulations. In real space, the pixel size of the potential sampling is determined by the simulation box size and the number of sampling points. Sufficient sampling avoids aliasing artefacts [Richardson 1978]. Additionally, in order to obtain a good sampling in reciprocal space, the simulation box size should be sufficiently large (50Å for example), even if the goal is to simulate a nanoparticle with smaller dimensions. A large simulation box yields a small pixel size for reciprocal space sampling ($1/50\text{Å}^{-1}$ in the aforementioned example). This set-up can be accomplished by adding a border of vacuum around the specimen when the sample size is smaller. Furthermore, this vacuum is useful in order to avoid so-called wrap-around errors when simulating a finite crystal [Kirkland 2010]. The wrap-around error arises from self-interference of the electron probe. Specifically, when the electron probe extends beyond the boundary of the simulation box, as it is wrapped around and re-enters the simulation box as a result of the periodicity requirement for the Fourier transforms performed during the image simulations [Richardson 1978]. Finally, sufficient sampling is also required to ensure enough coverage of the reciprocal space. The maximum spatial frequency in the simulations should exceed the maximum spatial frequency that corresponds to the outer detector angle, as well as the maximum spatial frequency at which the transfer function of the atom is still contributing [Van Dyck 2003]. A larger covering of the reciprocal space is always better, but also more time consuming. In practice, the reciprocal space should at least be covered up to 10Å^{-1}. More details on good practices for image simulations can be found in [Kirkland 2010].
The quantitative methods presented in the remainder of this thesis rely on image simulations as well as on statistical parameter estimation theory. Therefore in the next section, some basic principles of parameter estimation are introduced.

2.4 Accurate and precise model-based statistical parameter estimation

In order to perform a reliable quantitative analysis of STEM data, statistical parameter estimation theory has been introduced in the field of electron microscopy [den Dekker 2005, Van Aert 2005, Van Aert 2009]. This statistical framework considers the data recorded during a STEM experiment as the outcome of a statistical event. Therefore, the observed data should be regarded as a stochastic variables $\boldsymbol{X} = (X_1, \cdots, X_M)$. The expectation value of a stochastic variable X_m is expressed as follows:

$$\mathbb{E}[X_m] = \int_{-\infty}^{+\infty} x_m p(\boldsymbol{x}) d\boldsymbol{x}, \tag{2.1}$$

in case of continuous observed data. In this expression, $p(\boldsymbol{x})$ represents the continuous joint probability density function of the stochastic variables $\boldsymbol{X}$, where $\boldsymbol{x} = (x_1, \cdots, x_M)^{\mathsf{T}}$ are continuous independent variables related to the observed data, used to evaluate the joint probability density function. For discrete data, the integral should be replaced by a summation, and $p(\boldsymbol{x})$ is referred to as the joint probability function.
The variance of a stochastic variable X_m is defined as follows:

$$\text{var}(X_m) = \mathbb{E}\left[(X_m - \mathbb{E}[X_m])^2\right]. \tag{2.2}$$

In model-based statistical parameter estimation, the joint probability (density) function $p(\boldsymbol{x})$ is described as a parametric model $p(\boldsymbol{x}|\boldsymbol{\theta})$ depending on one or more parameters $\boldsymbol{\theta} = (\theta_1, \cdots, \theta_K)^\mathsf{T}$ [van den Bos 2007]. Different estimators $\hat{\theta}_k$ can be constructed to estimate the value of the parameter θ_k. Therefore, the estimator is also regarded as a stochastic variable, with an accuracy and precision that can be assessed using the expectation value and variance. Accurate and precise estimates of the unknown parameter(s) θ_k of this model can then be used to reliably quantify relevant physical parameters based on the experimental dataset. An estimator $\hat{\theta}_k$ of a parameter θ_k is accurate, or unbiased, if the expectation value coincides with the true value of the parameter. In this case, the bias is zero:

$$\mathbb{E}[\hat{\theta}_k] - \theta_k = 0. \tag{2.3}$$

For estimators of multiple parameters, the variance of equation (2.2) is generalised to the covariance matrix:

$$\begin{aligned} \mathrm{cov}(\hat{\boldsymbol{\theta}}, \hat{\boldsymbol{\theta}}) &= \mathbb{E}\left[\left(\hat{\boldsymbol{\theta}} - \mathbb{E}\left[\hat{\boldsymbol{\theta}}\right]\right)\left(\hat{\boldsymbol{\theta}} - \mathbb{E}\left[\hat{\boldsymbol{\theta}}\right]\right)^\mathsf{T}\right], & (2.4) \\ &= \begin{pmatrix} \mathrm{var}(\hat{\theta}_1) & \mathrm{cov}(\hat{\theta}_1, \hat{\theta}_2) & \cdots & \mathrm{cov}(\hat{\theta}_1, \hat{\theta}_K) \\ \mathrm{cov}(\hat{\theta}_2, \hat{\theta}_1) & \mathrm{var}(\hat{\theta}_2) & \cdots & \mathrm{cov}(\hat{\theta}_2, \theta_K) \\ \vdots & & \ddots & \vdots \\ \mathrm{cov}(\hat{\theta}_K, \hat{\theta}_1) & \mathrm{cov}(\hat{\theta}_K, \hat{\theta}_2) & \cdots & \mathrm{var}(\hat{\theta}_K) \end{pmatrix}. & (2.5) \end{aligned}$$

Each different estimator $\hat{\theta}_k$ that can be constructed to estimate the same unknown parameter θ_k can have a different precision, quantified by $var(\hat{\theta}_k)$. For unbiased estimators, the attainable precision is quantified by the Cramér-Rao lower bound, which defines the lower bound on the variance [Rao 1945, Cramér 1946]:

$$\mathrm{cov}(\hat{\boldsymbol{\theta}}, \hat{\boldsymbol{\theta}}) \geq F_{\boldsymbol{\theta}}^{-1}, \tag{2.6}$$

with $\hat{\boldsymbol{\theta}}$ the estimator of the parameters $\boldsymbol{\theta}$, and $F_{\boldsymbol{\theta}}$ the Fisher information matrix, which is defined as follows:

$$F_{\boldsymbol{\theta}} = -\mathbb{E}\left[\frac{\partial^2 \ln p(\mathbf{X}|\boldsymbol{\theta})}{\partial \boldsymbol{\theta} \partial \boldsymbol{\theta}^\mathsf{T}}\right], \tag{2.7}$$

where $p(\mathbf{x}|\boldsymbol{\theta})$ represents the joint probability (density) function.
The efficiency of an unbiased estimator can now be defined as the ratio of the Cramér-Rao lower bound and the variance of the estimator. An estimator whose efficiency tends to unity for an increasing sample size is called asymptotically efficient [van den Bos 2007]. An example of an unbiased estimator whose variance asymptotically reaches the Cramér-Rao lower bound is the maximum likelihood estimator (MLE). A maximum likelihood estimate of the parameter vector can then be obtained by maximising the likelihood function:

$$\hat{\boldsymbol{\theta}} = \arg\max_{\boldsymbol{t}} L(\boldsymbol{t}) \tag{2.8}$$

where the likelihood is derived from the joint probability (density) function by evaluating it at the observed data points $\mathbf{x} = (\mathsf{x}_1, \cdots, \mathsf{x}_M)^\mathsf{T}$ as a function of the independent variables $\boldsymbol{t}$ that are substituted for the unknown parameters $\boldsymbol{\theta}$ and used to evaluate the likelihood function during the maximisation procedure:

$$L(\boldsymbol{t}) = p(\mathbf{x}|\boldsymbol{t}). \tag{2.9}$$

Under the assumed statistical model, described by the joint probability (density) function, the maximum likelihood estimates of the parameters are most likely to have produced the observed data. Throughout this thesis, maximum likelihood estimators will be used to draw conclusions on the atomic structure of nanomaterials studied using electron microscopy. In a quantitative STEM experiment, the aim is to quantify the atomic structure properties, such as atomic column positions, number of atoms, the type of atoms present in the nanomaterial, which are not directly observed, but can be studied using STEM images. The observations are in first instance the pixel values of the STEM image, related to these atomic structure properties. Model-based parameter estimation theory aims at estimating the parameters of a parametric model that describes the expectation values of the observed data as a function of the relevant physical parameters.
In the next section, we will discuss how the image intensities from an ADF STEM image are interpreted as a dataset for statistical parameter estimation theory.

2.5 Parametric imaging model for ADF STEM images

In this section, we will discuss how experimental atomic resolution ADF STEM images can be treated in order to perform a reliable quantitative analysis. To this purpose, the pixel values w_{kl} for each pixel (k, l) of a $K \times L$ ADF STEM image are summarised in a vector:

$$\mathbf{w} = (w_{11}, w_{12}, \cdots, w_{KL}). \tag{2.10}$$

This is the set of observations obtained from the ADF STEM experiment. An example is shown in Figure 2.3a for a gold nanorod. The inset of the figure shows a magnified part of the image. Each set of observations obtained from an experiment performed under the same experimental conditions will unavoidably be different due to the presence of noise. In other words, any other image acquired of the same gold nanorod under the same conditions will display slightly different pixel values. Therefore, the pixel intensities are stochastic variables. The expectation value of the ADF STEM image intensity at pixel (k, l) can be described using a parametric imaging model:

$$\mathbb{E}[w_{kl}] = f_{kl}(\boldsymbol{\theta}), \tag{2.11}$$

with $\boldsymbol{\theta}$ the parameter vector that contains the unknown parameters. In the parametric imaging model, ADF STEM image intensities are modelled as incoherent contributions originating from the different atomic columns in the crystalline nanomaterial. As discussed in Section 2.2, the image intensities in an ADF STEM image increase with an increasing atomic mass number Z and with increasing specimen thickness. Furthermore, image intensities are peaked at the atomic column positions. The expectation values of the image intensities are therefore modelled as a superposition of 2D Gaussian peaks [Van Aert 2009, De Backer 2013, De Backer 2016, De Backer 2021a]. The expectation value of the image intensity at pixel (k, l) with position (x_k, y_l) in the image is given by:

$$f_{kl}(\boldsymbol{\theta}) = \zeta + \sum_{n=1}^{N} \eta_n \exp\left(-\frac{(x_k - \beta_{x_n})^2 + (y_l - \beta_{y_n})^2}{2\rho^2}\right). \tag{2.12}$$

In this expression, ζ is a constant background present in the image, ρ is the width of the 2D Gaussian peaks, η_n is the height of the n^{th} Gaussian peak, β_{x_n} and β_{y_n} are the x- and y-coordinate of the n^{th} atomic column, and N is the total number of atomic columns in the image. The unknown parameters are summarised in the parameter vector:

$$\boldsymbol{\theta} = (\beta_{x_1}, ..., \beta_{x_N}, \beta_{y_1}, ..., \beta_{y_N}, \rho, \eta_1, ..., \eta_N, \zeta)^{\mathsf{T}}. \tag{2.13}$$

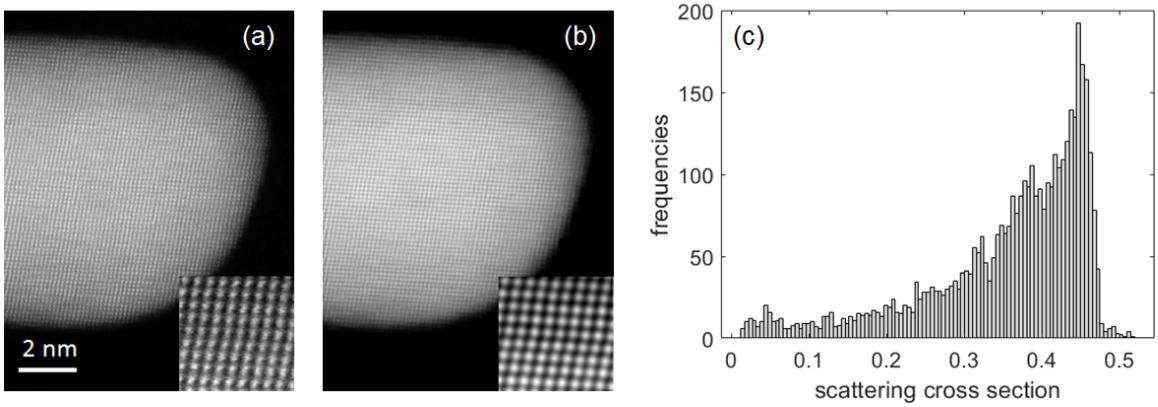

Figure 2.3: *(a) HAADF STEM image of a gold nanorod [Van Aert 2013]. (b) Estimated parametric imaging model consisting of superimposed 2D Gaussian peaks. (c) Set of estimated scattering cross sections, estimated using Equations* (2.14) *and* (2.15)*.*

The parametric model of Equation (2.12) is fitted to the experimental ADF STEM image using a least squares criterion, which is identical to the maximum likelihood estimator for independent and identically normally distributed pixel values [van den Bos 2007, De Backer 2016]. In this manner we obtain a least squares estimate for the unknown parameter vector:

$$\hat{\theta} = \arg\min_{\mathbf{t}} \sum_{k=1}^{K} \sum_{l=1}^{L} (w_{kl} - f_{kl}(\mathbf{t}))^2. \tag{2.14}$$

This is done using an iterative optimisation algorithm, which was implemented efficiently in the StatSTEM software package [De Backer 2016]. The parametric model estimated for the gold nanorod in this manner is shown in Figure 2.3b. Starting values for the atomic column positions can be obtained manually or from a simple peak finding routine. However, especially for low electron doses, noise in the images can make it difficult to discern the individual atomic columns, and a statistical approach is recommended. The so-called maximum *a posteriori* (MAP) rule for detection of atomic columns was specifically designed for challenging images with low doses or very light elements [Fatermans 2018, Fatermans 2019]. In this manner, the least squares estimates $(\hat{\beta}_{x_n}, \hat{\beta}_{y_n})$ are an accurate and precise estimate for the atomic column positions [den Dekker 2005, Van Aert 2005, De Backer 2016].
Furthermore, the so-called scattering cross section for each atomic column n can be estimated as the volume under the 2D Gaussian peaks in the model:

$$\hat{V}_n = 2\pi\hat{\eta}_n\hat{\rho}^2. \tag{2.15}$$

The scattering cross section is a measure for the total intensity of electrons scattered from an atomic column in the nanomaterial towards the ADF STEM detector. The set of scattering cross sections estimated from the gold nanorod in this manner is shown in Figure 2.3c. Alternatively, the scattering cross section can also be estimated from the ADF STEM images directly, without statistical parameter estimation, by integrating the experimental intensities in Voronoi cells [E 2013]. In this approach, however, the overlap between neighbouring atomic columns is not taken into account, and it was shown that the volumes of the 2D Gaussian peaks are more reliable for a correct quantification [De Backer 2016]. Scattering cross sections increase with increasing sample thickness and with increasing atomic mass number Z. They

have therefore been used to analyse atomic composition [Van Aert 2009, Rosenauer 2011, Martinez 2014b] and for atom-counting [LeBeau 2008a, Van Aert 2011, De Backer 2013, Jones 2014, De Backer 2015b]. The procedure for atom-counting using scattering cross sections will be discussed in more detail in the next part of this chapter.

2.6 Image simulations-based atom-counting

Two approaches exist for counting the number of atoms in each atomic column of a nanomaterial in a main zone axis orientation from ADF STEM images. The first approach uses a direct comparison of the experimental image intensities with image intensities obtained from image simulations. The second approach is independent of image simulations and uses statistical parameter estimation theory. This will be the topic of Section 2.7. In this part, we discuss the procedure for atom-counting using image simulations.
This first atom-counting procedure is based on a direct comparison of the scattering cross sections estimated from the experimental image with scattering cross sections obtained from carefully performed image simulations [LeBeau 2010, Jones 2014]. In the remainder of this thesis, this method will be referred to as the image simulations-based method for atom-counting. To this purpose, a so-called library of simulated scattering cross sections is created. An example of such a library corresponding to the gold nanorod shown previously in Figure 2.3 is shown in Figure 2.4a. The scattering cross sections are obtained from image simulations of a bulk crystal of the same element and crystallographic orientation as the nanomaterial in the experiment. Note that scattering cross sections are preferred over peak intensities as a measure for atom-counting, thanks to their robustness to aberrations [Martinez 2014a]. Furthermore, they increase monotonically with thickness, whereas the peak intensities reach a plateau [De Backer 2015a, Martinez 2018]. Importantly, the image simulations are performed using the same microscope parameters such as acceleration voltage, detector angles etc., as the experiment. Note that channelling causes a non-linear increase of the scattering cross sections with increasing thickness [Van Dyck 1996]. Therefore, image simulations are performed for a range of sample thicknesses. Using multislice simulations, running multiple calculations can be avoided by saving intermediate results at slices in steps of the lattice parameter c. Additional computation time can be saved by only scanning one unit cell of the bulk crystal. It is important to note that a sample with larger xy-dimensions should be used during the simulations, even when scanning only one unit cell, in order to avoid wrap-around errors and use sufficient sampling, as mentioned before in Section 2.3. In order to obtain the scattering cross sections from the image simulations, the intensities from the simulated unit cell can be summed, or the central column can be fitted using the parametric imaging model introduced in the previous section. In the latter case, an additional convolution with a Gaussian is performed, in order to account for the source size broadening caused by spatial incoherence of the incident electron probe [Klenov 2007, Kirkland 2010].
From these image simulations, scattering cross sections are quantified for the material of interest, using the used experimental imaging parameters, as a function of the number of atoms in an atomic column. Note that the library has to be tailored to each individual experiment. Image intensities in the simulated ADF STEM images are expressed in fractions of the incident electron dose. Therefore, in order to allow for a quantitative comparison, the ADF STEM image intensities of the experimental image need to be normalised to the incident electron beam by taking into account the detector sensitivity [LeBeau 2008b, Rosenauer 2009, Martinez 2015, Krause 2016]. Atom counts can then be assigned to each atomic column based on the closest match between the (normalised) experimental and simulates scattering cross sec-

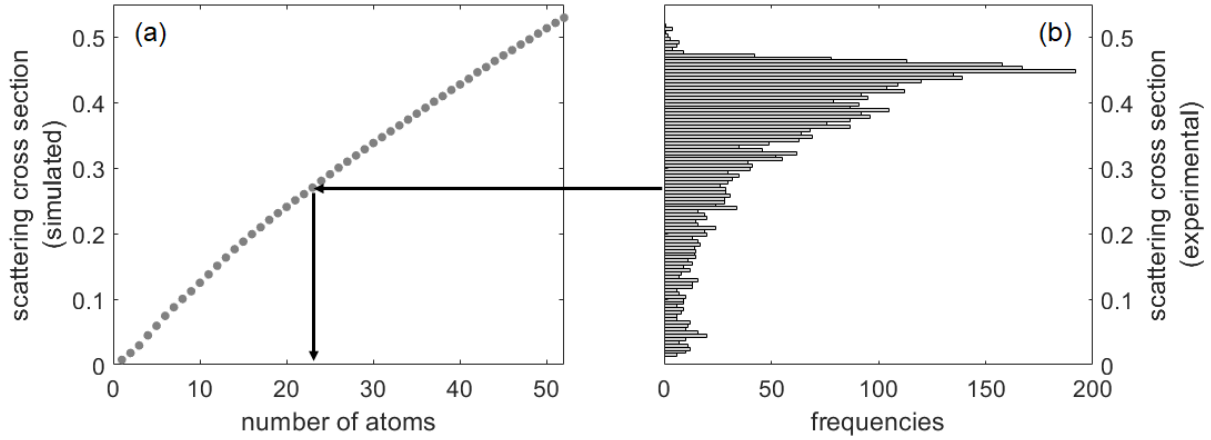

Figure 2.4: *(a) Library with scattering cross sections determined from simulations at different thicknesses. (b) Set of scattering cross sections estimated from the parametric imaging model of the HAADF STEM image of a gold nanorod shown in Figure 2.3. Atom-counts are obtained by a direct comparison of the scattering cross sections estimated from the experimental image with scattering cross sections obtained from image simulations.*

tions. In Figure 2.4, the principle of this atom-counting method is visualised.
This image simulations-based method for atom-counting is therefore very intuitive and simple to implement. Among several applications, this approach was used to count the number of atoms from a wedge-shaped gold film [LeBeau 2010] and catalyst platinum nanoparticles [Jones 2014, Aarons 2017]. An important limitation of this atom-counting approach is that small mismatches between the actual and the simulated experimental set-up, such as a different detector inner angle or sample tilt, can influence the simulated image intensities significantly. These systematic errors can remain undetected and the reliability of the quantitative analysis therefore depends solely on the accuracy of the simulations to match the experiment [Van Aert 2013, Jones 2016]. Furthermore, this method does not provide a measure for the precision of the atom-counts. It is worth noting that over the last few years, techniques for the characterisation of these experimental parameters have strongly improved [Jones 2016, Dwyer 2012, Findlay 2013, Mehrtens 2013, Martinez 2015, Krause 2016].
Alternatively, atoms can be counted using a statistical parameter estimation theory framework. In this statistics-only based method, simulations are no longer needed, and undetected systematic errors can be avoided, as will be discussed in the next section.

2.7 Statistics-based atom-counting

The scattering cross sections estimated from an ADF STEM image are inherently random in nature as a consequence of various noise contributions such as electron counting statistics, instabilities of the microscope, different vertical onset of columns of the same number of atoms, vacancies, relaxation at the boundaries, contamination, intensity transfer between columns, and the influence of neighbouring columns of different number of atoms. Scattering cross sections corresponding to various atomic columns with a given number of atoms g will therefore not be identical, but fluctuate around an average scattering cross section μ_g. This distribution can be modelled as a Gaussian distribution for each thickness g present in the sample [Van Aert 2011, Van Aert 2013, De Backer 2013, De Backer 2021b]. Together, this results in a Gaussian mixture

model with G Gaussian components[†], where G is the number of different thicknesses present in the sample:

$$f_{\text{mix}}\left(V_n|\mathbf{\Psi}_G^{\text{stat}}\right) = \sum_{g=1}^{G} \pi_g \mathcal{N}\left(V_n|\mu_g, \sigma\right), \tag{2.16}$$

with

$$\mathcal{N}\left(V_n|\mu_g, \sigma\right) = \frac{1}{\sqrt{2\pi}\sigma} \exp\left(-\frac{(V_n - \mu_g)^2}{2\sigma^2}\right), \tag{2.17}$$

the Gaussian components. The joint probability density function of all scattering cross sections is then given by

$$p(\mathbf{V}|\mathbf{\Psi}_G^{\text{stat}}) = \prod_{n=1}^{N} \sum_{g=1}^{G} \pi_g \mathcal{N}\left(V_n|\mu_g, \sigma\right). \tag{2.18}$$

The mixing proportion π_g of the g^{th} component indicates which fraction of the columns in the image have a specific number of atoms corresponding to the g^{th} component, i.e. the weight of the g^{th} component in the Gaussian mixture model. Furthermore, in this expression μ_g represents the location, i.e. the average scattering cross section value, of the g^{th} component in the mixture model and σ the width of the components, while V_n represents the stochastic variable related to the n^{th} scattering cross section, estimated by Equation (2.15). The stochastic variables for all scattering cross sections are summarised in the vector $\mathbf{V}$. The vector $\mathbf{\Psi}_G^{\text{stat}}$ is the parameter vector containing all unknown parameters to be estimated in a Gaussian mixture model with G components:

$$\mathbf{\Psi}_G^{\text{stat}} = (\pi_1, ..., \pi_{G-1}, \mu_1, ..., \mu_G, \sigma)^{\mathsf{T}}. \tag{2.19}$$

Note that π_G is not estimated, since the sum of all G mixing proportions must equal one, and therefore $\pi_G = 1 - \sum_{g=1}^{G-1} \pi_g$. This means that $2G$ parameters need to be estimated to determine the mixture model completely, and therefore be able to count atoms.

The width of the components σ relates to the amount of fluctuation on the scattering cross sections corresponding to atomic columns with the same thickness. It is common practice to assume homoscedastic components, i.e. a constant width σ for all components, in order to estimate the contribution of all noise contributions in a robust manner [De Backer 2013].

The parameters $\mathbf{\Psi}_G^{\text{stat}}$ of the probability distribution of the scattering cross sections are estimated, by maximising the likelihood function. As described earlier in Section 2.4, the expression for the likelihood function has the same functional form as the joint probability density function, but is evaluated as a function of the parameters rather than as a function of the stochastic variables related to the observed data. Specifically for this expression, the observed scattering cross sections $\hat{\mathbf{V}}$, estimated from the ADF STEM image as described in Section 2.5, are inserted:

$$L(\mathbf{\Psi}_G^{\text{stat}}) = p(\hat{\mathbf{V}}|\mathbf{\Psi}_G^{\text{stat}}) = \prod_{n=1}^{N} f_{\text{mix}}\left(\hat{V}_n|\mathbf{\Psi}_G^{\text{stat}}\right). \tag{2.20}$$

The parameter estimates are iteratively calculated using the expectation maximisation (EM) algorithm [Dempster 1977]. In Figure 2.5a, the Gaussian mixture model from Equation (2.16) with parameters estimated using the maximum likelihood estimation in this manner for the gold nanorod of Figure 2.3 is plotted on top of the set of scattering cross sections represented in a

[†]Throughout this thesis, the term Gaussian peaks will be used for the 2D Gaussians used in the parametric imaging model introduced in Section 2.5, while the term Gaussian components will be used for the 1D Gaussian distributions that model the distribution of the scattering cross sections for a given thickness.

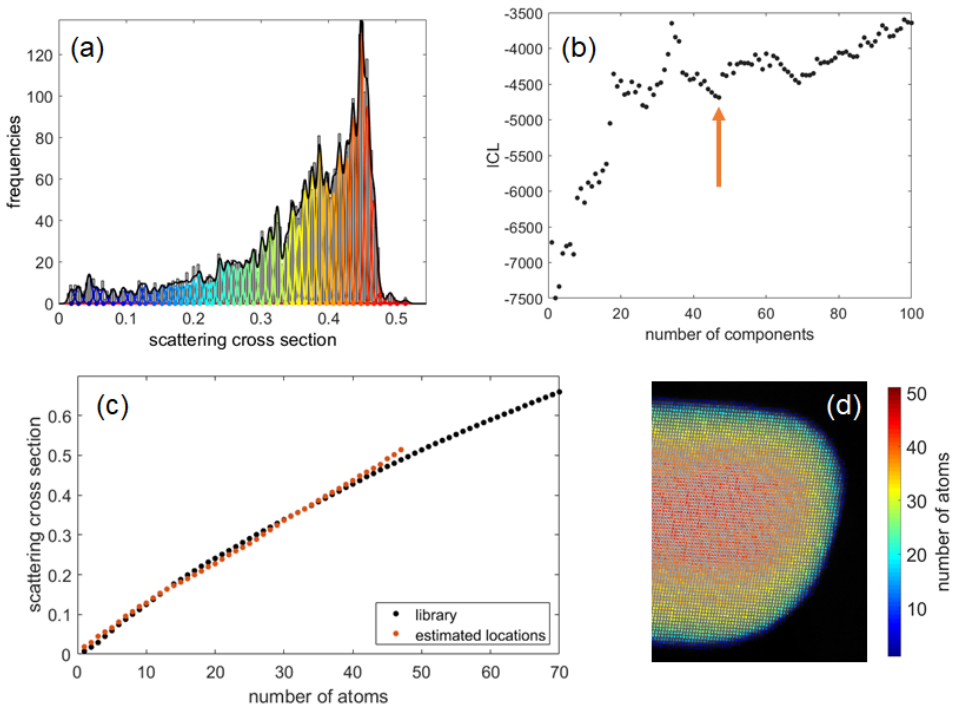

Figure 2.5: *(a) Set of scattering cross sections estimated from the parametric imaging model of the HAADF STEM image of a gold nanorod shown in Figure 2.3. The solid black curve shows the estimated Gaussian mixture model, whereas the coloured curves indicate the individual components. (b) ICL criterion. The arrow indicates the selected number of components of the Gaussian mixture model. (c) The estimated locations of the Gaussian mixture model are validated by the library from image simulations. (d) Atom-counts for the gold nanorod obtained by the statistics-based method for atom-counting.*

histogram. Note that the parameters are estimated independently from the arbitrary choice of the number of bins used to represent the scattering cross sections in a histogram.

So far, we have considered the estimation of the probability distribution of the scattered intensities presuming a specific number of components G. However, due to the noise, it is impossible to accurately determine the correct number of components based on a visual interpretation of the set of scattering cross sections displayed in the histogram. Furthermore, this would be subjectively dependent on the chosen number of bins to represent the scattering cross sections in the histogram. Therefore, an order selection criterion which balances the model likelihood against the model complexity is introduced to select the correct number of components G. The model order corresponds to a local minimum in the order selection criterion evaluated as a function of the number of components. Many different information criteria exist [McLachlan 2000], but the Integrated Classification Likelihood (ICL) criterion [Biernacki 2000] has been shown to have the best performance for atom-counting [De Backer 2013]. The ICL criterion is expressed as follows:

$$ICL(G) = -2 \log L(\hat{\boldsymbol{\Psi}}_G^{\text{stat}}) + 2EN(\hat{\tau}) + d \log N, \tag{2.21}$$

with $-2 \log L(\hat{\boldsymbol{\Psi}}_G^{\text{stat}})$ the likelihood term depending on the estimated parameters $\hat{\boldsymbol{\Psi}}_G^{\text{stat}}$ and $2EN(\hat{\tau})+d \log N$ the penalty term depending on the sample size N, the number of parameters $d = 2G$

and an entropy term:

$$EN(\hat{\tau}) = -\sum_{g=1}^{G}\sum_{n=1}^{N} \tau_g\left(\hat{V}_n|\hat{\mathbf{\Psi}}_G^{\text{stat}}\right)\log\tau_g\left(\hat{V}_n|\hat{\mathbf{\Psi}}_G^{\text{stat}}\right), \tag{2.22}$$

with $\tau_g\left(\hat{V}_n|\hat{\mathbf{\Psi}}_G^{\text{stat}}\right)$ the posterior probability that the estimated scattering cross section of the n^{th} column $\hat{V}_n$ belongs to the g^{th} component. This entropy term favours mixture models with well-separated components, in order to estimate physically relevant Gaussian mixture models. The ICL criterion for the gold nanorod is shown in Figure 2.5b. The arrow indicates the selected local minimum at 47 components. The selection of this local minimum was aided by prior knowledge on the symmetric shape of the nanorod, and is validated by comparison with independent image simulations, as shown in Figure 2.5c.
For the true number of components G, the obtained locations μ_g of the components correspond to the average scattering cross sections for sets of atomic columns with the same number of atoms. Counting results can therefore be obtained by assigning the scattering cross section of each atomic column to the component of the estimated probability distribution with the largest probability for this scattering cross section. The precision of the counting results is therefore limited by the overlap between the Gaussian components.
For the gold nanorod example, the counting results were obtained with single atom sensitivity in this manner, and are shown in Figure 2.5d.

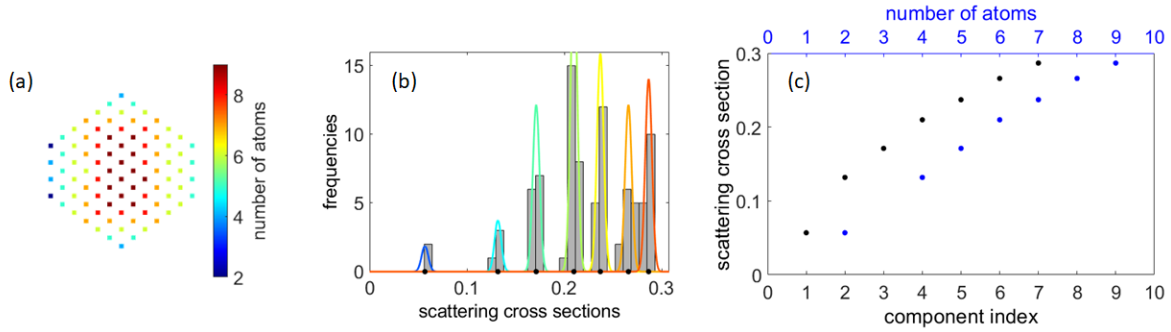

Figure 2.6: *(a) Number of atoms in each column of a nanoparticle. There are no atomic columns with 1 or 3 atoms. (b) Gaussian mixture model plotted on top of the set of estimated scattering cross sections using the same colour scale as in (a) to indicate the number of atoms. (c) Intensity/thickness graph, displaying the estimated locations of the Gaussian mixture model as a function of the component number (in black) and as a function of the number of atoms in an atomic column (in blue). There are 7 components, while the maximum thickness is 9 atoms.*

Note that G does not automatically equal the maximum thickness present in the sample. This is illustrated in Figure 2.6, using a hypothetical Pt nanoparticle. The number of atoms in each atomic column of the nanoparticle is illustrated in Figure 2.6a. The nanoparticle has a maximum thickness of 9 atoms in an atomic column. There are no atomic columns with 1 or 3 atoms in the nanoparticle. Therefore, only $G = 7$ components need to be estimated in the Gaussian mixture model, shown in Figure 2.6b. It is important to correctly relate each component of the Gaussian mixture model to a number of atoms in an atomic column. This subjective manual intervention will be avoided in the hybrid statistics-simulations based atom-counting method which will be introduced in Chapter 4.
Using the statistical parameter estimation theory framework, atoms can be counted with single atom sensitivity from ADF STEM images of model-like nanomaterials which are relatively

stable under the incoming electron beam, i.e. large nanoparticles and/or images recorded using a high electron dose [Van Aert 2013, De Backer 2013]. When the electron dose is low and very small nanoparticles are analysed, reliable counting results can no longer be obtained from a single image using the statistics-based method, as demonstrated in [De Backer 2015b] for a small Pt/Ir nanoparticle. The statistics-based counting procedure was performed independent from image simulations in order to obtain counting results of the Pt/Ir nanoparticle at different electron doses. The comparison with independent image simulations was used to validate the accuracy of the counting results. This validation could be achieved for the high electron doses, but is no longer possible for lower electron doses. The analysis revealed that the inaccurate selection of the model order could be attributed to the lowering of the electron dose, which causes the components of the Gaussian mixture model to overlap more. The reduced electron dose leads to less precise measurements of the scattering cross sections resulting in insufficient statistics for the determination of the number of components by the evaluation of the ICL criterion. In Chapter 4, a new atom-counting method will be proposed to overcome these limitations. The ADF STEM image of this Pt/Ir nanoparticle with the lowest electron dose will be analysed in Section 4.8 to demonstrate the potential of this hybrid statistics-simulations based method for atom-counting.

2.8 Conclusions

In this chapter, an overview of the basic concepts of quantitative STEM was given. We described the principle of the image formation for ADF STEM, and the main features of the image intensities. The Z-contrast and thickness dependence of this imaging mode, make it particularly suitable for quantification. Therefore, throughout this thesis, ADF STEM images will be used to determine quantitative atomic structural information. Next, we introduced image simulations and highlight some important aspects to take into account when performing image simulations for quantitative analysis of STEM images. In this thesis we will use statistical parameter estimation theory in order to accurately and precisely quantify the atomic structure. Therefore, some of the basic concepts of model-based parameter estimation have been introduced. This framework enables us to estimate the parameters of a parametric imaging model that can be used to quantify ADF STEM image intensities of a nanomaterial oriented along a main zone axis. This model provides accurate and precise estimates for the atomic column positions and for the scattering cross sections, which quantify the total intensity of electrons scattered towards the annular detector from a given atomic column. Finally, these scattering cross sections are used to count the number of atoms in each atomic column of a nanomaterial. We have described two possible approaches. The first is based on a direct comparison with image simulations. This approach is very intuitive, but prone to errors if a mismatch between experimental and simulated parameters remains undetected. The second approach for atom-counting employs the framework of statistical parameter estimation theory. This method provides accurate and precise counting results. The method is independent from image simulations. An important advantage is that the statistical framework provides a measure for the precision of the counting results. At high electron dose and/or for large nanoparticles this method was shown to provide atom counts with single atom sensitivity. However, when the electron dose is lowered, it is no longer possible to retrieve reliable counting results.
The concepts introduced in this chapter will be used and extended in the remainder of this thesis. In Chapter 3, an alternative parametric imaging model is proposed in order to quantify the ADF STEM image intensities of nanomaterials which are slightly tilted away from a main zone axis orientation. In Chapter 4, a new approach for atom-counting from ADF STEM

images will be introduced that combines the two approaches introduced in this chapter. Finally, in Chapters 5 and 6, this counting procedure will be further extended to allow the reliable analysis of a time series of ADF STEM images.

3

Quantitative analysis of ADF STEM images of tilted nanomaterials

3.1 Introduction

The parametric imaging model introduced in Section 2.5 was developed for quantitative analysis of ADF STEM image intensities of nanomaterials in zone axis orientation. However, aligning the sample in exact zone axis orientation might not always be possible for various reasons, such as sample bending in very thin specimens [Brown 2017]. Many interesting nanoparticles, for example for catalytic applications, are very small and therefore highly sensitive to small amounts of tilt [Li 2008, Altantzis 2019]. This can affect the quantification of the atomic structure from the ADF STEM image intensities [De Backer 2015b]. The effects of tilt on high resolution ADF STEM images have been studied using multislice calculations [Maccagnano-Zacher 2008, So 2012], revealing that the contrast between background and bright column intensities is decreased when the specimen is tilted slightly off zone-axis orientation. This can be explained using electron channelling theory [Loane 1988, Van Dyck 1996, E 2013, MacArthur 2015]. An atomic column aligned with the incident beam exhibits a small lensing effect on the beam, keeping the intensity on the atomic column [Loane 1988, Van Dyck 1996, van den Bos 2016, van den Bos 2019]. This leads to a larger scattering cross section than the sum of the individual scattering cross sections of the separate atoms in the atomic column. Tilting the sample away from zone axis orientation reduces the channelling and leads to a decrease in the intensity scattered from the atomic column towards the annular detector, as compared to the zone axis oriented situation [Garcia-Gutierrez 2004, Yu 2008, Langlois 2010, E 2013, MacArthur 2015]. Nonetheless, the crystal lattice remains clearly visible for specimen tilts up to one degree in different directions and for a range of specimen thicknesses. While acquiring images, a small amount of tilt can therefore remain unnoticed despite the decrease in contrast, as the intensity range displayed when acquiring the images is rescaled [Jones 2016].
Empirically, sample tilt also causes an elongation of the atomic columns in the ADF STEM

This chapter is based on [De wael 2021].

images. An often posed research question is therefore whether the parametric imaging model consisting of symmetrical Gaussian peaks can still yield a reliable quantification. The effect of sample tilt on quantitative ADF STEM has previously been studied by estimating scattering cross sections as a function of tilt using integration of intensity in Voronoi cells [MacArthur 2015]. However, the scattering cross sections are estimated more reliably when overlap between neighbouring atomic columns is taken into account [De Backer 2016]. In a tilted specimen, these overlapping intensities will become even more important, and a parametric imaging model consisting of overlapping peaks to model the expected values of the ADF STEM image intensities is essential. The Gaussian peaks were shown to provide an adequate description of the experimental ADF STEM image intensities [den Dekker 2005, Van Aert 2005]. We therefore propose to use two-dimensional (2D) elliptical Gaussian peaks rather than 2D symmetrical Gaussian peaks, in order to better describe the elongated ADF STEM image intensities in the presence of sample tilt. In this chapter, we investigate whether physical parameters such as scattering cross sections or atomic column positions can be estimated more reliably using a parametric imaging model that consists of superimposed 2D elliptical Gaussian peaks. In Section 3.2, the proposed parametric imaging model is introduced. In Section 3.3, the possibilities and limitations of the elliptical imaging model are studied using ADF STEM images of a simulated Pt(110) nanocrystal with variable sample tilt. The amount of elongation of the atomic columns is quantified by the elliptical model[†] and the effect of sample tilt on the estimated atomic column positions, intercolumn distance and scattering cross sections is studied using the proposed elliptical model and compared to the results obtained using the existing symmetrical model. Finally, in Section 3.4, we formulate conclusions and make a suggestion for the most reliable quantification of ADF STEM images in the presence of small sample tilts.

3.2 Parametric imaging model in the presence of tilt

In Section 2.5, we introduced a parametric imaging model for ADF STEM image intensities of nanoparticles consisting of 2D symmetrical Gaussian peaks. Here, we describe a parametric imaging model consisting of 2D elliptical Gaussian peaks, rather than symmetrical peaks. The pixel values w_{kl} for each pixel (k, l) of a $K \times L$ ADF STEM image are summarised in a vector:

$$\mathbf{w} = (w_{11}, w_{12}, \cdots, w_{KL}). \tag{3.1}$$

This is the set of observations obtained from the ADF STEM experiment. Each set of observations obtained from an experiment performed under the same experimental conditions will unavoidably be different due to the presence of noise. Therefore, the set of observed image intensities of an ADF STEM are stochastic variables. The aim of statistical parameter estimation theory is to describe the expectation values of the observations as a function of relevant physical parameters:

$$\mathbb{E}[w_{kl}] = f_{kl}(\boldsymbol{\Theta}), \tag{3.2}$$

with $\boldsymbol{\Theta}$ the parameter vector that contains the unknown parameters. In the presence of sample tilt, we now propose the following expression for the expectation value of the image intensity at pixel (k, l) with position (x_k, y_l) in the image is given by:

$$f_{kl}(\boldsymbol{\Theta}) = \zeta + \sum_{n=1}^{N} \eta_n \exp\left(-\frac{\left[\cos\alpha\left(x_k-\beta_{x_n}\right)+\sin\alpha\left(y_l-\beta_{y_n}\right)\right]^2}{2{\rho_x}^2} - \frac{\left[-\sin\alpha\left(x_k-\beta_{x_n}\right)+\cos\alpha\left(y_l-\beta_{y_n}\right)\right]^2}{2{\rho_y}^2}\right) \tag{3.3}$$

[†]The terms symmetrical/elliptical model are used to refer to the superposition of 2D symmetrical/elliptical Gaussian peaks jointly fitted to all atomic columns, not to individual symmetrical/elliptical Gaussian peaks fitted to the individual atomic columns.

In this expression, ζ is a constant background present in the image, ρ_x is the width of the 2D elliptical Gaussian peaks in the x-direction, ρ_y is the width of the 2D elliptical Gaussian peaks in the y-direction, α is the angle that describes the orientation of the elliptical Gaussian peaks, η_n is the height of the n^{th} Gaussian peak, β_{x_n} and β_{y_n} are the x- and y-coordinate of the n^{th} atomic column, and N is the total number of atomic columns in the image. The unknown parameters are summarised in the parameter vector:

$$\boldsymbol{\Theta} = (\beta_{x_1}, \cdots, \beta_{x_N}, \beta_{y_1}, \cdots, \beta_{y_N}, \rho_x, \rho_y, \alpha, \eta_1, \cdots, \eta_N, \zeta)^{\mathsf{T}}. \tag{3.4}$$

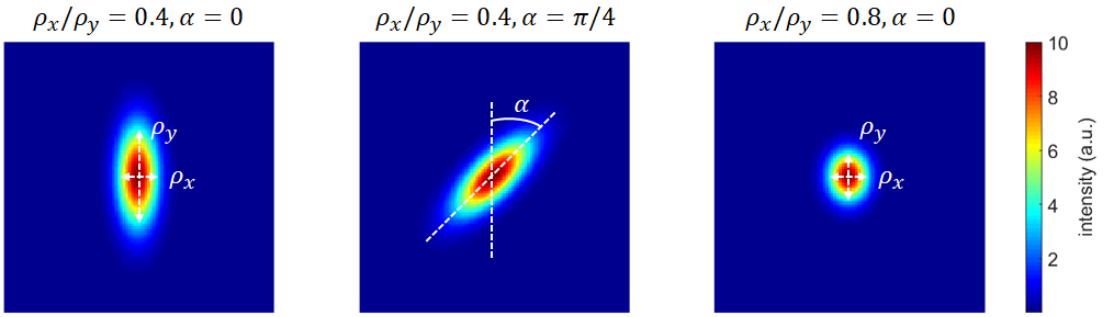

Figure 3.1: *2D elliptical Gaussian peak with different elongations ρ_x/ρ_y and angles α.*

In Figure 3.1, the influence of the parameters ρ_x, ρ_y and α introduced specifically to describe the ellipticity of the Gaussian peaks is illustrated. These parameters can either be imposed to be the same for all atomic columns in the estimation process, as in Equation (3.3), or can be different for each atomic column. However, in case of sample tilt, we expect the effective elongation of the atomic column intensities to be all in the same direction. For atomic columns with varying thickness, however, it is necessary to fit different widths in x and y direction, since the same amount of sample tilt will lead to a larger effective elongation in case of a thicker atomic column, as the difference in projected xy-position between the top and bottom atom is larger.

$$f_{kl}(\boldsymbol{\Theta}) = \zeta + \sum_{n=1}^{N} \eta_n \exp\left(-\frac{\left[\cos\alpha\left(x_k-\beta_{x_n}\right)+\sin\alpha\left(y_l-\beta_{y_n}\right)\right]^2}{2{\rho_{x_n}}^2} - \frac{\left[-\sin\alpha\left(x_k-\beta_{x_n}\right)+\cos\alpha\left(y_l-\beta_{y_n}\right)\right]^2}{2{\rho_{y_n}}^2}\right) \tag{3.5}$$

with the parameter vector $\boldsymbol{\Theta}$ now given by:

$$\boldsymbol{\Theta} = (\beta_{x_1}, \cdots, \beta_{x_N}, \beta_{y_1}, \cdots, \beta_{y_N}, \rho_{x_1}, \cdots, \rho_{x_N}, \rho_{y_1}, \cdots, \rho_{y_N}, \alpha, \eta_1, \cdots, \eta_N, \zeta)^{\mathsf{T}}. \tag{3.6}$$

The parametric model is fitted to the experimental ADF STEM image using a least squares criterion. In this manner we obtain a least squares estimate for the unknown parameter vector:

$$\hat{\boldsymbol{\Theta}} = \arg\min_{\mathbf{t}} \sum_{k=1}^{K} \sum_{l=1}^{L} (w_{kl} - f_{kl}(\mathbf{t}))^2. \tag{3.7}$$

This is done using an iterative optimisation algorithm in the same manner as for the symmetrical model introduced in Section 2.5. The so-called scattering cross section for each atomic column n can now be estimated as the volume under the 2D elliptical Gaussian peaks in the model:

$$\hat{V}_n = 2\pi\hat{\eta}_n\hat{\rho}_x\hat{\rho}_y. \tag{3.8}$$

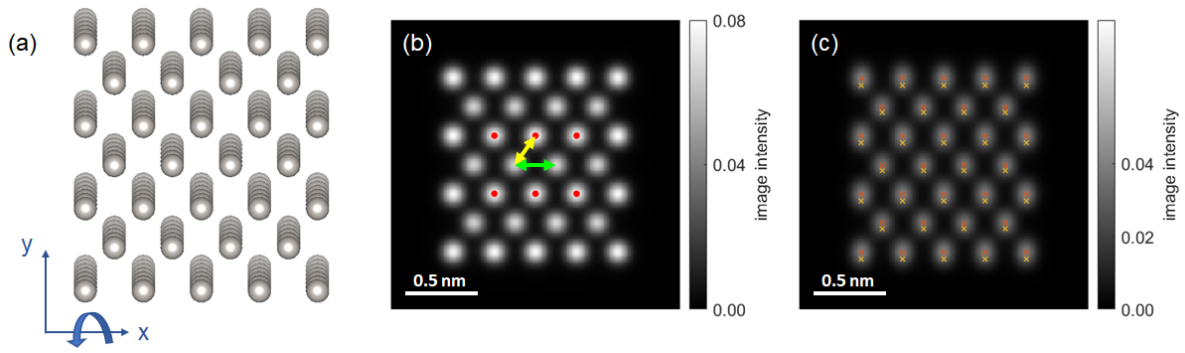

Figure 3.2: *(a) Visualisation of a Pt(110) nanocrystal of* 4×3 *unit cells, with a thickness of 6 unit cells. The tilt direction used in the simulation study is shown schematically. (b) Simulated ADF STEM image of the Pt(110) nanocrystal in zone axis orientation. Red dots indicate the columns used to determine the position bias and scattering cross sections as a function of tilt in Figures 3.5a and 3.6. The arrows indicate the columns for which the nearest and next nearest neighbour distance is assessed in Figure 3.5b. (c) Simulated ADF STEM image of the Pt(110) nanocrystal with a sample tilt of 60 mrad. Yellow crosses indicate the positions of the top atoms of each atomic column, while red crosses indicate the estimated atomic column positions by the elliptical model. Image intensities are expressed in fractions of the incident electron dose on the same scale in (b) and (c), colour bar labels indicate the range of intensities present in the image.*

The scattering cross section is a measure for the total intensity of electrons scattered from an atomic column in the nanomaterial towards the ADF STEM detector.
In the next section, we demonstrate the quantification of ADF STEM images using the elliptical Gaussians by analysing a simulated Pt nanocrystal at different tilt angles. The possibilities and limitations of this approach are investigated through comparison with the existing parametric model defined previously in Section 2.5.

3.3 Possibilities and inherent limitations

In order to study the possibilities and limitations of quantification using a superposition of elliptical 2D Gaussian peaks, we simulated a Pt(110) nanocrystal with a sample tilt ranging from 0 to 60 mrad - approximately 3.5° - towards a [100] zone axis orientation. We consider a nanocrystal with two different thicknesses, respectively 6 and 18 unit cells, corresponding to 16.64Å and 49.92Å. The atomic structure of the Pt(110) nanocrystal at 6 unit cells thickness used for the simulation study is shown in Figure 3.2a. Figure 3.2b and 3.2c show simulated ADF STEM images of the sample in zone axis orientation and with 60 mrad tilt towards a [100] zone axis orientation, respectively. The tilting direction is indicated schematically in Figure 3.2a. The parameters of the image simulations are summarised in Table A.1 of Appendix A. The nanocrystal is created with a homogeneous thickness by replicating the crystal unit cell in the x, y and z directions. As a result, there are two types of atomic columns in the nanocrystal, corresponding to the corners or the central atom of the projected unit cell of a face centered cubic (FCC) lattice. This leads to a variation in the number of atoms per atomic column of only 1 atom. Therefore, the elongation will be approximately the same for all atomic columns, and the images are fitted using the model with constant width for each direction, expressed by Equation (3.3).
In Figure 3.3, we display the residual intensities obtained by subtracting the simulated im-

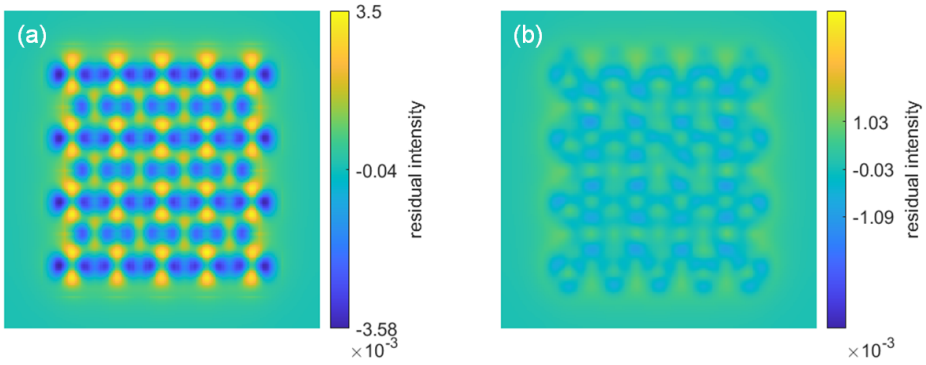

Figure 3.3: *Residual intensities of the tilted Pt(110) nanocrystal from Figure 3.2c after fitting with a superposition of (a) symmetrical and (b) elliptical 2D Gaussian peaks. Intensities are expressed in fractions of the incident electron dose on the same scale in (a) and (b), colour bar labels indicate the range of intensities present in the image.*

age intensities of the tilted Pt(110) nanocrystal [Figure 3.2c] from the fitted image intensities obtained respectively by the symmetrical and the elliptical 2D Gaussian peaks. By visualising the intensities on the same colour scale, we can now easily understand why one would want to consider fitting 2D elliptical Gaussian peaks: the residual intensities for this tilted Pt nanocrystal are up to a factor of 3.5 smaller as compared to the commonly used symmetrical model, yielding a qualitatively better description of the ADF STEM image intensities in the presence of sample tilt. In the remainder of this section we will quantitatively study whether this improvement can also yield better estimates of physical parameters such as atomic column positions and scattering cross sections. Furthermore, the model also provides an estimate for the angle, which can be used to determine the tilting direction. Based on the widths in the x and y direction, we can study the elongation of the atomic columns, which is related to the amount of sample tilt.

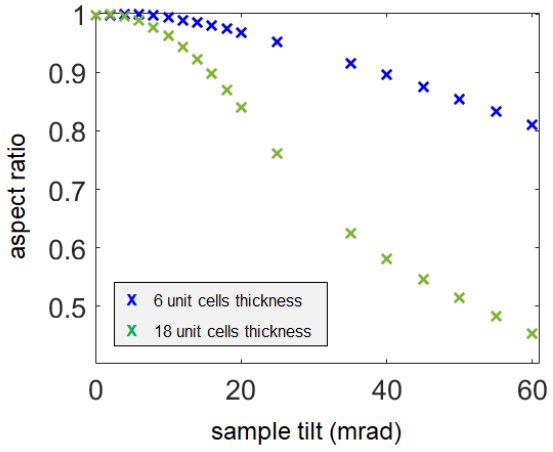

Figure 3.4: *Aspect ratio ϵ of the atomic columns estimated using a parametric imaging model with elliptical Gaussian peaks, evaluated as a function of the amount of sample tilt for the Pt nanocrystal, as shown in Figure 3.2, at 6 and 18 unit cells thickness (*16.64Å *and* 49.92Å*).*

3.3.1 Atomic column elongation

The elliptical model, expressed by Equation (3.3), allows us to quantify the amount of elongation visible in the tilted image using the aspect ratio of the ellipse:

$$\epsilon = \frac{\rho_x}{\rho_y} \leq 1. \tag{3.9}$$

The aspect ratio is equal to or smaller than one by definition. This is achieved by consistently defining ρ_x as the smallest width of the ellipse after the parameter estimation procedure. The aspect ratio ϵ decreases with increasing sample tilt. This is shown in Figure 3.4 for two different thicknesses of the Pt(110) nanocrystal of Figure 3.2. For a larger sample thickness, the aspect ratio decreases faster with increasing sample tilt. When the sample thickness is known, the combination of image simulation and elliptical fitting can be used to estimate the amount of sample tilt.

3.3.2 Atomic column positions

Next, we assess the accuracy of the estimated atomic column positions using the proposed elliptical parametric imaging model and compare this to the existing parametric model with symmetrical Gaussians. To this purpose, we quantify the bias of the position estimate for the atomic columns indicated by red dots in Figure 3.2b, which have the same z-height in the FCC crystal lattice. The results are summarised in Figure 3.5a for different amounts of sample tilt and sample thickness. The bias of the position estimate is quantified as the distance between the reference coordinate and the estimated position coordinate. During this analysis, we have set the reference position of an atomic column in a tilted sample equal to the xy-position of the top atom of that atomic column. In Figure 3.2c, the estimated and reference coordinates are plotted on top of the image with red and yellow crosses respectively. A shift of the estimated atomic column positions as compared to the actual position of the top atoms occurs when the sample is tilted. This was noted before, especially for annular bright field (ABF) STEM images [So 2012, Zhou 2016, Gao 2018, Fatermans 2020]. The bias of the estimated atomic column positions increases with increasing sample tilt and sample thickness. At 18 unit cells thickness, for example, the bias on the estimated atomic column position is 11.4% of the nearest neighbour distance at a sample tilt of 16 mrad (approximately 1°). Despite this bias, the intercolumn distance is still estimated accurately, as shown in Figure 3.5b for the thickness of 18 unit cells. The estimated intercolumn distance by the elliptical model differs at most 1.8 pm from the reference value. This enables us to reliably quantify the lattice parameter using the proposed imaging model.

Finally, we see that the accuracy of the estimated position coordinate and the intercolumn distance is identical for the parametric imaging model using symmetrical or elliptical 2D Gaussian peaks up to 50 mrad (almost 3°) in case of 18 unit cells thickness (approximately 50 Å). Only at larger tilt angles, the bias on the estimated intercolumn distances by the symmetrical model increases from maximum 1.3 pm to 4.5 pm. A drawback of the elliptical model on the other hand is the increased parameter space, which can lead to less precise parameter estimates. Therefore, when the goal is to quantify the atomic column positions from an ADF STEM image of a slightly tilted sample, we recommend to use the existing parametric imaging model, rather than increasing the complexity of the model.

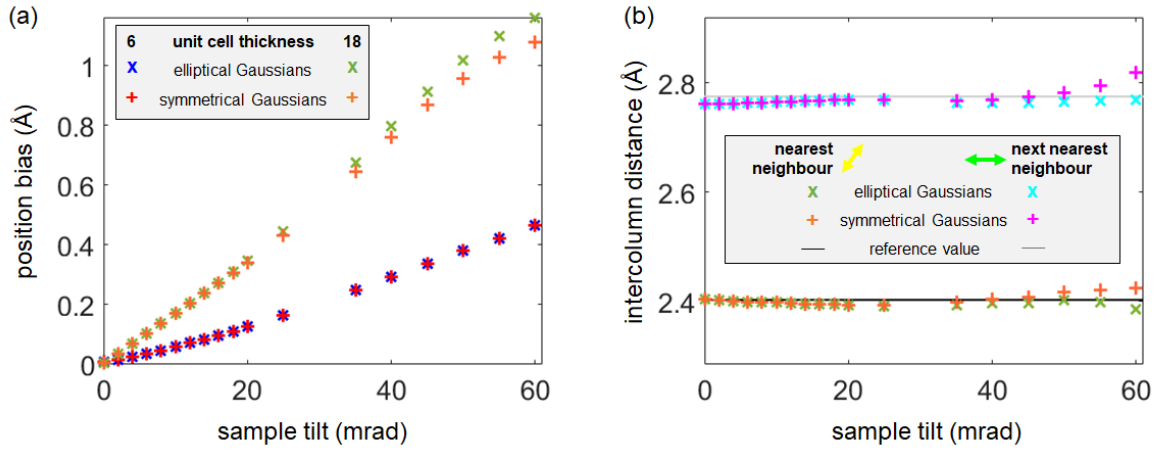

Figure 3.5: *(a) Bias between the actual atomic column position - equal to the position of the top atom - and the atomic column position estimated using a parametric imaging model with elliptical and symmetrical Gaussian peaks, evaluated as a function of the amount of sample tilt for the Pt nanocrystal at 6 and 18 unit cell thickness (*16.64Å *and* 49.92Å*). The bias was calculated for the atomic columns indicated with red dots in Figure 3.2b. (b) Distance between two nearest neighbour atomic columns and between two next nearest neighbour atomic columns, indicated respectively using a yellow and a green arrow in Figure 3.2b, estimated using a parametric imaging model with elliptical and symmetrical Gaussian peaks, evaluated as a function of the amount of sample tilt for the Pt nanocrystal at 18 unit cells thickness. Full lines indicate the reference value, determined from the lattice parameters.*

3.3.3 Scattering cross sections

The total intensity scattered from an atomic column towards the annular detector is quantified by the so-called scattering cross section, which can be estimated by the volume under the 2D Gaussian peaks of the parametric imaging model given by Equation (2.12). As mentioned before, tilting of a sample away from zone axis orientation reduces the channelling effect, leading to a decrease in the contrast and in the peak intensity at the atomic column positions. This effect is indeed observed when we evaluate the scattering cross sections estimated according to Equation (2.15) as a function of sample tilt, shown by the pluses in Figure 3.6.

One might expect that the elliptical model introduced in this chapter yields more reliable estimates for the total scattered intensity from each column, since the model seems to empirically better describe the shape of the atomic columns of tilted nanomaterials in ADF STEM images, as was shown by the residual image intensities in Figure 3.3. We therefore estimate the scattering cross sections from the elliptical model of Equation (3.3), using Equations (3.7) and (3.8). The crosses in Figure 3.6 show the estimated scattering cross sections from the proposed elliptical model as a function of sample tilt. Note that they are identical to the scattering cross sections estimated by the existing symmetrical model, for both sample thicknesses considered in this study. We therefore conclude that we do not gain extra intensity information by adapting the parametric imaging model using elliptical peaks.

Note that lens aberrations such as coma can also cause elongation of the atomic columns, which might potentially be mistaken as sample tilt [So 2012]. It was however shown previously that the scattering cross section estimated from the parametric imaging model using 2D symmetrical Gaussian peaks is robust to inaccuracies in both cylindrically symmetrical and non-cylindrically symmetrical aberrations [Martinez 2018]. Therefore, we do not expect problems for the quantification of slightly aberrated ADF STEM images with the existing sym-

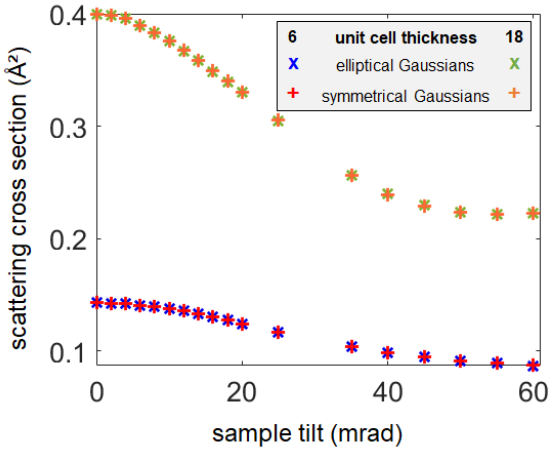

Figure 3.6: *Scattering cross sections estimated using a parametric imaging model with elliptical and symmetrical Gaussian peaks, evaluated as a function of the amount of sample tilt. The scattering cross sections were estimated for a set of atomic columns with equal thickness indicated by the red dots in Figure 3.2b.*

metrical Gaussian model.
Finally, it is important to realise that this elliptical model, like the existing symmetrical model, does not allow us to reliably count the number of atoms using a direct comparison to zone axis image simulations. Therefore, when a small amount of sample tilt remains undetected, the image simulations-based atom-counting procedure, introduced in Section 2.6, will yield inaccurate counting results. Furthermore, the statistics-based atom-counting procedure, introduced in Section 2.7, can also suffer from sample tilt, leading to an underestimation of the order of the Gaussian mixture model used to unravel the different thicknesses present in the sample [De Backer 2015b]. This underestimation was detected through independent comparison of the results obtained by the statistical analysis and the image simulations. In the next chapter, a hybrid statistics-simulations based method for atom-counting is introduced which immediately incorporates prior knowledge from image simulations in the statistical analysis through a parametric relationship. In this manner, counting from tilted nanomaterials in a reliable manner will become possible, despite the decrease of the scattering cross sections with increasing sample tilt. Optimisation of the imaging parameters such as probe convergence angle and collection angles of the annular detector can further aid towards a tilt-robust image quantification by balancing the elastic and thermal diffuse scattering (TDS) contributions to the ADF STEM signal [MacArthur 2015].

3.4 Conclusions and discussion

In this chapter, we investigated a parametric imaging model consisting of overlapping 2D elliptical Gaussian peaks. Our goal was to ascertain whether this model can quantify the ADF STEM images of slightly tilted nanomaterials more reliably than the existing parametric imaging model, which consists of overlapping 2D symmetrical Gaussian peaks. Intuitively, such an elliptical model might seem better suited for the description of the elongated atomic columns observed in tilted ADF STEM images. This can be clearly understood by visualising the residual intensities, i.e. the difference between the ADF STEM image intensities and the fitted intensities by the model. The elliptical model yields significantly smaller residual intensities

as compared to the existing symmetrical model. Qualitatively, it can therefore be considered as a better model. On the other hand, the elliptical model is more complex, and therefore fitting the parameters is more time consuming, as compared to the symmetrical model. For the zone axis orientation image of Figure 3.2b, the elliptical fitting takes 2 times longer. At higher tilt angles, even more computation time is needed to fit the extra parameters. For the simulated image with sample thickness of 6 unit cells at a tilt angle of 60 mrad, shown in Figure 3.2c, fitting the elliptical model took 3 times longer than fitting the symmetrical model. For the sample thickness of 18 unit cells the time difference was even a factor of 6. Furthermore, an increased parameter space generally leads to less precise parameter estimates. Therefore, it is important to quantitatively study what can be gained from using this elliptical model for quantitative ADF STEM in terms of physical parameters. To this purpose, we investigated a simulated Pt(110) nanocrystal at different tilt angles. A benefit of the elliptical model is that it allows us to quantify two properties of the tilted sample which are not quantified by the existing symmetrical model: the elongation of the atomic columns and the angle of the elongation. The angle quantifies the direction of sample tilt, while the elongation is strongly related to the amount of sample tilt. Furthermore, we have shown that the proposed elliptical model yields equivalent atomic column position estimates as compared to the existing symmetrical model up to 50 mrad sample tilt. Although the estimated atomic column positions are shifted with respect to the positions of the top atom of each atomic column, the intercolumn distances are quantified accurately. In this manner, both parametric imaging models can still be used to obtain reliable structural information from ADF STEM images of tilted nanomaterials. Finally, we quantified the scattering cross section at different tilt angles up to 60 mrad - approximately 3.5° - using both models. The scattering cross sections decrease with increasing sample tilt in the same manner, regardless whether they are estimated from the elliptical or the symmetrical model. This intensity loss is entirely caused by a loss of the channelling conditions, and cannot be (partially) retrieved by an elliptical Gaussian peak to fit rather than a symmetrical Gaussian peak. Note that this implies that the scattering cross sections from tilted nanomaterials can not be used to count the number of atoms using a simulations-based atom-counting procedure. The statistics-based approach for atom-counting on the other hand might still reveal a correct clustering of the scattering cross sections, but the unavoidable mismatch with the independent image simulations impedes truly reliable atom-counting in the presence of tilt. Therefore, in the next chapter, a hybrid statistics based atom-counting procedure is proposed to overcome this limitation.

In conclusion, we do not consider fitting the larger parameter space of the model with overlapping 2D elliptical Gaussian peaks worth the extra effort over fitting the existing model of overlapping 2D symmetrical Gaussian peaks, since we do not gain more reliable quantitative estimates for the atomic column positions and scattering cross sections. The comparison shown in this chapter confirms that the existing parametric imaging model - which consists of overlapping 2D symmetrical Gaussian peaks - remains a very reliable method for the quantitative analysis of ADF STEM images in the presence of sample tilt. Correct lattice parameters can still be retrieved using the estimated atomic column positions. The scattering cross sections decrease with sample tilt, but an increased complexity of the parametric model does not help to retrieve (part of) this intensity loss. In short, we advise the use of overlapping 2D Gaussian peaks - previously implemented in the freely available StatSTEM software [De Backer 2016] - for the quantification of the ADF STEM image intensities, even in the presence of a small amount of sample tilt.

4

Hybrid statistics-simulations based method for atom-counting from an ADF STEM image

4.1 Introduction

By counting the number of atoms in each atomic column from two-dimensional (2D) annular dark field scanning transmission electron microscopy (ADF STEM) images recorded under a few different viewing directions, a three-dimensional (3D) reconstruction of the structure can be obtained [Van Aert 2011, Bals 2011], allowing for the quantification of the shape and size of the nanoparticle. Furthermore, atom-counting results from a single viewing direction can be combined with structural energy minimisation [Bals 2012, Jones 2014, Geuchies 2016, De Backer 2017, Altantzis 2019], in order to obtain a visualisation of the 3D atomic structure from a 2D image without the need for the large electron doses and long acquisition times generally required for electron tomography. We have discussed two existing approaches for atom-counting, based on image simulations (Section 2.6) or based on statistical parameter theory (Section 2.7) in Chapter 2. The image simulations-based method for atom-counting is very intuitive, but highly sensitive to small mismatches between the actual and the simulated experimental set-up, such as a different detector inner angle or sample tilt. The described statistics-based method on the other hand is independent of image simulations and results in atom-counts with single atom sensitivity [Van Aert 2013], provided that the inherent limitations of the method are not exceeded [De Backer 2013, De Backer 2015b]. The method becomes less reliable for very small nanoparticles due to the limited number of columns present in the image and for low electron doses, due to the low signal-to-noise ratio. The increasing relevance of radiation damage, not only in biological studies, but also in the study of nanostructures [Meyer 2014], demands a method that allows for a reliable quantitative analysis of low dose images with a low signal-to-noise ratio. A hybrid statistics-simulations based method is proposed to overcome the limitations of the statistics-based method, and thus progress towards the quantitative analysis of small, beam-sensitive materials [De wael 2017]. This hybrid method will be realised by incorporating prior knowledge, obtained from carefully performed

This chapter is based on [De wael 2017].

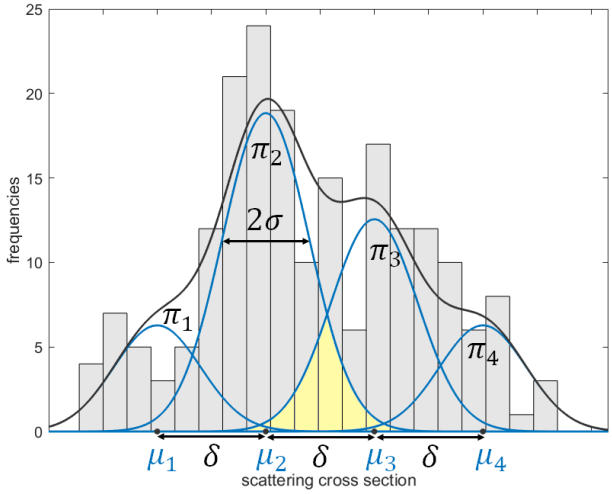

Figure 4.1: *Hypothetical set of scattering cross sections represented in a histogram. The blue lines show the Gaussian components for each thickness, with locations μ_g and width σ. The sum of Gaussian components, weighted by their mixing proportions π_g, yields the Gaussian mixture model, shown by the black line. The (average) distance between the locations is expressed by δ. The overlap between the components (highlighted in yellow) depends on the relative width of the components σ/δ and limits the atom-counting precision.*

image simulations, into the statistics-based method.
In Section 4.2 we introduce the hybrid statistics-simulations based method for atom-counting and derive the probability distribution of the scattering cross sections. In Section 4.3, we discuss the estimation of the parameters of the probability distribution, and assess the accuracy and precision of the estimated parameters. Next, an order selection criterion is introduced in Section 4.4. In Section 4.5, we verify whether the well-established statistics-based and the newly proposed hybrid methods yield equivalent counting results for model-like systems, i.e. large nanoparticles or ADF STEM images recorded using high electron doses. Next, we compare the performance for atom-counting of the hybrid statistics-simulations based method with the statistics-based method for atom-counting in more detail in Section 4.6. In Section 4.7, we demonstrate the capability of the hybrid method to achieve reliable counting results, despite the presence of sample tilt, using a simulated Pt nanoparticle. Finally, we show where the hybrid method for atom-counting exceeds the limitations of the statistics-based method by means of an experimental example and image simulations in Section 4.8, before drawing conclusions in Section 4.9.

4.2 Probability distribution of scattering cross sections

As mentioned before in Section 2.7, the unavoidable presence of noise in the experimental images causes fluctuations on the values of the scattering cross sections of atomic columns with identical thickness g around an average scattering cross section value μ_g. Represented in a histogram, we therefore do not see isolated peaks corresponding to the different numbers of atoms in a column, but broadened components, often overlapping each other, as shown in Figure 4.1. The distribution of the scattering cross sections can be modelled as a Gaussian distribution for each thickness g present in the sample (blue lines in Figure 4.1), resulting in

the Gaussian mixture model (black line in Figure 4.1), expressed by Equation (2.16).
Here, in order to overcome the limitations of the statistics-based method discussed in Section 2.7, we will incorporate prior knowledge from image simulations in the probability distribution of the scattering cross sections. It is important to note that such a hybrid statistics-simulations based method for atom-counting is not equivalent to statistics-based methods for atom-counting, validated using independent image simulations. When the scattering cross sections are normalised with respect to the incident electron beam, comparison with image simulations is possible, using a so-called library of simulated scattering cross sections as described in Section 2.6. An intuitive first suggestion could be to combine the statistics-based and the image simulations-based atom-counting procedures by fixing the locations of the Gaussian components at the library values, rather than estimating these parameters freely. In this case, only the widths and mixing proportions of the Gaussian components would still be estimated. In this manner, the benefits of prior knowledge from image simulations could be combined with the benefits of a statistical framework such as an estimate for the precision of the counting results which can be derived from the width of the Gaussian components.

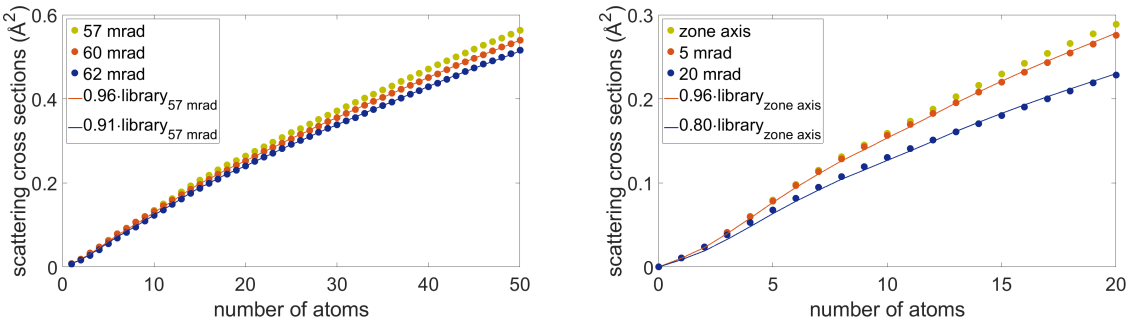

Figure 4.2: *The effect of small mismatches between experimental and simulation parameters such as detector inner angle or sample tilt on the library of simulated scattering cross sections evaluated as a function of the number of atoms in an atomic column can be approximated as a linear scaling. Libraries are shown for Au in [100] zone axis orientation with (a) different detector inner angles and (b) different amounts of sample tilt around the [001] axis. Solid lines show how the library can be scaled to fit the libraries for different detector inner angles or different tilt values.*

However, systematic errors in the image simulations are difficult to detect, and therefore this is not an optimal approach. Figure 4.2 shows simulated scattering cross sections evaluated as a function of the number of atoms per column for different values of the detector inner angle or sample tilt. The solid lines in both figures indicate that linearly scaled libraries are a good approximation for the scattering cross sections simulated using different parameters. In Figure 4.2a, simulated scattering cross sections for Au in [100] zone axis obtained with different detector inner angles 57 mrad, 60 mrad and 62 mrad are shown. The scattering cross sections simulated using an inner angle of 60 or 62 mrad can be approximated by linearly scaling the scattering cross sections corresponding to 57 mrad, acting as the library in this example. These detector inner angles correspond to reasonable measurement errors in the detector inner angle of up to ±5 mrad [Jones 2016]. The procedure for measuring the detector inner angle is described in [Martinez 2015]. The scattering cross sections are less sensitive to the outer detector angle [Jones 2016]. In Figure 4.2b, simulated scattering cross sections are shown for a sample tilt around the [001] axis, up to 15 mrad, which can experimentally still

yield an atomic resolution image [MacArthur 2015, Jones 2016]. Small sample tilt can easily remain undetected due to a rescaling of the intensity range of the observed data during an experiment, but leads to a loss of contrast and a decrease in the scattering cross sections, which becomes more apparent at higher thickness. Also in this case, the scaled library for the sample in zone axis is an acceptable approximation for the scattering cross sections corresponding to different sample tilt values.
Therefore, rather than freely estimating the locations μ_g, they will now be restricted to a linear scaling factor a multiplied with the library values $\mathcal{M}_g$ resulting from simulations:

$$\mu_g = a\mathcal{M}_g. \tag{4.1}$$

The Gaussian mixture model of Equation (2.16) is therefore altered:

$$f_{\text{mix}}\left(V_n|\mathbf{\Psi}_G\right) = \sum_{g=1}^{G} \pi_g \mathcal{N}\left(V_n|a\mathcal{M}_g, \sigma\right), \tag{4.2}$$

with

$$\mathcal{N}\left(V_n|a\mathcal{M}_g, \sigma\right) = \frac{1}{\sqrt{2\pi}\sigma} \exp\left(-\frac{(V_n - a\mathcal{M}_g)^2}{2\sigma^2}\right), \tag{4.3}$$

the Gaussian components. The joint probability density function of the (normalised) scattering cross sections is therefore given by:

$$p(\mathbf{V}|\mathbf{\Psi}_G) = \prod_{n=1}^{N} \sum_{g=1}^{G} \pi_g \mathcal{N}\left(V_n|a\mathcal{M}_g, \sigma\right). \tag{4.4}$$

The mixing proportion π_g of the g^{th} component represents the probability for an atomic column to have precisely g atoms. Note that in this manner the component index g will automatically coincide with the number of atoms g in an atomic column. This is in contrast with the statistics-based method where the total number of components G corresponding to all atomic columns did not necessarily equal the maximum number of atoms in any of the atomic columns, as visualised in Figure 2.6. In case no atomic columns with 3 atoms are present in the sample, for example, the hybrid method will estimate the mixing proportion $\pi_3 = 0$. The locations of the components in the mixture models $\mu_g = a\mathcal{M}_g$ correspond to the location of the g^{th} component in the mixture model, and therefore to the average scattering cross section for an atomic column of the sample with exactly g atoms. The width of the components is denoted by σ and V_n represents the stochastic variable related to the scattering cross section of atomic column n. All scattering cross sections are summarised in the vector $\mathbf{V}$. The vector $\mathbf{\Psi}_G$ is the parameter vector containing all unknown parameters to be estimated in a Gaussian mixture model with G components:

$$\mathbf{\Psi}_G = (\pi_1, ..., \pi_{G-1}, a, \sigma)^{\mathsf{T}}. \tag{4.5}$$

Note that π_G is not estimated, since the sum of all G mixing proportions must equal one, and therefore $\pi_G = 1 - \sum_{g=1}^{G-1} \pi_g$. This means that $G + 1$ parameters need to be estimated, instead of $2G$ parameters for the statistics-based method.

4.3 Parameter estimation

The parameters summarised by the parameter vector $\mathbf{\Psi}_G$ defined in Equation (4.5) are estimated by maximising the likelihood function. As described earlier in Section 2.4, the expression for

the likelihood function has the same functional form as the joint probability density function, but is evaluated as a function of the parameters rather than as a function of the stochastic variables related to the observed data. Therefore, the stochastic variables $\mathbf{V}$ from Equation (4.4) are substituted by the observed scattering cross sections $\hat{\mathbf{V}}$, estimated from the ADF STEM image as described in Section 2.5. The likelihood function is therefore expressed as follows:

$$L(\mathbf{\Psi}_G) = p(\hat{\mathbf{V}}|\mathbf{\Psi}_G) = \prod_{n=1}^{N} \sum_{g=1}^{G} \pi_g \mathcal{N}\left(\hat{V}_n | a\mathcal{M}_g, \sigma\right). \tag{4.6}$$

The likelihood is maximised with respect to the unknown parameters using an Expectation-Maximisation (EM) algorithm [Dempster 1977]. This algorithm consists of two steps that are repeated iteratively until convergence of the likelihood is reached. In the E-step, the likelihood function is evaluated, and during the M-step updates for the parameter estimates are calculated in order to maximise the (log) likelihood. The update formulas are obtained by solving the likelihood equation:

$$\begin{aligned}
\frac{\partial \ln L(\mathbf{\Psi}_G)}{\partial \mathbf{\Psi}_G} &= \sum_{n=1}^{N} \frac{\partial}{\partial \mathbf{\Psi}_G} \left[\ln \left(\sum_{g=1}^{G} \pi_g \mathcal{N}\left(\hat{V}_n | a\mathcal{M}_g, \sigma\right) \right) \right] \\
&= \sum_{n=1}^{N} \sum_{g=1}^{G} \frac{\pi_g \mathcal{N}\left(\hat{V}_n | a\mathcal{M}_g, \sigma\right)}{\sum_{h=1}^{G} \pi_h \mathcal{N}\left(\hat{V}_n | a\mathcal{M}_h, \sigma\right)} \frac{\partial}{\partial \mathbf{\Psi}_G} \left[\ln \left(\pi_g \mathcal{N}\left(\hat{V}_n | a\mathcal{M}_g, \sigma\right) \right) \right] \\
&= \sum_{n=1}^{N} \sum_{g=1}^{G} \tau_g \left(\hat{V}_n | \mathbf{\Psi}_G\right) \frac{\partial}{\partial \mathbf{\Psi}_G} \left[\ln \left(\pi_g \mathcal{N}\left(\hat{V}_n | a\mathcal{M}_g, \sigma\right) \right) \right] \\
&= 0,
\end{aligned} \tag{4.7}$$

where $\tau_g\left(\hat{V}_n|\mathbf{\Psi}_G\right)$ is calculated in the E-step for each iteration k, according to Equation (4.15). The parameter updates are expressed as follows:

$$\pi_g^{(k+1)} = \frac{1}{N} \sum_{n=1}^{N} \tau_g \left(\hat{V}_n | \mathbf{\Psi}_G^{(k)}\right), \tag{4.8}$$

$$a^{(k+1)} = \frac{\sum_{n=1}^{N} \sum_{g=1}^{G} \tau_g \left(\hat{V}_n | \mathbf{\Psi}_G^{(k)}\right) \hat{V}_n \mathcal{M}_g}{\sum_{n=1}^{N} \sum_{g=1}^{G} \tau_g \left(\hat{V}_n | \mathbf{\Psi}_G^{(k)}\right) \mathcal{M}_g^2}, \tag{4.9}$$

$$\sigma^{(k+1)} = \sqrt{\frac{1}{N} \sum_{g=1}^{G} \sum_{n=1}^{N} \tau_g \left(\hat{V}_n | \mathbf{\Psi}_G^{(k)}\right) \left(\hat{V}_n - a^{(k)} \mathcal{M}_g\right)^2}. \tag{4.10}$$

By means of simulations, the following starting values for the parameters were found to result in unbiased estimates for the parameters of the mixture model for the statistics-based atom-counting procedure [De Backer 2013], and will be used for the hybrid method as well:

$$\pi_g^{(0)} = \frac{1}{G}, \tag{4.11}$$

for the mixing proportions, and

$$\sigma^{(0)} = \frac{\max(\hat{\mathbf{V}}) - \min(\hat{\mathbf{V}})}{2G}, \tag{4.12}$$

for the width of the components. For the starting values of the scaling parameter, different values are used, ranging between a minimum and maximum expected scaling value, usually between 0.7 and 1.3. For each different starting value of the scaling parameter, the algorithm is iterated until convergence is reached. The final estimates $\hat{\mathbf{\Psi}}_G$ of the parameters in the mixture model with G components are then given by the set of estimated parameters for the highest likelihood was reached after convergence.
The parameter estimates of the parameter vector $\mathbf{\Psi}_G$ are used to determine counting results. To this purpose, each atomic column is assigned the number of atoms corresponding to the highest probability based on the estimated probability distribution. In the following, we will demonstrate the accuracy and precision of the parameter estimates obtained in this manner.

4.3.1 Accuracy & precision

In the present section, we evaluate the accuracy and precision of the estimated parameters. Ultimately, in order to perform a reliable quantitative analysis, the parameters of the probability distribution of the scattering cross sections, given by Equation (4.5), need to be estimated as accurately and precisely as possible. A statistical estimator of a parameter is accurate when the expectation value of the estimator equals the actual value of the corresponding parameter. For such an unbiased estimator, a lower bound on the variance exists, which expresses the highest attainable precision. This lower bound on the variance is given by the so-called Cramér-Rao lower bound [Rao 1945, Cramér 1946], defined earlier in Section 2.4, and calculated for the hybrid method for atom-counting in Appendix 4A.
In order to assess the accuracy and precision of the estimated parameters by the hybrid method, 100 noise realisations were created by performing random draws from a Gaussian mixture model with 5 components and parameters π_g, a and σ for which the input values are given in Table 4.1. For each noise realisation, the mixing proportions π_g for the different components are multinomially distributed with equal probabilities. Furthermore, an equally spaced library is used. The relative width of the components, defined as the ratio between the width of the components σ and the average difference between the locations of successive components δ, visualised in Figure 4.1, equals $\sigma/\delta = 0.25$. The average number of observations per component equals $N/G = 20$. The values of the estimated parameters, obtained for the true number of components G, are summarised in Table 4.1 and confirm that the parameter estimates are accurate, as the input value of each parameter is enclosed by the 95% confidence interval on the sample mean. Table 4.2 summarises the sample variances of the parameter estimates for the same sets of scattering cross sections used to validate the accuracy, together with a 95% confidence interval and the Cramér-Rao lower bound for each parameter. We conclude that the Cramér-Rao lower bound is indeed attained, as the 95% confidence intervals on the sample variances include the Cramér-Rao lower bound for each parameter. Thus, the parameter estimates are obtained with the highest possible precision by the hybrid method.
An important drawback of the statistics-based method is the underestimation of the value of the width of the components σ in case of a small average number of columns per component N/G [De Backer 2013]. In order to assess the accuracy of the estimated width of the components, noise realisations were again created by performing random draws from Gaussian mixture models with 10 components, in the same manner as described before. Different combinations of N/G and σ/δ were used, and 100 noise realisations were performed for each of these combinations. In Figure 4.3 the estimated width of the components is evaluated as a function of the true width of the components, for different values of the average number of columns per component N/G. Estimated widths are shown for both the statistics-based method

Parameter	Input value	Sample mean	95% confidence interval	
			Lower bound	Upper bound
π_1	0.2	0.2005	0.1922	0.2088
π_2	0.2	0.1979	0.1901	0.2057
π_3	0.2	0.1987	0.1901	0.2073
π_4	0.2	0.1990	0.1913	0.2066
π_5	0.2	0.2039	0.1951	0.2128
a	1	0.9990	0.9970	1.0011
σ	0.25	0.2468	0.2427	0.2508

Table 4.1: ***Accuracy*** *of the parameter estimates that determine the Gaussian mixture model estimated by the hybrid method. The sample means are computed from parameter estimates obtained from 100 noise realisations of the Gaussian mixture model and compared with the input values of the model parameters.*

Parameter	CRLB	Sample variance	95% confidence interval	
			Lower bound	Upper bound
π_1	0.0017	0.0018	0.0013	0.0023
π_2	0.0018	0.0016	0.0017	0.0020
π_3	0.0018	0.0019	0.0013	0.0025
π_4	0.0018	0.0015	0.0015	0.0019
π_5	0.0017	0.0021	0.0016	0.0026
a	$9.8 \cdot 10^{-5}$	$11.0 \cdot 10^{-5}$	$8.9 \cdot 10^{-5}$	$14.0 \cdot 10^{-5}$
σ	$4.4 \cdot 10^{-4}$	$5.5 \cdot 10^{-4}$	$3.4 \cdot 10^{-4}$	$6.2 \cdot 10^{-4}$

Table 4.2: ***Precision*** *of the parameter estimates that determine the Gaussian mixture model estimated by the hybrid method. The sample variances are computed from parameter estimates obtained from 100 noise realisations of the Gaussian mixture model and compared with the Cramér-Rao lower bound for the model parameters.*

and the hybrid method, with 95% confidence intervals. We conclude from Figure 4.3 that the hybrid method provides more accurate estimates for the width of the components as compared to the statistics-based method, which severely underestimates the width of the components at low values of N/G. The parameter estimates for the width σ obtained by the hybrid method are thus more reliable, resulting in more reliable atom-counts, as compared to the statistics-based method. Furthermore, this implies that the hybrid method allows for a more accurate estimate of the relative width of the components σ/δ, which determines the overlap between Gaussian components, so as visualised in Figure 4.1. Therefore, the precision of the atom-counts themselves - inherently determined by the amount of overlap between the components - can be quantified more accurately. Very recently, the finite atom-counting precision estimated in this manner was used in a Bayesian genetic algorithm to reconstruct the 3D atomic structure based on 2D atom-counting results [De Backer 2021c].

4.4 Assessing the model order of the mixture model using an order selection criterion

The above described parameter estimation procedure assumes a given number of components G. As mentioned before, the number of components G is equal to the maximum thickness,

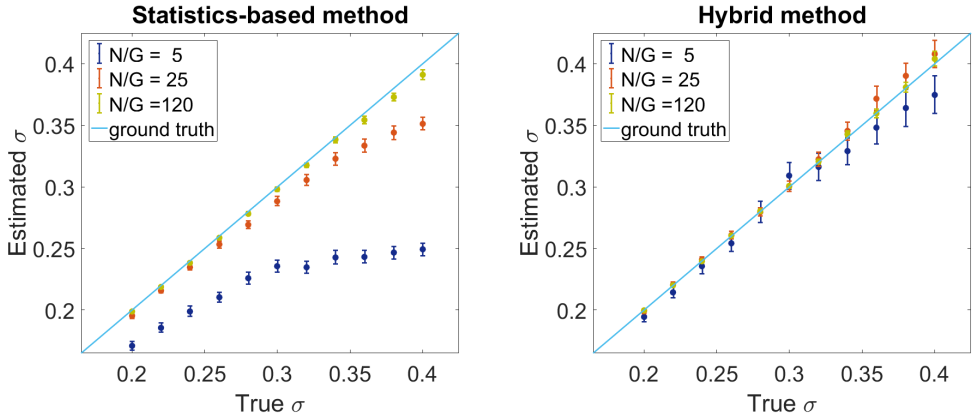

(a) **(b)**

Figure 4.3: *Accuracy of the estimated width of the components σ. The estimated width of the components is evaluated as a function of the true value of σ used in the Gaussian mixture models for (a) the statistics-based method and (b) the hybrid method.*

and is therefore equal to the length of the library needed to incorporate the prior knowledge from image simulations in the statistical framework. In this thesis, we will refer to the number of components in the context of the hybrid method as the "library length". Unfortunately, this library length G is not known beforehand. In principle, a large enough library length can be used to obtain the same correct model, since mixing proportions of components that exceed the maximum thickness can be estimated zero. However, in practice, a smaller scaling parameter a in combination with non-zero mixing proportions often results in a better fit of the Gaussian mixture model to the underlying scattering cross sections. The resulting model has a higher likelihood, but is not the correct model. A selection criterion therefore needs to be used to determine the physically meaningful library length, required to estimate the correct probability distribution of the scattering cross sections. Such a criterion includes a likelihood term, as well as a penalty term. Many different information criteria exist, accounting for the complexity of the estimated model in a different manner [McLachlan 2000]. The Integrated Classification Likelihood (ICL) criterion was shown to have the best performance for atom-counting [De Backer 2013]:

$$ICL(G) = -2\log L(\hat{\boldsymbol{\Psi}}_G) + 2EN(\hat{\tau}) + d\log N, \tag{4.13}$$

with a negative log likelihood term $-2\log L(\hat{\boldsymbol{\Psi}}_G)$, and a penalty term $2EN(\hat{\tau}) + d\log N$ depending on the sample size N, the number of parameters $d = G + 1$ to be estimated, and the entropy, expressed by

$$EN(\hat{\tau}) = -\sum_{g=1}^{G}\sum_{n=1}^{N} \tau_g\left(\hat{V}_n|\hat{\boldsymbol{\Psi}}_G\right)\log \tau_g\left(\hat{V}_n|\hat{\boldsymbol{\Psi}}_G\right), \tag{4.14}$$

with $\tau_g\left(\hat{V}_n|\boldsymbol{\Psi}_G\right)$ the posterior probability that the estimated scattering cross section of the n^{th} column $\hat{V}_n$ belongs to the g^{th} component:

$$\tau_g\left(\hat{V}_n|\hat{\boldsymbol{\Psi}}_G\right) = \frac{\pi_g \mathcal{N}\left(\hat{V}_n|\hat{a}\mathcal{M}_g, \hat{\sigma}\right)}{\sum_{h=1}^{G}\pi_h \mathcal{N}\left(\hat{V}_n|\hat{a}\mathcal{M}_h, \hat{\sigma}\right)}. \tag{4.15}$$

A large library length is penalised, while a larger likelihood is favoured. The entropy term favours mixture models with well-separated components, as to obtain a physically meaningful trade-off between the goodness of fit and the complexity of the model.
In Section 4.5, we will discuss the practical application of the ICL criterion for the hybrid method in more detail, using the Au nanorod that was previously also discussed in Section 2.7.

4.5 Atom-counting from an ADF STEM image of a Au nanorod

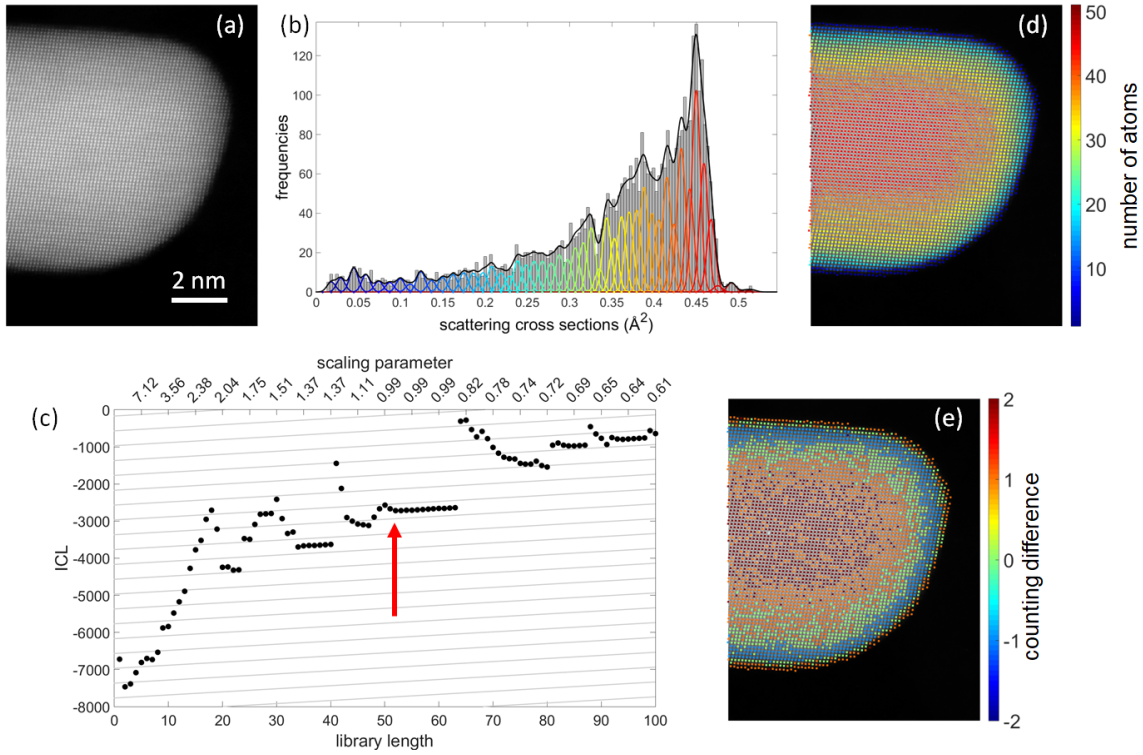

Figure 4.4: *(a) HAADF STEM image of a gold nanorod [Van Aert 2013]. (b) Set of estimated scattering cross sections. The solid black curve shows the estimated Gaussian mixture model, whereas the coloured curves indicate the individual components. (c) ICL criterion, with two axes, indicating library length and estimated value of the scaling parameter a. (d) Atom-counts for the gold nanorod. (e) Difference in atom-counts between the hybrid method and the statistics-based method.*

In this section, an experimental HAADF STEM image of a gold (Au) nanorod, previously also shown in Figure 2.5, will be analysed in order to illustrate the methodology of the hybrid method for atom-counting. The number of atoms in this Au nanorod could already be counted reliably using the statistics-based atom-counting method [Van Aert 2013], as an agreement between independent image simulations and the estimated locations of the components in the Gaussian mixture model was then found within the expected 5%-10% error range [Van Aert 2013, Rosenauer 2011, LeBeau 2008a]. Therefore, this well-conditioned experimental example can be used to validate the results obtained with the hybrid method. The image was recorded by Bart Goris and Gerardo Martinez along the [100] zone axis at the QuAntEM, a double corrected FEI Titan^3 working at 300 kV, and is shown in Figure 4.4a. A library of simulated scattering cross sections was created, as described in Section 2.6.

The scattering cross sections calculated from the refined model of the experimental image are shown in Figure 4.4b. In an ideal case, we would observe separated components, corresponding to sets of atomic columns with the same number of atoms. However, due to the unavoidable presence of noise, these components are broadened and they therefore overlap each other. This broadening is described by the probability distribution given by Equations (4.4) and (4.3). Such a probability distribution is then estimated for each library length ranging between 1 and 100. The values of the ICL criterion, given by Equation (4.13), for each of these library lengths are evaluated in Figure 4.4c. The top axis indicates the estimated scaling parameter corresponding to the models at different library lengths. In this example, the minimum at a library length equal to 51 is selected, corresponding to a scaling parameter of $a = 0.99$, reflecting the high accuracy of the measured experimental parameters. The estimated probability distribution at this library length is shown as a full black curve in Figure 4.4b. The individual components are shown in colour, corresponding to the number of atoms per column. In Figure 4.4d, each atomic column was assigned the number of atoms corresponding to the highest probability based on the estimated probability distribution from Figure 4.4b.

The interpretation of the ICL criterion obtained by the hybrid method slightly differs from the interpretation of the ICL criterion as obtained by the statistics-based method, discussed previously in Section 2.7. We are still looking for a local minimum, but additional information is provided by the value of the scaling parameter and can be used to determine the correct local minimum. Usually, multiple local minima, corresponding to different values of the scaling parameter, are present in the ICL criterion. If the experiment was conducted carefully, discrepancies between actual and simulated experimental conditions are expected to be small, i.e. within the expected 5%-10% error range [Van Aert 2013, Rosenauer 2011, LeBeau 2008a]. This would imply a scaling value approximately equal to 1. However, it is inadvisable to discard other local minima based only on their unexpected scaling values. A local minimum at a scaling value which differs strongly from 1 can be selected as the minimum of interest when one can explain the nature of these large discrepancies, e.g. by means of additional image simulations using different values for sample tilt or inner detector angle. If this is not the case, the local minimum corresponding to a scaling value close to 1 is selected as the minimum of interest.

Note that inclined grey lines with slope $\log N$ are added to the plot of the ICL criterion. In the ICL criterion in Figure 4.4c, we see linear features where the values increase parallel to the grey lines, i.e. with the same slope of $\log N$. These features indicate that the estimated probability distribution for these library lengths is essentially the same. In fact, the mixing proportions of components corresponding to a library length exceeding the first library length of the feature are estimated equal to zero. As a consequence, the entropy term and the likelihood term for these library lengths remain the same, leaving $d \log N$ as the only changing term in the expression for the ICL criterion given by Equation (4.13). Such linear features indicate a very good mathematical fit to the data, and can be used for interpretation of the ICL minimum. However, such features may not always be present due to for example large amounts of noise, as for the example given here. If such features appear and coincide with a scaling value close to 1, we can choose the first library length of the feature as the minimum of interest.

Figure 4.4e displays the difference between the atom-counts obtained by the hybrid method and the statistics-based method for each atomic column. On average the number of atoms per column differs by only 1.02 atoms between both methods. This confirms the reliability of the results obtained with the hybrid method. In the next section, the performance of the hybrid method will be examined in detail and compared to the statistics-based method.

4.6 Atom-counting performance

The atom-counting performance can be quantified by the percentage of correctly counted atomic columns. Therefore, we will calculate this percentage for different combinations of the average number of columns per component N/G and the relative width of the components σ/δ for the hybrid method, as well as for the statistics-based method. The relative width of the components σ/δ is large when the signal-to-noise ratio is low, as is for example the case for low dose images. In such cases, the fluctuations of the scattering cross section values for atomic columns with the same thickness are large, causing subsequent Gaussian components to overlap significantly. This overlap is illustrated in Figure 4.1. Atomic columns in the tails of the Gaussian components are then attributed to the wrong number of atoms, since the overlapping neighbouring Gaussian component yields a higher probability. The average number of columns per component N/G can be related to the size of the particle. A small particle corresponds to a small value of N/G. The values of σ/δ and N/G determine how difficult it is to count the number of atoms. They can therefore be referred to as the conditions for atom-counting. Note that the value of N/G can be increased during an experiment by increasing the number of atomic columns by for example imaging a larger field of view. The largest improvement in the percentage of correctly counted atomic columns attained by the hybrid method is expected at difficult conditions for atom-counting, corresponding to noisy images of small nanoparticles.

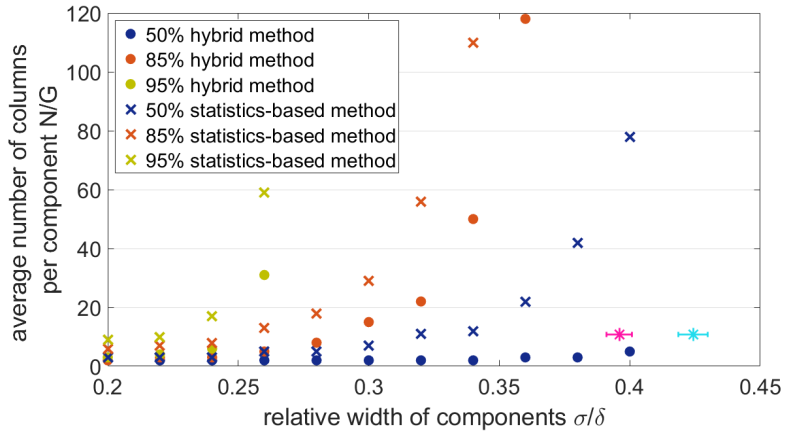

Figure 4.5: *The average number of columns per component needed to obtain 50%, 85% or 95% correctly counted atomic columns by the hybrid method or the statistics-based method, for a certain relative width of the components. Pink and cyan error bars correspond to the images analysed respectively in Figures 4.8 and 4.9.*

Noise realisations were created by performing random draws from Gaussian mixture models with 10 components, as described in Section 4.3.1. The values of σ and N are varied. For each combination, 100 such noise realisations were performed. The percentages of correctly counted atomic columns, after evaluation of the ICL criterion, are displayed in Figure 4.5. The ICL criterion, defined by Equation (4.13), was evaluated between library lengths 8 and 12. The interpretation of the ICL criterion as discussed in Section 4.5 was applied in order to select the minimum of interest. The average number of columns per component N/G required to correctly count 50%, 85% and 95% of the atomic columns is evaluated as a function of the relative width of the components σ/δ. The percentage of correctly counted atomic columns increases with increasing average number of columns per component N/G and decreasing relative width of the components σ/δ. However, the required N/G to reach a given percentage with the

hybrid method is lower than the N/G needed to reach the same percentage using the statistics-based method for constant σ/δ. In other words, the hybrid method does indeed outperform the statistics-based method, especially for small nanostructures. Note that the percentage of correctly counted atomic columns is determined by the selection of the library length after an evaluation of the ICL criterion on the one hand, and by the overlap between the Gaussian components, limiting the precision, on the other hand. We conclude from the results in Figure 4.5 that the most significant improvement is achieved at high values of σ/δ. These results therefore suggest the possibility of reliably counting the number of atoms in samples where counting was previously impossible, specifically in images of small, beam-sensitive particles recorded using a lower electron dose.
In the remainder of this chapter, the hybrid method will be applied to two non-model like systems: a tilted Pt nanoparticle and a Pt/Ir nanoparticle imaged using a low electron dose.

4.7 Atom-counting in the presence of sample tilt

The scaling relationship of Equation (4.1) was introduced to account for a possible mismatch between experimental and simulated conditions, such as a difference in detector angles or sample mistilt. In this section, we will explicitly impose such a mismatch, by considering simulated ADF STEM images of a hypothetical Pt nanoparticle with various amounts of sample tilt, while the image simulations for the library were performed in zone axis orientation. The effect of sample tilt on the quantification of ADF STEM image intensities was previously studied in Chapter 3. Scattering cross sections decrease when the sample is tilted away from zone axis orientation, due to a loss of the channelling conditions [Loane 1988, Van Dyck 1996, E 2013, MacArthur 2015]. We concluded that this loss in intensity can not be recovered by altering the parametric imaging model fitted to the ADF STEM image intensities using 2D elliptical Gaussians, although the residual intensities on a pixel by pixel basis are in fact smaller. Therefore, the validation of the counting results obtained from a tilted sample by the statistics-based method for atom-counting using independent image simulations of the crystal in zone axis orientation is not straightforward. Nonetheless, reliable atom-counting is possible, using the hybrid method introduced in this chapter. In this section, we apply the hybrid method to an example with sample tilt. To this purpose, we simulated ADF STEM images of a hypothetical Pt nanoparticle for which the atomic structure is shown in Figure 4.6a. Images were simulated corresponding to zone axis orientation, shown in Figure 4.6b, and with different amounts of sample tilt, up to 40 mrad, shown in Figure 4.6c. Simulation parameters are summarised in Appendix A. Furthermore, we create a library of scattering cross sections with the same microscope settings, corresponding to a zone axis oriented Pt crystal, as described in Section 2.6. Note that the ADF STEM images are analysed without noise, i.e. at infinite dose. In this manner, we can evaluate how well the scaling parameter a can compensate for the sample tilt, without mixing the interpretation of the results with dose effects.
Figure 4.7a evaluates the estimated scaling parameter as a function of the sample tilt, as well as the percentage of correctly counted atomic columns. The hybrid method achieves more than 95% correctly counted atomic columns, even in the presence of sample tilt. At all tilt angles, at most one or two atomic columns are miscounted by 1 atom, as shown in Figure 4.7b-e. The ground truth number of atoms per atomic column is visualised in Figure 2.6a of Section 2.7, where this hypothetical Pt nanoparticle was previously used to demonstrate the difference between component number and number of atoms in the statistics-based method.
As expected, the scaling parameter is estimated close to 1 for the zone axis orientation. Then, after a plateau at small tilt angles, similar to the results of [MacArthur 2015], the scaling pa-

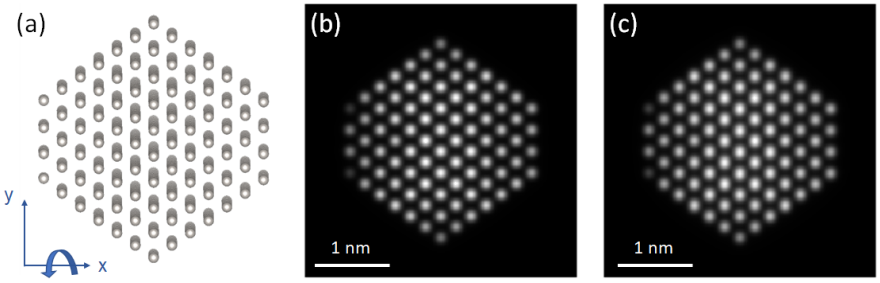

Figure 4.6: *(a) Visualisation of the Pt nanoparticle. The tilt direction used in the simulation study is shown schematically. (b) Simulated ADF STEM image of the Pt nanoparticle in zone axis orientation. (c) Simulated ADF STEM image of the Pt nanoparticle with a sample tilt of 40 mrad.*

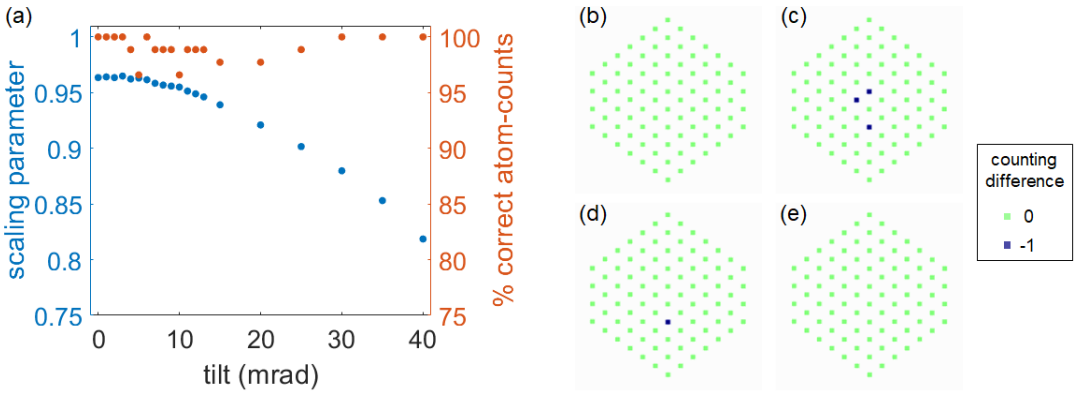

Figure 4.7: *(a) Estimated scaling parameter and percentage of correctly counted atomic columns using the hybrid method for atom-counting from simulated ADF STEM images of the hypothetical Pt nanoparticle shown in Figure 4.6, evaluated as function of sample tilt. (b-d) Difference counts as compared to the ground truth (Figure 2.6a) at 0, 10, 25 and 40 mrad sample tilt respectively.*

rameter decreases with increasing sample tilt. This demonstrates the applicability of the hybrid method for atom-counting in case of sample tilt, which is often unavoidable for small, beam-sensitive nanoparticles. Beam-sensitive nanomaterials furthermore should be images using a low electron dose, in order to avoid radiation damage. Therefore, in the next section, an experimental low dose image is analysed for which reliable atom-counting was previously not possible using the statistics-based counting procedure.

4.8 Atom-counting from a low dose ADF STEM image of a Pt/Ir nanoparticle

In the present section, the hybrid method is used to count the number of atoms in a challenging experimental, relatively low dose image of a small Pt/Ir particle, shown in Figure 4.8a and previously discussed in Section 2.7. The particle was supported on a three-dimensional carbon black support and was received in powder form dusted onto a carbon coated copper grid. The image was taken by Armand Béché at the QuAntEM, a double corrected FEI Titan^3 working at 300 kV. The difference in atomic number between Ir (Z=77) and Pt (Z=78) is only one, causing a difference of less than 3% in the scattering cross sections up to 15 atoms in

a projected atomic column. Therefore, Pt and Ir can be analysed together for the purpose of counting the number of atoms per column. The library of simulated scattering cross sections was created, as described in Section 2.6, assuming Pt only. Using the statistics-based method, a significant mismatch between the estimated locations and the simulated scattering cross sections was found [De Backer 2015b]. This can be understood from Figure 4.5, where the pink error bar corresponds to the estimated N/G and σ/δ values for this low dose image. It was shown that the statistics-based method underestimates the model order due to the insufficient electron dose [De Backer 2015b].

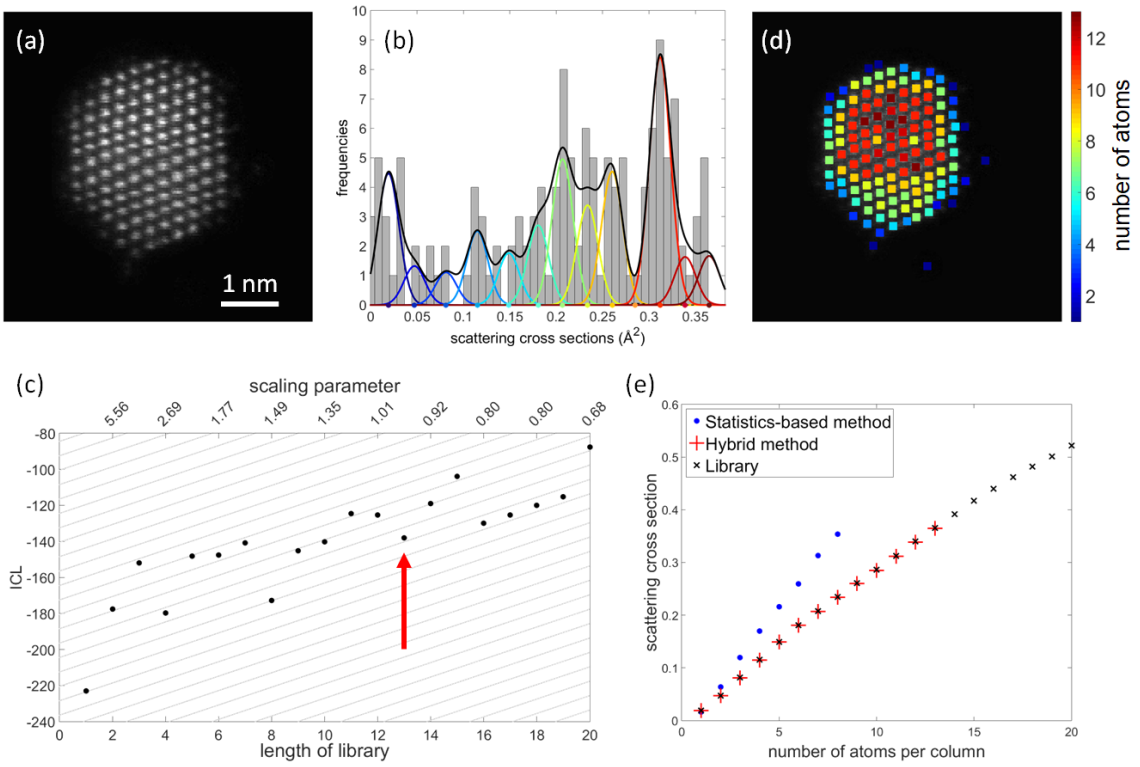

Figure 4.8: *(a)* ***Experimental*** *ADF STEM image of a platinum-iridium nanoparticle recorded using an electron dose of* $6.5 \cdot 10^4$ $e^-/\text{Å}^2$ *[De Backer 2015b]. (b) Set of estimated scattering cross sections. The solid black curve shows the estimated Gaussian mixture model, whereas the coloured curves indicate the individual components. (c) ICL criterion, with two axes, indicating library length and estimated value of the scaling parameter a. (d) Atom-counts for the platinum-iridium nanoparticle. (e) Scattering cross sections evaluated as a function of the number of atoms per column.*

Figure 4.8 summarises the analysis of this relatively low dose image of the Pt/Ir particle using the hybrid method. The set of estimated scattering cross sections is shown in Figure 4.8b. By assessing the ICL criterion as a function of the library length and the scaling parameter, the minimum of interest is chosen at the significant local minimum which occurs at library length 13, as indicated in Figure 4.8c. The estimated scaling parameter at this library length is close to the expected value of 1. The resulting estimated probability distribution of the scattering cross sections is shown in Figure 4.8b by a black curve. The individual components that compose the distribution are displayed in different colours. In Figure 4.8d, each atomic column was assigned the number of atoms corresponding to the highest probability based on the estimated probability distribution. The intensity/thickness graph in Figure 4.8e evaluates the estimated locations by the statistics-based method, the estimated locations by the hybrid method, and the

simulated scattering cross sections (library), as a function of the number of atoms per column. A mismatch between estimated cross sections and simulated cross sections is no longer found by the hybrid method, since the scaling parameter is estimated almost equal to 1. The hybrid method therefore enables us to overcome the limitations of the statistics-based method. Note that the local minimum in the ICL criterion at library length 16 should also be considered. The corresponding scaling parameter of 0.8 can however not be explained. High dose experiments on the same day confirm that the detector inner angle was accurately determined and visual interpretation of the image excludes a large sample tilt [De Backer 2015b]. Therefore, we have sufficient arguments to accept the local minimum at the scaling value closest to 1.

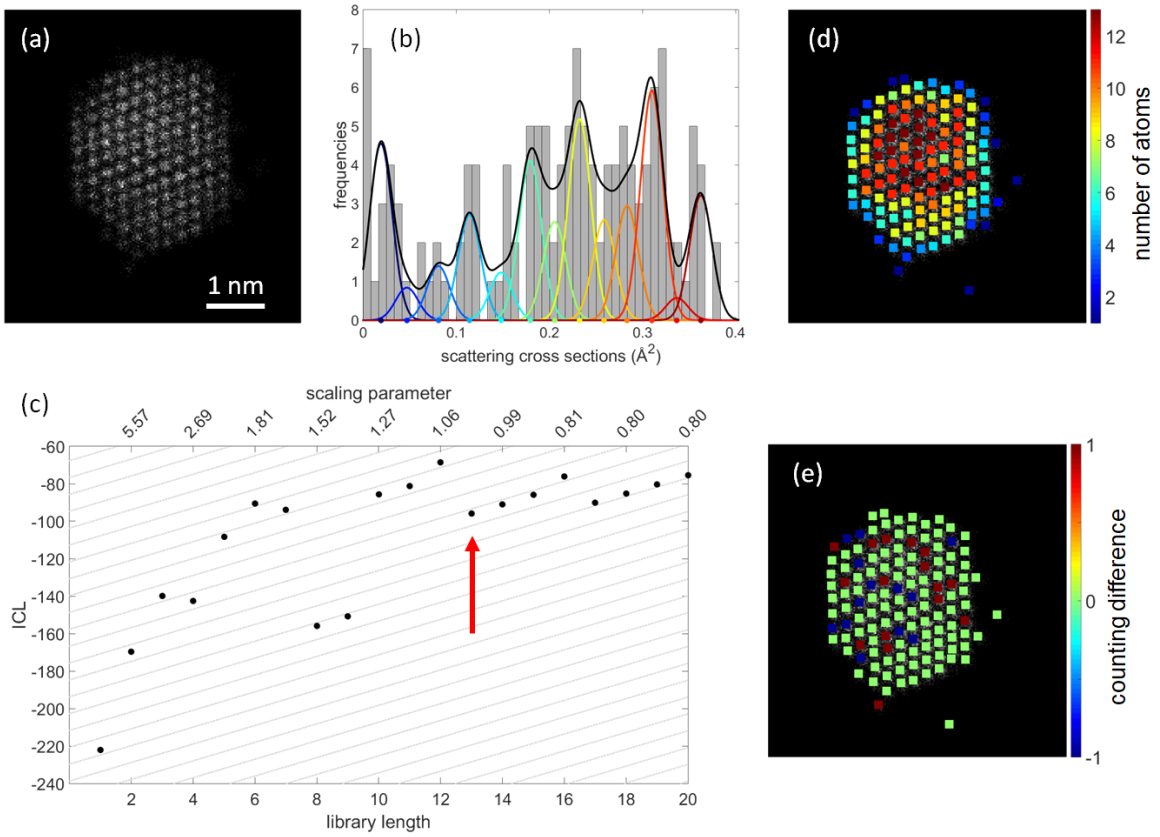

Figure 4.9: *(a)* ***Hypothetical*** *ADF STEM image corresponding to a low electron dose of* 10^3 $e^-/\text{Å}^2$*, based on the platinum-iridium nanoparticle from Figure 4.8. (b) Set of estimated scattering cross sections. The solid black curve shows the estimated Gaussian mixture model, whereas the coloured curves indicate the individual components. (c) ICL criterion, with two axes, indicating library length and estimated value of the scaling parameter a. (d) Atom-counts for the simulated low dose image of a nanoparticle. (e) Difference in atom-counts between original image and the simulated lower dose image.*

Thus far, we have shown that the hybrid method enables us to reliably count the number of atoms per column in an experimental image from which reliable atom-counting was previously impossible due to an insufficient electron dose. In order to investigate the possibilities at even lower electron doses, a hypothetical low dose image of the small nanoparticle is now treated with the hybrid method. This analysis is summarised in Figure 4.9. The simulated image is obtained by performing a Poisson distributed random draw from the model fitted to the Pt/Ir nanoparticles, corresponding to an electron dose of only 10^3 $e^-/\text{Å}^2$. The resulting image

is shown in Figure 4.9a. The estimated scattering cross sections obtained from this image are displayed in Figure 4.9b. Based on the ICL criterion from Figure 4.9c, the minimum of interest is chosen at a library length of 13, as was also the case for the original image of the Pt/Ir nanoparticle. The corresponding scaling parameter is estimated equal to $a = 0.99$. The estimated probability distribution at this library length is shown in Figure 4.9b. The lowering of the electron dose resulted in a broadening of the components estimated in the Gaussian mixture model from $\sigma/\delta = 0.3960 \pm 0.0049$ (pink error bar in Figure 4.5) to $\sigma/\delta = 0.4243 \pm 0.0056$ (cyan error bar in Figure 4.5), resulting unavoidably in a more limited precision. However, the correct library length is still retrieved, despite the low electron dose. Atom-counts are shown in Figure 4.9d. The atom-counts obtained from the analysis of this low dose image of the Pt/Ir nanoparticle differ no more than ±1 atom as compared to the results obtained from the original, relatively low dose image of the Pt/Ir nanoparticle, as shown by the difference map in Figure 4.9e.
We conclude from the results in the present section that the hybrid method for atom-counting holds promise for quantitative analysis of challenging, beam-sensitive nanoparticles, thanks to its ability to overcome challenges presented by very low electron doses.

4.9 Conclusions

In this chapter, an improved method for atom-counting from ADF STEM images of monatomic crystalline nanostructures has been presented. This method was shown to exceed the limitations of the existing atom-counting methods, by directly combining image simulations and statistical parameter estimation theory. The method exploits prior knowledge obtained from image simulations, without suffering from the unknown accuracy of the experimental parameters used in these image simulations. We have demonstrated that the parameters are estimated accurately and precisely. Interestingly, the relative width of the Gaussian components that describe the fluctuations of scattering cross sections that correspond to atomic columns with the same thickness, is estimated more accurately. This leads to a more reliable quantification of the atom-counting precision.
Similarly to the statistics-based method, an order selection criterion is required for the selection of the physically correct number of components in the probability distribution of the scattering cross sections. We demonstrated how the linear scaling parameter, that is introduced in the hybrid method in order to incorporate the library values in the probability distribution, can facilitate the interpretation of this order selection criterion. In this manner, this becomes a less subjective part of the quantitative analysis.
Counting results have been validated using a high dose image of a gold nanorod. A simulation study shows that the largest improvement in atom-counting performance is realised for low dose images of small nanoparticles, conditions for which the statistics-based method can no longer obtain reliable atom-counts. Furthermore, image simulations of a hypothetical platinum nanoparticle demonstrate that reliable atom-counting is even possible in the presence of sample tilt with the hybrid method. The improved low-dose performance is confirmed by the analysis of a small platinum-iridium nanoparticle imaged using a relatively low electron dose, which could not be analysed reliably using the statistics-based method, and by the successful analysis of a simulated image at an even lower electron dose.
It should be noted that the description of the performance for atom-counting in Section 4.6 in fact assumes that the linear scaling relationship between simulated scattering cross sections and experimental scattering cross sections accurately describes the combined effect of measurement errors in different experimental input parameters of the image simulations. Although

it is shown that this linear scaling relationship provides a good first approximation, especially for thin samples, the performance of the hybrid method may improve by refining this parametric function. Nonetheless, we have shown that the hybrid method is a promising first step towards reliable atom-counting from low electron dose images of beam-sensitive materials.

Appendix 4A: Cramér-Rao lower bound

We introduced the Cramér-Rao lower bound in Section 2.4 for a general estimator, and will now apply this to the hybrid method for atom-counting. For unbiased estimators, the Cramér-Rao lower bound defines the lower bound on the variance [Rao 1945, Cramér 1946]:

$$\text{cov}(\hat{\mathbf{\Psi}}_G, \hat{\mathbf{\Psi}}_G) \geq F^{-1}_{\mathbf{\Psi}_G}, \tag{4.16}$$

with $\hat{\mathbf{\Psi}}_G$ the vector containing the estimators of the parameters summarised in the parameter vector $\mathbf{\Psi}_G$, and $F_{\mathbf{\Psi}_G}$ the Fisher information matrix, which is defined as follows for the hybrid method for atom-counting:

$$F_{\mathbf{\Psi}_G} = -\mathbb{E}\left[\left.\frac{\partial^2 \ln p(\mathbf{V}|\mathbf{\Psi}_G)}{\partial \mathbf{\Psi}_G \partial \mathbf{\Psi}_G^T}\right|_{\mathbf{\Psi}_G=\mathbf{\Psi}_0}\right], \tag{4.17}$$

where $\mathbb{E}$ expresses the expectation value. In this expression, $p(\mathbf{V}|\mathbf{\Psi}_G)$ represents the joint probability density function, in this case determined by the Gaussian mixture model $f_{\text{mix}}(\mathbf{V}|\mathbf{\Psi}_G)$, defined in Equations (4.6)-(4.2). This Gaussian mixture model describes the probability distribution of the set of scattering cross sections $\mathbf{V}$, and is determined by the unknown parameters expressed by the parameter vector $\mathbf{\Psi_G}$, given in Equation (4.5). The vector $\mathbf{\Psi}_0$ contains the actual values of the parameters to be estimated. In practice, the following integral is numerically integrated:

$$F_{\mathbf{\Psi}_G} = -N \int_{-\infty}^{\infty} \left.\frac{\partial^2 \ln f_{\text{mix}}(V|\mathbf{\Psi}_G)}{\partial \mathbf{\Psi}_G \partial \mathbf{\Psi}_G^T}\right|_{\mathbf{\Psi}_G=\mathbf{\Psi}_0} f_{\text{mix}}(V|\mathbf{\Psi}_G) dV, \tag{4.18}$$

with N the total number of columns in the image.
Notation is simplified as follows:

$$\mathcal{N}(V_n|a\mathcal{M}_g, \sigma) = \mathcal{N}_g, \tag{4.19}$$
$$f_{\text{mix}}(V_n|\mathbf{\Psi}_G) = f_{\text{mix}}, \tag{4.20}$$
$$p(\mathbf{V}|\mathbf{\Psi}_G) = p. \tag{4.21}$$

The necessary first and second order derivatives to obtain the Fisher information matrix for all parameters in the parameter vector $\mathbf{\Psi}_G$ are listed here:

$$\frac{\partial \ln p}{\partial \pi_i} = \sum_{n=1}^{N} \frac{\mathcal{N}_i - \mathcal{N}_G}{f_{\text{mix}}}, \tag{4.22}$$
$$\frac{\partial \ln p}{\partial a} = \sum_{n=1}^{N} \frac{1}{f_{\text{mix}}} \sum_{g=1}^{G} \pi_g \mathcal{N}_g \frac{(V_n - a\mathcal{M}_g)\mathcal{M}_g}{\sigma^2}, \tag{4.23}$$
$$\frac{\partial \ln p}{\partial \sigma} = \sum_{n=1}^{N} \frac{1}{f_{\text{mix}}} \sum_{g=1}^{G} \pi_g \mathcal{N}_g \left(\frac{(V_n - a\mathcal{M}_g)^2}{\sigma^3} - \frac{1}{\sigma}\right), \tag{4.24}$$

and

$$\frac{\partial^2 \ln p}{\partial \pi_i \partial \pi_k} = -\sum_{n=1}^{N} \frac{(\mathcal{N}_i - \mathcal{N}_G)(\mathcal{N}_k - \mathcal{N}_G)}{f_{\text{mix}}^2}, \tag{4.25}$$

$$\frac{\partial^2 \ln p}{\partial \pi_i \partial a} = \sum_{n=1}^{N}\left[\frac{1}{f_{\text{mix}}}\left(\mathcal{N}_i\frac{(V_n - a\mathcal{M}_i)\mathcal{M}_i}{\sigma^2} - \mathcal{N}_G\frac{(V_n - a\mathcal{M}_G)\mathcal{M}_G}{\sigma^2}\right) - \frac{\mathcal{N}_i - \mathcal{N}_G}{f_{\text{mix}}^2}\sum_{g=1}^{G}\pi_g\mathcal{N}_g\frac{(V_n - a\mathcal{M}_g)\mathcal{M}_g}{\sigma^2}\right], \tag{4.26}$$

$$\frac{\partial^2 \ln p}{\partial \pi_i \partial \sigma} = \sum_{n=1}^{N}\left[\frac{1}{f_{\text{mix}}}\left(\mathcal{N}_i\left(\frac{(V_n - a\mathcal{M}_i)^2}{\sigma^3} - \frac{1}{\sigma}\right) - \mathcal{N}_G\left(\frac{(V_n - a\mathcal{M}_G)^2}{\sigma^3} - \frac{1}{\sigma}\right)\right) - \frac{\mathcal{N}_i - \mathcal{N}_G}{f_{\text{mix}}^2}\sum_{g=1}^{G}\pi_g\mathcal{N}_g\left(\frac{(V_n - a\mathcal{M}_g)^2}{\sigma^3} - \frac{1}{\sigma}\right)\right], \tag{4.27}$$

$$\frac{\partial^2 \ln p}{\partial a \partial \sigma} = \sum_{n=1}^{N}\left[-\frac{1}{f_{\text{mix}}^2}\left(\sum_{g=1}^{G}\pi_g\mathcal{N}_g\left(\frac{(V_n - a\mathcal{M}_g)^2}{\sigma^3} - \frac{1}{\sigma}\right)\right)\left(\sum_{g=1}^{G}\pi_g\mathcal{N}_g\frac{(V_n - a\mathcal{M}_g)\mathcal{M}_g}{\sigma^2}\right) + \frac{1}{f_{\text{mix}}}\sum_{g=1}^{G}\pi_g\mathcal{N}_g\frac{(V_n - a\mathcal{M}_g)\mathcal{M}_g}{\sigma^2}\left(\frac{(V_n - a\mathcal{M}_g)^2}{\sigma^3} - \frac{3}{\sigma}\right)\right], \tag{4.28}$$

$$\frac{\partial^2 \ln p}{\partial a^2} = \sum_{n=1}^{N}\left[-\frac{1}{f_{\text{mix}}^2}\left(\sum_{g=1}^{G}\pi_g\mathcal{N}_g\frac{(V_n - a\mathcal{M}_g)\mathcal{M}_g}{\sigma^2}\right)^2 + \frac{1}{f_{\text{mix}}}\sum_{g=1}^{G}\pi_g\mathcal{N}_g\left(\left(\frac{(V_n - a\mathcal{M}_g)\mathcal{M}_g}{\sigma^2}\right)^2 - \frac{\mathcal{M}_g^2}{\sigma^2}\right)\right], \tag{4.29}$$

$$\frac{\partial^2 \ln p}{\partial \sigma^2} = \sum_{n=1}^{N}\left[-\frac{1}{f_{\text{mix}}^2}\left(\sum_{h=1}^{G}\pi_h\mathcal{N}_h\left(\frac{(V_n - a\mathcal{M}_h)^2}{\sigma^3} - \frac{1}{\sigma}\right)\right)\left(\sum_{g=1}^{G}\pi_g\mathcal{N}_g\left(\frac{(V_n - a\mathcal{M}_g)^2}{\sigma^3} - \frac{1}{\sigma}\right)\right) + \frac{1}{f_{\text{mix}}}\sum_{g=1}^{G}\pi_g\mathcal{N}_g\left[\left(\frac{(V_n - a\mathcal{M}_g)^2}{\sigma^3} - \frac{1}{\sigma}\right)^2 + \left(-\frac{3(V_n - a\mathcal{M}_g)^2}{\sigma^4} + \frac{1}{\sigma^2}\right)\right]\right]. \tag{4.30}$$

Finally, the lower bound on a function of estimated parameters is determined by Equation (4.31).

$$\text{cov}(\hat{\gamma}) \geq \frac{\partial \gamma(\theta)}{\partial \theta^T} F_\theta^{-1} \frac{\partial \gamma(\theta)^T}{\partial \theta} \tag{4.31}$$

Since $\pi_G = \pi_G(\pi_1, \pi_2, ..., \pi_{G-1}) = 1 - \sum_{g=1}^{G-1}\pi_g$, the lower bound on the variance of π_G is expressed as follows:

$$\text{var}(\pi_G) \geq \frac{\partial \pi_G(\theta)}{\partial \theta^T} F_{(\pi_1\pi_2...\pi_{G-1})}^{-1} \frac{\partial \pi_G(\theta)^T}{\partial \theta}, \tag{4.32}$$

with

$$\frac{\partial \pi_G(\theta)}{\partial \theta^T} = \begin{pmatrix} \frac{\partial \pi_G}{\partial \pi_1} & \frac{\partial \pi_G}{\partial \pi_2} & \dots & \frac{\partial \pi_G}{\partial \pi_{G-1}} \end{pmatrix}, \tag{4.33}$$

and

$$\frac{\partial \pi_G}{\partial \pi_i} = \frac{\partial}{\partial \pi_i}\left(1 - \sum_{g=1}^{G-1}\pi_g\right) = -1. \tag{4.34}$$

Using these expressions, we obtain all elements of the Fisher information matrix of Equation (4.18).

5

Hidden Markov model for atom-counting from an ADF STEM time series

5.1 Introduction

In the previous chapter a so-called hybrid statistics-simulations based method for atom-counting from an ADF STEM image was introduced. This approach allows us to reliably count the number of atoms in a nanomaterial, also at lower electron doses, as compared to the statistics-based atom-counting procedure, introduced in Section 2.7. However, this approach was designed for the analysis of a single ADF STEM image. In many cases, the atomic structure of the nanomaterial of interest will not remain constant through time. The atomic structure can change for example via adatom dynamics [Chang 2014, Furnival 2018], surface diffusion and reconstruction [Surrey 2012, Schneider 2014, Cherepanov 2004, Buffat 2003, Yu 2019], beam effects [Iijima 1986, Batson 2008, Egerton 2010, Lee 2013] or during *in situ* experiments [Taheri 2016, Altantzis 2019]. As such, the insight in the structural dynamics is missing from the analysis of only a single electron microscopy image. Therefore, we suggest an approach for atom-counting from a time series of ADF STEM images, using a so-called hidden Markov model [De wael 2020a, De wael 2020b]. Hidden Markov models were successful in other fields of science for applications such as speech recognition, sequence alignment of protein structures, electrocardiogram characterisation and condition-based maintenance of industrial machines [Rabiner 1989, Bilmes 1998, Eddy 2004, Bishop 2006, Dymarski 2011] and have optimal properties for modelling and analysing time series data. Here, for the first time, we apply hidden Markov models to ADF STEM data.

We start by introducing the general framework of the hidden Markov model in Section 5.2. Next, in Section 5.3, we discuss in detail how this model can be used to determine the probability distribution of the scattering cross sections, which enables atom-counting from a time series of ADF STEM images. Then, in Section 5.4, we discuss the estimation of the parameters of this probability distribution using an iterative Expectation-Maximisation algorithm, called a Baum-Welch algorithm in the context of hidden Markov models. These estimated parameters can then be used to retrieve the most likely counting results for the entire time series by

This chapter is based on [De wael 2020a, De wael 2020b].

applying the Viterbi algorithm. Next, we study the accuracy and precision of the parameter estimation, in order to assure that we can perform a reliable quantification. Finally, in Section 5.5, we discuss the performance for atom-counting of this hidden Markov model and show the improvement as compared to the hybrid method for atom-counting from the previous chapter, before concluding this chapter in Section 5.6.

5.2 The hidden Markov model

A hidden Markov model consists of two layers. The first layer is "hidden", and is observed only indirectly through the observed sequence that constitutes the second layer of the hidden Markov model. These two layers are respectively shown in light and dark grey in the schematic representation of a general hidden Markov model in Figure 5.1a. In the following, $\mathbf{h}_t$ will represent the hidden state at time t, and $\mathbf{o}_t$ will represent the observation at the same time t. The hidden state sequence is called $\mathbf{H} = \{\mathbf{h}_1, \cdots, \mathbf{h}_T\}$, with T the length of the time series, and the observed sequence is called $\mathbf{O} = \{\mathbf{o}_1, \cdots, \mathbf{o}_T\}$. The first layer is a first order Markov chain. This implies that the state at a given time t depends only on the previous state, at time $t-1$, and not on the state of the system before that [Drake 1967]:

$$p(\mathbf{h}_t|\mathbf{h}_{t-1}, \mathbf{h}_{t-2}, \cdots, \mathbf{h}_1) = p(\mathbf{h}_t|\mathbf{h}_{t-1}). \tag{5.1}$$

The (hidden) states of the Markov chain have an initial probability $p(\mathbf{h}_1)$ - blue in Figure 5.1, and can subsequently change state with a probability $p(\mathbf{h}_t|\mathbf{h}_{t-1})$, called the transition probability - green in Figure 5.1. Each hidden state is observed via an observation $\mathbf{o}_t$, with a probability $p(\mathbf{o}_t|\mathbf{h}_t)$, called the emission probability - red in Figure 5.1. The joint probability density function of the hidden state sequence $\mathbf{H}$ and the observed sequence $\mathbf{O}$ can be expressed as follows:

$$p(\mathbf{H}, \mathbf{O}) = p(\mathbf{h}_1) \prod_{t=2}^{T} p(\mathbf{h}_t|\mathbf{h}_{t-1}) \prod_{t'=1}^{T} p(\mathbf{o}_{t'}|\mathbf{h}_{t'}). \tag{5.2}$$

In the remainder of this chapter, we will specifically consider discrete hidden states that change according to discrete transition probabilities, and that emit continuous observations according to a continuous emission probability. The (discrete) transition probabilities that describe the state changes in the Markov chain are therefore summarised by a transition matrix, while a continuous probability density function will be used to model the emission probability.
In the context of atom-counting, the hidden states of the first layer correspond to the number of atoms in each atomic column at each image of the time series. This is schematically shown in the top row of Figure 5.1b. The number of atoms in each atomic column of the nanoparticle in each frame can only be observed indirectly through the ADF STEM images - shown in the bottom row of Figure 5.1b, from which scattering cross sections can be estimated, as described in Section 2.5. The transition probabilities will be related to the probability for an atomic column to lose or gain atoms from frame to frame during the time series. In this manner, the hidden Markov model will allow for the quantification of structural changes in nanoparticles. In the next section, we will discuss in detail how the hidden Markov model can be applied to atom-counting from time series of ADF STEM images.

5.3 Probability distribution of scattering cross sections

In order to apply hidden Markov models to atom-counting, we will consider the number of atoms in each atomic column n in each image t of the time series as a hidden state, visualised in

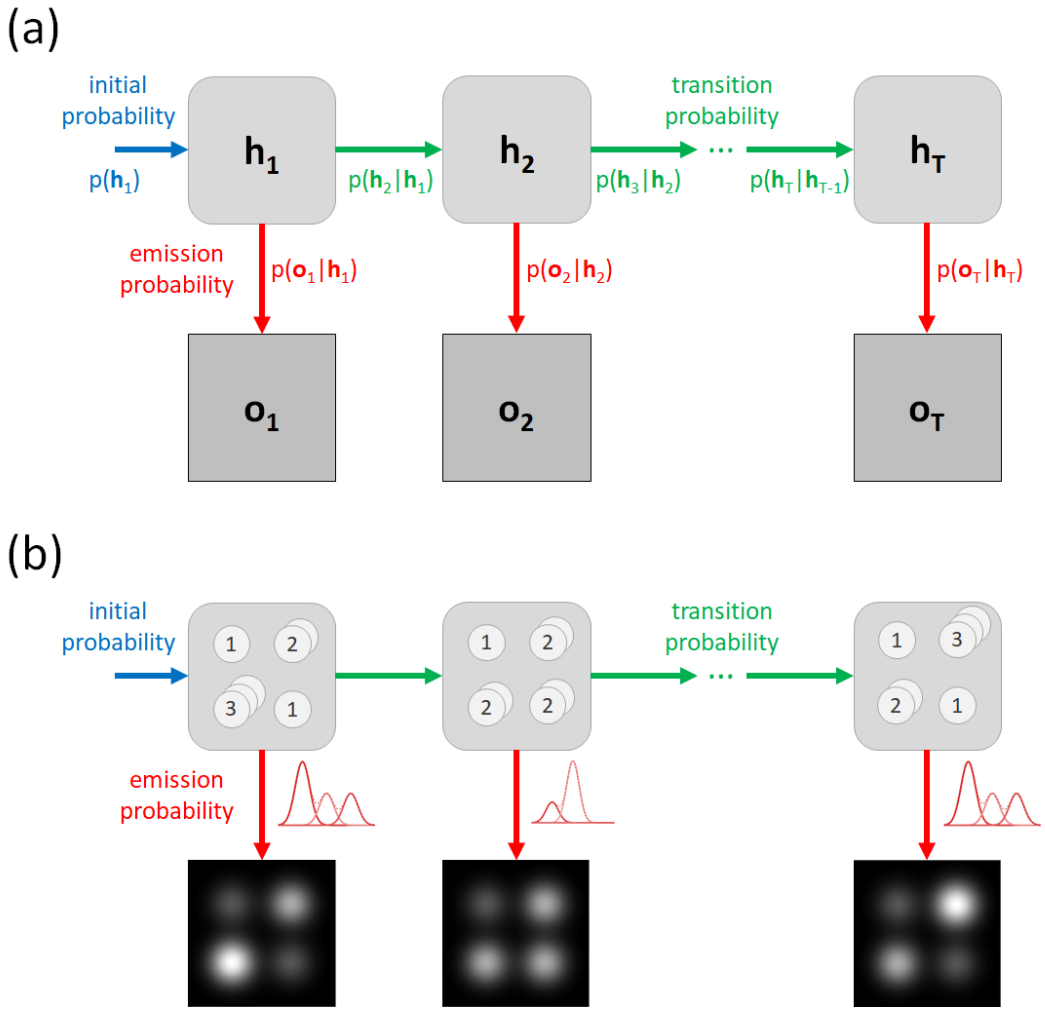

Figure 5.1: *Schematic representation of the hidden Markov model. (a) General hidden Markov model. (b) Hidden Markov model for atom-counting from time series of ADF STEM images.*

the top row of Figure 5.1b. A specific type of hidden Markov models, called the factorial hidden Markov model is used, in which the states are factorised [Ghahramani 1997]. We introduce the notation $\mathbf{h}_t^{(n)}$ to represent the hidden state (number of atoms) at time t for atomic column n. In the context of hidden Markov models, this is commonly chosen as a binary vector, rather than directly expressing the value of the hidden state, as this will facilitate further calculations. The g^{th} element of this binary vector, $h_{tg}^{(n)}$, equal to 1 if the number of atoms in the atomic column n in frame t equals g, otherwise $h_{tg}^{(n)} = 0$. The observations for each atomic column n at each time t are the scattering cross sections

$$\hat{o}_t^{(n)} = \hat{V}_n, \tag{5.3}$$

estimated from the ADF STEM images using Equations (2.14) and (2.15), as described in Section 2.5. This is visually represented in the bottom row of Figure 5.1b.
In order to understand the meaning of the initial, transition and emission probability (blue, green and red in Figure 5.1 respectively) introduced in the previous section in the context of time series atom-counting, we first consider the limit of atom-counting from a single ADF

STEM image. Indeed, for a single image, the probability distribution of the scattering cross sections should correspond to that of the single frame counting procedure, previously expressed in Equations (4.2)-(4.4):

$$p(\mathbf{O}) = \prod_{n=1}^{N} \sum_{g=0}^{G} \pi_g \mathcal{N}\left(o_n | a\mathcal{M}_g, \sigma\right), \tag{5.4}$$

with o_n the stochastic variable related to the scattering cross section of atomic column n in the single frame. All scattering cross sections are summarised in the vector $\mathbf{O}$. In order to see the analogy, we approach the single frame counting procedure as an incomplete data problem. In this approach, the component indices g of the Gaussian mixture model are considered as hidden data. It is important to note that the component index g corresponds immediately to the number of atoms g in the atomic column, as a result of Equation (4.1) introduced for the hybrid approach discussed in the previous chapter. The complete data description then corresponds to the joint observations of the scattering cross sections with the corresponding (hidden) number of atoms for each atomic column. We can define $\mathbf{H} = \{\mathbf{h}^{(n)}\}$ as the matrix that contains these hidden states, expressed by binary vectors with elements $h_g^{(n)} = 1$ if and only if atomic column n contains precisely g atoms. This leads to the following joint probability density for the hidden states $\mathbf{H}$ and the observations $\mathbf{O}$:

$$p(\mathbf{O}, \mathbf{H}) = \prod_{n=1}^{N} \prod_{g=0}^{G} \left(\pi_g \mathcal{N}\left(o_n | a\mathcal{M}_g, \sigma\right)\right)^{h_g^{(n)}}, \tag{5.5}$$

which reduces to Equation (5.4) after marginalising over all combinations of possible hidden states $\mathbf{H}$. In this expression, $h_g^{(n)}$ is the stochastic variable related to the binary vector that expresses the hidden state.

By substituting $T = 1$ in Equation (5.2), and comparing this with Equation (5.5), it follows that the emission probability $p(\mathbf{o}_t|\mathbf{h}_t)$ - red in Figure 5.1 - should be modelled using a Gaussian distribution around the average scattering cross sections at given thickness. The probability to observe a scattering cross section with value $o_t^{(n)}$ when g atoms are in the atomic column, is modelled by a Gaussian emission probability as follows:

$$p(o_t^{(n)}|h_{tg}^{(n)}) = \mathcal{N}\left(o_t^{(n)}|\mu_g, \sigma\right), \tag{5.6}$$

with mean value μ_g and width σ. In this expression, the average scattering cross section for an atomic column with g atoms is determined by $\mu_g = a\mathcal{M}_g$, with a a linear scaling parameter and $\mathcal{M}_g$ the library value, i.e. the scattering cross section determined from image simulations, for an atomic column with g atoms, as in Chapter 4. In this manner, we include prior knowledge from image simulations, but allow for small deviations between the parameters used for the image simulations and the actual experimental imaging conditions by estimating the linear scaling parameter a.

The mixing proportions π_g are equivalent to the initial probabilities used in the hidden Markov model - blue in Figure 5.1, and quantify the probability that an atomic column will have g atoms. The initial probabilities will be written as ι_g in the remainder of this chapter:

$$p(h_{1g}^{(n)}) = \iota_g. \tag{5.7}$$

The extension from single frame to time series atom-counting is done by introducing the discrete transition probabilities $p(\mathbf{h}_t|\mathbf{h}_{t-1})$. The probability that an atomic column n has j atoms at a given time t and g atoms at the next time $t+1$ is written as

$$p(h_{t+1,g}^{(n)}|h_{t,j}^{(n)}) = A_{jg}. \tag{5.8}$$

All possible transition probabilities A_{jg} are summarised in the transition matrix

$$\mathbf{A} = \left\{A_{jg}\right\}. \tag{5.9}$$

The mixing proportions correspond to the probability of having g atoms in an atomic column. During the time series, these probabilities are modified by the transition probabilities A_{jg}. We can therefore derive mixing proportions at each frame t, to quantify how the probability of having g atoms in an atomic column is changed after each transition from one frame to the next. The mixing proportion at frame $t = 1$ is given by

$$\pi_g^{(1)} = \iota_g. \tag{5.10}$$

In a frame $t > 1$, the probability of having g atoms in an atomic column depends on the probabilities for all possible transitions $j \rightarrow g$ from frame $t-1$ to frame t, and on the probability distribution for the different thicknesses j in the previous frame, such that:

$$\pi_g^{(t)} = \sum_{j=0}^{G} \pi_j^{(t-1)} A_{jg}. \tag{5.11}$$

In Section 6.2, we will use this expression to link the transition probabilities to a physical cross section related to structural changes. Note that the transition probabilities defined in this manner do not pose any restrictions on the physical mechanism causing the changes in the atomic structure during the time series.
We now obtain the following joint probability density function of the observed sequence $\mathbf{O}$ and hidden state sequence $\mathbf{H}$ for the factorial hidden Markov model for atom-counting:

$$p(\mathbf{O}, \mathbf{H}|\mathbf{\Omega}) = \prod_{n=1}^{N} \prod_{g=0}^{G} \left(\iota_g\right)^{h_{1g}^{(n)}} \tag{5.12a}$$

$$\times \prod_{t=2}^{T} \prod_{n=1}^{N} \prod_{j=0}^{G} \prod_{g=0}^{G} \left(A_{jg}\right)^{h_{t-1,j}^{(n)} h_{tg}^{(n)}} \tag{5.12b}$$

$$\times \prod_{t=1}^{T} \prod_{g=0}^{G} \prod_{n=1}^{N} \left(\mathcal{N}(o_t^{(n)}|a\mathcal{M}_g, \sigma)\right)^{h_{tg}^{(n)}}, \tag{5.12c}$$

with $h_{tg}^{(n)}$ and $o_t^{(n)}$ the stochastic variables related to the number of atoms g and the scattering cross section of atomic column n in frame t, summarised in $\mathbf{H}$ and $\mathbf{O}$ respectively. Note that we have now included the explicit dependence on the parameter vector $\mathbf{\Omega}$ in the complete data likelihood function of Equation (5.12). The parameter vector summarises all unknown parameters of the hidden Markov model:

$$\mathbf{\Omega} = (\iota_0, \iota_1, \cdots, \iota_{G-1}, A_{00}, \cdots, A_{0,G-1}, A_{10}, \cdots A_{G,G-1}, a, \sigma)^{\mathsf{T}}. \tag{5.13}$$

In Equation (5.12), G is the maximum number of atoms in any atomic column of the time series and T is the number of frames in the time series. The product over the number of atoms starts from 0, in order to allow atomic columns to be absent in some of the frames. The initial probability ι_g expresses the probability for an atomic column to contain g atoms in the first frame. Only G initial probabilities are estimated, since

$$\sum_{g=0}^{G} \iota_g = 1. \tag{5.14}$$

The transition probability A_{jg} expresses the probability that an atomic column has j atoms in one frame and g atoms in the next frame. All transition probabilities, for $0 \leq j \leq G$ and $0 \leq g \leq G$ are summarised in the $(G+1)\times(G+1)$ transition matrix $\mathbf{A}$. Only $(G+1)G$ transition probabilities are estimated, since

$$\sum_{g=0}^{G} A_{jg} = 1, \forall 0 \leq j \leq G. \tag{5.15}$$

The incomplete data likelihood is derived from Equation (5.12) after marginalising over all combinations of possible hidden state sequences $\mathbf{H}$:

$$\begin{aligned} p(\mathbf{O}|\mathbf{\Omega}) &= \sum_{\mathbf{H}} p(\mathbf{O},\mathbf{H}|\mathbf{\Omega}) \\ &= \prod_{n=1}^{N}\left(\sum_{g_1^{(n)}=0}^{G}\cdots\sum_{g_T^{(n)}=0}^{G}\iota_{g_1^{(n)}}\prod_{t=2}^{T}A_{g_{t-1}^{(n)}g_t^{(n)}}\prod_{t'=1}^{T}\mathcal{N}\left(o_n^{(t')}|a\mathcal{M}_{g_{t'}^{(n)}},\sigma\right)\right), \end{aligned} \tag{5.16}$$

where $g_t^{(n)}$ expresses the effective number of atoms in a column n at a given time t. When $g_t^n = k$, this is equivalent to $h_{tk}^{(n)} = 1$, while all other elements of the state vector $\mathbf{h}_t^{(n)}$ are zero. This expression indeed reduces to the Gaussian mixture model from Equation (5.4) for $T = 1$. In this manner, it is clear that the factorial hidden Markov model for atom-counting from a time series can be considered as a generalisation of the hybrid statistics-simulations based method for atom-counting from the previous chapter.
Next, we will discuss how to estimate the parameters of the factorial hidden Markov model for atom-counting, which has been implemented in the freely available StatSTEM software package [De Backer 2016, De wael 2020a, De wael 2020b].

5.4 Parameter estimation

5.4.1 Baum-Welch algorithm

The parameters of the factorial hidden Markov model are estimated using an Expectation-Maximisation (EM) algorithm [Dempster 1977, McLachlan 1996]. For hidden Markov models, this algorithm was formulated by Baum et al. before the appearance of the EM algorithm, and it is therefore typically called the Baum-Welch algorithm in the context of hidden Markov models [Baum 1968]. The EM algorithm is an iterative updating algorithm, consisting of two steps: an E-step, and an M-step. During the E-step, the likelihood is evaluated, and this quantity is maximised during the M-step.
The complete data likelihood for the factorial hidden Markov model for atom-counting has the same functional form as the joint probability density function expressed in Equation (5.12), but is evaluated as a function of the model parameters $\mathbf{\Omega}$:

$$\begin{aligned} L(\mathbf{\Omega}) &= p(\hat{\mathbf{O}},\mathbf{H}|\mathbf{\Omega}) \\ &= \prod_{n=1}^{N}\prod_{g=0}^{G}\left(\iota_g\right)^{h_{1g}^{(n)}} \\ &\quad\times\prod_{t=2}^{T}\prod_{n=1}^{N}\prod_{j=0}^{G}\prod_{g=0}^{G}\left(A_{jg}\right)^{h_{t-1,j}^{(n)}h_{tg}^{(n)}} \end{aligned}$$

$$\times \prod_{t=1}^{T} \prod_{g=0}^{G} \prod_{n=1}^{N} \left(\mathcal{N}(\hat{o}_t^{(n)} | a\mathcal{M}_g, \sigma) \right)^{h_{tg}^{(n)}} . \tag{5.17}$$

In practice, the parameter estimates are obtained by maximising the following auxiliary function, which is in fact the expectation value of the logarithm of the complete data likelihood function [Baum 1968, Rabiner 1989, McLachlan 2000, Bishop 2006]:

$$\begin{aligned} Q(\mathbf{\Omega}, \mathbf{\Omega}^{\text{old}}) &= \mathbb{E}\left[\ln p(\hat{\mathbf{O}}, \mathbf{H} | \mathbf{\Omega}) \right] \\ &= \sum_{n=1}^{N} \sum_{g=0}^{G} \mathbb{E}\left[h_{1g}^{(n)} \right] \ln \iota_g \\ &\quad + \sum_{t=2}^{T} \sum_{n=1}^{N} \sum_{j=0}^{G} \sum_{g=0}^{G} \mathbb{E}\left[h_{t-1,j}^{(n)} h_{tg}^{(n)} \right] \ln A_{jg} \\ &\quad + \sum_{t=1}^{T} \sum_{n=1}^{N} \sum_{g=0}^{G} \mathbb{E}\left[h_{tg}^{(n)} \right] \ln \mathcal{N}\left(\hat{o}_t^{(n)} | a\mathcal{M}_g, \sigma \right). \end{aligned} \tag{5.18}$$

In order to evaluate the likelihood, or equivalently this auxiliary function, the expectation values $\mathbb{E}\left[h_{tg}^{(n)}\right]$ and $\mathbb{E}\left[h_{t-1,j}^{(n)} h_{tg}^{(n)}\right]$ need to be determined. This is done during the E-step of the EM algorithm, and is described in more detail in Appendix 5A. Note that when $T = 1$, the expectation value $\mathbb{E}\left[h_{tg}^{(n)}\right]$ is equivalent to Equation (4.15) used during the E-step of the Expectation-Maximisation algorithm for the hybrid method, discussed in Section 4.3. These expectation values can then be used during the M-step to determine the updates for each parameter in the parameter vector $\mathbf{\Omega}$. The update formulas are expressed by the following equations:

$$\iota_g^{(k+1)} = \frac{\sum_{n=1}^{N} \mathbb{E}\left[h_{1g}^{(n)}\right]^{(k)}}{\sum_{n=1}^{N} \sum_{j=0}^{G} \mathbb{E}\left[h_{1j}^{(n)}\right]^{(k)}}, \tag{5.19}$$

$$A_{jg}^{(k+1)} = \frac{\sum_{t=2}^{T} \sum_{n=1}^{N} \mathbb{E}\left[h_{tg}^{(n)} h_{t-1,j}^{(n)}\right]^{(k)}}{\sum_{t=2}^{T} \sum_{n=1}^{N} \sum_{g'=0}^{G} \mathbb{E}\left[h_{tg'}^{(n)} h_{t-1,j}^{(n)}\right]^{(k)}}, \tag{5.20}$$

$$a^{(k+1)} = \frac{\sum_{t=1}^{T} \sum_{n=1}^{N} \sum_{g=0}^{G} \mathbb{E}\left[h_{tg}^{(n)}\right]^{(k)} \hat{o}_t^{(n)} \mathcal{M}_g}{\sum_{t=1}^{T} \sum_{n=1}^{N} \sum_{g=0}^{G} \mathbb{E}\left[h_{tg}^{(n)}\right]^{(k)} \mathcal{M}_g^2}, \tag{5.21}$$

$$\sigma^{(k+1)} = \sqrt{\frac{\sum_{t=1}^{T} \sum_{n=1}^{N} \sum_{g=0}^{G} \mathbb{E}\left[h_{tg}^{(n)}\right]^{(k)} (\hat{o}_t^{(n)} - a^{(k)} \mathcal{M}_g)^2}{\sum_{t=1}^{T} \sum_{n=1}^{N} \sum_{g=0}^{G} \mathbb{E}\left[h_{tg}^{(n)}\right]^{(k)}}}. \tag{5.22}$$

Note that when $T = 1$, these update formulas for ι_g, a and σ are equivalent to the update formulas for the π_g, a and σ expressed by Equations (4.8), (4.9) and (4.10) used during the M-step of the Expectation-Maximisation algorithm for the hybrid method, discussed in Section 4.3.

The expected values $\mathbb{E}\left[h_{tg}^{(n)}\right]$ and $\mathbb{E}\left[h_{tg}^{(n)} h_{t-1,j}^{(n)}\right]$ of the hidden states are evaluated during each iteration k of the E-step of the EM algorithm. Note that when $T = 1$, the expectation value $\mathbb{E}\left[h_{tg}^{(n)}\right]$ is equivalent to Equation (4.15) used during the E-step of the Expectation-Maximisation algorithm for the hybrid method, discussed in Section 4.3. The iterative parameter updates are

initialised by starting values. For the initial probabilities and transition probabilities, uniform starting values are used:

$$\iota_g^{(0)} = \frac{1}{G+1}, \tag{5.23}$$

$$A_{jg}^{(0)} = \frac{1}{G+1}, \tag{5.24}$$

where $G+1$ is the number of different thicknesses considered during the analysis, as the counting is allowed to start from 0 atoms. In this manner, no prior knowledge on the thickness distribution of the nanostructure or the amount of structural changes that might occur during the time series is included in the parameter estimation procedure. The scaling parameter is initialised by $a = 1$, which implies that we expect no or only small deviations between the parameters used to perform the image simulations and the actual experimental settings. Estimating the scaling parameter will nonetheless allow for some small variations, enabling us to account for small mismatches between experiment and image simulation. The width is initialised by

$$\sigma^{(0)} = \frac{\max(\hat{\mathbf{O}}) - \min(\hat{\mathbf{O}})}{2(G+1)}. \tag{5.25}$$

The maximum number of atoms in an atomic column G that is considered during the analysis should be chosen larger than the maximum number of atoms one might expect from prior knowledge about the material such as sample preparation or additional information resulting from extra viewing directions.

5.4.2 Retrieving counting results: Viterbi algorithm

Once the parameters of the hidden Markov model are estimated, we can use them to determine the counting results. We could determine the individually most likely number of atoms in atomic column n at time t as

$$q_t^{(n)} = \underset{0 \leqslant g \leqslant G}{\arg\max} \left(\mathbb{E}\left[h_{tg}^{(n)} \right] \right), \text{ for } 1 \leqslant t \leqslant T. \tag{5.26}$$

In fact, this would correspond to the procedure for retrieving counting results using the hybrid method discussed in Chapter 4, if this would be used to collectively analyse the scattering cross sections of a time series. This so-called collective hybrid method for atom-counting, which will be used in Chapter 6 to compare the performance of the hidden Markov model with single frame approaches, then discards the time aspect, and analyses all scattering cross sections in a single vector, as if they would have originated from a single frame. Then, after finding the most likely number of atoms that corresponds to each scattering cross section, the counts can be reattributed to the different frames of the time series.

However, the transition probability from $t-1$ to the state at time t may be estimated equal or close to zero during the hidden Markov model parameter estimation, causing this state to be invalid or highly unlikely. Therefore, an algorithm is required to consider the entire time series, given the set of estimated transition probabilities: the Viterbi algorithm will determine the most likely hidden state sequence $\mathbf{H}$ [Viterbi 1967, Forney 1973]. A derivation of this path backtracking algorithm is provided in Appendix 5A.

5.4.3 Accuracy & precision

Now that we have introduced the algorithm to perform the parameter estimation of the hidden Markov model for atom-counting, we will evaluate the accuracy and precision of the estimated parameters using a simulation example. In Section 2.4, we introduced the concepts of accuracy and precision, and the Cramér-Rao lower bound (CRLB). The CRLB expresses the highest attainable precision for an accurate estimator. In order to perform a reliable quantitative analysis, the parameters of the probability distribution should be estimated accurately and precisely.
In order to assess accuracy and precision, we study a hypothetical hidden Markov model with $T = 6$ frames, $N = 20$ atomic columns in each frame and a maximum number of atoms in a column of $G = 2$, without taking columns with zero atoms into account. We use a relative width of the Gaussian emission probability of $\sigma/\delta = 0.1$. The initial probabilities are uniformly distributed, and from frame to frame the number of atoms changes according to a transition matrix with a Gaussian distribution around the diagonal. Input values for the transition probabilities, and all other parameters of the hidden Markov model, are listed in the second column of Table 5.1. In the emission probability, we use a Pt library that consists of simulated scattering cross sections, i.e. the library values $\mathcal{M}_g$, obtained from HAADF STEM image simulations using the MULTEM software [Lobato 2014, Lobato 2015, Lobato 2016] for Pt(110) at 300 keV, using a 21 mrad semi-convergence angle, 58-190 mrad detector collection range, and a pixel size of 9.1 pm. This library corresponds to the experimental images of a Pt wedge that will be discussed in Sections 6.3 and 6.2. In the second column of Table 5.2, we list the Cramér-Rao lower bound for each parameter. The derivation of the Cramér-Rao lower bound is given in more detail in Appendix 5B.

Parameter	Input value	Sample mean	95% confidence interval	
			Lower bound	Upper bound
ι_1	0.5000	0.4970	0.4758	0.5182
ι_2	0.5000	0.5030	0.4818	0.5242
A_{11}	0.7742	0.7752	0.7568	0.7937
A_{12}	0.2258	0.2248	0.2063	0.2432
A_{21}	0.2258	0.2385	0.2201	0.2570
A_{22}	0.7742	0.7615	0.7430	0.7799
a	1.0000	1.0006	0.9993	1.0018
σ	$1.110 \cdot 10^{-3}$	$1.114 \cdot 10^{-3}$	$1.100 \cdot 10^{-3}$	$1.127 \cdot 10^{-3}$

Table 5.1: ***Accuracy*** *of the parameter estimates of the hidden Markov model for atom-counting. The sample means are computed from parameter estimates obtained from 100 noise realisations of the hidden Markov model and compared with the input values of the model parameters.*

In order to study whether the parameter estimation as described before in Section 5.4 is performed accurately and precisely, we created 100 noise realisations of this hypothetical hidden Markov model. For each noise realisation, multinomially distributed random draws from the initial probabilities described above are used. For the transition probabilities, multinomially distributed random draws are performed from each row of the input transition matrix, and the scattering cross sections for each frame of the observed sequence for the time series are drawn randomly from the Gaussian emission probability. From these noise realisations, 95% confidence intervals on the mean and variance of the estimated parameters are calculated and summarised in Tables 5.1 and 5.2. From these results, we can conclude that parameter estimation is performed accurately and very precisely. For the initial probabilities ι_g, scaling parameter a and width σ, we even have most precise parameter estimation, as the CRLB for these parame-

Parameter	CRLB	Sample variance	95% confidence interval	
			Lower bound	Upper bound
ι_1	0.0139	0.0113	0.0088	0.0155
ι_2	0.0139	0.0113	0.0088	0.0155
A_{11}	0.0027	0.0085	0.0067	0.0117
A_{12}	0.0027	0.0085	0.0067	0.0117
A_{21}	0.0027	0.0086	0.0067	0.0117
A_{22}	0.0027	0.0086	0.0067	0.0117
a	$3.46 \cdot 10^{-3}$	$4.18 \cdot 10^{-3}$	$3.22 \cdot 10^{-3}$	$5.64 \cdot 10^{-3}$
σ	$3.94 \cdot 10^{-7}$	$4.72 \cdot 10^{-7}$	$3.64 \cdot 10^{-7}$	$6.37 \cdot 10^{-7}$

Table 5.2: ***Precision*** *of the parameter estimates of the Hidden Markov model for atom-counting. The sample variances are computed from parameter estimates obtained from 100 noise realisations of the hidden Markov model and compared with the Cramér-Rao lower bound for the model parameters.*

ters falls within the 95% confidence intervals on the variance. The 95% confidence interval on the sample variance of the transition probabilities however, does not include the Cramér-Rao lower bound. In Figure 5.2, the precision of the estimated transition probabilities is evaluated as a function of the length of the time series T. At larger lengths, the sample precision of the estimated transition probabilities approaches closer to the Cramér-Rao lower bound, indicating that the maximum likelihood estimates reach the Cramér-Rao lower bound.

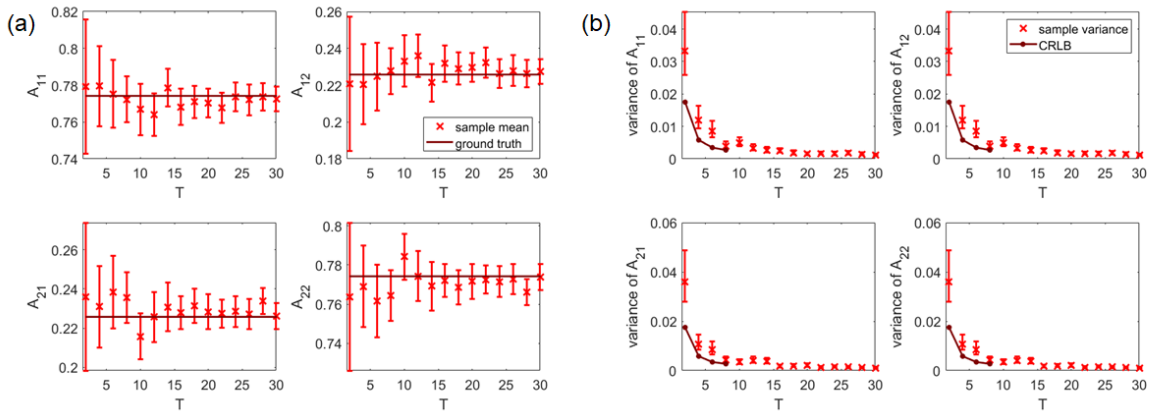

Figure 5.2: *Accuracy (a) and precision (b) of the estimated transition probabilities A_{jg} as a function of the length of the time series T. When the number of frames T increases, the sample precision (displayed with 95% confidence intervals) approaches the Cramér-Rao lower bound (CRLB).*

We conclude that we can reliably use this procedure to estimate the parameters of the hidden Markov model for atom-counting, and thus perform a reliable quantification of the number of atoms in a time series of ADF STEM images of a changing nanostructure.

5.5 Atom-counting performance

In order to illustrate the benefits of the hidden Markov model for atom-counting from a time series of ADF STEM images, introduced in Chapter 5, we compare its performance to the hybrid statistics-simulations based method for atom-counting from Chapter 4, which was shown to outperform the statistics- and simulations-based atom-counting procedures. For the hybrid

method, the scattering cross sections of all frames of the time series are jointly analysed, such that the counting results are based on the same set of observations as the hidden Markov model. The counting results are then extracted per frame from this so-called collective analysis, analogous to the collective analysis performed previously in [De Backer 2015b] and [Varambhia 2016]. In the remainder of this thesis, we will call this approach the collective hybrid method for atom-counting. First, we will study the performance as a function of electron dose for a fixed length of time series. Later in this section, we will also study the effect of the length of the time series on the atom-counting performance of the hidden Markov model.

5.5.1 Dose-dependent performance

We will study the performance using hypothetical time series generated from known counting results. We start by comparing the atom-counting performance of the hidden Markov model to that of the collective hybrid method at different electron doses. To this purpose we create different hidden state sequences, based on the atomic structure of a changing Pt nanoparticle with 215 atomic columns, and a thickness up to 15 atoms, similar to the experimental example discussed in Section 6.4. We allow the number of atoms in each atomic column to change by ± 1 from frame to frame throughout the time series, with a probability of 10%. An example of the 3D atomic structure of the Pt nanoparticle and how it changes over time is shown in Figure 5.3a. Note that, in this manner, we do not impose that the hidden state sequence is a Markov chain. As such, we can assess the accuracy of modelling the changes in the number of atoms during the time series as a Markov chain determined by discrete initial and transition probabilities. From the hidden state sequence, a set of scattering cross sections is generated, corresponding to the number of atoms in each atomic column. A Pt library was simulated that matches the experimental conditions of the Pt nanoparticle that will be discussed in Section 6.4. The scattering cross sections of each atomic column are generated from this Pt library, using Poisson random draws in order to replicate the uncertainty from the finite electron dose. Additionally, scan-distortion is included in the simulation of the scattering cross sections. Based on a previous study, the effect of scan-distortion has been modelled as a normal distribution, with an experimentally determined variance of $4.5 \cdot 10^{-4} \mu_g$, with μ_g the average scattering cross section of an atomic column with g atoms [Van Aert 2019].
For each electron dose, 200 different noise realisations of such time series were constructed. In Figure 5.3b, 95% confidence intervals on the average percentage of correctly counted atomic columns by the hidden Markov model and the collective hybrid method are evaluated as a function of the electron dose. The hidden Markov model counts the number of atoms in each column more accurately, both at low electron doses, where Poisson noise dominates, and at high electron dose, where the scan-distortion is the dominant noise contribution [Van Aert 2019].
The sequence of the number of atoms in each column in the hypothetical time series were generated without imposing a discrete transition matrix. Nonetheless, it is possible to extract a transition matrix that describes the changes in the state sequence, by considering the underlying sequence of numbers of atoms as a Markov chain. This ground truth transition matrix is shown in Figure 5.3c and 5.3d, for a noise realisation at low and high electron dose respectively. In Figure 5.3e-5.3h, we show the estimated transition matrices using both methods for the respective low and high dose noise realisations.

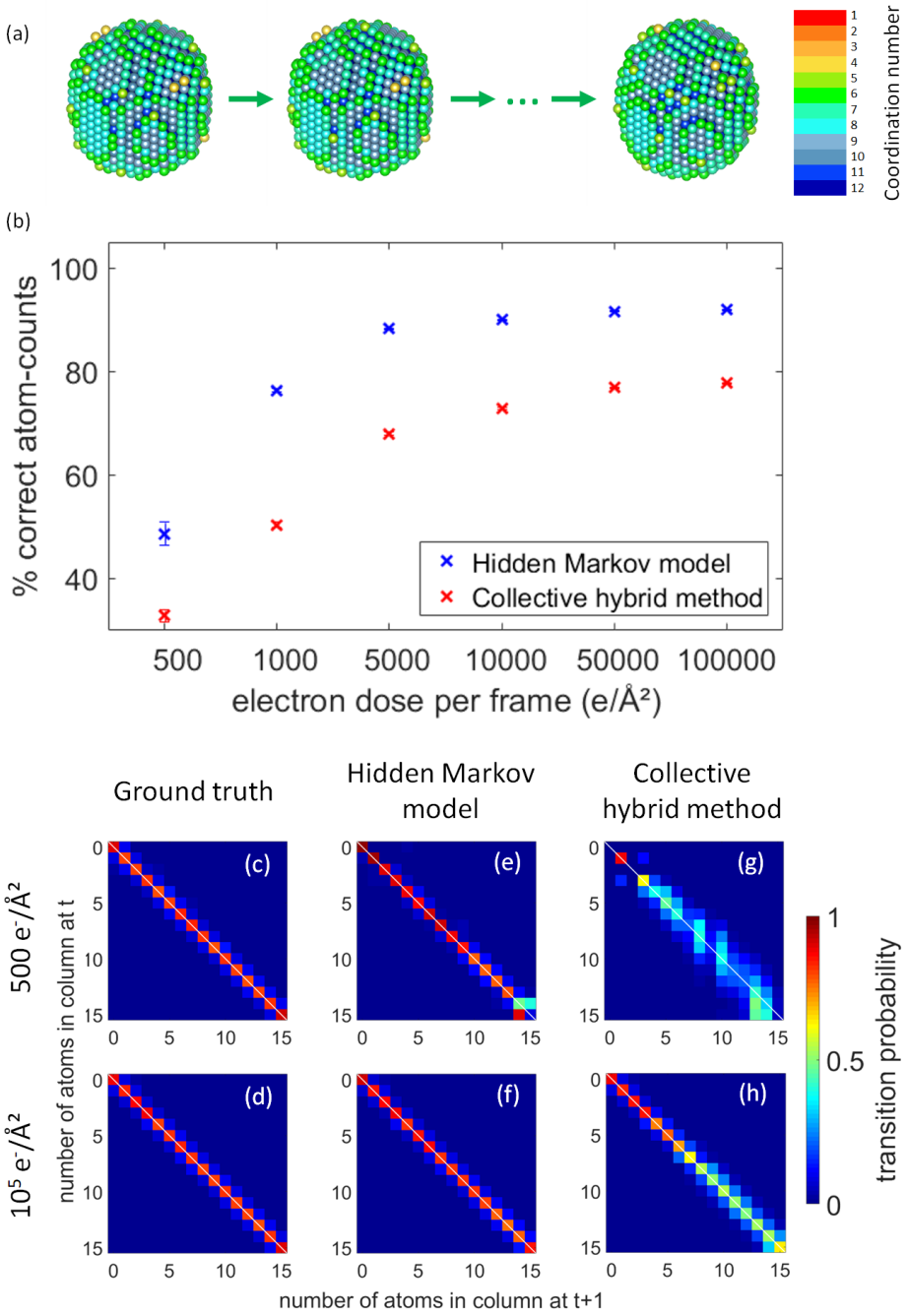

Figure 5.3: *(a) Example of the 3D atomic structure of the changing Pt nanoparticle discussed in Section 5.5.1. (b) Percentage of correctly counted atomic columns, with a 95% confidence interval as a function of the electron dose in each individual frame. (c-h) Ground truth and estimated transition matrices using the hidden Markov model analysis and the collective hybrid method with electron dose* $5 \cdot 10^2$ $e^-/\text{Å}^2$ *and* 10^5 $e^-/\text{Å}^2$.

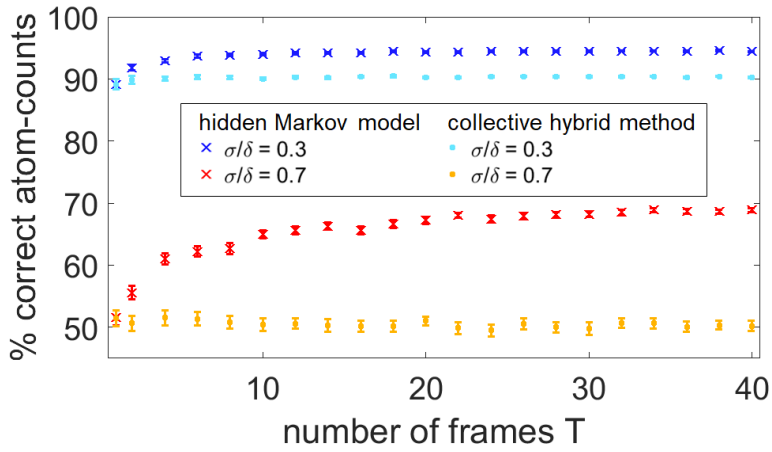

Figure 5.4: *Comparison of the performance for atom-counting from a time series of the hidden Markov model and the collective hybrid method for atom-counting, at different noise levels σ/δ, evaluated as a function of the length of the time series T.*

The transition matrix for the collective hybrid method was estimated by considering the obtained atom-counting results as a Markov chain. The transition matrix summarises the estimated structural changes of the nanoparticle: diagonal elements correspond to the probabilities that the number of atoms in an atomic column with a given thickness does not change from one frame to the next and off-diagonal elements in the lower and upper triangle correspond to the probabilities for an atomic column to lose or gain atoms respectively. From the comparison of Figure 5.3g and 5.3h with the respective ground truth in Figure 5.3c and 5.3d, it is clear that the collective hybrid method overinterprets intensity variations during the time series as actual thickness changes, both at low and high electron doses. From Figure 5.3e and 5.3f on the other hand, it is clear that the hidden Markov model far more accurately retrieves the transition probabilities, in agreement with the findings in Section 5.4.3. The interpretation of the transition probabilities in terms of dynamic structural changes of nanoparticles at the atomic scale will be discussed in more detail in Section 6.2.

5.5.2 Time-dependent performance

Next, we study the effect of the length of the time series on the performance for atom-counting. The results summarised in Figure 5.3 confirm that the hidden Markov model can be applied to a time series of a nanomaterial with random changes in the number of atoms in an atomic column from frame to frame. Therefore, for the next step in our study of the atom-counting performance, we can generate the hidden state sequences using known transition probabilities and initial probabilities. A set of hypothetical time series of scattering cross sections with different lengths was generated by creating hidden state sequences corresponding to $N = 100$ atomic columns with up to $G = 10$ atoms in an atomic column. Uniform initial probabilities ι_g were used, which represents a uniform distribution of thicknesses ranging between 1 and the maximum thickness G in the first frame. No missing atomic columns were included in the state sequences. The number of atoms in each state sequence is then changed according to a transition matrix $\mathbf{A}$ with a Gaussian spread around the diagonal with full width at half maximum (FWHM) equal to 1.5, shown in Figure B.1 of Appendix B. This implies that some structural changes will occur during the time series, but the probability that large jumps in the number of atoms, i.e. ± 2 or more, are generated from frame to frame is small. A unitary transition matrix

would imply no structural changes. The observed sequences of scattering cross sections are created using a Gaussian emission probability $\mathcal{N}(o_t^{(n)}|a\mathcal{M}_g, \sigma)$, with average scattering cross section equal to the scattering cross sections $\mathcal{M}_g$ obtained from HAADF STEM image simulations of Pt(110) using the MULTEM software [Lobato 2014, Lobato 2015, Lobato 2016] at 300 keV, using a 21 mrad semi-convergence angle, 58-190 mrad detector collection range, and a pixel size of 9.1 pm. This library corresponds to the experimental images of the Pt wedge discussed in Sections 6.3 and 6.2, and which have previously been analysed in [Van Aert 2019] as well. The relative width of the Gaussian emission probability considered in the simulation to study the performance is $\sigma/\delta = 0.3$ and 0.7. This width accounts for fluctuations of the scattering cross sections around the average value, caused by various effects such as scan noise, counting statistics or neighbouring atomic columns. Note that this simulation set-up implicitly assumes that all structural changes are described by the transition matrix, regardless of the process that causes the changes.

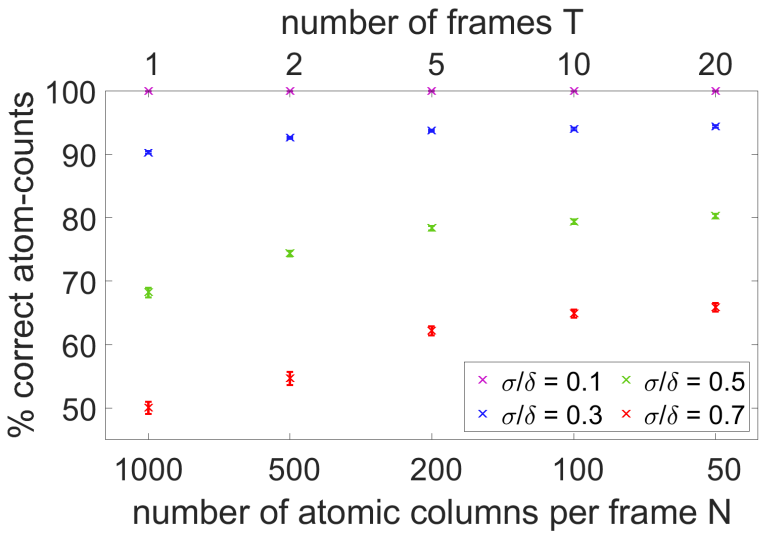

Figure 5.5: *Performance for atom-counting from a time series of the hidden Markov model at different noise levels σ/δ, evaluated as a function of the length of the time series T and the number of atomic columns in each frame N, while the product $N \times T$ was kept constant.*

The parameters used to generate the hypothetical hidden Markov models are summarised in Table B.1 of Appendix B. At each length of the time series T and noise level, i.e. relative width of the Gaussian emission probability σ/δ, 100 noise realisations of the hypothetical time series with the above mentioned settings were analysed. In Figure 5.4, we evaluate the average percentage of correctly counted atomic columns from the hypothetical time series, with a 95% confidence interval, obtained by the hidden Markov model and the collective hybrid method. From these results, it is clear that the hidden Markov model counts the number of atoms more reliably than the collective hybrid method, especially for longer time series. Note that in the case of $T = 1$, both methods indeed yield exactly the same result, as mentioned before in Section 5.3. Adding even only a few extra frames allows the hidden Markov model to quickly exceed the performance of the collective hybrid method. One could argue that this improvement of the counting performance with an increasing time series length T is simply the result of the better statistics obtained by analysing the increasing set of $N \times T$ scattering cross sections. This is however not the main reason for the improved performance. We demonstrate this by analysing hypothetical hidden Markov models with the same parameters used for the

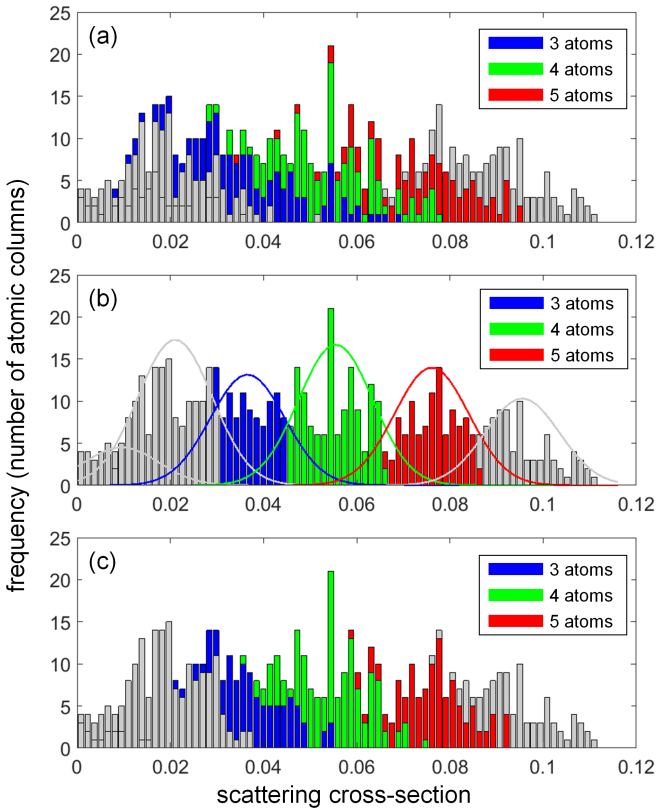

Figure 5.6: *Histogram showing all scattering cross sections of a hypothetical time series, colour coded according to the number of atoms in an atomic column: blue for 3 atoms, green for 4 atoms, red for 5 atoms and grey for any different number of atoms. (a) Ground truth. (b) Atoms counted using the collective hybrid method, with the estimated Gaussian mixture model. (c) Atoms counted using the hidden Markov model.*

analysis shown in Figure 5.4, as summarised in Table B.1 of Appendix B, but with a constant total number of scattering cross sections $T \times N = 1000$ considered during the analysis. Figure 5.5 shows the average percentage of correctly counted atomic columns with 95% confidence intervals for the analysis of these hypothetical hidden Markov models as a function of the number of frames in the time series T and the number of atomic columns in each frame N. For the collective hybrid method, increasing the number of atomic columns N or the number of frames T would both result in a larger set of scattering cross sections that are jointly analysed. For the hidden Markov model on the other hand, there is a difference, and increasing the number of frames improves the atom-counting performance, as shown in Figure 5.5. In other words, it is beneficial to increase the length of the time series, rather than increasing the number of atomic columns in each frame of the time series.

5.5.3 Understanding the origin of the improved performance

The improved performance of the hidden Markov model over the collective hybrid method for the same noise level (i.e. the same relative width of the Gaussian emission probability σ/δ) can therefore be attributed to the inclusion of transition probabilities to explicitly model structural changes over time. By increasing the number of frames T, the amount of frame transitions increases. Moreover, the precision with which the transition probabilities that model the changes

in the number of atoms in an atomic column through time can be estimated also increases, as demonstrated in Section 5.4.3. Instead of estimating one set of mixing proportions π_g for the entire time series, as is the case for the collective hybrid method, initial probabilities ι_g and transition probabilities A_{jg} are estimated by the hidden Markov model analysis, to allow for changes in the distribution of different thicknesses in the nanostructure from frame to frame. In this manner, we previously defined the frame dependent mixing proportions $\pi_g^{(t)}$ in Equations 5.10 and 5.11. Modelling the transition probabilities allows us to use the Viterbi path backtracking algorithm, discussed in Section 5.4.2, to determine the number of atoms in each atomic column in each frame of the time series by considering the most likely sequence, rather than the most likely number of atoms to fit the scattering cross section values in each frame separately. In this manner, we exceed the limitations imposed by the overlapping Gaussian distributions. To demonstrate this, a hypothetical time series with up to $G = 6$ atoms thickness was created using parameters summarised in the last column of Table B.1 of Appendix B. Figure 5.6a shows the set of scattering cross sections of the entire time series. The scattering cross sections corresponding to atomic columns with 3, 4 and 5 atoms are colour-coded in blue, green and red respectively. The scattering cross sections that correspond to atomic columns with 1, 2 or 6 atoms are all in grey. Figures 5.6b and 5.6c show the same colour-codings for the atomic columns that are counted as 3, 4 and 5 atoms respectively, using the collective hybrid method for atom-counting and the hidden Markov model for atom-counting. In the collective hybrid method, atomic columns in the tails of the Gaussian components are miscounted when components overlap [Figure 5.6b]. This limitation is no longer present for the hidden Markov model [Figure 5.6c], thanks to the Viterbi path backtracking algorithm which exploits the information on the structural changes captured by the transition probabilities. This means that the hidden Markov model for atom-counting from a time series of ADF STEM images yields more accurate counting results, as compared to the existing atom-counting approach.

5.6 Conclusions

In this chapter, we have introduced the theoretical framework for the hidden Markov model for atom-counting from a time series of ADF STEM images. The framework is constructed as an extension of the single frame counting procedure using the hybrid method for atom-counting introduced in Chapter 4. For a single frame, both approaches are indeed identical. We have derived the probability distribution of the scattering cross sections estimated from each ADF STEM image in the time series, and have discussed the parameter estimation. The parameter estimation algorithm has been implemented in the freely available StatSTEM software package [De Backer 2016]. We show that the parameters are estimated accurately and precisely. The ultimate lower bound on the precision of the parameters, expressed by the Cramér-Rao lower bound, is asymptotically attained. The sample variance of the transition probabilities approaches closer to the lower bound as the length of the time series increases. Therefore, the accurate and precise parameter estimates of the hidden Markov model can yield a reliable quantification of the number of atoms in a time series. Furthermore, we have discussed the possibilities and limitations of the hidden Markov model for atom-counting from time series of ADF STEM images. We demonstrated a significant improvement in the atom-counting performance, both at low and at high electron dose, corresponding to a high and low noise level, quantified by the relative width of the Gaussian distributions σ/δ. Furthermore, we show that the percentage of correctly counted atomic columns increases when more frames are added to the time series analysis. By considering time series with a constant total number of atomic columns, redistributed over one or more frames, we confirm that the length of the time series

indeed causes this improvement. When selecting the imaging parameters for acquiring an ADF STEM time series, increasing the number of frames is therefore preferred over increasing the number of atomic columns in each frame of the time series by for example imaging a larger field of view. The improved performance of the hidden Markov model over the collective hybrid method for the same noise level is attributed to the inclusion of transition probabilities to explicitly model structural changes over time. These transition probabilities are used during the Viterbi algorithm which allows us to surpass the limitations posed by the overlap between distributions of the scattering cross sections of atomic columns with different thicknesses. In the next chapter, we discuss the physical interpretation of the transition probabilities and further demonstrate the time series atom-counting procedure using relevant experimental applications.

Appendix 5A: Parameter estimation

Baum-Welch algorithm

The parameters of the factorial hidden Markov model are estimated using the iterative Expectation-Maximisation (EM) or Baum-Welch algorithm [Baum 1968,Dempster 1977,McLachlan 1996]. The algorithm consists of two steps: an E-step, and an M-step. During the E-step, the likelihood is evaluated, and this quantity is maximised during the M-step. In practice, the parameter estimates are obtained by maximising the following auxiliary function, which is in fact the expectation value of the logarithm of the complete data likelihood function of Equation (5.17) [Baum 1968, Rabiner 1989, McLachlan 2000, Bishop 2006]:

$$\begin{aligned} Q(\mathbf{\Omega}, \mathbf{\Omega}^{\text{old}}) &= \sum_{\mathbf{H}} p(\mathbf{H}|\hat{\mathbf{O}}, \mathbf{\Omega}^{\text{old}}) \ln p(\hat{\mathbf{O}}, \mathbf{H}|\mathbf{\Omega}) \\ &= \mathbb{E}\left[\ln p(\hat{\mathbf{O}}, \mathbf{H}|\mathbf{\Omega})\right] \\ &= \sum_{n=1}^{N}\sum_{g=0}^{G} \mathbb{E}\left[h_{1g}^{(n)}\right] \ln \iota_g \\ &\quad + \sum_{t=2}^{T}\sum_{n=1}^{N}\sum_{j=0}^{G}\sum_{g=0}^{G} \mathbb{E}\left[h_{t-1,j}^{(n)} h_{tg}^{(n)}\right] \ln A_{jg} \\ &\quad + \sum_{t=1}^{T}\sum_{n=1}^{N}\sum_{g=0}^{G} \mathbb{E}\left[h_{tg}^{(n)}\right] \ln \mathcal{N}\left(\hat{o}_t^{(n)}|a\mathcal{M}_g, \sigma\right). \end{aligned} \tag{5.27}$$

In order to evaluate the likelihood, or equivalently this auxiliary function, the expectation values $\mathbb{E}\left[h_{tg}^{(n)}\right]$ and $\mathbb{E}\left[h_{t-1,j}^{(n)} h_{tg}^{(n)}\right]$ need to be determined. This is done during the E-step of the EM algorithm. Note that when $T = 1$, the expectation value $\mathbb{E}\left[h_{tg}^{(n)}\right]$ is equivalent to Equation (4.15) used during the E-step of the Expectation-Maximisation algorithm for the hybrid method, discussed in Section 4.3. These expectation values can then be used during the M-step to determine the updates for each parameter in the parameter vector $\mathbf{\Omega}$.

E-step

In this step, the likelihood is evaluated, and the expectation values that occur in the update formulas in the M-step are determined. First, we introduce the following notation:

$$\gamma(h_{tg}^{(n)}) = \mathbb{E}\left[h_{tg}^{(n)}\right], \tag{5.28}$$

$$\xi(h_{t-1,j}^{(n)}, h_{tg}^{(n)}) = \mathbb{E}\left[h_{t-1,j}^{(n)} h_{tg}^{(n)}\right]. \tag{5.29}$$

The derivation is similar to the E-step of the general Baum-Welch algorithm, but factorised over the atomic columns n. The expectation value of a binary variable, equals the probability for this binary variable to be equal to 1. Therefore, the expectation values can be written as the following probabilities:

$$\begin{aligned} \gamma(h_{tg}^{(n)}) &= \mathbb{E}\left[h_{tg}^{(n)}\right] \\ &= p\left(h_{tg}^{(n)} = 1|\hat{\mathbf{O}}, \mathbf{\Omega}\right), \end{aligned} \tag{5.30}$$

the posterior probability that atomic column n contains g atoms at time t, often called the state occupation probability, and

$$\begin{aligned}\xi(h_{t-1,j}^{(n)}h_{tg}^{(n)}) &= \mathbb{E}\left[h_{t-1,j}^{(n)}h_{tg}^{(n)}\right] \\ &= p\left(h_{t-1,j}^{(n)}=1, h_{tg}^{(n)}=1|\hat{\mathbf{O}},\mathbf{\Omega}\right),\end{aligned} \tag{5.31}$$

the joint posterior probability that atomic column n contains j atoms at time $t-1$ and g atoms at time t.

Equations (5.30) and (5.31) are determined using a so-called forward-backward algorithm [Bishop 2006]. Therefore, the probabilities are rewritten using Bayes' theorem and conditional independence properties of hidden Markov models. In order to simplify the notation, we omit the explicit dependence on $\mathbf{\Omega}$ in the following:

$$\begin{aligned}\gamma(h_{tg}^{(n)}) &= p\left(h_{tg}^{(n)}=1|\hat{\mathbf{O}}\right) \\ &= \frac{p\left(\hat{\mathbf{O}}|h_{tg}^{(n)}=1\right)p\left(h_{tg}^{(n)}=1\right)}{p\left(\hat{\mathbf{O}}\right)} \\ &= \frac{p\left(\hat{o}_1^{(n)},\cdots,\hat{o}_t^{(n)},h_{tg}^{(n)}=1\right)p\left(\hat{o}_{t+1}^{(n)},\cdots,\hat{o}_T^{(n)}|h_{tg}^{(n)}=1\right)}{p\left(\hat{\mathbf{O}}\right)},\end{aligned} \tag{5.32}$$

and

$$\begin{aligned}\xi(h_{t-1,j}^{(n)}h_{tg}^{(n)}) &= p\left(h_{t-1,j}^{(n)}=1, h_{tg}^{(n)}=1|\hat{\mathbf{O}}\right) \\ &= \frac{p\left(\mathbf{O}|h_{t-1,j}^{(n)}=1, h_{tg}^{(n)}=1\right)p\left(h_{t-1,j}^{(n)}=1, h_{tg}^{(n)}=1\right)}{p\left(\hat{\mathbf{O}}\right)} \\ &= \frac{1}{p\left(\hat{\mathbf{O}}\right)}\Bigg[p\left(\hat{o}_1^{(n)},\cdots,\hat{o}_{t-1}^{(n)},h_{t-1,j}^{(n)}=1\right)p\left(h_{t-1,j}^{(n)}=1|h_{tg}^{(n)}=1\right) \\ &\quad \times p\left(\hat{o}_t^{(n)}|h_{tg}^{(n)}=1\right)p\left(\hat{o}_{t+1}^{(n)},\cdots,\hat{o}_T^{(n)}|h_{tg}^{(n)}=1\right)\Bigg].\end{aligned} \tag{5.33}$$

Forward-Backward algorithm

We can now define the forward variables $\alpha(h_{tg}^{(n)})$ and the backward variables $\beta(h_{tg}^{(n)})$ that are used during the forward-backward algorithm to determine Equations (5.32) and (5.33):

$$\alpha(h_{tg}^{(n)}) = p\left(\hat{o}_1^{(n)},\cdots,\hat{o}_t^{(n)},h_{tg}^{(n)}=1\right) \tag{5.34}$$

$$\beta(h_{tg}^{(n)}) = p\left(\hat{o}_{t+1}^{(n)},\cdots,\hat{o}_T^{(n)}|h_{tg}^{(n)}=1\right) \tag{5.35}$$

In practice, additional scaling factors c_t^n are used, analogous to the description given in [Bishop 2006], but with an additional factorisation over the atomic columns n:

$$\begin{aligned}\hat{\alpha}(h_{tg}^{(n)}) &= p\left(h_{tg}^{(n)}=1|\hat{o}_1^{(n)},\cdots,\hat{o}_t^{(n)}\right) \\ &= \frac{p\left(\hat{o}_1^{(n)},\cdots,\hat{o}_t^{(n)},h_{tg}^{(n)}=1\right)}{p\left(\hat{o}_1^{(n)},\cdots,\hat{o}_t^{(n)}\right)}\end{aligned}$$

$$= \frac{\alpha(h_{tg}^{(n)})}{\prod_{q=1}^{t} c_t^n}, \tag{5.36}$$

with

$$c_t^{(n)} = p(\hat{o}_t^{(n)}|\hat{o}_1^{(n)}, ..., \hat{o}_{t-1}^{(n)}). \tag{5.37}$$

In this way, we can rewrite Equations (5.32) and (5.33) as follows:

$$\gamma(h_{tg}^{(n)}) = \hat{\alpha}(h_{tg}^{(n)})\hat{\beta}(h_{tg}^{(n)}), \tag{5.38}$$

$$\xi(h_{t-1,j}^{(n)} h_{tg}^{(n)}) = \hat{\alpha}(h_{t-1,j}^{(n)}) A_{jg} \mathcal{N}(\hat{o}_t^{(n)}|a\mathcal{M}_g, \sigma)\hat{\beta}(h_{tg}^{(n)}), \tag{5.39}$$

with the forward and backward variables determined recursively. For computational reasons, an additional normalisation of $\xi(h_{t-1,j}^{(n)} h_{tg}^{(n)})$ is performed. Initialisation of the scaled forward variable is done by

$$\hat{\alpha}(h_{1g}^{(n)}) = \frac{\iota_g \mathcal{N}(\hat{o}_1^{(n)}|a\mathcal{M}_g, \sigma)}{c_1^{(n)}}. \tag{5.40}$$

Then we forwards propagate through time (hence the name), in order to recursively obtain the next forward variables:

$$\hat{\alpha}(h_{tg}^{(n)}) = \frac{1}{c_t^{(n)}} \mathcal{N}(\hat{o}_t^{(n)}|a\mathcal{M}_g, \sigma) \sum_{j=1}^{G} \hat{\alpha}(h_{t-1,j}^{(n)}) A_{jg}.$$

Initialisation of the scaled backward variable is done by

$$\hat{\beta}(h_{Tg}^{(n)}) = 1. \tag{5.41}$$

Then we backwards propagate through time (hence the name), in order to recursively obtain the other backward variables:

$$\hat{\beta}(h_{tg}^{(n)}) = \frac{1}{c_{t+1}^{(n)}} \sum_{j=1}^{G} \mathcal{N}(\hat{o}_{t+1}^{(n)}|a\mathcal{M}_j, \sigma)\hat{\beta}(h_{t+1,j}^{(n)}) A_{gj}. \tag{5.42}$$

The likelihood is obtained as the product of the scaling parameters $c_t^{(n)}$ that are used to avoid numerical issues with the forward-backward algorithm:

$$p(\hat{\mathbf{O}}) = \prod_{n=1}^{N} \prod_{q=1}^{T} c_q^{(n)}. \tag{5.43}$$

M-step

The update formulas for the model parameters are calculated in the M-step using the expected values $\gamma(h_{tg}^{(n)}) = \mathbb{E}\left[h_{tg}^{(n)}\right]$ and $\xi(h_{t-1,j}^{(n)}, h_{tg}^{(n)}) = \mathbb{E}\left[h_{t-1,j}^{(n)} h_{tg}^{(n)}\right]$ calculated during the E-step. These expressions are obtained by maximising the expectation value of the log likelihood from Equation (5.27), while taking into account that ι_G and A_{jG} $\forall 0 \leq j \leq G$ need not be estimated, since $\sum_{g=0}^{G} \iota_g = 1$ and $\sum_{g=0}^{G} A_{jg} = 1$. This results in the following expressions:

$$\iota_g = \frac{\sum_{n=1}^{N} \mathbb{E}\left[h_{1g}^{(n)}\right]}{\sum_{n=1}^{N} \sum_{j=0}^{G} \mathbb{E}\left[h_{1j}^{(n)}\right]}, \tag{5.44}$$

$$A_{jg} = \frac{\sum_{t=2}^{T}\sum_{n=1}^{N}\mathbb{E}\left[h_{tg}^{(n)}h_{t-1,j}^{(n)}\right]}{\sum_{t=2}^{T}\sum_{n=1}^{N}\sum_{g'=0}^{G}\mathbb{E}\left[h_{tg'}^{(n)}h_{t-1,j}^{(n)}\right]}, \tag{5.45}$$

$$a = \frac{\sum_{t=1}^{T}\sum_{n=1}^{N}\sum_{g=0}^{G}\mathbb{E}\left[h_{tg}^{(n)}\right]\hat{o}_t^{(n)}\mathcal{M}_g}{\sum_{t=1}^{T}\sum_{n=1}^{N}\sum_{g=0}^{G}\mathbb{E}\left[h_{tg}^{(n)}\right]\mathcal{M}_g^2}, \tag{5.46}$$

$$\sigma = \sqrt{\frac{\sum_{t=1}^{T}\sum_{n=1}^{N}\sum_{g=0}^{G}\mathbb{E}\left[h_{tg}^{(n)}\right](\hat{o}_t^{(n)}-a\mathcal{M}_g)^2}{\sum_{t=1}^{T}\sum_{n=1}^{N}\sum_{g=0}^{G}\mathbb{E}\left[h_{tg}^{(n)}\right]}}. \tag{5.47}$$

Viterbi algorithm

Once the parameters of the hidden Markov model are estimated, we can use them to determine the counting results. The transition probability from $t-1$ to the state at time t may be estimated equal or close to zero during the hidden Markov model parameter estimation, causing this state to be invalid or highly unlikely at time t. Therefore, an algorithm is required to consider the entire time series, given the set of estimated transition probabilities. The goal of the Viterbi path backtracking algorithm for hidden Markov models is to determine the most likely hidden state sequence $\mathbf{H}$ [Viterbi 1967, Forney 1973].
In order to retrieve the state sequence, the so-called best score $\delta^{(n)}(t,g)$ is introduced. This records the highest probability out of all possible state sequences that could account for the first t observations and that end in state g at time t:

$$\delta^{(n)}(t,g) = \max_{\mathbf{h}_1^{(n)}\cdots\mathbf{h}_{t-1}^{(n)}} P(\mathbf{h}_1^{(n)},\cdots,\mathbf{h}_{t-1}^{(n)},h_{tg}^{(n)}=1,\hat{o}_1^{(n)}\cdots\hat{o}_t^{(n)}|\mathbf{\Omega}). \tag{5.48}$$

The best score at the next time $t+1$ can be retrieved using a recursion relation:

$$\delta^{(n)}(t+1,j) = \max_g\left[\delta^{(n)}(t,g)\cdot A_{gj}\right]\mathcal{N}(\hat{o}_{t+1}^{(n)}|a\mathcal{M}_j,\sigma). \tag{5.49}$$

In order to keep the numerical range of the best score computationally feasible, in practice this expression is normalised for each time t and each atomic column n. In order to retrieve the most likely state sequence, we need to keep track of the argument that maximises this expression. Note that this is not affected by the additional normalisation. Therefore, an argument array $\phi^{(n)}(t,g)$ is introduced.
We can now summarise the Viterbi algorithm as follows. First, we initialise the best score and the argument array:

$$\delta^{(n)}(1,g) = \iota_g\mathcal{N}(\hat{o}_1^{(n)}|a\mathcal{M}_g,\sigma), \tag{5.50}$$

$$\phi^{(n)}(1,g) = 0. \tag{5.51}$$

Then the recursion formula is applied for each next time t:

$$\delta^{(n)}(t,g) = \max_{0\leqslant j\leqslant G}\left[\delta^{(n)}(t-1,j)A_{jg}\right]\mathcal{N}(\hat{o}_t^{(n)}|a\mathcal{M}_g,\sigma), \tag{5.52}$$

$$\phi^{(n)}(t,g) = \arg\max_{0\leqslant j\leqslant G}\left[\delta^{(n)}(t-1,j)A_{jg}\right]. \tag{5.53}$$

Next, we perform a termination step at time T:

$$\hat{P} = \max_{0\leqslant g\leqslant G}\left[\delta^{(n)}(T,g)\right], \tag{5.54}$$

$$\hat{\mathbf{h}}_T^{(n)} = \underset{0 \leqslant g \leqslant G}{\arg\max} \left[\delta^{(n)}(T, g) \right]. \tag{5.55}$$

Finally, path backtracking is performed in order to determine the most likely hidden state sequence:

$$\hat{\mathbf{h}}_t^{(n)} = \phi^{(n)}(t+1, \hat{h}_{t+1}^{(n)}) \tag{5.56}$$

Appendix 5B: Cramér-Rao lower bound

We introduced the Cramér-Rao lower bound in Section 2.4 for a general estimator, and will now apply this to the hidden Markov model for atom-counting. For unbiased estimators, the Cramér-Rao lower bound defines the lower bound on the variance [Rao 1945, Cramér 1946]:

$$\text{cov}(\hat{\mathbf{\Omega}}, \hat{\mathbf{\Omega}}) \geq F_{\mathbf{\Omega}}^{-1}, \tag{5.57}$$

with $\hat{\mathbf{\Omega}}$ the vector containing the estimators of the parameters summarised in the parameter vector $\mathbf{\Omega}$, and $F_{\mathbf{\Omega}}$ the Fisher information matrix, which is defined as follows for the hidden Markov model for atom-counting:

$$F_{\mathbf{\Omega}} = -\mathbb{E}\left[\left.\frac{\partial^2 \ln p(\mathbf{O}|\mathbf{\Omega})}{\partial \mathbf{\Omega} \partial \mathbf{\Omega}^T}\right|_{\mathbf{\Omega}=\mathbf{\Omega}_0}\right], \tag{5.58}$$

where $\mathbb{E}$ expresses the expectation value. In this expression, $p(\mathbf{O}|\mathbf{\Omega})$ represents the joint probability density function, given by Equation (5.16), which describes the probability distribution of the observed sequence of scattering cross sections $\mathbf{O}$, determined by the unknown parameters expressed by the parameter vector $\mathbf{\Omega}$, defined by Equation (5.13). The vector $\mathbf{\Omega}_0$ contains the actual values of the parameters to be estimated. Note that the joint probability density function is expressed by the incomplete data likelihood of the hidden Markov model, as this is in fact the problem solved by the parameter estimation using the Baum-Welch algorithm, described in Section 5.4.1. The highest attainable precision of the unknown parameters in the parameter vector $\mathbf{\Omega}$ is not determined by the hidden state sequence $\mathbf{H}$. The incomplete data likelihood is obtained by summing Equation (5.12) over all possible hidden state sequences $\mathbf{H}$. Equation (5.16) can be written as follows:

$$\begin{aligned} p(\mathbf{O}|\mathbf{\Omega}) &= \prod_{n=1}^{N}\left(\sum_{g_1^{(n)}=0}^{G}\cdots\sum_{g_T^{(n)}=0}^{G}\iota_{g_1^{(n)}}\prod_{t=2}^{T}A_{g_{t-1}^{(n)}g_t^{(n)}}\prod_{t'=1}^{T}\mathcal{N}\left(o_n^{(t)}|a\mathcal{M}_{g_t^{(n)}},\sigma\right)\right) \\ &= \prod_{n=1}^{N}p\left(\mathbf{O}^{(n)}|\mathbf{\Omega}\right), \end{aligned} \tag{5.59}$$

where we have introduced the abbreviated notation $p\left(\mathbf{O}^{(n)}|\mathbf{\Omega}\right)$ which represents the incomplete data likelihood for the observed sequence of atomic column n. In this expression, $g_t^{(n)}$ expresses the effective number of atoms in a column n at a given time t. When $g_t^n = k$, this is equivalent to $h_{tk}^{(n)} = 1$, while all other elements of the state vector $\mathbf{h}_t^{(n)}$ are zero. In practice, the following multiple integral is numerically integrated, using Monte Carlo integration [Kroese 2011]:

$$F_{\mathbf{\Omega}} = -N\int_{-\infty}^{+\infty}\left.\frac{\partial^2 \ln p\left(\mathbf{O}^{(n)}|\mathbf{\Omega}\right)}{\partial \mathbf{\Omega}\partial\mathbf{\Omega}^T}\right|_{\mathbf{\Omega}=\mathbf{\Omega}_0} p\left(\mathbf{O}^{(n)}|\mathbf{\Omega}\right)d\mathbf{O}^{(n)} \tag{5.60}$$

$$= -N\int_{-\infty}^{+\infty}\int_{-\infty}^{+\infty}\cdots\int_{-\infty}^{+\infty}\left.\frac{\partial^2 \ln p\left(\mathbf{O}^{(n)}|\mathbf{\Omega}\right)}{\partial \mathbf{\Omega}\partial\mathbf{\Omega}^T}\right|_{\mathbf{\Omega}=\mathbf{\Omega}_0} p\left(\mathbf{O}^{(n)}|\mathbf{\Omega}\right)do_1^{(n)}do_2^{(n)}\cdots do_T^{(n)}. \tag{5.61}$$

In order to obtain the Fisher information matrix following Equation (5.61), the second order derivatives of the logarithm of the incomplete data likelihood with respect to the parameters of

the hidden Markov model are calculated. For two general parameters Ω_1 and Ω_2, this second order derivative is expressed as follows:

$$\frac{\partial^2 \ln p}{\partial \Omega_1 \partial \Omega_2} = -\frac{1}{p^2}\frac{\partial p}{\partial \Omega_1}\frac{\partial p}{\partial \Omega_2} + \frac{1}{p}\frac{\partial^2 p}{\partial \Omega_1 \partial \Omega_2}, \tag{5.62}$$

where we used the abbreviated notation

$$p = p\left(\mathbf{O}^{(n)}|\mathbf{\Omega}\right). \tag{5.63}$$

We further abbreviate the notation by omitting the index n from the effective number of atoms in a column at a given time, since the derivation is independent of the column index, and introduce an abbreviated notation for the Gaussian function that describes the emission probability:

$$g_t = g_t^{(n)}, \tag{5.64}$$
$$\mathcal{N}_g^{(t)} = \mathcal{N}\left(o_n^{(t)}|a\mathcal{M}_g, \sigma\right). \tag{5.65}$$

The necessary first and second order derivatives to obtain the Fisher information matrix using Equation (5.63) for all parameters in the parameter vector $\mathbf{\Omega}$ are listed here:

$$\begin{aligned}
\frac{\partial p}{\partial \iota_k} &= \sum_{g_1=0}^{G}\cdots\sum_{g_T=0}^{G}\frac{\partial \iota_{g_1}}{\partial \iota_k}\prod_{t=2}^{T}A_{g_{t-1}g_t}\prod_{t'=1}^{T}\mathcal{N}_{g_{t'}}^{(t')},\\
\frac{\partial p}{\partial A_{jk}} &= \sum_{g_1=0}^{G}\cdots\sum_{g_T=0}^{G}\iota_{g_1}\frac{\partial}{\partial A_{jk}}\left[\prod_{t=2}^{T}A_{g_{t-1}g_t}\right]\prod_{t'=1}^{T}\mathcal{N}_{g_t}^{(t)},\\
\frac{\partial p}{\partial a} &= \sum_{g_1=0}^{G}\cdots\sum_{g_T=0}^{G}\iota_{g_1}\prod_{t=2}^{T}A_{g_{t-1}g_t}\frac{\partial}{\partial a}\left[\prod_{t'=1}^{T}\mathcal{N}_{g_t}^{(t)}\right],\\
\frac{\partial p}{\partial \sigma} &= \sum_{g_1=0}^{G}\cdots\sum_{g_T=0}^{G}\iota_{g_1}\prod_{t=2}^{T}A_{g_{t-1}g_t}\frac{\partial}{\partial \sigma}\left[\prod_{t'=1}^{T}\mathcal{N}_{g_t}^{(t)}\right].
\end{aligned}$$

and

$$\begin{aligned}
\frac{\partial^2 p}{\partial \iota_k \partial \iota_l} &= 0,\\
\frac{\partial^2 p}{\partial \iota_k \partial A_{lm}} &= \sum_{g_1=0}^{G}\cdots\sum_{g_T=0}^{G}\frac{\partial \iota_{g_1}}{\partial \iota_k}\frac{\partial}{\partial A_{lm}}\left[\prod_{t=2}^{T}A_{g_{t-1}g_t}\right]\prod_{t'=1}^{T}\mathcal{N}_{g_{t'}}^{(t')},\\
\frac{\partial^2 p}{\partial \iota_k \partial a} &= \sum_{g_1=0}^{G}\cdots\sum_{g_T=0}^{G}\frac{\partial \iota_{g_1}}{\partial \iota_k}\prod_{t=2}^{T}A_{g_{t-1}g_t}\frac{\partial}{\partial a}\left[\prod_{t'=1}^{T}\mathcal{N}_{g_{t'}}^{(t')}\right],\\
\frac{\partial^2 p}{\partial \iota_k \partial \sigma} &= \sum_{g_1=0}^{G}\cdots\sum_{g_T=0}^{G}\frac{\partial \iota_{g_1}}{\partial \iota_k}\prod_{t=2}^{T}A_{g_{t-1}g_t}\frac{\partial}{\partial \sigma}\left[\prod_{t'=1}^{T}\mathcal{N}_{g_{t'}}^{(t')}\right],\\
\frac{\partial^2 p}{\partial A_{jk}\partial A_{lm}} &= \sum_{g_1=0}^{G}\cdots\sum_{g_T=0}^{G}\iota_{g_1}\frac{\partial^2}{\partial A_{jk}\partial A_{lm}}\left[\prod_{t=2}^{T}A_{g_{t-1}g_t}\right]\prod_{t'=1}^{T}\mathcal{N}_{g_t}^{(t)},
\end{aligned}$$

$$
\begin{aligned}
\frac{\partial^2 p}{\partial A_{jk}\partial a} &= \sum_{g_1=0}^{G}\cdots\sum_{g_T=0}^{G}\iota_{g_1}\frac{\partial}{\partial A_{jk}}\left[\prod_{t=2}^{T}A_{g_{t-1}g_t}\right]\frac{\partial}{\partial a}\left[\prod_{t'=1}^{T}\mathcal{N}_{g_t}^{(t)}\right],\\
\frac{\partial^2 p}{\partial A_{jk}\partial \sigma} &= \sum_{g_1=0}^{G}\cdots\sum_{g_T=0}^{G}\iota_{g_1}\frac{\partial}{\partial A_{jk}}\left[\prod_{t=2}^{T}A_{g_{t-1}g_t}\right]\frac{\partial}{\partial \sigma}\left[\prod_{t'=1}^{T}\mathcal{N}_{g_t}^{(t)}\right],\\
\frac{\partial^2 p}{\partial a\partial \sigma} &= \sum_{g_1=0}^{G}\cdots\sum_{g_T=0}^{G}\iota_{g_1}\prod_{t=2}^{T}A_{g_{t-1}g_t}\frac{\partial^2}{\partial a\partial \sigma}\left[\prod_{t'=1}^{T}\mathcal{N}_{g_t}^{(t)}\right],\\
\frac{\partial^2 p}{\partial^2 a} &= \sum_{g_1=0}^{G}\cdots\sum_{g_T=0}^{G}\iota_{g_1}\prod_{t=2}^{T}A_{g_{t-1}g_t}\frac{\partial^2}{\partial^2 a}\left[\prod_{t'=1}^{T}\mathcal{N}_{g_t}^{(t)}\right],\\
\frac{\partial^2 p}{\partial^2 \sigma} &= \sum_{g_1=0}^{G}\cdots\sum_{g_T=0}^{G}\iota_{g_1}\prod_{t=2}^{T}A_{g_{t-1}g_t}\frac{\partial^2}{\partial^2 \sigma}\left[\prod_{t'=1}^{T}\mathcal{N}_{g_t}^{(t)}\right],
\end{aligned}
$$

with

$$
\begin{aligned}
\frac{\partial}{\partial A_{jk}}\left[\prod_{t=2}^{T}A_{g_{t-1}g_t}\right] &= \left(\prod_{t=2}^{T}A_{g_{t-1}g_t}\right)\left(\sum_{t=2}^{T}\frac{1}{A_{g_{t-1}g_t}}\frac{\partial A_{g_{t-1}g_t}}{\partial A_{jk}}\right),\\
\frac{\partial}{\partial a}\left[\prod_{t=1}^{T}\mathcal{N}_{g_t}^{(t)}\right] &= \left(\prod_{t=1}^{T}\mathcal{N}_{g_t}^{(t)}\right)\left(\sum_{t=1}^{T}\frac{1}{\mathcal{N}_{g_t}^{(t)}}\frac{\partial \mathcal{N}_{g_t}^{(t)}}{\partial a}\right),\\
\frac{\partial}{\partial \sigma}\left[\prod_{t=1}^{T}\mathcal{N}_{g_t}^{(t)}\right] &= \left(\prod_{t=1}^{T}\mathcal{N}_{g_t}^{(t)}\right)\left(\sum_{t=1}^{T}\frac{1}{\mathcal{N}_{g_t}^{(t)}}\frac{\partial \mathcal{N}_{g_t}^{(t)}}{\partial \sigma}\right),
\end{aligned}
$$

$$
\begin{aligned}
\frac{\partial^2}{\partial A_{jk}\partial A_{lm}}\left[\prod_{t=2}^{T}A_{g_{t-1}g_t}\right] &= \left(\prod_{t=2}^{T}A_{g_{t-1}g_t}\right)\left(\sum_{t=2}^{T}\frac{1}{A_{g_{t-1}g_t}}\frac{\partial A_{g_{t-1}g_t}}{\partial A_{jk}}\right)\left(\sum_{t=2}^{T}\frac{1}{A_{g_{t-1}g_t}}\frac{\partial A_{g_{t-1}g_t}}{\partial A_{lm}}\right)\\
&\quad-\left(\prod_{t=2}^{T}A_{g_{t-1}g_t}\right)^2\left(\sum_{t=2}^{T}\frac{1}{A_{g_{t-1}g_t}^2}\frac{\partial A_{g_{t-1}g_t}}{\partial A_{jk}}\frac{\partial A_{g_{t-1}g_t}}{\partial A_{lm}}\right),\\
\frac{\partial^2}{\partial a\partial \sigma}\left[\prod_{t=1}^{T}\mathcal{N}_{g_t}^{(t)}\right] &= \left(\prod_{t=1}^{T}\mathcal{N}_{g_t}^{(t)}\right)\left(\sum_{t=1}^{T}\frac{1}{\mathcal{N}_{g_t}^{(t)}}\frac{\partial \mathcal{N}_{g_t}^{(t)}}{\partial a}\right)\left(\sum_{t=1}^{T}\frac{1}{\mathcal{N}_{g_t}^{(t)}}\frac{\partial \mathcal{N}_{g_t}^{(t)}}{\partial \sigma}\right)\\
&\quad+\left(\prod_{t=1}^{T}\mathcal{N}_{g_t}^{(t)}\right)^2\left(\sum_{t=1}^{T}\left[-\frac{1}{\left(\mathcal{N}_{g_t}^{(t)}\right)^2}\frac{\partial \mathcal{N}_{g_t}^{(t)}}{\partial a}\frac{\partial \mathcal{N}_{g_t}^{(t)}}{\partial \sigma}+\frac{1}{\mathcal{N}_{g_t}^{(t)}}\frac{\partial^2 \mathcal{N}_{g_t}^{(t)}}{\partial a\partial \sigma}\right]\right),\\
\frac{\partial^2}{\partial a^2}\left[\prod_{t=1}^{T}\mathcal{N}_{g_t}^{(t)}\right] &= \left(\prod_{t=1}^{T}\mathcal{N}_{g_t}^{(t)}\right)\left(\sum_{t=1}^{T}\frac{1}{\mathcal{N}_{g_t}^{(t)}}\frac{\partial \mathcal{N}_{g_t}^{(t)}}{\partial a}\right)^2\\
&\quad+\left(\prod_{t=1}^{T}\mathcal{N}_{g_t}^{(t)}\right)^2\left(\sum_{t=1}^{T}\left[-\frac{1}{\left(\mathcal{N}_{g_t}^{(t)}\right)^2}\left(\frac{\partial \mathcal{N}_{g_t}^{(t)}}{\partial a}\right)^2+\frac{1}{\mathcal{N}_{g_t}^{(t)}}\frac{\partial^2 \mathcal{N}_{g_t}^{(t)}}{\partial a^2}\right]\right),\\
\frac{\partial^2}{\partial \sigma^2}\left[\prod_{t=1}^{T}\mathcal{N}_{g_t}^{(t)}\right] &= \left(\prod_{t=1}^{T}\mathcal{N}_{g_t}^{(t)}\right)\left(\sum_{t=1}^{T}\frac{1}{\mathcal{N}_{g_t}^{(t)}}\frac{\partial \mathcal{N}_{g_t}^{(t)}}{\partial \sigma}\right)^2
\end{aligned}
$$

$$+\left(\prod_{t=1}^{T}\mathcal{N}_{g_t}^{(t)}\right)^2\left(\sum_{t=1}^{T}\left[-\frac{1}{\left(\mathcal{N}_{g_t}^{(t)}\right)^2}\left(\frac{\partial\mathcal{N}_{g_t}^{(t)}}{\partial\sigma}\right)^2+\frac{1}{\mathcal{N}_{g_t}^{(t)}}\frac{\partial^2\mathcal{N}_{g_t}^{(t)}}{\partial\sigma^2}\right]\right),$$

and

$$\begin{aligned}
\frac{\partial\iota_g}{\partial\iota_k} &= \begin{cases}\delta_{gk} & \text{If } g<G\\ -1 & \text{If } g=G\end{cases},\\
\frac{\partial A_{jk}}{\partial A_{lm}} &= \begin{cases}\delta_{jl}\delta_{km} & \text{If } k<G\\ -\delta_{jl} & \text{If } k=G\end{cases},\\
\frac{\partial\mathcal{N}_g^{(t)}}{\partial a} &= \frac{\left(o_t^{(n)}-a\mathcal{M}_g\right)\mathcal{M}_g}{\sigma^2}\mathcal{N}_g^{(t)},\\
\frac{\partial\mathcal{N}_g^{(t)}}{\partial\sigma} &= \left(\frac{\left(o_t^{(n)}-a\mathcal{M}_g\right)^2}{\sigma^3}-\frac{1}{\sigma}\right)\mathcal{N}_g^{(t)},\\
\frac{\partial^2\mathcal{N}_g^{(t)}}{\partial a\partial\sigma} &= -\frac{2\left(o_t^{(n)}-a\mathcal{M}_g\right)\mathcal{M}_g}{\sigma^3}\mathcal{N}_g^{(t)}+\frac{\left(o_t^{(n)}-a\mathcal{M}_g\right)\mathcal{M}_g}{\sigma^2}\left(\frac{\left(o_t^{(n)}-a\mathcal{M}_g\right)^2}{\sigma^3}-\frac{1}{\sigma}\right)\mathcal{N}_g^{(t)},\\
\frac{\partial^2\mathcal{N}_g^{(t)}}{\partial a^2} &= -\frac{\mathcal{M}_g^2}{\sigma^2}\mathcal{N}_g^{(t)}+\left(\frac{\left(o_t^{(n)}-a\mathcal{M}_g\right)\mathcal{M}_g}{\sigma^2}\right)^2\mathcal{N}_g^{(t)},\\
\frac{\partial^2\mathcal{N}_g^{(t)}}{\partial\sigma^2} &= \left(-\frac{3\left(o_t^{(n)}-a\mathcal{M}_g\right)^2}{\sigma^4}+\frac{1}{\sigma^2}\right)\mathcal{N}_g^{(t)}+\left(\frac{\left(o_t^{(n)}-a\mathcal{M}_g\right)^2}{\sigma^3}-\frac{1}{\sigma}\right)^2\mathcal{N}_g^{(t)}.
\end{aligned}$$

Using these expressions, we obtain all elements of the Fisher information matrix of Equation (5.61).

6

Measuring dynamic structural changes at the atomic scale from ADF STEM time series

6.1 Introduction

Different time-resolving techniques, such as dynamic transmission electron microscopy [Armstrong 2007, Browning 2012], ultrafast electron diffraction [Siwick 2003, Zewail 2006, Barwick 2008, Ruan 2009, Ischenko 2014], and ultrafast X-ray imaging [Rischel 1997, Lindenberg 2017] have been developed in order to study structural dynamics with very high temporal resolution. Since these techniques sacrifice direct atomic resolution imaging, high-resolution transmission electron microscopy [Jia 2014], off-axis electron holography [Linck 2012] or annular dark field (ADF) scanning transmission electron microscopy (STEM) [Van Aert 2011, Van Aert 2013] are needed to obtain local structural information at atomic resolution and sub-second temporal resolution. This time resolution is adequate in order to study transient atomic scale phenomena [Isaacson 1977, Liao 2014, Kotakoski 2014, Mishra 2017, Liu 2019, Zhou 2019, Altantzis 2019]. The concomitant advantage for ADF STEM images is that the intensities are peaked at the atomic column positions and depend monotonically on the atomic mass number Z and the thickness of the material enabling to count the number of atoms in each atomic column. In the previous chapter, we have introduced the hidden Markov model for atom-counting from an ADF STEM time series. When the atom-counting results are combined with structural energy minimisation [Bals 2012, Jones 2014, Geuchies 2016, De Backer 2017, Altantzis 2019], we can obtain a visualisation of the three-dimensional (3D) atomic structure from a two-dimensional (2D) image without the need for the large electron doses and long acquisition times generally required for electron tomography. Although high-resolution electron tomography has been used to investigate the atomic structure of nanoparticles in 3D, the combination with *in situ* measurements is far from straightforward because of several technical and more fundamental reasons. The main limitation is the time required to collect a tilt series of images, which is typically equal to 1 or several hours, although fast acquisition schemes have recently been developed [Vanrompay 2018]. Since catalysts are in active and non-equilibrium

This chapter is based on [De wael 2020a, De wael 2020b, Liu 2021].

states, conventional tomography approaches cannot be applied to investigate the fast changes that supported catalyst nanoparticles undergo when being exposed to a relevant environment. The hidden Markov model can be used to measure dynamic structural changes at the atomic scale during a time series based on the reliable counting results. We derive the probability for such structural changes in Section 6.2. In Section 6.3, an experimental time series of a Pt wedge is analysed using the hidden Markov model. A cross section for surface diffusion can be estimated for this Pt wedge, which is then compared to the theoretical value for this type of material. Next, in Section 6.4, we analyse a catalyst Pt nanoparticle using the hidden Markov model, and study the stability of its facetted morphology, which is of great importance for the activity of the catalyst. In Section 6.5, the hidden Markov model is then applied to a supported Au nanoparticle imaged at a constant elevated temperature. The obtained counting results are combined with molecular dynamics simulations to investigate the 3D atomic structure. Finally, we consider the structural changes driven by time-varying experimental conditions in Section 6.6. We simulate such changes by generating time series corresponding to multiple transition matrices, and study the applicability of the hidden Markov model with only one transition matrix. The chapter is concluded in Section 6.7.

6.2 Probability and cross section related to structural changes

So far, we have shown that the hidden Markov model yields more reliable counting results for the analysis of a time series of a changing nanostructure. In order to obtain these atom-counts, the parameters of the hidden Markov model are estimated as discussed in Section 5.4. An important parameter of the hidden Markov model is the transition matrix $\mathbf{A}$, as this is used to model the probability that the number of atoms in an atomic column changes, and thus the probability of structural changes. In this section, we will discuss the link between the transition matrix and the cross section related to the process that drives the structural changes throughout the time series. Intensity variations during a time series can be caused either by noise fluctuations, or by actual structural changes. The hidden Markov model estimates two separate parameters to model both contributions. The noise is modelled by the width σ of the Gaussian emission probability, and the structural changes are modelled by the transition matrix $\mathbf{A}$. We will assess the accuracy of the estimated probability of structural changes using a combined measure for the $G(G+1)$ estimated transition probabilities and the G estimated initial probabilities:

$$P = \frac{\sum_{g=0}^{G} \pi_g (1 - A_{gg})}{G+1}. \tag{6.1}$$

This expresses the weighted average probability that the number of atoms in an atomic column changes during the time series, as $1 - A_{gg}$ corresponds to the probability that the number of atoms in an atomic column will not stay the same from frame to frame. The weights π_g correspond to the probability for an atomic column to have g atoms in any frame of the time series and follow from the estimated transition and initial probabilities:

$$\pi_g = \frac{1}{T-1} \sum_{t=1}^{T-1} \pi_g^{(t)}, \tag{6.2}$$

with $\pi_g^{(t)}$ the probability for an atomic column to have g atoms at time t, as defined in Equation (5.11). Note that, when all parameters are estimated accurately, these weights π_g are equivalent to the mixing proportions estimated from the collective hybrid method.

In order to validate the physical interpretation of the estimated transition matrix in terms of atomic structural changes, we created 50 noise realisations of a hypothetical time series. The parameters of the hidden Markov model used to create these time series are equal to the parameters estimated from the experimental time series of the Pt wedge shown in Section 6.3. The structural changes of this Pt wedge will also be analysed further in this section. The width of the Gaussian emission probability σ is varied to obtain different noise levels. The width σ can be related to the electron dose d through $\sigma = \sqrt{\frac{\mu_g}{d}}$ when only Poisson noise is present, with μ_g the scattering cross section for g atoms in an atomic column [Van Aert 2019]. In this manner, at the average sample thickness, the noise levels σ/δ used during the following analysis can be translated to electron doses ranging between 7×10^4 e$^-$/Å^2 and 9×10^2 e$^-$/Å^2. Table 6.1 summarises the 95% confidence intervals for the mean estimated values of the probability of structural changes P from Equation (6.1) and the relative width of the Gaussian emission probability σ/δ, at the different noise levels, together with the ground truth of these parameters. The percentage of correctly counted atomic columns is also summarised using a 95% confidence interval. Furthermore, results are shown for an analysis of 50 noise realisations of a hypothetical time series with the same settings, but with a more diffuse transition matrix, as to allow for more structural changes during the time series. This transition matrix is shown in Figure B.2 of Appendix B. In this manner, we can assess the accuracy of the estimated parameters that quantify noise and structural changes. For a small underlying probability of structural changes P, the estimated values of P and σ/δ are accurate up to high noise levels. This indicates that intensity variations due to structural changes are indeed quantified by the transition matrix $\mathbf{A}$, while noise fluctuations are quantified by the width of the Gaussian emission probability σ. When the underlying probability of structural changes P is larger, the estimated values of P and σ/δ still remain accurate up to a reasonably high noise level, but are slightly more inaccurate, as well as less precise, at high noise levels. This also leads to a lower percentage of correct atom-counts. We conclude that the separation of noise fluctuations from atomic structural changes is reliably done by the hidden Markov model analysis for small values of P, even at a low electron dose, i.e. at large σ/δ. When the probability of structural changes P is larger, the separation of noise and structural changes can still be performed reasonably well, although slight inaccuracies arise when the electron dose is lowered, making it more difficult to discern the origin of the fluctuations in the scattering cross sections from frame to frame.
Therefore, when the electron dose is sufficiently high, i.e. when σ/δ is sufficiently low, Equation (6.1) reliably describes the probability of structural changes. In this manner, we can now estimate the probability of structural changes from an experimental ADF STEM time series. This will be applied to the examples in the next two sections.

6.3 Analysis of a Pt wedge time series

In this section, we illustrate the proposed hidden Markov model for time series atom-counting using an experimental time series of a Pt wedge, shown in Figure 6.1a. The time series consists of $T = 6$ frames and was previously also analysed in [Van Aert 2019]. The consecutive ADF STEM images of the Pt wedge were recorded by Armand Béché, using a beam current of 37 pA and pixel size 9.1 pm, corresponding to an electron dose of 2.8×10^4 e$^-$/Å^2. All consecutive ADF STEM images of the Pt wedge are shown in Figure B.3 of Appendix B.
In order to apply the hidden Markov model to an experimental series [Figure 6.2a], several preprocessing steps are required. These are schematically shown in Figure 6.2. On the one hand, we want to compare the experimental image intensities to simulated intensities. There-

P (%)			σ/δ			correct atom-counts (%)	
	95% CI			95% CI		95% CI	
ground truth	lower bound	upper bound	ground truth	lower bound	upper bound	lower bound	upper bound
	12.42	12.69	0.1	0.0998	0.1002	99.99	100.00
	12.35	12.70	0.3	0.2990	0.3010	97.16	97.28
12.55	12.38	12.81	0.5	0.4968	0.5003	88.69	89.00
	11.67	12.44	0.7	0.6945	0.6998	79.02	79.53
	11.55	12.74	0.9	0.8908	0.8972	69.83	71.12
	59.01	59.38	0.1	0.1000	0.1004	99.99	100.00
	59.01	59.47	0.3	0.2974	0.2992	92.89	93.05
59.52	59.60	60.34	0.5	0.4818	0.4888	75.88	76.16
	61.50	63.26	0.7	0.6603	0.6762	61.54	62.07
	63.72	66.70	0.9	0.8363	0.8525	50.07	51.35

Table 6.1: *Accuracy of the probability of structural changes P, the relative width of the Gaussian emission probability σ/δ and the atom-counts estimated by the hidden Markov model.*

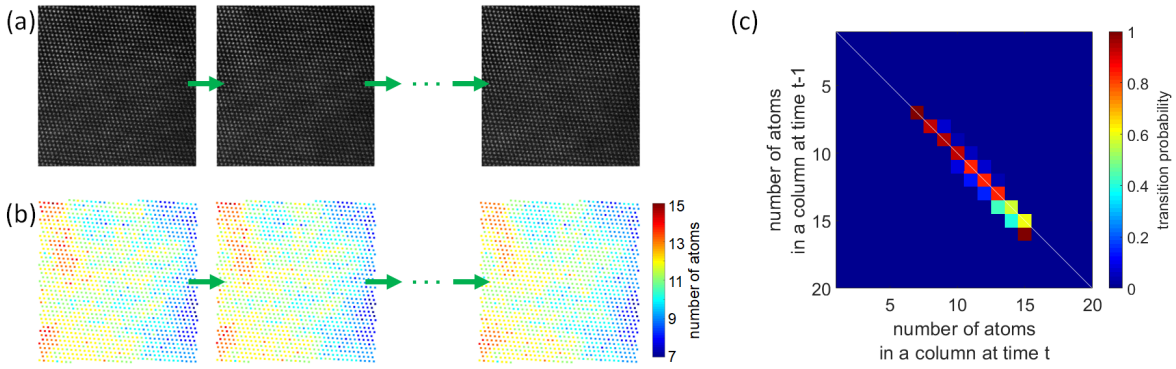

Figure 6.1: *(a) Experimental ADF STEM images of the time series of the Pt wedge discussed in Section 6.3. (b) Counting results obtained by the hidden Markov model analysis. (c) Transition matrix estimated by the hidden Markov model analysis.*

fore, the ADF STEM image intensities need to be normalised to the incident electron beam, as mentioned earlier in Section 2.6. On the other hand, the theoretical framework of the hidden Markov model assumes that we can track each atomic column n through the entire series. In order to reliably quantify the changes for each atomic column of the nanostructure, the time series needs to be aligned [Figure 6.2b]. This is achieved using rigid registration to account for sample drift and/or rotation. One can also apply non-rigid registration of the images to compensate for scan distortions in order to improve the precision of the quantification of the ADF STEM images performed during the next steps [Jones 2015]. Next, the atomic column positions need to be reliably quantified in each frame [Figure 6.2c]. In case of high electron dose recordings, a simple peak finding routine is sufficient. However, when the electron dose is low, and the noise level in the images is high, it becomes difficult to distinguish atomic columns from noise fluctuations. It is however crucial to correctly select all atomic columns. This can be done using the maximum *a posteriori* (MAP) probability rule, as mentioned in Section 2.5. Using these atomic column positions, a parametric imaging model is fitted to each ADF STEM image as described in Section 2.5. From this model, the scattering cross sections can now be

estimated for each atomic column [Figure 6.2d]. In order to apply the hidden Markov model to the ADF STEM time series, the atomic columns of the nanostructure are tracked in each image, and the scattering cross sections of each atomic column are sorted accordingly [Figure 6.2e]. Together, the scattering cross sections of all atomic columns in each ADF STEM image of the time series are the input for the hidden Markov model analysis [Figure 6.2f]. The output of the hidden Markov model is the set of atom-counting results for each ADF STEM image of the time series [Figure 6.2g].

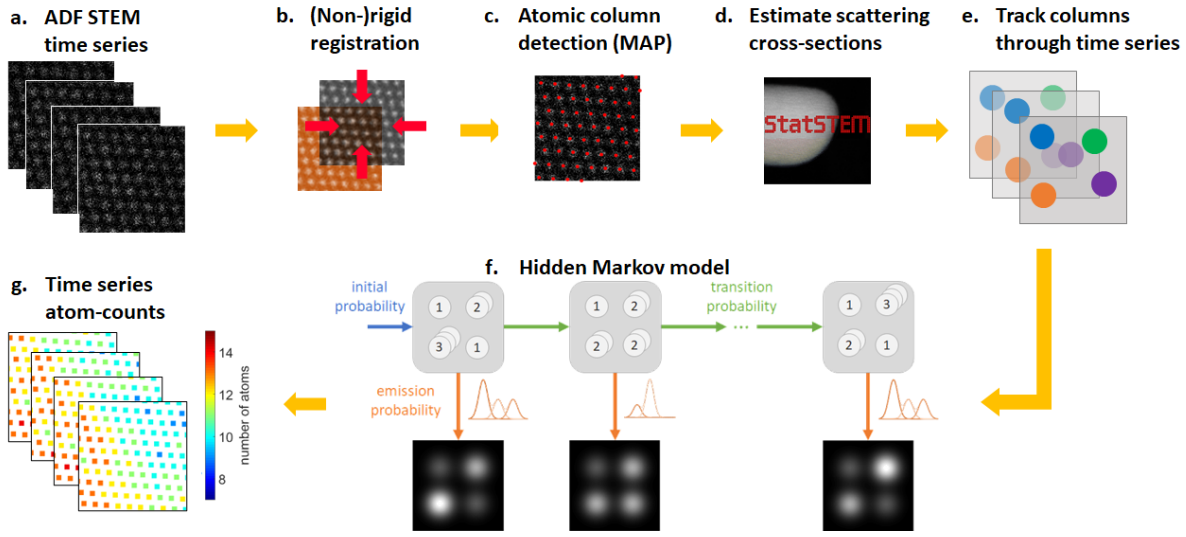

Figure 6.2: *Workflow for atom-counting from a time series of ADF STEM images using hidden Markov models.*

The counting results for the ADF STEM time series of the Pt wedge, obtained in this manner, are summarised in Figure 6.1b. The counting results obtained for each image of the time series are shown in Figure B.4 of Appendix B. The hidden Markov model analysis also provides an estimate for the transition probabilities. The transition matrix $\mathbf{A}$ estimated for this time series is shown in Figure 6.1c. The white diagonal line plotted on top of the transition matrix indicates the transitions where the number of atoms in an atomic column stays the same. The upper and lower triangles contain the probabilities for an atomic column to respectively gain or lose one or more atoms. The physical interpretation of these transition probabilities was discussed in the previous section. This is now applied, and we estimate the probability of structural changes for this experimental ADF STEM time series of the Pt wedge. Using Equation (6.1), the probability of structural changes is estimated equal to $P = 12.6\%$. We do not expect structural changes to be caused by sputtering of atoms from the surface, only by surface diffusion, since the threshold energy for sputtering Pt atoms from a convex surface with step sites is 379 keV, well above the incident electron energy of 300 keV [Egerton 2010, Van Aert 2019]. In order to relate the probability of structural changes to the probability of surface displacement, a factor of $\frac{1}{2}$ should be added in Equation (6.1), to account for the top and bottom surface of the nanostructure:

$$P_{\mathrm{sd}} = \frac{1}{2}\frac{\sum_{g=0}^{G}\pi_g(1-A_{gg})}{G+1}. \tag{6.3}$$

The cross section σ_{sd} and probability P_{sd} for surface displacement are related as follows [Van Aert 2019]:

$$P_{\mathrm{sd}} = \sigma_{\mathrm{sd}} d \frac{N_{\mathrm{ad}}}{N}, \tag{6.4}$$

with d the electron dose, N the total number of atomic columns, and N_{ad} the number of adatoms. An adatom is an atom that lies on top of the surface. Therefore, the coordination number of an adatom is lower than that of atoms embedded in surface facets or in the bulk of the particle. Here, the number of adatoms N_{ad} is estimated equal to the number of atoms with coordination number less than or equal to 6 in the symmetrical 3D atom configuration based on the atom-counting. In this manner, we estimate the cross section related to surface diffusion for this Pt wedge to be equal to $\sigma_{sd} = (5.60 \pm 0.05) \times 10^{-6}$Å^2 from the probability of surface displacement $P_{sd} = 6.3\%$ and the estimated fraction of adatoms $\frac{N_{\text{ad}}}{N} = 0.4$. The error bar in this expression is equal to the standard deviation of the mean estimated cross section from 100 hypothetical time series using the same parameters estimated for the experimental Pt wedge. This value for the cross section related to surface displacement corresponds to a surface diffusion threshold energy of 1.09 eV [Egerton 2013]. This is in close agreement with the theoretical threshold energy for surface diffusion for Pt(110), which is calculated as 1.07 eV, corresponding to a cross section of $\sigma_{sd} = 16 \times 10^{-6}$Å^2 [Halicioglu 1979]. The underestimation of the cross section by the hidden Markov model analysis can be understood since the estimated transition probabilities describe net structural changes from frame to frame. These net structural changes can however be the result of multiple hops of atoms, potentially in opposite directions, yielding a smaller amount of net changes after the frame is acquired as compared to the actual amount of structural changes. In this manner, we unavoidably underestimate the cross section related to surface diffusion. However, this methodology gets a closer match with the theory as compared to the current state-of-the-art analysis of variance method, where a cross section of $\sigma_{sd} = (0.74 \pm 0.20) \times 10^{-6}$Å^2 was estimated [Van Aert 2019], and is therefore a promising approach for the reliable quantification of physical cross sections from experimental ADF STEM time series.

6.4 Analysis of a catalyst Pt nanoparticle time series

In this section, we apply the hidden Markov model to an experimental time series of a catalyst Pt nanoparticle. ADF STEM images were recorded by Aakash Varambhia and Lewys Jones, on a JEOL ARM200CF fitted with a probe-aberration corrector using an acceleration voltage of 200 kV, a probe convergence angle of 22.48 mrad, an annular detector ranging from 52-248 mrad, a dwell time of 4μs and an electron dose of $1.38 \cdot 10^4$ e$^-$/Å^2 per frame. All images of the time series are shown in Figure B.5 of Appendix B. In order to apply the hidden Markov model, several preprocessing steps were applied to the time series, as discussed in Section 6.3. The images from the time series were corrected for drift and other distortions using non-rigid registration [Jones 2015]. Coordinates of the atomic columns were selected in each frame using the maximum a posteriori probability (MAP) rule for atomic column detection introduced in [Fatermans 2018]. As such, we could reliably determine all atomic columns present in the nanoparticle throughout the time series.

During the time series, the Pt nanoparticle tilts slightly away from zone axis orientation and back, which affects the scattering cross sections, as shown in Chapter 3. However, the hidden Markov model only estimates one linear scaling parameter for all frames of the time series. Therefore, the scattering cross sections of the individual frames need to be compensated for tilt, prior to the hidden Markov model analysis. In order to perform such a tilt compensation, a reference frame for which the nanoparticle is in zone axis orientation is selected from the time series. For this reference frame, no elongation of the atomic columns is observed. Furthermore, the reference frame of the time series is chosen such that the ICL criterion of the hybrid method for atom-counting, discussed in Section 4.4, shows a clear local minimum corresponding to a scaling parameter close to 1. This implies a close match between the experimental and simula-

tion settings, while sample tilt would cause a decrease in the scattering cross section values and therefore also a decrease in the estimated scaling parameter as compared to the zone axis orientation, as discussed in Section 4.7. The number of atoms is then counted from this reference frame using the hybrid method for atom-counting. Next, we can assume that the total number of atoms in the nanoparticle remains constant throughout the time series. This assumption is valid since the threshold energy for sputtering Pt atoms from a convex surface with step sites is 379 keV [Egerton 2010], well above the incident electron energy of 200 keV. We therefore do not expect sputtering of atoms from the surface, only surface diffusion [Van Aert 2019]. Based on this assumption, the scattering cross sections are divided by the scaling parameter that yields approximately the same total number of atoms as the reference value from a single frame analysis. As such, the decrease in the scattering cross sections due to the sample tilt is compensated. Next, dynamic structural changes are determined from the time series analysis using a hidden Markov model, of which the results are shown schematically in Figure 6.3. The counting results for all frames are shown in Figure B.6 of Appendix B.

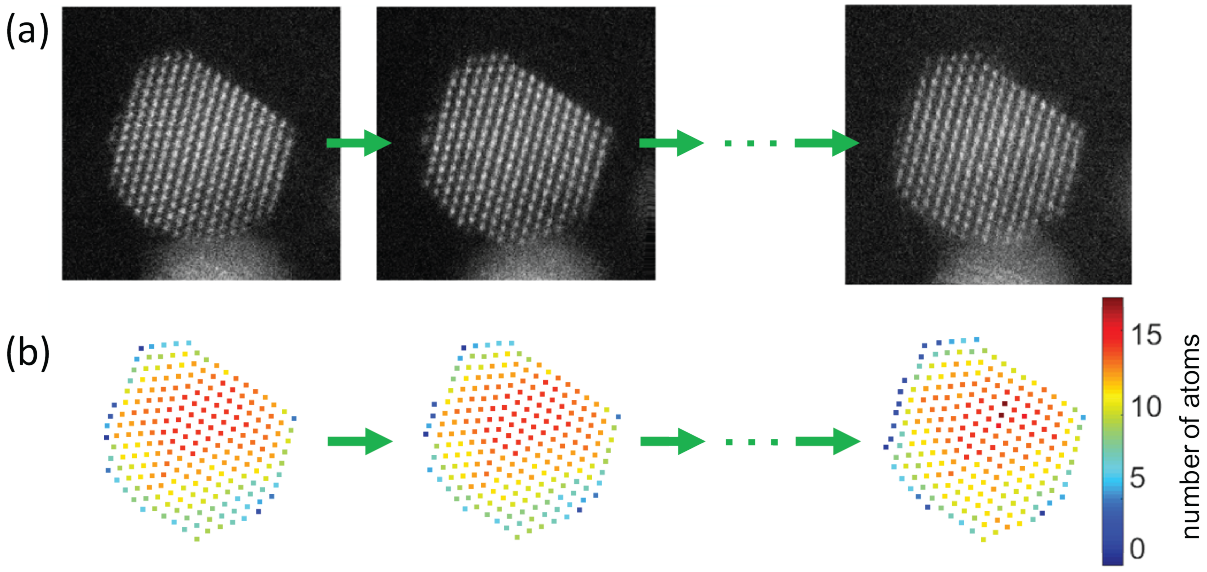

Figure 6.3: *(a) The experimental ADF STEM time series of a Pt nanoparticle. (b) From the estimated hidden Markov model, the hidden state sequence is retrieved.*

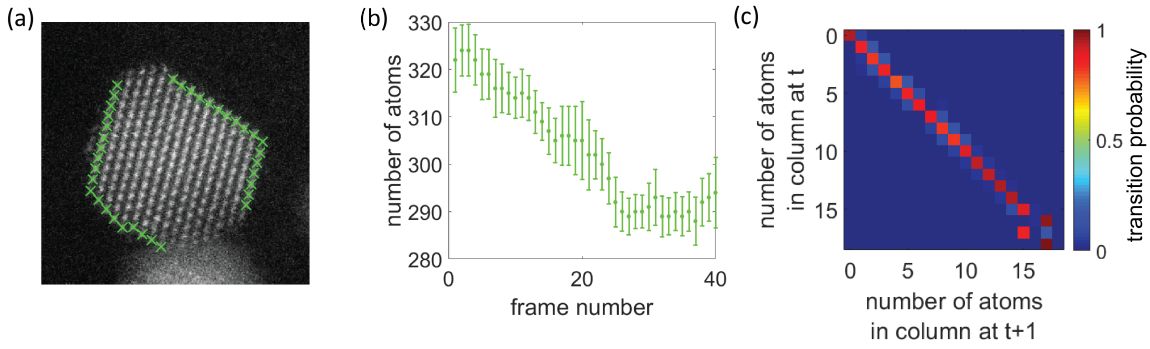

Figure 6.4: *(a) The Pt nanoparticle shows clear facets along the beam direction. Atomic columns in {111} facets are indicated. (b) Number of atoms in the {111} facets indicated in (a). (c) Estimated transition probability matrix.*

The HAADF STEM projection images reveal the facetted shape of the Pt nanoparticle. The {111} facets, on occasion decorated by additional atoms [Wang 2012b], are indicated by green crosses in Figure 6.4a. Using the counting results from our hidden Markov model analysis, we can now quantify the evolution of the number of atoms in these facets for each frame of the time series (Figure 6.4b). While the total number of atoms in the Pt nanoparticle remains the same, the number of atoms in the {111} facets along the beam direction decreases and the Pt nanoparticle gradually loses its facetted morphology during electron beam irradiation. This result is consistent with earlier observations of the same type of Pt nanoparticles [Jones 2014] and can be explained by beam-induced surface diffusion. The hidden Markov model analysis has the added advantage that it enables us to quantify the probability for surface diffusion. From the transition probabilities shown in Figure 6.4c it follows that the average probability for a surface atom to move to another column equals 4.6%. This value was determined as discussed in Section 6.2. Taking into account the electron dose, the experimental value for the average cross section for surface diffusion is estimated equal to $\sigma_{\mathrm{sd}} = 3.3 \cdot 10^{-6}$ Å^2, as described in Section 6.2. This cross section for surface diffusion includes the contributions of different migration mechanisms, such as hopping, atomic exchange, and vacancy diffusion, and from different types of surfaces [Oura 2003, Egerton 2019]. This value is of great importance in order to unravel dominant mechanisms and surfaces in the diffusion process and to gain new insights in surface related phenomena such as catalysis and nanoparticle growth.

6.5 Analysis of in situ heating of Au nanoparticles

In the previous section, we have discussed a time series of a catalyst Pt nanoparticle, where images were acquired at room temperature. The Au nanoparticle that will be discussed in this section is imaged at elevated temperatures, as this affects its catalytic activity. This work has been performed in collaboration with Pei Liu, Ece Arslan Irmak et al. [Liu 2021]. I was responsible for performing the atom-counting of the time series using the hidden Markov model. Supported Au nanoparticles smaller than 3-5 nm are highly effective catalysts in a wide range of catalytic reactions, e.g. CO oxidation and the water-gas shift reaction [Hvolbæk 2007, Haruta 1989, Zhang 2011, Paier 2013, Wang 2015]. It is generally recognised that the activity of Au nanoparticles depends on their size and surface structure. However, the general shape and surface facets of supported nanoparticles are also highly dependent on environmental conditions, such as pressure [Yoshida 2012, Uchiyama 2011, Liu 2020] or temperature [Schlexer 2019, Foster 2019, Barnard 2009]. Quantitative investigations of the atomic configuration at the surface under relevant conditions are thus essential to reveal the active sites of the nanoparticles. Supported nanoparticles are used as thermal catalysts since it is expected that the morphology of the nanoparticles is stable at elevated temperatures. Experimentally imaging changes of the 3D atomic structure of catalytic nanoparticles at high temperature is technically challenging. However, studying the facet distribution and surface dynamics in 3D is an essential tool toward design and control over the catalyst structure and performance. In this section, first, the equilibrium morphology of CeO_2 supported Au nanoparticles at room temperature is investigated. Next, the dynamic structural changes of the nanoparticles at high temperatures are characterised in 3D, by applying molecular dynamics (MD) simulations to the counting results obtained from the hidden Markov model. The experimental images in this section were acquired by Pei Liu.

In order to study the equilibrium shape of the CeO_2 supported Au nanoparticles, ten consecutive time frames were averaged based on a rigid and non-rigid image registration procedure [Jones 2015]. Prior to averaging, an in-house developed deep convolutional neural net-

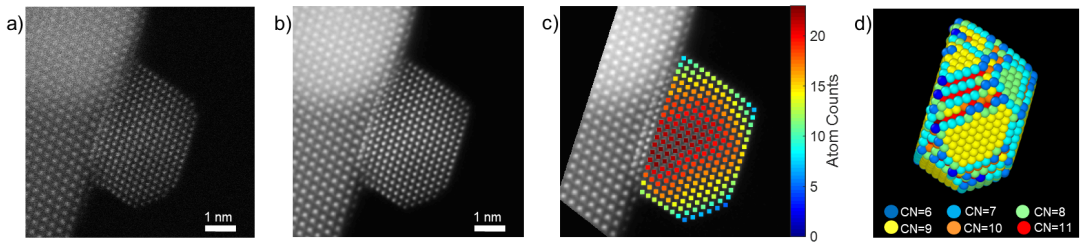

Figure 6.5: *Schematic illustration of the methodology to obtain a 3D model for Au nanoparticles on a CeO_2 substrate. (a) Raw HAADF STEM image of a Au nanoparticle on a CeO_2 support at room temperature. (b) Restored, registered and averaged image (based on ten consecutive frames). (c) Total number of atoms in each atomic column. (d) The final 3D model obtained through MD simulations. The colour code corresponds to the coordination number (CN) of each atom. CN=6: atom located on a corner, CN=7: atom located at an edge between two facets, CN=8: atom that is part of a {100} facet, CN=9: atom that is part of a {111} facet, CN=10 or CN=11: atom located in the second layer of an edge, CN=12: inner atom.*

work (CNN) approach for STEM image restoration was applied to each individual time frame, enabling us to correct distortions in the images [Altantzis 2019]. Figure 6.5a shows an uncorrected image of a Au nanoparticle on CeO_2 at room temperature. The analysis of this image was performed by Ece Arslan Irmak. The number of atoms in each of the atomic columns of the Au nanoparticle was counted from the averaged image, shown in Figure 6.5b, using the statistics-based atom-counting method introduced in Section 2.7. The counting results were validated using scattering cross sections obtained from independent image simulations by taking the detector sensitivity [Krause 2016] and the temperature-dependent root mean square deviation of Au atoms into account. The counting results, displayed in Figure 6.5c, were used to generate a 3D starting configuration by positioning the atoms in each atomic column parallel to the beam direction based on an Au crystalline structure and symmetrically around a central plane. By means of MD simulations that employ the embedded atom method [Grochola 2005], a relaxed 3D model for the structure of the nanoparticle was obtained, as illustrated in Figure 6.5d. During the MD simulations, the substrate was assumed to have a constant thickness, and a model for CeO_2 was generated based on the fluorite structure [Balaji Gopal 2017, Da Silva 2007]. To incorporate the interaction between the particle and the substrate, we used the Lennard-Jones potential. All MD simulations were performed by taking the substrate effect into account, although the substrate is not displayed in the figures.

Using a similar methodology, the non-equilibrium shape transformations for CeO_2 supported Au nanoparticles at elevated temperature are investigated. For this purpose, a time series of images at 400°C was acquired by Pei Liu. The individual images were restored using the CNN, and in contrast to the procedures for Figures 6.5, no averaging of consecutive images was performed. The temporal resolution of the time series is equal to 0.629 s, corresponding to a frame size of 1024 by 1024 pixels and dwell time of 0.5 μs. At these temperatures, it has been shown previously that entire surface layers of atoms abruptly displace, a phenomenon which is referred to as layer jumping [Liu 2020]. The number of atoms in each atomic column in each frame of $T = 46$ consecutive ADF STEM images was counted using the hidden Markov model. The observations and counting results are displayed for 5 consecutive frames of interest around such a layer jumping event in Figure 6.6a and 6.6b. Note that the analysis was performed on a longer time series as compared to the series shown here, in order to ensure reliability of the hidden Markov model analysis for a larger T, as demonstrated in Section 5.5.

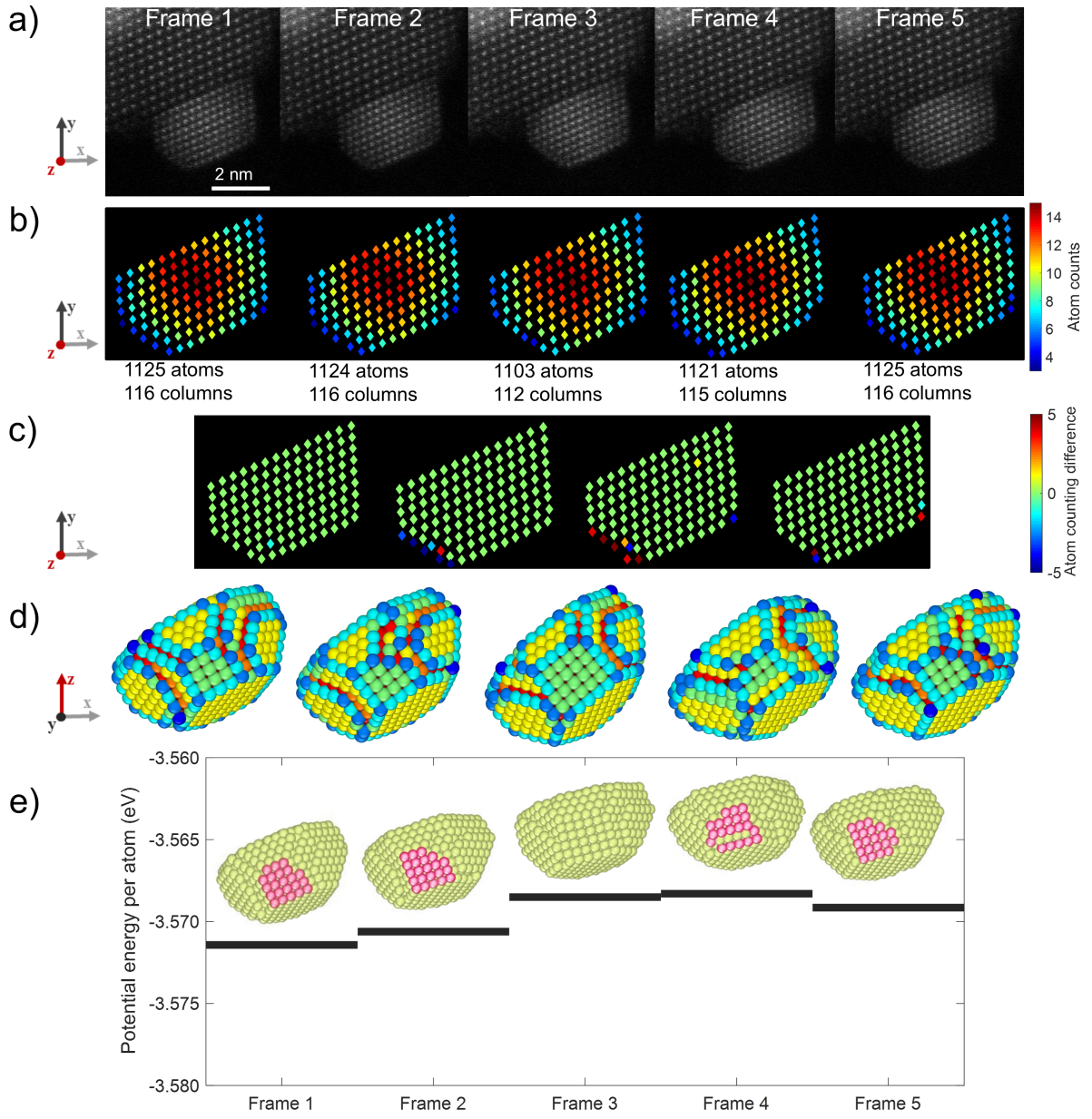

Figure 6.6: *Reversible shape transformation of the supported Au nanoparticle. (a) Time series HAADF-STEM images of a supported Au nanoparticle at 400°C (b) Atom counting results of the Au nanoparticle at different time frames obtained using the hidden Markov model. The total number of columns and the total number of atoms are listed for each time snapshot. (c) The change in the number of atoms for all atomic columns between consecutive time frames. (d) 3D relaxed structure of the Au nanoparticle at each time frame. The atoms are presented in different colours according to the coordination numbers, as in Figure 6.5d. (e) Averaged total potential energy per atom for each time shot.*

The estimated transition matrix is shown in Figure 6.7. From this transition matrix, it is clear that the number of atoms in most of the atomic columns does not change from frame to frame. This is also clear from the difference maps in Figure 6.6c, illustrating the counting difference between the consecutive frames. The blue colour code indicates a decreasing number of atoms, and the red colour code corresponds to an increase in the number of atoms. There are however a few significant changes where the number of atoms changes from 0 to around 5 or vice versa. This corresponds to atomic columns that appear and disappear from frame to frame. This observation is related to the layer jump. Figure 6.6 demonstrates that a layer on the (010) surface facet disappears on the third frame and reappears in frame 4.

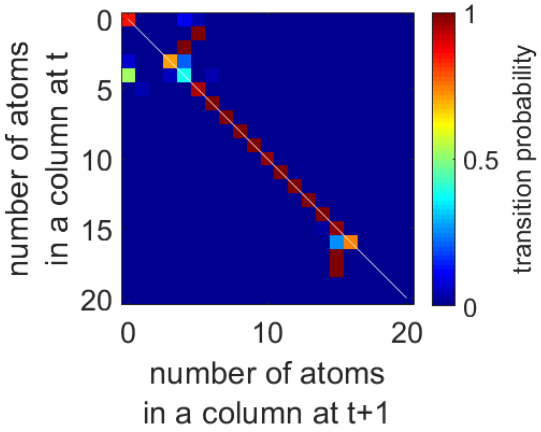

Figure 6.7: *Transition matrix from the hidden Markov model analysis of 46 subsequent ADF STEM images of the Au nanoparticle at 400°C. For this Au nanoparticle, 5 frames of interest are shown in Figure 6.6.*

Based on the counting results, input structures for MD simulations were created by Ece Arslan Irmak, and the results are illustrated in Figure 6.6d and Figure 6.6e. The nanoparticle in Figure 6.6 has a morphology similar to the equilibrium shape of such Au nanoparticles at elevated temperature, with {100} and {111} surface facets [Liu 2021]. Based on the 3D models, we can see that an entire (100) plane disappears and reappears (pink atoms in Figure 6.6e). Moreover, from the MD simulations, the potential energy was extracted for each system. In the potential energy curve, shown in Figure 6.6d, it can be seen that the energy slightly increases after frame 2. This means that the particle becomes less stable around the event of the layer jump. Afterwards, the potential energy decreases and the particle becomes more stable again. It can be seen in Figure 6.6e that for the model corresponding to frame 4, the layer (in pink) is not in exact agreement with the original plane (frame 1 and 2) and deviates from a perfect (010) facet. In frame 5, however, the facet is recovered, and the potential energy decreases. Our 3D models indicate that the process of layer jumping cannot be simply considered as a reversible rigid displacement of an entire facet. Indeed, there is a significant change in the surface structure and sites (e.g. frame 3 and 4).

The methodology that is presented here enables direct description of dynamic changes in the 3D atomic structure in a quantitative manner, at high temperature. Moreover, it is clear from the experiments that events such as layer jumping are accompanied by intermediate disordered structures with higher potential energies, which may have an influence on the catalytic activity of the particle. The results can be regarded as realistic 3D input structures and can directly be used as an input for further simulation studies to connect the structure of these catalytic nanoparticles to their activity. The method used in the present work could eventually be ex-

tended to a gaseous environment, which will enable real-time 3D characterisations for *in situ* and *operando* catalytic reactions.
In conclusion, by combining atom-counting using the hidden Markov model with MD relaxation, the surface dynamics, including atomic layer jumping, which is most likely driven by surface atom diffusion, of a supported Au nanoparticle at elevated temperature could be investigated in 3D at atomic resolution.

6.6 Multiple transition matrices

So far, we have assumed that the experimental conditions driving the structural changes, such as electron irradiation, temperature or gas flow, are time-invariant. In such cases, the hidden Markov model summarises all structural changes in one transition matrix $\mathbf{A}$. In order to incorporate nanomaterials in real applications, a fundamental understanding of the mechanisms behind atomic structure evolutions under variable environmental conditions is of crucial importance. We therefore need to test whether the method presented here can be used to reliably quantify, for example, changes during reduction and oxidation reactions. To this purpose, we will look at the atomic structure of a Pt catalyst nanoparticle, shown in Figure 6.8a, previously studied in an alternating hydrogen (H_2) and oxygen (O_2) flow using the existing state-of-the-art atom-counting procedure for single ADF STEM images [Altantzis 2019]. During the gas flow experiment, the Pt nanoparticle changes from a facetted to a round morphology and vice versa. Therefore, the underlying transition probabilities are not the same for each frame transition. In fact, two alternating transition matrices can be recognised, as illustrated in Figure 6.8a. In this section, we examine the effect on the quantification when we nonetheless assume one transition matrix during the estimation procedure.
To this purpose, we created a hypothetical time series with $T = 10$ frames, based on the atom-counts that were previously quantified from the single ADF STEM images of a catalyst Pt nanoparticle in an H_2 and O_2 environment [Altantzis 2019]. The initial probabilities ι_g are set equal to the mixing proportions quantified previously for the Pt nanoparticle in an H_2 environment. A direct Markov chain analysis of a transition from the atom-counts previously quantified for the Pt nanoparticle in an H_2 environment to the atom-counts quantified in the O_2 environment yields the transition matrix for the first process $\mathbf{A}_{H_2 \to O_2}$, shown in Figure 6.8b. Figure 6.8c shows the transition matrix for the inverse process $\mathbf{A}_{O_2 \to H_2}$. Note that Figure 6.8b clearly shows non-zero probabilities for transitions of 0 atoms to multiple atoms, which indicate the appearance of extra atomic columns during the transition from a facetted to a round morphology. The frame transitions of the state sequence are then generated alternately from the two transition matrices $\mathbf{A}_{H_2 \to O_2}$ and $\mathbf{A}_{O_2 \to H_2}$. The number of atoms in an atomic column ranges between 0 and $G = 26$, and the total number of atomic columns analysed in each frame is $N = 2457$. The observed sequence of scattering cross sections is created using a Gaussian emission probability with average scattering cross sections equal to the Pt library values $\mathcal{M}_g$ previously also used in the simulations in Sections 5.5 and 6.2. The relative width of the Gaussian emission probability is $\sigma/\delta = 0.1$ and 0.7, which corresponds approximately to an electron dose of respectively 10^5 $e^-/Å^2$ and 2×10^3 $e^-/Å^2$ per frame, assuming Poisson noise only. These parameters are also summarised in Table B.2 of Appendix B. At each noise level σ/δ, 50 noise realisations of the observed sequence have been analysed. The hidden Markov model analysis is performed assuming a maximum thickness of $G = 30$ atoms. Figure 6.8d shows the transition matrix estimated from a time series with $\sigma/\delta = 0.1$ by the hidden Markov model which assumes only one transition matrix during the time series. This estimated transition matrix for the time series with alternating structural changes is close to the average of both

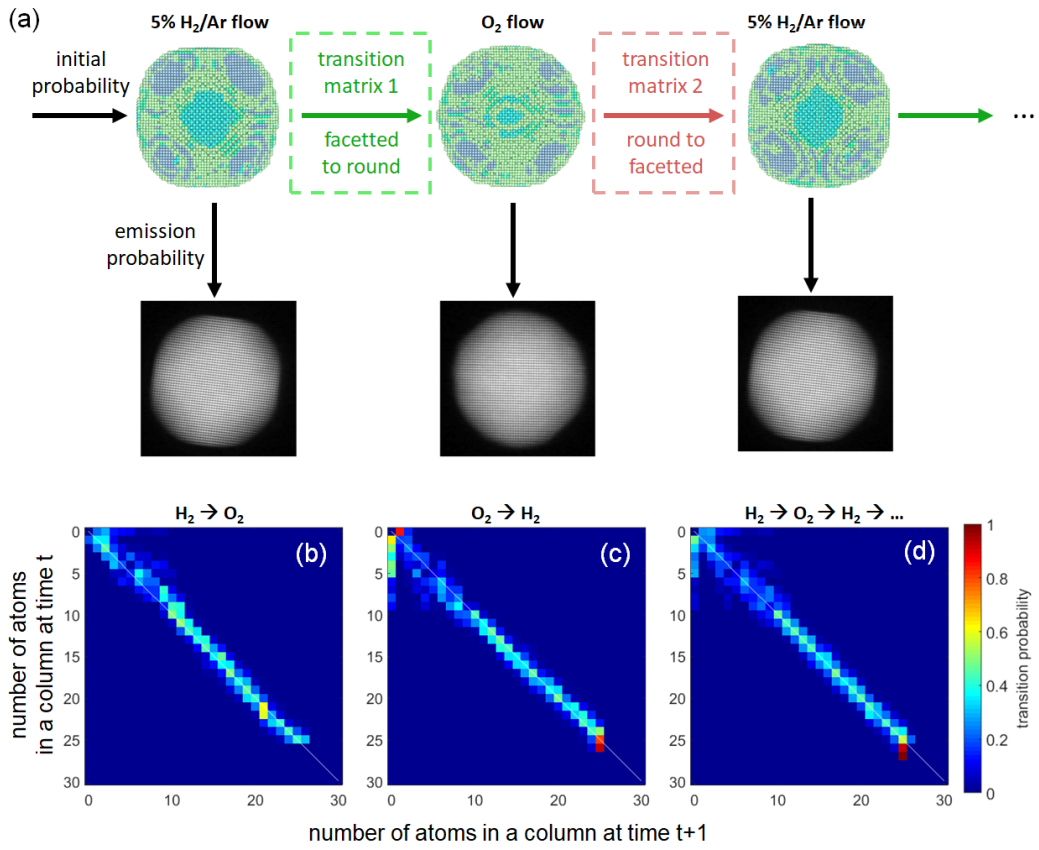

Figure 6.8: *(a) A Pt catalyst nanoparticle in an alternating hydrogen and oxygen flow changes morphology from facetted to round and vice versa, analysed previously using single frame atom-counting [Altantzis 2019]. These structural changes can be described by alternating transition matrices. (b-c) Transition matrices 1 & 2, estimated from the atom-counts previously quantified in [Altantzis 2019] using a direct Markov chain analysis for the changes from facetted to round morphology and vice versa respectively. (d) Transition matrix estimated using a hidden Markov model assuming only one transition matrix from a hypothetical time series corresponding to a Pt nanoparticle with alternating facetted and round morphology with* $\sigma/\delta = 0.1$.

underlying transition matrices ($\mathbf{A}_{\mathrm{H_2}\rightarrow\mathrm{O_2}}$ and $\mathbf{A}_{\mathrm{O_2}\rightarrow\mathrm{H_2}}$, shown in Figure 6.8b and 6.8c), weighted with the number of times a frame transition occurred driven by each type of transition matrix (5 and 4 times respectively, in case of this time series with 10 frames and alternating gaseous environment). The percentages of correctly counted atomic columns for the different time series are summarised in the first two columns of Table 6.2 using 95% confidence intervals obtained from the 50 noise realisations. Next, we compare these results to the performance discussed in Section 5.5. The analysis shown in Figures 5.4 and 5.5 yields $(99.99 \pm 0.01)\%$ and $(64.66 \pm 0.67)\%$ correctly counted atomic columns for $T = 10$ at $\sigma/\delta = 0.1$ and 0.7 respectively. From Table 6.2, it follows that the performance for atom-counting from a time series with two underlying transition matrices using the hidden Markov model as described in this thesis remains unaffected for low enough σ/δ, corresponding to high enough electron doses. However, at higher σ/δ, or equivalently at lower electron doses, the performance is slightly worse as compared to atom-counting from a time series with only one underlying transition matrix, as discerning between noise and structural changes becomes more challenging. Nonetheless, the hidden Markov model, with $(58.00 \pm 0.78)\%$ correctly counted atomic columns as summarised in Table

6.2, still outperforms the collective hybrid analysis, which reached only (51.44 ± 0.82)% correctly counted atomic columns for $T = 10$ and $\sigma/\delta = 0.7$, as shown in Figure 5.4. We conclude that at high electron doses the assumption of a constant transition matrix does not pose any restrictions for applying the hidden Markov model for counting the number of atoms in a time series of ADF STEM images of an *in situ* experiment with strongly alternating environmental conditions. When the electron dose is lower, the performance for atom-counting decreases, but nonetheless reasonably reliable counting results can still be obtained.

	correct atom-counts (%)	$P_{H_2 \to O_2}$ (%)	$P_{O_2 \to H_2}$ (%)
expected value		70.09	64.20
$\sigma/\delta = 0.1$ (95% CI)	[99.99; 100.00]	[69.65; 70.08]	[63.92; 64.29]
$\sigma/\delta = 0.7$ (95% CI)	[57.28; 58.72]	[65.87; 68.37]	[64.85; 67.17]

Table 6.2: *Performance for atom-counting and accuracy of the estimated probability of structural changes P for the two processes of the variable gas flow illustrated in Figure 6.8.*

One should however be careful when interpreting the transition probabilities in terms of physical cross sections in the same manner as discussed in Section 6.2. In order to estimate physical cross sections related to the two separate processes, we analyse the estimated atom-counts of the time series as a Markov chain with two transition matrices. The probabilities of structural changes for both processes can then be estimated from these two transition matrices, similarly to the approach discussed in Section 6.2. The counting results obtained from this analysis can be regarded as a Markov chain. Because we know which process drives the structural changes at each of the transitions, we are able to estimate a Markov chain with two transition matrices $\mathbf{A}_1$ and $\mathbf{A}_2$, instead of one. We can again derive a probability of structural changes from each transition matrix, according to Equations (6.5) and (6.6):

$$P_1 = \frac{\sum_{g=0}^{G} \pi_g^{[1]}(1 - [\mathbf{A}_1]_{gg})}{G+1}, \tag{6.5}$$

$$P_2 = \frac{\sum_{g=0}^{G} \pi_g^{[2]}(1 - [\mathbf{A}_2]_{gg})}{G+1}. \tag{6.6}$$

In this expression, the weights $\pi_g^{[x]}$, with $x = 1, 2$, are determined by which type of transition occurs from frame to frame:

$$\pi_g^{[x]} = \frac{1}{T_x} \sum_{t \in \mathcal{T}_x} \pi_g^{(t)}, \tag{6.7}$$

with $\mathcal{T}_x$ the set of T_x frames that change to the next frame according to transition matrix $\mathbf{A}_x$, with $x = 1, 2$. In this expression, $\pi_g^{(t)}$ remains the same, as defined by Equation (5.11).
The probabilities of structural changes $P_{H_2 \to O_2}$ and $P_{O_2 \to H_2}$ estimated in this manner from the hypothetical time series discussed above are summarised in the last two columns of Table 6.2 using 95% confidence intervals on the mean estimated value, together with the expected values. The expected probabilities of structural changes $P_{H_2 \to O_2}$ and $P_{O_2 \to H_2}$ are estimated using Equation (6.1) from the transition matrices $\mathbf{A}_{\mathrm{H_2 \to O_2}}$ and $\mathbf{A}_{\mathrm{O_2 \to H_2}}$ obtained from the previously quantified counting results, shown in Figure 6.8b and 6.8c. At a low noise level σ/δ, the hidden Markov model accurately estimates the probabilities of structural changes for both processes. When the noise increases, the estimated probabilities are slightly inaccurate, as it becomes more difficult to separate structural changes from noise fluctuations. These results show that through post-processing of the results obtained from the hidden Markov model analysis, probabilities of structural changes and even cross sections can still be quantified for the different

physical processes causing structural changes during a time series with alternating environmental conditions.
We can now go a step further, and consider more than two transition matrices. In order to test the performance for atom-counting of the hidden Markov model analysis for, for example, an *in situ* heating experiment where the temperature is increased gradually, we simulated a hypothetical observed sequence of scattering cross sections. The observed sequence is generated from a state sequence corresponding to $T = 22$ frames. The initial probabilities ι_g are uniformly distributed. The number of atoms in an atomic column ranges between 0 and $G = 10$, and the total number of atomic columns analysed in each frame is $N = 100$. The observed sequence of scattering cross sections is created using a Gaussian emission probability with average scattering cross sections equal to the same Pt library values $\mathcal{M}_g$ used in the previous example discussed in this section. The relative width of the Gaussian emission probability is $\sigma/\delta = 0.3$ and 0.7. The transition matrix that describes the structural changes in the state sequence is changed at each frame transition. At each transition from frame to frame, a transition matrix with a Gaussian spread around the diagonal is used, each time with an increasing value for the FWHM, in order to mimic the increasing mobility of the atoms in the nanostructure when the temperature increases. The transition matrices used for this simulation are shown in Figure B.7 of Appendix B. The parameters for this simulation study are also summarised in Table B.2 of Appendix B. At a low and high noise level ($\sigma/\delta = 0.3$ and 0.7), we obtain a percentage of respectively 93.6% and 60.8% correctly counted atomic columns during the time series. This performance is close to the results shown previously in Figure 5.4, where at $T = 22$ the respective obtained percentages of correct atom-counts are $(94.34 \pm 0.13)\%$ and $(68.00 \pm 0.41)\%$. This implies that we can still obtain reasonably reliable counting results from a time series with non-constant underlying transition matrix.
In conclusion, it is possible to use the existing framework of hidden Markov model for atom-counting when the underlying driving process is non-constant. This opens up possibilities for the analysis of *in situ* heating or gas flow experiments.

6.7 Conclusions

In this chapter, we have discussed applications of the hidden Markov model for atom-counting from time series of ADF STEM images, introduced in Chapter 5, for measuring dynamic structural changes at the atomic scale. We show that the transition probabilities can be used to determine the probability of structural changes from one frame to the next during the time series. We validated that intensity variations during the time series that result from structural changes are estimated by the transition matrix, while noise fluctuations are estimated by the width of the Gaussian emission probability. When the probability of structural changes is small, this is valid for all noise levels. When the probability of structural changes is larger, the separation of noise and structural changes can still be performed reasonably well, although slight inaccuracies arise when the electron dose is lowered, making it more difficult to discern the origin of the fluctuations in the scattering cross sections from frame to frame.
We could therefore reliably quantify the probability of structural changes for an experimental ADF STEM time series of a Pt wedge using the hidden Markov model analysis. For this Pt wedge, the structural changes occur due to beam-induced surface diffusion. From the probability of structural changes, we can therefore quantify the cross section for surface diffusion, and its corresponding threshold energy for surface diffusion. We conclude that the cross section for surface diffusion is inherently underestimated by the hidden Markov model as compared to the expected theoretical value, since the estimated transition probabilities describe net structural

changes from frame to frame. These net structural changes can be the result of multiple hops of atoms, potentially in opposite directions, yielding a smaller amount of net changes after the frame is acquired as compared to the actual amount of structural changes. Nonetheless, we can provide a reasonable lower bound for the cross section related to surface diffusion, since this methodology gets a closer match with the theory as compared to the current state-of-the-art analysis of variance method [Van Aert 2019]. The hidden Markov model is therefore a promising approach for the reliable quantification of physical cross sections from experimental ADF STEM time series.

Next, we discussed the application of the hidden Markov model for an experimental ADF STEM time series of a Pt nanoparticle with catalytic properties. The analysis of the catalyst Pt nanoparticle reveals that the particle gradually loses its facetted morphology, due to beam-induced surface diffusion. We also estimated a cross section for surface diffusion for this nanoparticle. The value includes the contributions of different migration mechanisms, such as hopping, atomic exchange, and vacancy diffusion, and from different types of surfaces. The cross section for structural changes is therefore of great importance in order to unravel dominant mechanisms and surfaces in the diffusion process and to gain new insights in surface related phenomena such as catalysis and nanoparticle growth.

Then, the analysis of a thermal catalyst Au nanoparticle was discussed. The atom-counting results, obtained using the hidden Markov model analysis of this supported Au nanoparticle at elevated temperature, are combined with a molecular dynamics relaxation. This allows us to study the surface dynamics in 3D. The catalytic properties of this thermal catalyst are related to the facets and surface dynamics. Our quantification reveals that the process of layer jumping, which was also studied previously for this type of nanoparticles, cannot be simply considered as a reversible rigid displacement of an entire facet. Indeed, there is a significant change in the surface structure and sites.

The frames of the Au nanoparticle time series were all acquired at the same elevated temperature during an *in situ* heating experiment. In the last part of this chapter, we also consider the possibility of *in situ* experiments with variable environmental conditions such as a gradually increasing temperature or an alternating gas flow. Therefore, we consider a hypothetical time series generated using two transition matrices based on an alternating gas flow experiment, where a Pt nanoparticle was previously shown to change from a round to a facetted morphology and vice versa. We show that, even when the structural changes are caused by two transition matrices, we can still reliably count the number of atoms without alterations to the parameter estimation of the hidden Markov model. We even show that reliable counting is possible when the transition matrix changes for each frame transition during the time series, for example during a heating experiment where the temperature is increased in steps. We should however quantify the probability of structural changes with caution. If we know when the environmental conditions change, it is nonetheless possible to estimate the probabilities of structural changes and even cross sections for the different physical processes causing structural changes during a time series with alternating environmental conditions. This can be achieved through post-processing of the results obtained from the hidden Markov model analysis. In conclusion, it is possible to use the hidden Markov model presented in this thesis for atom-counting when the underlying driving process is non-constant. This opens up possibilities for the analysis of *in situ* heating or gas flow experiments.

In general, we have shown that the hidden Markov model allows us to obtain more reliable counting results from a time series of ADF STEM images as compared to the existing single frame counting procedures thanks to the explicit modelling of the structural changes using the

transition probabilities. The hidden Markov model even allows us to quantify the probability of structural changes and relate it to a dose independent cross section related to the physical process(es) that cause the changes during the time series. As such, the hidden Markov model for atom-counting is promising for revealing and quantifying the atomic structure when it evolves over time via adatom dynamics, surface diffusion, beam effects or during *in situ* experiments.

7

General conclusions and future perspectives

The goal of the research presented in this thesis was to develop model-based quantitative techniques to reliably measure dynamic structural changes at the atomic scale from a time series of annular dark field scanning transmission electron microscopy (ADF STEM) images. In order to achieve this goal, advanced atom-counting procedures for single frames and for time series have been proposed. To this purpose, statistical parameter estimation theory and image simulations were used extensively and intertwined to develop truly hybrid approaches.

As a starting point, the ADF STEM image intensities are quantified using a parametric imaging model. The intensities of atomic resolution ADF STEM images are peaked at the atomic column positions and sensitive to the chemical content and thickness of the nanomaterial. By estimating the parameters of a model with superimposed two-dimensional (2D) Gaussian peaks, the atomic column positions and the so-called scattering cross sections of the atomic columns can be estimated. The scattering cross section quantifies the total intensity of electrons scattered towards the annular detector from an atomic column and can be estimated as the volume of the Gaussian peaks in the parametric imaging model. The scattering cross sections of a monatomic crystalline nanomaterial increase monotonically with the number of atoms in the atomic column, making them particularly suitable for atom-counting.

The use of the parametric imaging model for the quantification of ADF STEM image intensities has therefore become a recognised approach in quantitative electron microscopy of nanomaterials oriented along a main zone axis. However, in the presence of sample tilt away from a zone axis orientation, an elongation of the intensity scattered from the atomic columns is observed in the ADF STEM images. Therefore, in our experience, an often posed research question in the quantitative STEM community is whether elliptical Gaussians should be used, rather than symmetrical Gaussians. In this thesis, we provide an answer to this question by implementing a parametric imaging model that consists of superimposed 2D elliptical, rather than symmetrical, Gaussian peaks. The parameters of this model are estimated in a least squares sense, and the possibilities and limitations of the model are quantitatively studied, using ADF STEM image simulations of platinum (Pt) nanocrystals at various amounts of sample tilt. The residual intensities after fitting the elliptical model to the ADF STEM image of the tilted nanocrystal are indeed significantly smaller as compared to the residual intensities after the fit with the

symmetrical model. A benefit of the elliptical model is that it allows us to quantify the elongation of the atomic columns and the angle of the elongation. The angle quantifies the direction of sample tilt, while the elongation is strongly related to the amount of sample tilt. However, the accuracy of the estimated atomic column positions and scattering cross sections can not be improved upon by the elliptical model as compared to the symmetrical model. Furthermore, the parameter space is larger, which generally leads to less precise parameter estimation. Therefore, our recommendation for a reliable quantification of ADF STEM image intensities is the use of the freely available StatSTEM software package which efficiently implements the parametric model that consists of superimposed 2D symmetrical Gaussian peaks, even in the presence of small amounts of sample tilt away from a main zone axis orientation.

Two approaches for atom-counting based on the scattering cross sections have been developed prior to the research presented in this thesis, based either only on image simulations or only on statistical parameter estimation theory. In the image simulations-based approach, the scattering cross sections of the atomic columns estimated from the experimental ADF STEM image are directly compared to a so-called library of scattering cross sections obtained from image simulations performed at different thicknesses. This simulations-based method is very simple and intuitive. However, the accuracy of the atom-counts critically depends on potentially undetected mismatches between experiment and simulations. The statistics-based method on the other hand, is independent of image simulations, and takes the inherently random nature of the scattering cross sections into consideration. An important advantage of this method is the possibility to quantify the precision of the atom-counting results. However, this method also has its limitations. Specifically, the performance of the statistics-based method for atom-counting is highly sensitive to small nanoparticles and low electron doses, leading to fewer data points per thickness and high noise levels respectively.

In order to overcome the limitations of these two existing procedures for atom-counting, we have introduced a so-called hybrid statistics-simulations based method for atom-counting. In this method, prior knowledge from image simulations is directly incorporated into the statistical framework by including the library values in the statistical model. Small undetected mismatches between simulated and experimental microscope/sample parameters, such as detector inner angle or sample tilt, can easily occur. The effect of such a mismatch on the scattering cross sections can be described by a linear scaling. Therefore, the hybrid method estimates the average scattering cross sections equal to the scaled library values, where the scaling parameter is estimated to account for any possible mismatch between experiment and simulations. As a result, the atom-counting procedure becomes more robust and atom-counting can be performed reliably at lower electron doses. In this manner, the hybrid method opens up possibilities for the quantitative analysis of truly beam-sensitive nanomaterials.

Indeed, we have shown in this thesis that the hybrid method for atom-counting outperforms the current state-of-the-art statistics-based atom-counting method. Simulations show that a lower electron dose is required to reach the same level of accuracy for the counting results. The counting procedure is validated using a high dose experimental ADF STEM image of a stable gold (Au) nanorod. Next, simulated ADF STEM images of a Pt nanoparticle at various tilt angles are analysed. Reliable atom-counting remains possible, owing to the linear scaling parameter of the hybrid method that can account for the sample tilt. Finally, reliable counting results could be obtained from a low dose experimental ADF STEM image of a platinum-iridium (Pt/Ir) nanoparticle for which this was not feasible using the statistics-based method. Using a simulation based on this low dose experimental ADF STEM image, the capabilities of the hybrid method are demonstrated for the analysis of images recorded using even lower

electron doses.
It is important to note that there is a fundamental difference between the hybrid statistics-simulations based atom-counting method presented in this thesis, and the previously used combination of the statistics-based atom-counting method, validated using the library obtained from image simulations. By incorporating the prior knowledge from image simulations directly into the statistical framework, this approach is more robust, and atom-counting is directly put on an absolute scale. In this manner, unravelling the relation between estimated components of the probability distribution of the scattering cross sections and the number of atoms is straightforward, which is highly useful in order to realise atom-counting from a time series.

In order to extend the atom-counting procedure from a single ADF STEM image to a time series, we have introduced the so-called hidden Markov model in the field of electron microscopy. In this model, two layers can be recognised: a "hidden" state sequence, and an observed sequence. In the case of atom-counting, the hidden states correspond to the number of atoms in each atomic column in each frame of the time series. Those states are only indirectly observed via the scattering cross sections estimated from the ADF STEM images. In fact, when only one frame is considered, this method is equivalent to the hybrid statistics-simulations based atom-counting procedure. During a time series of ADF STEM images, the atomic structure can change from frame to frame. This can be modelled explicitly using the so-called transition probabilities, summarised by the transition matrix. The transition probabilities summarise the probability that an atomic column gains or loses atoms from one frame to the next during the time series. Estimating the transition matrix is the key to the improved performance for atom-counting achieved by the hidden Markov model as compared to the hybrid method. As a consequence, the performance of the hidden Markov model further improves when the length of the time series increases.
Additionally, the probability that the atomic structure changes from one frame to the next during the time series can be derived from the transition matrix. Indeed, the hidden Markov model allows to reliably distinguish between intensity fluctuations caused by structural changes and noise fluctuations. The probability of structural changes can therefore be used to reliably characterise the dynamic changes in the time series. Taking into account the electron dose, the cross section related to structural changes can be derived from the probability of structural changes. Two experimental examples were discussed for which a cross section related to structural changes could be quantified, a Pt catalyst nanoparticle and a Pt wedge. The structural changes for these two experimental time series could be attributed to surface diffusion. Sputtering, i.e. the removal of atoms from the sample, could be excluded based on the incident electron energy. In this manner, a cross section for surface diffusion could be quantified. In case of the Pt nanoparticle, this cross section for surface diffusion includes the contributions from different surface orientations. For the Pt wedge, only one surface orientation is present, and the cross section for surface diffusion estimated from the Pt wedge can be compared to the theoretical value. In this manner, a close agreement with the expected theoretical cross section and threshold energy for surface diffusion is found. In the presence of sputtering, the probability of structural changes can not be related directly to a threshold energy for surface diffusion, as an interplay of various dynamic processes determines the atomic structural changes. The probability of structural changes in this case summarises the joint effect of sputtering and surface diffusion, and can be used to unravel dominant mechanisms and surfaces in dynamic processes such as the diffusion process and to gain new insights in surface related phenomena such as catalysis and nanoparticle growth.
Owing to the improved reliability for atom-counting of the hidden Markov model, a reliable 3D

atomic structural characterisation for an experimental time series of an *in situ* heated supported catalytic Au nanoparticle could be obtained by combining the (2D) time series counting results with a molecular dynamics relaxation. In this manner, the facets and surface dynamics of a thermal catalyst could be quantified in three dimensions (3D). As a next step, using a simulations study, we advance towards the application of the hidden Markov model to *in situ* experiments with variable environmental conditions such as a gradually increasing temperature or an alternating gas flow. Although caution is advised upon attributing a physical interpretation to the estimated transition probabilities, we show that it is indeed possible to use the hidden Markov model when the underlying process that causes the dynamic structural changes is non-constant. This opens up possibilities for the analysis of *in situ* heating or gas flow experiments. In summary, the hidden Markov model for atom-counting is promising for revealing and quantifying the atomic structure when it evolves over time via adatom dynamics, surface diffusion, beam effects or during *in situ* experiments.

The quantitative methods presented in this thesis can be applied to a range of monatomic nanomaterials. In future work, it would be interesting to extend this framework to the quantification of dynamic structural changes in heterogeneous nanomaterials as well. At present, only a simulations-based method for atom-counting from heterogeneous nanomaterials exists [van den Bos 2016, van den Bos 2019]. This method is based on a direct comparison of the experimental and simulated scattering cross sections. To this purpose, the so-called lensing model was introduced to enable efficient simulations of scattering cross sections for all possible combinations of mixed atomic columns. In a sense, this set of simulated scattering cross sections is a heterogeneous library, which could be included in the statistical framework of the hidden Markov model. The hidden states in this case correspond to the total number of the atomic columns and the different types of each atom in the atomic column. In this manner, the parameter space is increased tremendously. Therefore, the combination with multiple detectors and/or spectroscopic information is envisaged, in order to increase the available dataset as well. Scattering cross sections for two different types of atomic columns that are highly similar in HAADF STEM can, for example, differ significantly in LAADF STEM. Using the principles of optimal experimental design, the ideal detector settings can be extracted from a 4D STEM dataset in order to correctly unravel the set of scattering cross sections. Furthermore, scattering cross sections estimated from EDX and EELS can be used to unravel the types of atoms present in the atomic columns. In this manner, the hidden Markov model for atom-counting could be extended to the reliable measurement of dynamic structural changes in heterogeneous nanomaterials.

In order to estimate the 3D atomic structure, based on the 2D atom-counting results, a structural relaxation method can be used. In this thesis, the counting results were combined with molecular dynamics, and very recently, counting results obtained using the hidden Markov model have been combined with a Bayesian genetic algorithm [De Backer 2021c]. As a next step, the hidden Markov model could be generalised such that the hidden states correspond to the 3D atomic structure, and can be inferred directly from the ADF STEM images, circumventing the intermediate 2D counting results altogether. In this case, factorising the hidden states over the atomic columns will no longer be possible, leading to a highly complex state space. This might be beyond the scope of the hidden Markov model, but could quite possibly be achieved using artificial neural networks. In this case, the training dataset could be constructed using the two-step process of atom-counting and then relaxing the structure. Alternatively, 3D atomic structures and corresponding image simulations can be used to train the artificial neural network directly.

Indeed, artificial neural networks are a highly interesting approach in order to develop fast quantitative methods. After training, neural networks are simply matrix multiplications, which can be performed (close to) real-time. Real-time quantification of the atomic structure, in parallel with the acquisition of experimental time series, can guide the experiment in order to study dynamic processes in a controlled manner, with optimal distribution of the electron dose over the time series. This opens up opportunities for the reliable quantification of extremely noisy images, for example, due to the low electron dose required for truly beam-sensitive nanostructures or due to a gaseous or liquid environment during *in situ* experiments. Furthermore, it would make quantitative electron microscopy more easily accessible for a wide range of applications, pushing the field of materials science towards materials design.

In this thesis, we have progressed towards this ultimate goal of reliable and fast quantitative electron microscopy. As a general conclusion, the interwoven combination of statistical parameter estimation theory and careful image simulations allows to accurately and precisely quantify the atomic structure for (monatomic) nanocrystalline materials. The inclusion of image simulations in a statistical framework allows us to exceed the limitations of independent statistics- or image simulations-based methods, while retaining an estimate for the accuracy and precision of the quantitative results. In this manner, the reliable quantification of atomic scale structural changes even becomes possible.

Appendix A: Image simulation parameters

The parameters of the image simulations I performed in Sections 3.3 and 4.7 are summarised respectively in Tables A.1 and A.2. Multislice simulations were performed using MULTEM [Lobato 2014, Lobato 2015, Lobato 2016], as described in Section 2.3.

Parameter	**Value**
Acceleration voltage	300 kV
Spherical aberration C_s	1 nm
Defocus C_1	14.03Å
Zero defocus reference plane	10.82Å
Specimen thickness	6 & 18 unit cells (16.64Å & 49.92Å)
Simulation box size (xy)	50×50Å^2
Probe convergence angle α	21 mrad
Annular detector inner angle	70 mrad
Annular detector outer angle	180 mrad
Number of phonon configurations	50
Spatial incoherence of source FWHM	1Å
Pixel size of simulated image	0.10Å
Pixel size to sample atomic potential	0.046Å
Pixel size to sample reciprocal space	0.02Å^{-1}
Maximum reciprocal lattice vector	10.8 Å^{-1}
Slice thickness	1.39Å
Debye-Waller factor	0.5705Å^2 [Gao 1999]
Zone axis	[110]
Tilt axis	[1$\bar{1}$0]
Rotation center	center of mass

Table A.1: *Parameters used for the multislice simulations of the Pt(110) nanocrystal discussed in Section 3.3.*

Parameter	Value
Acceleration voltage	200 kV
Spherical aberration C_s	0 nm
Defocus C_1	0Å
Zero defocus reference plane	17.83Å
Specimen thickness	23.58Å
Simulation box size	$50.09 \times 50.11 \times 35.66$Å^3
Probe convergence angle α	22.48 mrad
Annular detector inner angle	51.73 mrad
Annular detector outer angle	248.41 mrad
Number of phonon configurations	30
Spatial incoherence of source FWHM	1Å
Pixel size of simulated image	0.125Å
Pixel size to sample atomic potential	0.039Å
Pixel size to sample reciprocal space	0.02Å^{-1}
Maximum reciprocal lattice vector	12.77 Å^{-1}
Slice thickness	1.39Å
Debye-Waller factor	0.3836Å^2 [Gao 1999]
Zone axis	[110]
Tilt axis	[1$\bar{1}$0]
Rotation center	center of mass

Table A.2: *Parameters used for the multislice simulations of the Pt nanoparticle in Figure 4.6.*

Appendix B: Supplemental tables & figures

	Value		
Parameter	**Figure 5.4**	**Figure 5.5**	**Figure 5.6**
T	1 to 40	1, 2, 5, 10, 20	10
N	100	$1000/T$	60
G	10	10	6
ι_g	uniform	uniform	uniform
A_{jg}	Gauss diagonal (FWHM=1.5)	Gauss diagonal (FWHM=1.5)	Gauss diagonal (FWHM=1.5)
a	1	1	1
$\mathcal{M}_g$	Pt(110)	Pt(110)	Pt(110)
σ/δ	0.3 and 0.7	0.3 and 0.7	0.7

Table B.1: *Parameters of the hypothetical hidden Markov models used to obtain the results from Figures 5.4, 5.5 and 5.6 in Section 5.5.*

	Value	
Parameter	**2 A's**	**gradually changing A's**
T	10	22
N	2457	100
G	26	10
ι_g	estimated from atom-counts in H_2 [Altantzis 2019]	uniform
A_{jg}	estimated from atom-counts for $H_2 \rightarrow O_2$ and $O_2 \rightarrow H_2$ [Altantzis 2019]	Gauss diagonal FWHM = 1 to 3
a	1	1
$\mathcal{M}_g$	Pt(110)	Pt(110)
σ/δ	0.1 and 0.7	0.3 and 0.7

Table B.2: *Parameters of the hypothetical hidden Markov models used to study the effect of two transition matrices and of gradually changing transition matrices in Section 6.6.*

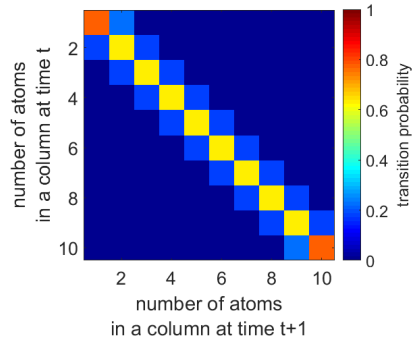

Figure B.1: *Transition matrix with a Gaussian spread around the diagonal with FWHM = 1.5 used in Section 5.5.*

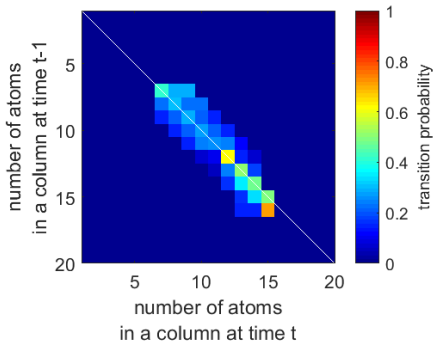

Figure B.2: *More diffuse transition matrix, based on the estimated transition matrix for the Pt wedge time series, used to obtain the results in Table 6.1 of Section 6.2.*

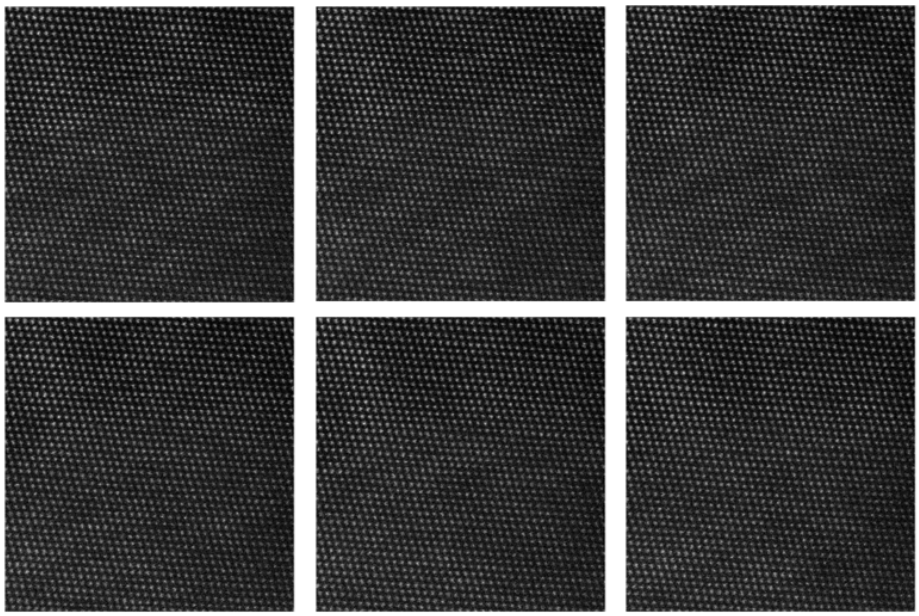

Figure B.3: *ADF STEM images of the time series of the Pt wedge discussed in Section 6.2.*

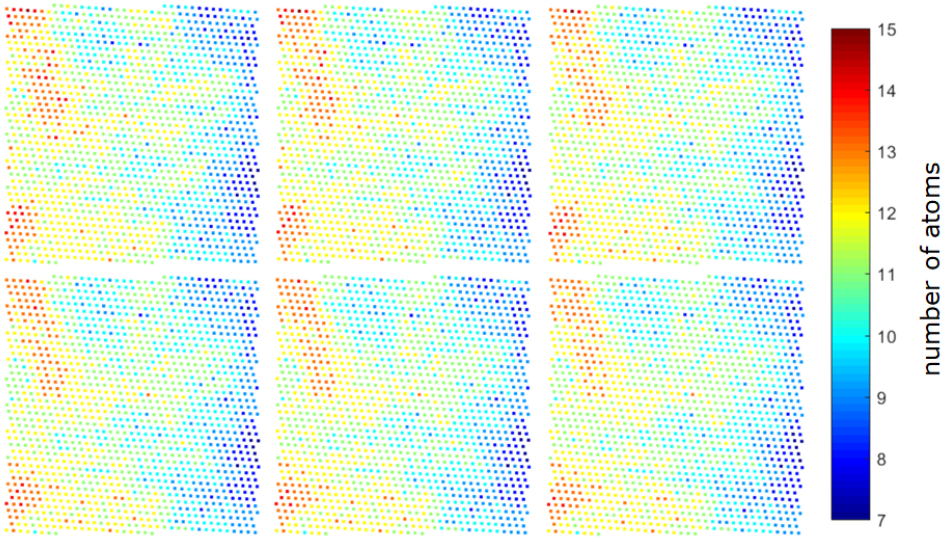

Figure B.4: *Counting results obtained by the hidden Markov model analysis of the time series of Figure B.3.*

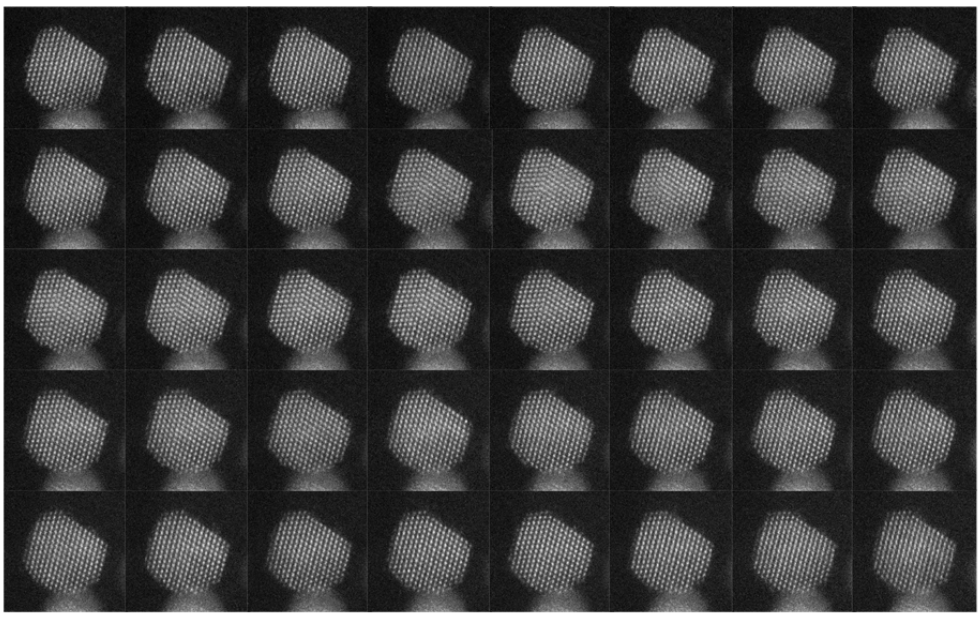

Figure B.5: *Experimental ADF STEM time series recorded of the Pt nanoparticle discussed in Section 6.4. Time progresses along the rows.*

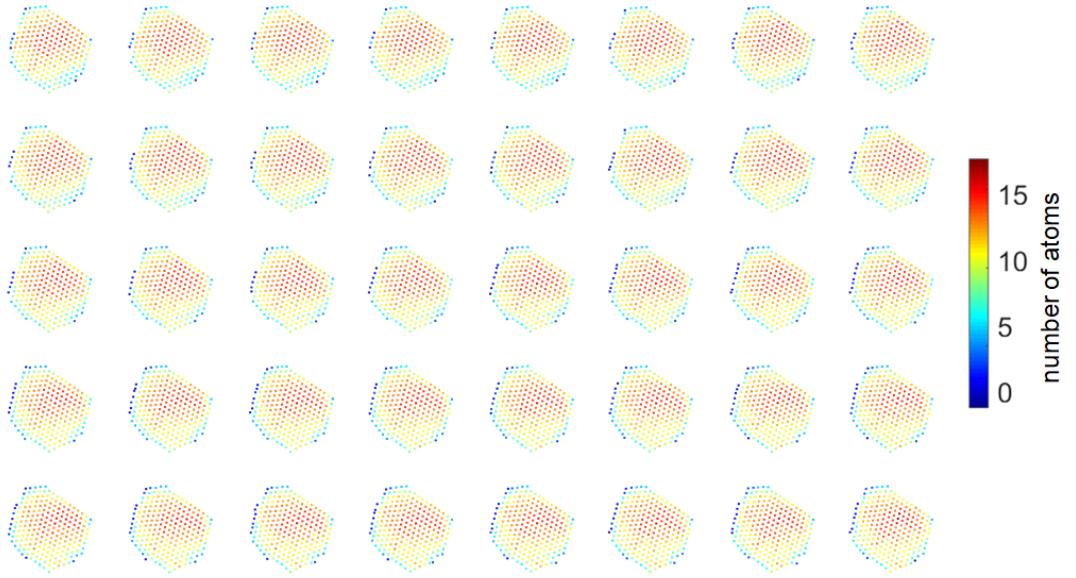

Figure B.6: *Counting results obtained by the hidden Markov model for the time series from Figure B.5.*

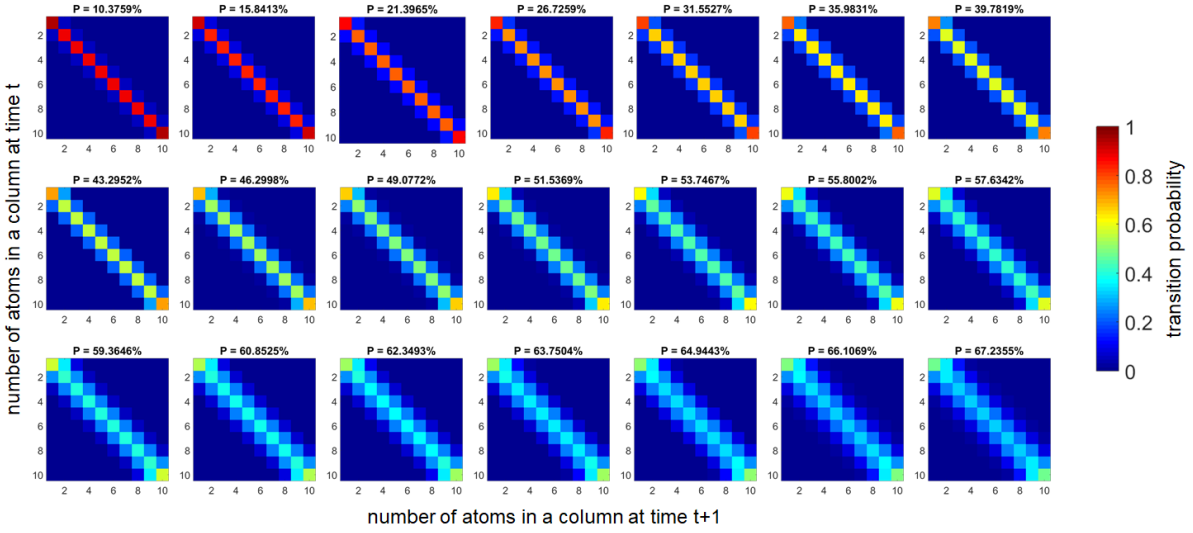

Figure B.7: *Transition matrices with a Gaussian spread around the diagonal with an increasing value for the FWHM (1 to 3, in steps of 0.1), and therefore an increasing probability of structural changes P, discussed in Section 6.6.*

Bibliography

[Aarons 2017] J. Aarons, L. Jones, A. Varambhia, K.E. MacArthur, D. Ozkaya, M. Sarwar, C.-K. Skylaris, and P.D. Nellist. *Predicting the Oxygen-Binding Properties of Platinum Nanoparticle Ensembles by Combining High-Precision Electron Microscopy and Density Functional Theory*. Nano Letters, vol. 17, 4003–4012, 2017.

[Abrams 2021] S. Abrams, J. Wambua, E. Santermans, L. Willem, E. Kuylen, P. Coletti, P. Libin, C. Faes, O. Petrof, S.A. Herzog, P. Beutels, and N. Hens. *Modelling the early phase of the Belgian COVID-19 epidemic using astochastic compartmental model and studying its implied future trajectories*. Epidemics, vol. 35, 100449, 2021.

[Agard 2014] D. Agard, Y. Cheng, R.M. Glaeser, and S. Subramaniam. *Chapter Two - Single-Particle Cryo-Electron Microscopy (Cryo-EM): Progress, Challenges, and Perspectives for Further Improvement*. Advances in Imaging and Electron Physics, vol. 185, 113–137, 2014.

[Akashi 2015] T. Akashi, Y. Takahashi, T. Tanigaki, T. Shimakura, T. Kawasaki, T. Furutsu, H. Shinada, H. Müller, M. Haider, N. Osakabe, and A. Tonomura. *Aberration corrected 1.2-MV cold field-emission transmission electron microscope with a sub-50-pm resolution*. Applied Physics Letters, vol. 49, 074101, 2015.

[Alania 2017] M. Alania. *Quantification of 3D atomic positions for nanoparticles using scanning transmission electron microscopy: statistical parameter estimation, dose-limited precision and optimal experimental design*. PhD thesis, University of Antwerp, 2017.

[Alania 2018] M. Alania, I. Lobato, and S. Van Aert. *Frozen lattice and absorptive model for high angle annular dark field scanning transmission electron microscopy: A comparison study in terms of integrated intensity and atomic column position measurement*. Ultramicroscopy, vol. 184, 188–198, 2018.

[Allen 2003] L.J. Allen, S.D. Findlay, M.P. Oxley, and C.J. Rossouw. *Lattice-resolution contrast from a focused coherent electron probe. Part I*. Ultramicroscopy, vol. 96, 47–63, 2003.

[Allen 2004] L.J. Allen, W. McBride, N.L. O'Leary, and M.P. Oxley. *Exit wave reconstruction at atomic resolution*. Ultramicroscopy, vol. 100, 91–104, 2004.

[Allen 2015] L.J. Allen, A.J. D'Alfonso, and S.D. Findlay. *Modelling the inelastic scattering of fast electrons*. Ultramicroscopy, vol. 151, 11–22, 2015.

[Altantzis 2019] T. Altantzis, I. Lobato, A. De Backer, A. Béché, Y. Zhang, S. Basak, M. Porcu, Q. Xu, A. Sánchez-Iglesias, L.M. Liz-Marzán, G. Van Tendeloo, S. Van Aert, and S. Bals. *Three-Dimensional Quantification of the Facet Evolution of Pt Nanoparticles in a Variable Gaseous Environment*. Nano Letters, vol. 19, 447–481, 2019.

[Anderson 1997] S.C. Anderson, C.R. Birkeland, G.R. Anstis, and D.J.H. Cockayne. *An approach to quantitative compositional profiling at near-atomic resolution using high-angle annular dark field imaging*. Ultramicroscopy, vol. 69, 83–103, 1997.

[Armstrong 2007] M. R. Armstrong, K. Boyden, N.D. Browning, G.H. Campbell, J.D. Colvin, W.J. DeHope, A.M. Frank, D.J. Gibson, F. Hartemann, J.S. Kim, W. E. King, T. B. LaGrange, B.J. Pyke, B.W. Reed, R.M. Shuttlesworth, B.C. Stuart, and B.R. Torralva. *Practical considerations for high spatial and temporal resolution dynamic transmission electron microscopy*. Ultramicroscopy, vol. 107, 356–367, 2007.

[Aveyard 2014] R. Aveyard, R. Ferrando, R.L. Johnston, and J. Yuan. *Modeling Nanoscale Inhomogeneities for Quantitative HAADF STEM Imaging*. Physical Review Letters, vol. 113, 075501, 2014.

[Balaji Gopal 2017] C. Balaji Gopal, M. García-Melchor, , S.C. Lee, Y. Shi, A. Shavorskiy, M. Monti, Z. Guan, R. Sinclair, H. Bluhm, A. Vojvodic, and W.C. Chueh. *Equilibrium oxygen storage capacity of ultrathin CeO2-δ depends non-monotonically on large biaxial strain*. Nature Communications, vol. 8, 15360, 2017.

[Bals 2011] S. Bals, M. Casavola, M.A. van Huis, S. Van Aert, K.J. Batenburg, G. Van Tendeloo, and D. Vanmaekelbergh. *Three-Dimensional Atomic Imaging of Colloidal Core–Shell Nanocrystals*. Nano Letters, vol. 11, 3420–3424, 2011.

[Bals 2012] S. Bals, S. Van Aert, C.P. Romero, K. Lauwaet, M.J. Van Bael, B. Schoeters, B. Partoens, E. Yücelen, P. Lievens, and G. Van Tendeloo. *Atomic scale dynamics of ultrasmall germanium clusters*. Nature Communications, vol. 3, 897, 2012.

[Bals 2014] S. Bals, B. Goris, T. Altantzis, H. Heidari, S. Van Aert, and G. Van Tendeloo. *Seeing and measuring in 3D with electrons*. Comptes Rendus Physique, vol. 15, 140–150, 2014.

[Barnard 2009] A.S. Barnard, N.P. Young, A.I. Kirkland, M.A. van Huis, and H. Xu. *Nanogold: A Quantitative Phase Map*. ACS Nano, vol. 3, 1431–1436, 2009.

[Barwick 2008] B. Barwick, H. S. Park, O.-H. Kwon, J.S. Baskin, and A.H. Zewail. *4D Imaging of Transient Structures and Morphologies in Ultrafast Electron Microscopy*. Science, vol. 322, 1227–1231, 2008.

[Batson 2008] P.E. Batson. *Motion of Gold Atoms on Carbon in the Aberration-Corrected STEM*. Microscopy and Microanalysis, vol. 14, 89–97, 2008.

[Baum 1968] L.E. Baum, and G.R. Sell. *Growth functions for transformations of manifolds*. Pacific Journal of Mathematics, vol. 27, 211–227, 1968.

[Béché 2016] A. Béché, B. Goris, B. Freitag, and J. Verbeeck. *Development of a fast electromagnetic beam blanker for compressed sensing in scanning transmission electron microscopy* . Applied Physics Letters, vol. 108, 093103, 2016.

[Beran 2010] T.N. Beran, and C. Violato. *Structural equation modeling in medical research: a primer*. BMC Research Notes, vol. 3, 267, 2010.

[Berebichez 2019] D. Berebichez. *Science is an ivory tower - Communicating science for the masses*, 2019.

[Berube 2008] D.M. Berube. *Rhetorical gamesmanship in the nano debates over sunscreens and nanoparticles*. Journal of Nanoparticle Research, vol. 10, 23–37, 2008.

[Biernacki 2000] C. Biernacki, G. Celeux, and G. Govaert. *Assessing a mixture model for clustering with the integrated classification likelihood*. IEEE Transactions on Pattern Analysis and Machine Intelligence, vol. 22, 719–725, 2000.

[Bilmes 1998] J.A. Bilmes. *A Gentle Tutorial of the EM Algorithm and its Application to Parameter Estimation for Gaussian Mixture and Hidden Markov Models*. International Computer Science Institute Berkeley, vol. TR-97-021, 1998.

[Bishop 2006] C. Bishop. *Pattern Recognition and Machine Learning*. New York: Springer-Verlag, 2006.

[Bollig 1996] B. Bollig, H.G. Fischer, and E. Kubalek. *Multislice simulation of high-resolution scanning transmission electron microscopy Z-contrast images of semiconductor heterointerfaces*. Scanning, vol. 18, 291–300, 1996.

[Boschker 2011] H. Boschker, M. Huijben, A. Vailionis, J. Verbeeck, S. Van Aert, M. Luysberg, S. Bals, G. Van Tendeloo, E.P. Houwman, G. Koster, D.H.A. Blank, and G. Rijnders. *Optimized fabrication of high-quality $La_{0.67}Sr_{0.33}MnO_3$ thin films considering all essential characteristics*. Journal of Physics D: Applied Physics, vol. 44, 205001, 2011.

[Brown 2017] H.G. Brown, R. Ishikawa, G. Sánchez-Santolino, N.R. Lugg, Y. Ikuhara, Allen L.J., and N. Shibata. *A new method to detect and correct sample tilt in scanning transmission electron microscopy bright-field imaging*. Ultramicroscopy, vol. 173, 76–83, 2017.

[Browning 2012] N.D. Browning, M.A. Bonds, G.H. Campbell, J.E. Evans, T. LaGrange, K. L. Jungjohann, D.J. Masiel, J. McKeown, S. Mehraeen, B.W. Reed, and M. Santala. *Recent developments in dynamic transmission electron microscopy*. Current Opinion in Solid State and Materials Science, vol. 16, 23–30, 2012.

[Buban 2010] J.P. Buban, Q. Ramasse, B. Gipson, N.D. Browning, and H. Stahlberg. *High-resolution low-dose scanning transmission electron microscopy*. Journal of Electron Microscopy, vol. 59, 103–112, 2010.

[Buffat 2003] P.A. Buffat. *Electron diffraction and HRTEM studies of multiply-twinned structures and dynamical events in metal nanoparticles: facts and artefacts*. Materials Chemistry and Physics, vol. 81, 368–375, 2003.

[Cao 2018] K. Cao, T. Zoberbier, J. Biskupek, A. Botos, R.L. McSweeney, A. Kurtoglu, C.T. Stoppiello, A.V. Markevich, E. Besley, T.W. Chamberlain, U. Kaiser, and A.N. Khlobystov. *Comparison of atomic scale dynamics for the middle and late transition metal nanocatalysts*. Nature Communications, vol. 9, 3382, 2018.

[Chang 2014] H. Chang, M. Saito, T. Nagai, Y. Liang, Y. Kawazoe, Z. Wang, H. Wu, K. Kimoto, and Y. Ikuhara. *Single adatom dynamics at monatomic steps of free-standing few-layer reduced graphene*. Scientific Reports, vol. 4, 6037, 2014.

[Chapman 2011] H.N. Chapman, P. Fromme, [...], and J.C.H. Spence. *Femtosecond X-ray protein nanocrystallography*. Nature, vol. 470, 73–77, 2011.

[Chen 2020] E. Chen, M. Bevilacqua, C. Tavagnacco, T. Montini, C.-M. Yang, and P. Fornasiero. *High surface area N/O co-doped carbon materials: Selective electrocatalysts for O_2 reduction to H_2O_2*. Catalysis Today, vol. 356, 132–140, 2020.

[Cherepanov 2004] V. Cherepanov, and B. Voigtländer. *Influence of material, surface reconstruction, and strain on diffusion at the Ge(111) surface*. Physical Review B, vol. 69, 125331, 2004.

[Claes 2018] N. Claes. *3D Characterization of coaded nanoparticles and soft-hard nanocomposites*. PhD thesis, University of Antwerp, 2018.

[Coralli 2019] A. Coralli, B.J.M. Sarruf, P.E.V. de Miranda, L. Osmieri, S. Specchia, and N.Q. Minh. *Chapter 2 - Fuel Cells*. Science and Engineering of Hydrogen-Based Energy Technologies, 39–122, 2019.

[Cowley 1959] J.M. Cowley, and A.F. Moodie. *The scattering of electrons by atoms and crystals. III. Single-crystal diffraction patterns*. Acta Crystallographica, vol. 12, 360–367, 1959.

[Cramér 1946] H. Cramér. *Mathematical Methods of Statistics*. New York: Princeton University Press, 1946.

[Croitoru 2006] M.D. Croitoru, D. Van Dyck, S. Van Aert, S. Bals, and J. Verbeeck. *An efficient way of including thermal diffuse scattering in simulation of scanning transmission electron microscopic images*. Ultramicroscopy, vol. 106, 933–940, 2006.

[Cruyff 2016] M.J.L.F. Cruyff, U. Böckenholt, P.G.M. van der Heijden, and L.E. Frank. *Chapter 18 - A Review of Regression Procedures for Randomized Response Data, Including Univariate and Multivariate Logistic Regression, the Proportional Odds Model and Item Response Model, and Self-Protective Responses*. Handbook of Statistics, vol. 34, 287–315, 2016.

[Cullity 1978] B.D. Cullity. *Elements of X-ray Diffraction*. Addison-Wesley Publishing Company Inc., 1978.

[Da Silva 2007] J.L.F. Da Silva, M.V. Ganduglia-Pirovano, J. Sauer, V. Bayer, and G. Kresse. *Hybrid functionals applied to rare-earth oxides: The example of ceria*. Physical Review B, vol. 75, 045121, 2007.

[Dahly 2009] D.L. Dahly, L.S. Adair, and K.A. Bollen. *A structural equation model of the developmental origins of blood pressure*. International Journal of Epidemiology, vol. 38, 538–548, 2009.

[De Backer 2011] A. De Backer, S. Van Aert, and D. Van Dyck. *High precision measurements of atom column positions using model-based exit wave reconstruction*. Ultramicroscopy, vol. 111, 1475–1482, 2011.

[De Backer 2013] A. De Backer, G.T. Martinez, A. Rosenauer, and S. Van Aert. *Atom counting in HAADF STEM using a statistical model-based approach: Methodology, possibilities, and inherent limitations*. Ultramicroscopy, vol. 134, 23–33, 2013.

[De Backer 2015a] A. De Backer, A. De wael, J. Gonnissen, and S. Van Aert. *Optimal experimental design for nano-particle atom-counting from high-resolution STEM images*. Ultramicroscopy, vol. 151, 46–55, 2015.

[De Backer 2015b] A. De Backer, G.T. Martinez, K.E. MacArthur, L. Jones, A. Béché, P.D. Nellist, and S. Van Aert. *Dose limited reliability of quantitative annular dark field scanning transmission electron microscopy for nano-particle atom-counting*. Ultramicroscopy, vol. 151, 56–61, 2015.

[De Backer 2016] A. De Backer, K.H.W. van den Bos, W. Van den Broek, J. Sijbers, and S. Van Aert. *StatSTEM: An efficient approach for accurate and precise model-based quantification of atomic resolution*

electron microscopy images. Ultramicroscopy, vol. 171, 104–116, 2016.

[De Backer 2017] A. De Backer, L. Jones, I. Lobato, T. Altantzis, B. Goris, P.D. Nellist, S. Bals, and S. Van Aert. *Three-dimensional atomic models from a single projection using Z-contrast imaging: verification by electron tomography and opportunities*. Nanoscale, vol. 9, 8791–8798, 2017.

[De Backer 2021a] A. De Backer, J. Fatermans, A.J. den Dekker, and S. Van Aert. *Chapter 2 - Statistical parameter estimation theory: principles and simulation studies*. Advances in Imaging and Electron Physics, vol. 217, 29–72, 2021.

[De Backer 2021b] A. De Backer, J. Fatermans, A.J. den Dekker, and S. Van Aert. *Chapter 4 - Atom counting*. Advances in Imaging and Electron Physics, vol. 217, 91–144, 2021.

[De Backer 2021c] A. De Backer, S. Van Aert, P.D. Nellist, and L. Jones. *Procedure for 3D atomic resolution reconstructions using atom-counting and a Bayesian genetic algorithm*. arXiv:2105.05562, 2021.

[De Graef 2003] M. De Graef. *Introduction to Conventional Transmission Electron Microscopy*. Cambridge University Press, 2003.

[de la Peña 2017] F. de la Peña, T. Ostasevicius, V.T. Fauske, P. Burdet, P. Jokubauskas, M. Nord, M. Sarahan, E. Prestat, D.N. Johnstone, J. Taillon, J. Caron, T. Furnival, K.E. MacArthur, A. Eljarrat, S. Mazzucco, V. Migunov, T. Aarholt, M. Walls, F. Winkler, G. Donval, B. Martineau, A. Garmannslund, L.F. Zagonel, and I. Iyengar. *Electron Microscopy (Big and Small) Data Analysis With the Open Source Software Package HyperSpy*. Microscopy and Microanalysis, vol. 214, 214–215, 2017.

[De Maeseneer 2021] W. De Maeseneer, S. Cardoen, and Belga. *Witte mondmaskers van overheid worden voorlopig afgeraden en getest: gevaar kan in nanodeeltjes schuilen*, 2021.

[De wael 2017] A. De wael, A. De Backer, L. Jones, P.D. Nellist, and S. Van Aert. *Hybrid statistics-simulations based method for atom-counting using scanning transmission electron microscopy*. Ultramicroscopy, vol. 177, 69–77, 2017.

[De wael 2020a] A. De wael, A. De Backer, L. Jones, A. Varambhia, P.D. Nellist, and S. Van Aert. *Measuring Dynamic Structural Changes of Nanoparticles at the Atomic Scale Using Scanning Transmission Electron Microscopy*. Physical Review Letters, vol. 124, 106105, 2020.

[De wael 2020b] A. De wael, A. De Backer, and S. Van Aert. *Hidden Markov model for atom-counting from sequential ADF STEM images: methodology, possibilities and limitations*. Ultramicroscopy, vol. 219, 113131, 2020.

[De wael 2021] A. De wael, A. De Backer, I. Lobato, and S. Van Aert. *Modelling ADF STEM images using elliptical Gaussian peaks and its effects on the quantification of structure parameters in the presence of sample tilt*. Submitted, 2021.

[Dempster 1977] A.P. Dempster, N.M. Laird, and D.B. Rubin. *Maximum Likelihood from Incomplete Data via the EM Algorithm*. Journal of the Royal Statistical Society. Series B (Methodological), vol. 39, no. 1, 1–38, 1977.

[den Dekker 2005] A.J. den Dekker, S. Van Aert, A. van den Bos, and D. Van Dyck. *Maximum likelihood estimation of structure parameters from high resolution electron microscopy images. Part I: a theoretical framework*. Ultramicroscopy, vol. 104, 83–106, 2005.

[Drake 1967] A. W. Drake. *Discrete-state Markov processes*. New York, NY: McGraw-Hill, 1967.

[Dwyer 2010] C. Dwyer. *Simulation of scanning transmission electron microscope images on desktop computers*. Ultramicroscopy, vol. 110, 195–198, 2010.

[Dwyer 2012] C. Dwyer, C. Maunders, C.L. Zheng, M. Weyland, P. C. Tiemeijer, and J. Etheridge. *Sub-0.1 nm-resolution quantitative scanning transmission electron microscopy without adjustable parameters*. Applied Physics Letters, vol. 100, 191915, 2012.

[Dwyer 2013] C. Dwyer. *Atomic-Resolution Core-Level Spectroscopy in the Scanning Transmission Electron Microscope*. Advances in Imaging and Electron Physics, vol. 175, 145–199, 2013.

[Dymarski 2011] P. Dymarski. *Hidden Markov Models, Theory and Applications*. InTech, 2011.

[E 2013] H. E, K.E. MacArthur, T.J. Pennycook, E. Okunishi, A.J. D'Alfonso, N.R. Lugg, L.J. Allen, and P.D. Nellist. *Probe integrated scattering cross sections in the analysis of atomic resolution HAADF STEM images*. Ultramicroscopy, vol. 133, 109–119, 2013.

[Eddy 2004] S.R. Eddy. *What is a hidden Markov model?* Nature Biotechnology, vol. 22, 1315–1316, 2004.

[Egerton 2010] R.F. Egerton, R. McLeod, F. Wang, and M. Malac. *Basic questions related to electron-induced sputtering in the TEM*. Ultramicroscopy, vol. 110, 991–997, 2010.

[Egerton 2013] R.F. Egerton. *Beam-Induced Motion of Adatoms in the Transmission Electron Microscope*. Microscopy and Microanalysis, vol. 19, 479–486, 2013.

[Egerton 2018] R.F. Egerton, and M. Watanabe. *Characterization of single-atom catalysts by EELS and EDX spectroscopy*. Ultramicroscopy, vol. 193, 111–117, 2018.

[Egerton 2019] R.F. Egerton. *Radiation damage to organic and inorganic specimens in the TEM*. Micron, vol. 119, 72–87, 2019.

[Erni 2009] R. Erni, M.D. Rossell, C. Kisielowski, and U. Dahmen. *Atomic-Resolution Imaging with a Sub-50-pm Electron Probe*. Physical Review Letters, vol. 102, 096101, 2009.

[Erni 2010] R. Erni, M.D. Rossell, and P.N.H. Nakashima. *Optimization of exit-plane waves restored from HRTEM through-focal series*. Ultramicroscopy, vol. 110, 151–161, 2010.

[Fang 2019] S. Fang, Y. Wen, C.S. Allen, C. Ophus, G.G.D. Han, A.I. Kirkland, E. Kaxiras, and J.H. Warner. *Atomic electrostatic maps of 1D channels in 2D semiconductors using 4D scanning transmission electron microscopy*. Nature Communications, vol. 10, 1127, 2019.

[Fatermans 2018] J. Fatermans, A.J. den Dekker, K. Müller-Caspary, I. Lobato, C. M. O'Leary, P.D. Nellist, and S. Van Aert. *Single Atom Detection from Low Contrast-to-Noise Ratio Electron Microscopy Images*. Physical Review Letters, vol. 121, 056101, 2018.

[Fatermans 2019] J. Fatermans, S. Van Aert, and A.J. den Dekker. *The maximum a posteriori probability rule for atom column detection from HAADF STEM images*. Ultramicroscopy, vol. 201, 81–91, 2019.

[Fatermans 2020] J. Fatermans, A.J. den Dekker, K. Müller-Caspary, N. Gauquelin, J. Verbeeck, and S. Van Aert. *Atom column detection from simultaneously acquired ABF and ADF STEM images*. Ultramicroscopy, vol. 219, 113046, 2020.

[Findlay 2003] S.D. Findlay, L.J. Allen, M.P. Oxley, and C.J. Rossouw. *Lattice-resolution contrast from a focused coherent electron probe. Part II*. Ultramicroscopy, vol. 96, 65–81, 2003.

[Findlay 2009] S.D. Findlay, N. Shibata, H. Sawada, E. Okunishi, Y. Kondo, T. Yamamoto, and Y. Ikuhara. *Robust atomic resolution imaging of light elements using scanning transmission electron microscopy*. Applied Physics Letters, vol. 95, 191913, 2009.

[Findlay 2013] S.D. Findlay, and J.M. LeBeau. *Detector non-uniformity in scanning transmission electron microscopy*. Ultramicroscopy, vol. 124, 52–60, 2013.

[Forbes 2010] B.D. Forbes, A.V. Martin, S.D. Findlay, A.J. D'Alfonso, and L.J. Allen. *Quantum mechanical model for phonon excitation in electron diffraction and imaging using a Born-Oppenheimer approximation*. Physical Review B, vol. 82, 104103, 2010.

[Forbes 2011] B.D. Forbes, A.J. D'Alfonso, S.D. Findlay, D. Van Dyck, J.M. LeBeau, S. Stemmer, and L.J. Allen. *Thermal diffuse scattering in transmission electron microscopy*. Ultramicroscopy, vol. 111, 1670–1680, 2011.

[Forney 1973] G.D. Forney. *The Viterbi algorithm*. IEEE Transactions on Information Theory, vol. 61, 268–278, 1973.

[Foster 2019] D.M. Foster, T. Pavloudis, J. Kioseoglou, and R.E. Palmer. *Atomic-resolution imaging of surface and core melting in individual size-selected Au nanoclusters on carbon*. Nature Communications, vol. 10, 2583, 2019.

[Frank 2006] J. Frank. *Three-Dimensional Electron Microscopy of Macromolecular Assemblies: Visualization of Biological Molecules in Their Native State*. Oxford University Press, 2006.

[Furnival 2018] T. Furnival, D. Knez, E. Schmidt, R.K. Leary, G. Kothleitner, F. Hofer, P.D. Bristowe, and P.A. Midgley. *Adatom dynamics and the surface reconstruction of Si(110) revealed using time-resolved electron microscopy*. Applied Physics Letters, vol. 113, 183104, 2018.

[Gales 2007] M. Gales, and S. Young. *The Application of Hidden Markov Models in Speech Recognition*. Foundations and Trends©in Signal Processing, vol. 1, 195–304, 2007.

[Galindo 2007] P.L. Galindo, S. Kret, A.M. Sanchez, J.-Y. Laval, A. Yáñez, J. Pizarro, E. Guerrero, T. Ben, and S.I. Molina. *The Peak Pairs algorithm for strain mapping from HRTEM images*. Ultramicroscopy, vol. 107, 1186–1193, 2007.

[Gao 1999] H. X. Gao, and L.-M. Peng. *Parameterization of the temperature dependence of the Debye–Waller factors*. Acta Crystallographica Section A, vol. 55, 926–932, 1999.

[Gao 2018] P. Gao, A. Kumamoto, R. Ishikawa, N. Lugg, N. Shibata, and Y. Ikuhara. *Picometer-scale atom position analysis in annular bright-field STEM imaging*. Ultramicroscopy, vol. 184, 177–187, 2018.

[Garcia-Gutierrez 2004] D. Garcia-Gutierrez, C. Gutierrez-Wing, M. Miki-Yoshida, and M. Jose-Yacaman. *HAADF study of Au-Pt core-shell bimetallic nanoparticles*. Applied Physics A, vol. 79, 481–487, 2004.

[Gemmi 2019] M. Gemmi, E. Mugnaioli, T.E. Gorelik, U. Kolb, L. Palatinus, P. Boullay, S. Hovmöller, and J.P. Abrahams. *3D Electron Diffraction: The Nanocrystallography Revolution*. ACS Central Science, vol. 5, 1315–1329, 2019.

[Geuchies 2016] J. J. Geuchies, C. van Overbeek, W.H. Evers, B. Goris, A. De Backer, G. P. Gantapara, F. T. Rabouw, J. Hilhorst, J.L. Peters, O. Konovalov, A. V. Petukhov, M. Dijkstra, L. D.A. Siebbeles, S. Van Aert, S. Bals, and D. Vanmaekelbergh. *In situ study of consecutive phase transitions in the formation of atomatomic coherent two-dimensional supperlattices from nanocrystals*. Nature Materials, vol. 15, 1248–1254, 2016.

[Ghahramani 1997] Z. Ghahramani, and M.I. Jordan. *Factorial Hidden Markov Models*. Machine Learning, vol. 29, 245–273, 1997.

[Glaeser 1993] R.M. Glaeser, and K.H. Downing. *High-resolution electron crystallography of protein molecules*. Ultramicroscopy, vol. 52, 478–486, 1993.

[Grochola 2005] Gregory Grochola, Salvy P. Russo, and Ian K. Snook. *On fitting a gold embedded atom method potential using the force matching method*. The Journal of Chemical Physics, vol. 123, 204719, 2005.

[Gross 2010] L. Gross, F. Mohn, N. Moll, G. Meyer, R. Ebel, W.M. Abdel-Mageed, and M. Jaspars. *Organic structure determination using atomicresolution scanning probe microscopy*. Nature Chemistry, vol. 2, 821–825, 2010.

[Hadrup 2020] N. Hadrup, A.K. Sharma, K. Loeschner, and N.J. Jacobsen. *Pulmonary toxicity of silver vapours, nanoparticles and fine dusts: A review*. Regulatory Toxicology and Pharmacology, vol. 15, 104690, 2020.

[Haider 1998] M. Haider, S. Uhlemann, E. Schwan, H. Rose, B. Kabius, and K. Urban. *Electron microscopy image enhanced*. Nature, vol. 392, 768–769, 1998.

[Halicioglu 1979] T. Halicioglu, and G.M. Pound. *A calculation of the diffusion energies for adatoms on surfaces of F.C.C. metals*. Thin Solid Films, vol. 57, 241–245, 1979.

[Han 2015] C.W. Han, H. Iddir, A. Uzun, L.A. Curtiss, N.D. Browning, B.C. Gates, and V. Ortalan. *Migration of Single Iridium Atoms and Triiridium Clusters on MgO Surfaces: Aberration-Corrected STEM Imaging and Ab Initio Calculations*. The Journal of Physical Chemistry Letters, vol. 6, 4675–4679, 2015.

[Haruta 1989] M. Haruta, N. Yamada, T. Kobayashi, and S. Iijima. *Gold catalysts prepared by coprecipitation for low-temperature oxidation of hydrogen and of carbon monoxide*. Journal of Catalysis, vol. 115, 301–309, 1989.

[Heintzmann 2006] R. Heintzmann, and G. Ficz. *Breaking the resolution limit in light microscopy*. Briefings in Functional Genomics, vol. 5, 289–301, 2006.

[Heintzmann 2009] R. Heintzmann, and M. G. L. Gustafsson. *Subdiffraction resolution in continuous samples*. Nature Photonics, vol. 3, 362–364, 2009.

[Henderson 1995] R. Henderson. *The potential and limitations of neutrons, electrons and X-rays for atomic resolution microscopy of unstained biological molecules*. Q Rev Biophys, vol. 28, 171–193, 1995.

[Hovden 2012] R. Hovden, and D.A. Muller. *Efficient elastic imaging of single atoms on ultrathin supports in a scanning transmission electron microscope*. Ultramicroscopy, vol. 123, 59–65, 2012.

[Howard 1994] C.J. Howard, and S.J. Kennedy. *Neutron Diffraction*. Materials Forum, vol. 18, 155–176, 1994.

[Huijben 2013] M. Huijben, G. Koster, M.K. Kruize, S. Wenderich, J. Verbeeck, S. Bals, E. Slooten, B. Shi, H.J.A. Molegraaf, J.E. Kleibeuker, S. Van Aert, J.B. Goedkoop, A. Brinkman, D.H.A. Blank, M.S. Golden, G. Van Tendeloo, H. Hilgenkamp, and G. Rijnders. *Defect Engineering in Oxide Heterostructures by Enhanced Oxygen Surface Exchange*. Advanced Functional Materials, vol. 24, 5240, 2013.

[Hvolbæk 2007] B. Hvolbæk, T.V.W. Janssens, B.S. Clausen, H. Falsig, C.H. Christensen, and J. K. Nørskov. *Catalytic activity of Au nanoparticles*. Nano Today, vol. 2, 14–18, 2007.

[Hÿtch 1994] M.J. Hÿtch, and W.M. Stobbs. *Quantitative comparison of high resolution TEM images with image simulations*. Ultramicroscopy, vol. 53, 191–203, 1994.

[Iijima 1986] S. Iijima, and T. Ichihashi. *Structural Instability of Ultrafine Particles of Metals*. Physical Review Letters, vol. 56, 616–619, 1986.

[Isaacson 1977] M. Isaacson, D. Kopf, M. Utlaut, N. W. Parker, and A. V. Crewe. *Direct observations of atomic diffusion by scanning transmission electron microscopy*. Proc. Natl. Acad. Sci., vol. 74, 1802–1806, 1977.

[Ischenko 2014] A.A. Ischenko, and S.A. Aseyev. *Ultrafast Electron Crystallography and Nanocrystallography*. 2014.

[Ishikawa 2014] R. Ishikawa, R. Mishra, A.R. Lupini, S.D. Findlay, T. Taniguchi, S.T. Pantelides, and S.J. Pennycook. *Direct Observation of Dopant Atom Diffusion in a Bulk Semiconductor Crystal Enhanced by a Large Size Mismatch*. Physical Review Letters, vol. 113, 155501, 2014.

[Ishikawa 2020] R. Ishikawa, Y. Jimbo, M. Terao, M. Nishikawa, S. Ueno Y. an Morishita, M. Mukai, N. Shibata, and Y. Ikuhara. *High spatiotemporal-resolution imaging in the scanning transmission electron microscope*. Microscopy, vol. 69, 240–247, 2020.

[Ishizuka 2002] K. Ishizuka. *A practical approach for STEM image simulation based on the FFT multislice method*. Ultramicroscopy, vol. 90, 71–83, 2002.

[Jia 2014] C.L. Jia, S.B. Mi, J. Barthel, D.W. Wang, R.E. Dunin-Borkowski, K.W. Urban, and A. Thust. *Determination of the 3D shape of a nanoscale crystal with atomic resolution from a single image*. Nature Materials, vol. 13, 1044–1049, 2014.

[Jones 2013] L. Jones, and P.D. Nellist. *Identifying and Correcting Scan Noise and Drift in the Scanning Transmission Electron Microscope*. Microscopy and Microanalysis, vol. 19, 1050–1060, 2013.

[Jones 2014] L. Jones, K.E. MacArthur, V.T. Fauske, A.T.J. van Helvoort, and P.D. Nellist. *Rapid estimation of catalyst nanoparticle morphology and atomic-coordination by high-resolution Z-contrast electron microscopy*. Nano Letters, vol. 14, 6336–6341, 2014.

[Jones 2015] L. Jones, H. Yang, T.J. Pennycook, M.S.J. Marshall, S. Van Aert, N.D. Browning, M. R. Castell, and P.D. Nellist. *Smart Align - a new tool for robust non-rigid registration of scanning microscope data*. Advanced Structural and Chemical Imaging, vol. 1, 2015.

[Jones 2016] L. Jones. *Quantitative ADF STEM: acquisition, analysis and interpretation*. IOP Conf. Series: Materials Science and Engineering, vol. 109, 012008, 2016.

[Joshi 2017] J.C. Joshi, K. Tankeshwar, and S. Srivastava. *Hidden Markov Model for quantitative prediction of snowfall and analysis of hazardous snowfall events over Indian Himalaya*. Journal of Earth System Science, vol. 126, 33, 2017.

[Khadr 2016] M. Khadr. *Forecasting of meteorological drought using Hidden Markov Model (case study: The upper Blue Nile river basin, Ethiopia)*. Ain Shams Engineering Journal, vol. 7, 47–56, 2016.

[Kirkland 2010] E.J. Kirkland. *Advanced computing in electron microscopy, Second Edition*. New York: Springer Science+Business Media LLC, 2010.

[Kisielowski 2001] C. Kisielowski, C.J.D. Hetherington, Y.C. Wang, R. Kilaas, M.A. O'Keefe, and A. Thust. *Imaging columns of the light elements carbon, nitrogen and oxygen with sub Ångstrom resolution*. Ultramicroscopy, vol. 89, 243–263, 2001.

[Kisielowski 2013] C. Kisielowski, L.-W. Wang, P. Specht, H.A. Calderon, B. Barton, B. Jiang, J.H. Kang, and R. Cieslinski. *Real-time sub-Ångstrom imaging of reversible and irreversible conformations in rhodium catalysts and graphene*. Physical Review B, vol. 88, 024305, 2013.

[Klenov 2007] D.O. Klenov, S.D. Findlay, L.J. Allen, and S. Stemmer. *Influence of orientation on the contrast of high-angle annular dark-field images of silicon*. Physical Review B, vol. 76, 014111, 2007.

[Koch 2002] C.T. Koch. *Determination of core structure periodicity and point defect density along dislocations*. Tempe, AZ: Arizona State University, 2002.

[Kotakoski 2014] J. Kotakoski, C. Mangler, and J.C. Meyer. *Imaging atomic-level random walk of a point defect in graphene*. Nature Communications, vol. 5, 3991, 2014.

[Krause 2013] F.F. Krause, K. Müller, D. Zillmann, J. Jansen, M. Schowalter, and A. Rosenauer. *Comparison of intensity and absolute contrast of simulated and experimental high-resolution transmission electron microscopy images for different multislice simulation methods*. Ultramicroscopy, vol. 134, 94–101, 2013.

[Krause 2016] F.F. Krause, M. Schowalter, T. Grieb, K. Müller-Caspary, T. Mehrtens, and A. Rosenauer. *Effects of instrument imperfections on quantitative scanning transmission electron microscopy*. Ultramicroscopy, vol. 161, 146–160, 2016.

[Kroese 2011] D.P. Kroese, T. Taimre, and Z.I. Botev. *Handbook of Monte Carlo methods*. Wiley Series in Probability and Statistics. Wiley, 2011.

[Kúlic 2008] D. Kúlic, W. Takano, and Y. Nakamura. *Incremental Learning, Clustering and Hierarchy Formation of Whole Body Motion Patterns using Adaptive Hidden Markov Chains*. The International Journal of Robotics Research, vol. 27, 761–784, 2008.

[LaGrange 2012] T. LaGrange, B.W. Reed, M.K. Santala, McKeown J.T., A. Kulovits, J.M.K. Wiezorek, L. Nikolova, F. Rosei, B.J. Siwick, and G.H. Campbell. *Approaches for ultrafast imaging of transient materials processes in the transmission electron microscope*. Micron, vol. 43, 1108–1120, 2012.

[Langlois 2010] C. Langlois, Z.W. Wang, D. Pearmain, C. Ricolleau, and Z.Y. Li. *HAADF-STEM imaging of CuAg core-shell nanoparticles*. Journal of Physics: Conference Series, vol. 241, 012043, 2010.

[LeBeau 2008a] J.M. LeBeau, S.D. Findlay, L.J. Allen, and S. Stemmer. *Quantitative Atomic Resolution Scanning Transmission Electron Microscopy*. Physical Review Letters, vol. 100, 206101, 2008.

[LeBeau 2008b] J.M. LeBeau, and S. Stemmer. *Experimental Quantification of Annular Dark-Field Images in Scanning Transmission Electron Microscopy*. Ultramicroscopy, vol. 108, 1653–1658, 2008.

[LeBeau 2010] J.M. LeBeau, S.D. Findlay, L.J. Allen, and S. Stemmer. *Standardless atom counting in scanning transmission electron microscopy*. Nano Letters, vol. 10, 4405–4408, 2010.

[Lee 2013] J. Lee, W. Zhou, J. Pennycook, J.-C. Idrobo, and S. T. Pantelides. *Direct visualization of reversible dynamics in a Si6 cluster embedded in a graphene pore*. Nature Communications, vol. 4, 1650, 2013.

[Li 2008] Z.Y. Li, N.P. Young, M. Di Vece, S. Palomba, R.E. Palmer, A.L. Bleloch, B.C. Curley, R.L. Johnston, J. Jiang, and J. Yuan. *Three-dimensional atomic-scale structure of size-selected gold nanoclusters*. Nature, vol. 451, 46–48, 2008.

[Liao 2014] H.-G. Liao, D. Zherebetskyy, H. Xin, C. Czarnik, P. Ercius, H. Elmlund, M. Pan, L.-W. Wang, and H. Zheng. *Facet development during platinum nanocube growth*. Science, vol. 345, 916–919, 2014.

[Linck 2012] M. Linck, B. Freitag, S. Kujawa, M. Lehmann, and T. Niermann. *State of the art in atomic resolution off-axis electron holography*. Ultramicroscopy, vol. 116, 13–23, 2012.

[Lindenberg 2017] A.M. Lindenberg, S. L. Johnson, and D.A. Reis. *Visualization of Atomic-Scale Motions in Materials via Femtosecond X-Ray Scattering Techniques*. Annu. Rev. Mater. Res., vol. 47, 425–449, 2017.

[Liu 2019] P. Liu, T. Wu, J. Madsen, J. Schiøtz, J. B. Wagner, and T.W. Hansen. *Transformations fo supported gold nanoparticles observed by in situ electron microscopy*. Nanoscale, vol. 11, 11885–11891, 2019.

[Liu 2020] P. Liu, J. Madsen, J. Schiøtz, K.B. Wagner, and T.W. Hansen. *Reversible and concerted atom diffusion on supported gold nanoparticles*. Journal of Physics: Materials, vol. 3, 024009, 2020.

[Liu 2021] P. Liu, E. Arslan Irmak, A. De Backer, A. De wael, I. Lobato, A. Béché, S. Van Aert, and S. Bals. *Three-dimensional atomic structure of supported Au nanoparticles at high temperature*. Nanoscale, vol. 13, 1770–1776, 2021.

[Loane 1988] R.F. Loane, E.J. Kirkland, and J. Silcox. *Visibility of single heavy atoms on thin crystalline silicon in simulated annular dark-field STEM images*. Acta Crystallographica A, vol. 44, 912–927, 1988.

[Loane 1991] R.F. Loane, P. Xu, and J. Silcox. *Thermal vibrations in convergent-beam electron diffraction*. Acta Crystallographica Section A, vol. 47, 267–278, 1991.

[Lobato 2014] I. Lobato, and D. Van Dyck. *An accurate parameterization for the scattering factors, electron densities and electrostatic potentials for neutral atoms that obey all physical constraints*. Acta Crystallographica Section A, vol. 70, 636–649, 2014.

[Lobato 2015] I. Lobato, and D. Van Dyck. *MULTEM: A new multislice program to perform accurate and fast electron diffraction and imaging simulations using Graphics Processing Units with CUDA*. Ultramicroscopy, vol. 156, 9–17, 2015.

[Lobato 2016] I. Lobato, S. Van Aert, and J. Verbeeck. *Progress and new advances in simulating electron microscopy datasets using MULTEM*. Ultramicroscopy, vol. 168, 17–27, 2016.

[Locquet 1998] J.-P. Locquet, J. Perret, J. Fompeyrine, E. Mächler, J.W. Seo, and G. Van Tendeloo. *Doubling the critical temperature of La1.9Sr0.1CuO4 using epitaxial strain*. Nature, vol. 394, 453–456, 1998.

[Lozano 2018] J.G. Lozano, G.T. Martinez, L. Jin, P.D. Nellist, and P.G. Bruce. *Low-Dose Aberration-Free Imaging of Li-Rich Cathode Materials at Various States of Charge Using Electron Ptychography*. Nano Letters, vol. 18, 6850–6855, 2018.

[Lu 2016] J. Lu, Z. Chen, Z. Ma, F. Pan, L.A. Curtiss, and K. Amine. *The role of nanotechnology in the development of battery materials for electric vehicles*. Nature Nanotechnology, vol. 11, 1031–1038, 2016.

[Lu 2018] P.J. Lu, S.W. Fang, W.L. Cheng, S.C. Huang, M.C. Huang, and H.F. Cheng. *Characterization of titanium dioxide and zinc oxide nanoparticles in sunscreen powder by comparing different measurement methods*. Journal of Food and Drug Analysis, vol. 26, 1192–1200, 2018.

[MacArthur 2015] K.E. MacArthur, A.J. D'Alfonso, D. Ozkaya, L.J. Allen, and P.D. Nellist. *Optimal ADF STEM imaging parameters for tilt-robust image quantification*. Ultramicroscopy, vol. 156, 1–8, 2015.

[Maccagnano-Zacher 2008] S.E. Maccagnano-Zacher, K.A. Mkhoyan, E.J. Kirkland, and J. Silcox. *Effects of tilt on high-resolution ADF-STEM imaging*. Ultramicroscopy, vol. 108, 718–726, 2008.

[Madsen 2018] J. Madsen, P. Liu, J. Kling, J. B. Wagner, T.W. Hansen, O. Winther, and J. Schiøtz. *A Deep Learning Approach to Identify Local Structures in Atomic-Resolution Transmission Electron Microscopy Images*. Advanced Theory and Simulations, vol. 1, 1800037, 2018.

[Manthiram 2017] A. Manthiram. *An Outlook on Lithium Ion Battery Technology*. ACS Central Science, vol. 3, 1063–1069, 2017.

[Martinez 2014a] G.T. Martinez, A. De Backer, A. Rosenauer, J. Verbeeck, and S. Van Aert. *The effect of probe inaccuracies on the quantitative model-based analysis of high angle annular dark field scanning transmission electron microscopy images*. Micron, vol. 63, 57–63, 2014.

[Martinez 2014b] G.T. Martinez, A. Rosenauer, A. De Backer, J. Verbeeck, and S. Van Aert. *Quantitative composition determination at the atomic level using model-based high-angle annular dark field scanning transmission electron microscopy*. Ultramicroscopy, vol. 137, 12–19, 2014.

[Martinez 2015] G.T. Martinez, L. Jones, A. De Backer, A. Béché, J. Verbeeck, S. Van Aert, and P.D. Nellist. *Quantitative STEM normalisation: The importance of the electron flux*. Ultramicroscopy, vol. 159, 46–58, 2015.

[Martinez 2018] G.T. Martinez, K.H.W. van den Bos, M. Alania, P.D. Nellist, and S. Van Aert. *Thickness dependence of scattering cross-sections in quantitative scanning transmission electron microscopy*. Ultramicroscopy, vol. 187, 84–92, 2018.

[McLachlan 1996] G. McLachlan, and T. Krishnan. *The EM Algorithm and Extensions*. Wiley Series in Probability and Statistics. Wiley, 1996.

[McLachlan 2000] G. McLachlan, and D. Peel. *Finite Mixture Models*. Wiley series in probability and statistics. John Wiley and Sons, inc., 2000.

[Mehrtens 2013] T. Mehrtens, M. Schowalter, D. Tytko, P. Choi, and D. Raabe. *Measurement of the indium concentration in high indium content InGaN layers by scanning transmission electron microscopy and atom probe tomography*. Applied Physics Letters, vol. 102, 132112, 2013.

[Meyer 2014] J.C. Meyer, J. Kotakoski, and C. Mangler. *Atomic structure from large-area, low-dose exposures of materials: A new route to circumvent radiation damage*. Ultramicroscopy, vol. 145, 13–21, 2014.

[Mishra 2017] R. Mishra, R. Ishikawa, A.R. Lupini, and S.J. Pennycook. *Single-atom dynamics in scanning transmission electron microscopy*. MRS Bulletin, vol. 42, 644–652, 2017.

[Mittelberger 2018] A. Mittelberger, C. Kramberger, and J.C. Meyer. *Software electron counting for low-dose scanning transmission electron microscopy*. Ultramicroscopy, vol. 188, 1–7, 2018.

[Mullarkey 2020] T. Mullarkey, C. Downing, and L. Jones. *Development of a Practicable Digital Pulse Read-Out for Dark-Field STEM*. Microscopy and Microanalysis, vol. 27, 99–108, 2020.

[Muller 1999] D.A. Muller, and M.J. Mills. *Electron microscopy: probing the atomic structure and chemistry of grain boundaries, interfaces and defects*. Materials Science and Engineering A, vol. 260, 12–28, 1999.

[Muller 2001] D.A. Muller, B. Edwards, E.J. Kirkland, and J. Silcox. *Simulation of thermal diffuse scattering including a detailed phonon dispersion curve*. Ultramicroscopy, vol. 86, 371–380, 2001.

[Nellist 2000] P.D. Nellist, and S.J. Pennycook. *The Principles and Interpretation of Annular Dark-Field Z-Contrast Imaging*. Advances in Imaging and Electron Physics, vol. 113, 147, 2000.

[Nord 2017] M. Nord, P.E. Vullum, I. MacLaren, T. Tybell, and R. Holmestad. *Atomap: a new software tool for automated analysis of atomic resolution images using two-dimensional Gaussian fitting*. Advanced Structural and Chemical Imaging, vol. 3, 2017.

[Okunishi 2009] E. Okunishi, I. Ishikawa, H. Sawada, F. Hosokawa, M. Hori, and Y. Kondo. *Visualization of Light Elements at Ultrahigh Resolution by STEM Annular Bright Field Microscopy*. Microscopy and Microanalysis, vol. 15, 164–165, 2009.

[Olson 2000] G. B. Olson. *Designing a New Material World*. Science, vol. 288, 993–998, 2000.

[Ophus 2017] C. Ophus. *A fast image simulation algorithm for scanning transmission electron microscopy*. Advanced Structural and Chemical Imaging, vol. 3, 13, 2017.

[Ophus 2019] C. Ophus. *Four-Dimensional Scanning Transmission Electron Microscopy (4D-STEM): From Scanning Nanodiffraction to Ptychography and Beyond*. Microscopy and Microanalysis, vol. 25, 563–582, 2019.

[Oura 2003] K. Oura, M. Katayama, A. V. Zotov, V. G. Lifshits, and A.A. Saranin. *Elementary Processes at Surfaces II. Surface Diffusion*. 2003.

[Paier 2013] J. Paier, C. Penschke, and J. Sauer. *Oxygen Defects and Surface Chemistry of Ceria: Quantum Chemical Studies Compared to Experiment*. Chemical Reviews, vol. 113, 3949–3985, 2013.

[Palatinus 2017] L. Palatinus, P. Brázda, P. Boullay, M. Klementová, S. Petit, V. Eigner, M. Zaarour, and S. Mintova. *Hydrogen positions in single nanocrystals revealed by electron diffraction*. Science, vol. 355, 166–169, 2017.

[Pennycook 2011] S.J. Pennycook, and P.D. Nellist. *Scanning Transmission Electron Microscopy - Imaging and Analysis*. Springer-Verlag New York, 2011.

[Peter 2017] N.J. Peter, C.H. Liebscher, C. Kirchlechner, and G. Dehm. *Beam-induced atomic migration at Ag-containing nanofacets at an asymmetric Cu grain boundary*. Journal of Materials Research, vol. 32, 968–982, 2017.

[Peters 2017] J.L. Peters, K.H.W. van den Bos, S. Van Aert, B. Goris, S. Bals, and D. Vanmaekelbergh. *Ligand-Induced Shape Transformation of PbSe Nanocrystals*. Chemistry of Materials, vol. 29, 4122–4128, 2017.

[Prabhakara 2020] V. Prabhakara, D. Jannis, G. Guzzinati, A. Béché, H. Bender, and J. Verbeeck. *HAADF-STEM block-scanning strategy for local measurement of strain at the nanoscale*. Ultramicroscopy, vol. 219, 113099, 2020.

[Price 2018] D.J. Price, N.G. Bean, J.V. Ross, and J. Tuke. *Designing group dose-response studies in the presence of transmission*. Mathematical Biosciences, vol. 304, 62–78, 2018.

[Rabiner 1989] L.R. Rabiner. *A tutorial on hidden Markov models and selected applications in speech recognition*. Proceedings of the IEEE, vol. 77, 257–286, 1989.

[Rao 1945] C.R. Rao. *Information and the Accuracy Attainable in the Estimation of Statistical Parameters*. Bulletin of the Calcutta Mathematical Society, vol. 37, 81–89, 1945.

[Rath 2003] T.M. Rath, M. Carreras, and P. Sebastiani. *Automated Detection of Influenza Epidemics with Hidden Markov Models*. Lecture Notes in Computer Science, 521–532, 2003.

[Richardson 1978] M.K. Richardson. *Fundamentals of the Discrete Fourier Transform*. Sound & Vibration Magazine, vol. 12, 40–46, 1978.

[Rischel 1997] C. Rischel, A. Rousse, I. Uschmann, P.-A. Albouy, J.-P. Geindre, P. Audebert, J.-C. Gauthier, E. Förster, J.-L. Martin, and A. Antonetti. *Femtosecond time-resolved X-ray diffreaction from laser-heated organic films*. Nature, vol. 390, 490–492, 1997.

[Rosenauer 2007] A. Rosenauer, and M. Schowalter. *STEMSIM - A new software tool for simulation of STEM HAADF Z-contrast imaging*. Springer Proceedings in Physics, vol. 120, 169, 2007.

[Rosenauer 2008] A. Rosenauer, M. Schowalter, J.T. Titantah, and D. Lamoen. *An emission-potential multislice approximation to simulate thermal diffuse scattering in high-resolution transmission electron microscopy.* Ultramicroscopy, vol. 108, 1504–1513, 2008.

[Rosenauer 2009] A. Rosenauer, K. Gries, K. Müller, A. Pretorius, M. Schowalter, A. Avramescu, K. Engl, and S. Lutgen. *Measurement of specimen thickness and composition in $Al_xGa_{1-x}N$/GaN using high-angle annular dark field images*. Ultramicroscopy, vol. 109, 1171–1182, 2009.

[Rosenauer 2011] A. Rosenauer, T. Mehrtens, K. Müller, K. Gries, M. Schowalter, P. V. Satyam, S. Bley, C. Tessarek, D. Hommel, K. Sebald, M. Seyfried, J. Gutowski, A. Avramescu, K. Engl, and S. Lutgen. *Composition mapping in InGaN by scanning transmission electron microscopy*. Ultramicroscopy, vol. 111, 1316–1327, 2011.

[Rosenthal 2016] P.B. Rosenthal. *Chapter Nine - Testing the Validity of Single-Particle Maps at Low and High Resolution*. Methods in Enzymology, vol. 579, 227–253, 2016.

[Ruan 2009] C.-Y. Ruan, Y. Murooka, R.K. Raman, and R.A. Murdick. *The Development and Applications of Ultrafast Electron Nanocrystallography*. Microscopy and Microanalysis, vol. 15, 323–337, 2009.

[Ruskin 2013] R.S. Ruskin, Z. Yu, and N. Grigorieff. *Quantitative characterization of electron detectors for transmission electron microscopy*. Journal of Structural Biology, vol. 184, 385–393, 2013.

[Sandbeck 2020] D.J.S. Sandbeck, N.M. Secher, F.D. Speck, J.E. Sórensen, J. Kibsgaard, I. Chorkendorff, and S. Cherevko. *Particle Size Effect on Platinum Dissolution: Considerations for Accelerated Stability Testing of Fuel Cell Catalysts*. ACS Catalysis, vol. 10, 6281–6290, 2020.

[Schlexer 2019] P. Schlexer, A. B. Andersen, B. Sebok, I. Chorkendorff, J. Schiøtz, and T.W. Hansen. *Size-Dependence of the Melting Temperature of Individual Au Nanoparticles*. Particle & Particle Systems Characterization, vol. 36, 1800480, 2019.

[Schmid 2016] O. Schmid, and T. Stoeger. *Surface area is the biologically most effective dose metric for acute nanoparticle toxicity in the lung*. Journal of Aerosol Science, vol. 99, 133–143, 2016.

[Schneider 2014] S. Schneider, A. Surrey, D. Pohl, L. Schultz, and B. Rellinghaus. *Atomic surface diffusion on Pt nanoparticles quantified by high-resolution transmission electron microscopy*. Micron, vol. 63, 52–56, 2014.

[Sciensano 2021] Sciensano. *TEM analysis of "Communitymasker M-VYG-A1" mouth masks*, 2021.

[Siwick 2003] B.J. Siwick, J.R. Dwyer, R.E. Jordan, and R. J.D. Miller. *An Atomic-Level View of Melting Using Femtosecond Electron Diffraction*. Science, vol. 302, 1382–1385, 2003.

[So 2012] Y.-G. So, and K. Kimoto. *Effect of specimen misalignment on local sturcture analysis using annular dark-field imaging*. Journal of Electron Microscopy, vol. 61, 207–215, 2012.

[Somorjai 1975] G.A. Somorjai, and D.W. Blakely. *Mechanism of catalysis of hydrocarbon reactions by platinum surfaces*. Nature, vol. 258, 580–583, 1975.

[Surrey 2012] A. Surrey, D. Pohl, L. Schultz, and B. Rellinghaus. *Quantitative Measurement of the Surface Self-Diffusion on Au Nanoparticles by Aberration-Corrected Transmission Electron Microscopy*. Nano Letters, vol. 12, 6071–6077, 2012.

[Taheri 2016] M. L. Taheri, E. A. Stach, I. Arslan, P.A. Crozier, B.C. Kabius, T. LaGrange, A.M. Minor, S. Takeda, M. Tanase, J. B. Wagner, and R. Sharma. *Current status and future directions for in situ*

transmission electron microscopy. Ultramicroscopy, vol. 170, 86–95, 2016.

[Takayanagi 2011] K. Takayanagi, S. Kim, S. Lee, Y. Oshima, T. Tanaka, Y. Tanishiro, H. Sawada, F. Hosokawa, T. Tomita, T. Kaneyama, and Y. Kondo. *Electron microscopy at a sub-50 pm resolution*. Journal of Electron Microscopy, vol. 60, 239–244, 2011.

[Thomas 2015] J.M. Thomas. *Tens of thousands of atoms replaced by one*. Nature, vol. 525, 325–326, 2015.

[Thust 2009] A. Thust. *High-Resolution Transmission Electron Microscopy on an Absolute Contrast Scale*. Physical Review Letters, vol. 102, 220801, 2009.

[Tian 2007] N. Tian, Z.-Y. Zhou, S.-G. Sun, Y. Ding, and Z. L. Wang. *Synthesis of Tetrahexahedral Platinum Nanocrystals with High-Index Facets and High Electro-Oxidation Activity*. Science, vol. 316, 732–735, 2007.

[Uchiyama 2011] T. Uchiyama, H. Yoshida, Y. Kuwauchi, S. Ichikawa, S. Shimada, M. Haruta, and S. Takeda. *Systematic Morphology Changes of Gold Nanoparticles Supported on CeO_2 during CO Oxidation*. Angewandte Chemie International Edition, vol. 50, 10157–10160, 2011.

[Van Aert 2005] S. Van Aert, A.J. den Dekker, A. van den Bos, D. Van Dyck, and J.H. Chen. *Maximum likelihood estimation of structure parameters from high resolution electron microscopy images. Part II: A practical example*. Ultramicroscopy, vol. 104, 83–106, 2005.

[Van Aert 2009] S. Van Aert, J. Verbeeck, R. Erni, S. Bals, M. Luysberg, D. Van Dyck, and G. Van Tendeloo. *Quantitative atomic resolution mapping using high-angle annular dark field scanning transmission electron microscopy*. Ultramicroscopy, vol. 109, 1236–1244, 2009.

[Van Aert 2011] S. Van Aert, K.J. Batenburg, M.D. Rossell, R. Erni, and G. Van Tendeloo. *Three-dimensional atomic imaging of crystalline nanoparticles*. Nature, vol. 470, 374–377, 2011.

[Van Aert 2013] S. Van Aert, A. De Backer, G.T. Martinez, B. Goris, S. Bals, G. Van Tendeloo, and A. Rosenauer. *Procedure to count atoms with trustworthy single-atom sensitivity*. Physical Review B, vol. 87, 064107, 2013.

[Van Aert 2016] S. Van Aert, A. De Backer, G.T. Martinez, A.J. den Dekker, D. Van Dyck, S. Bals, and G. Van Tendeloo. *Advanced electron crystallography through model-based imaging*. IUCrJ, vol. 3, 71–83, 2016.

[Van Aert 2019] S. Van Aert, A. De Backer, L. Jones, G.T. Martinez, A. Béché, and P.D. Nellist. *Control of Knock-On Damage for 3D Atomic Scale Quantification of Nanostructures: Making Every Electron Count in Scanning Transmission Electron Microscopy*. Physical Review Letters, vol. 122, 066101, 2019.

[van den Bos 2007] A. van den Bos. *Parameter Estimation for Scientists and Engineers*. John Wiley and Sons, inc., 2007.

[van den Bos 2016] K.H.W. van den Bos, A. De Backer, G.T. Martinez, N. Winckelmans, S. Bals, P.D. Nellist, and S. Van Aert. *Unscrambling Mixed Elements using High Angle Annular Dark Field Scanning Transmission Electron Microscopy*. Physical Review Letters, vol. 116, 246101, 2016.

[van den Bos 2019] K.H.W. van den Bos, L. Janssens, A. De Backer, and S. Van Aert. *The atomic lensing model: New opportunities for atom-by-atom metrology of heterogeneous nanomaterials*. Ultramicroscopy, vol. 203, 155–162, 2019.

[Van Dyck 1996] D. Van Dyck, and M. Op de Beeck. *A simple intuitive theory for electron diffraction*. Ultramicroscopy, vol. 64, 99–107, 1996.

[Van Dyck 2003] D. Van Dyck, S. Van Aert, A.J. den Dekker, and A. van den Bos. *Is atomic resolution transmission electron microscopy able to resolve and refine amorphous structures?* Ultramicroscopy, vol. 98, 27–42, 2003.

[Van Dyck 2009] D. Van Dyck. *Is the frozen phonon model adequate to describe inelastic phonon scattering?* Ultramicroscopy, vol. 109, 677–682, 2009.

[Van Dyck 2010] D. Van Dyck. *Wave reconstruction in TEM using a variable phase plate*. Ultramicroscopy, vol. 110, 571–572, 2010.

[Van Dyck 2011] D. Van Dyck. *Persistent misconceptions about incoherence in electron microscopy*. Ultramicroscopy, vol. 111, 894–900, 2011.

[Van Dyck 2012] D. Van Dyck. *Atomic Resolution Electron Microscopy*. 2012.

[Vanrompay 2018] H. Vanrompay, E. Bladt, W. Albrecht, A. Béché, M. Zakhozheva, A. Sánchez-Iglesias, L.M. Liz-Marzán, and S. Bals. *3D characterization of heat-induced morphological changes of Au nanostars by fast in situ electron tomography*. Nanoscale, vol. 10, 22792–22801, 2018.

[Varambhia 2016] A.M. Varambhia, L. Jones, A. De Backer, V.T. Fauske, S. Van Aert, D. Ozkaya, and P.D. Nellist. *Quantifying a Heterogeneous Ru Catalyst on Carbon Black Using ADF STEM*. Particle & Particle Systems Characterization, vol. 33, 438–444, 2016.

[Verleysen 2019] E. Verleysen, T. Wagner, H.-G. Lipinski, R. Kägi, R. Koeber, A. Boix-Sanfeliu, P.-J. De Temmerman, and J. Mast. *Evaluation of a TEM based Approach for Size Measurement of Particulate (Nano)materials*. Materials, vol. 12, 2274, 2019.

[Viterbi 1967] A.J. Viterbi. *Error bounds for convolutional codes and an asymptotically optimum decoding algorithm*. IEEE Transactions on Information Theory, vol. 13, 260–269, 1967.

[Wade 2016] C.A. Wade, I. MacLaren, R.P. Vinci, and M. Watanabe. *The Role of Grain Boundary Dislocations in the Segregation-Induced Grain Boundary Embrittlement of Copper by Bismuth*. Microscopy and Microanalysis, vol. 22, 1264–1265, 2016.

[Wang 2010] A. Wang, F. Chen, S. Van Aert, and D. Van Dyck. *Direct structure inversion from exit waves, Part I: Theory and simulations*. Ultramicroscopy, vol. 110, 527–534, 2010.

[Wang 2012a] A. Wang, F. Chen, S. Van Aert, and D. Van Dyck. *Direct structure inversion from exit waves, Part II: A practical example*. Ultramicroscopy, vol. 116, 77–85, 2012.

[Wang 2012b] Z.W. Wang, and R.E. Palmer. *Mass Spectrometry and Dynamics of Gold Adatoms Observed on the Surface of Size-Selected Au Nanoclusters*. Nano Letters, vol. 12, 91–95, 2012.

[Wang 2015] Y.-G. Wang, D. Mei, V.-A. Glezakou, J. Li, and R. Rousseau. *Dynamic formation of single-atom catalytic active sites on ceria-supported gold nanoparticles*. Nature Communications, vol. 6, 2015.

[Wang 2016] Y. Wang, U. Salzberger, W. Sigle, E. Suyolcu, and P.A. van Aken. *Oxygen octahedra picker: A software tool to extract quantitative information from STEM images*. Ultramicroscopy, vol. 168, 46–52, 2016.

[Watkins 2009] R.E. Watkins, S. Eagleson, B. Veenendaal, G. Wright, and A.J. Plant. *Disease surveillance using a hidden Markov model*. BMC Medical Informatics and Decision Making, vol. 9, 39, 2009.

[Wiesendanger 1994] R. Wiesendanger. *Scanning Probe Microscopy and Spectroscopy, Methods and Applications*. Cambridge: Cambridge University Press, 1994.

[Wilkinson 2011] L.J. Wilkinson, R.J. White, and J.K. Chipman. *Silver and nanoparticles of silver in wound dressings: a review of efficacy and safety*. Journal of Wound Care, vol. 20, 543–549, 2011.

[Williams 2007] D. Williams, M. Amman, H. Autrup, J. Bridges, F. Cassee, K. Donaldson, E. Fattal, C. Janssen, W. De Jong, and T. Jung.

The appropriateness of existing methodologies to assess the potential risks associated with engineered and adventitious products of nanotechnologies. Proceedings of the European Commission Health and Consumer Protection Directorate General by the Scientific Committee on Emerging and Newly Identified Health Risks, 2007.

[Yamazaki 2013] T. Yamazaki, M. Ohtsuka, Y. Kotaka, and K. Watanabe. *Bloch wave simulations in the frozen lattice approximation*. Ultramicroscopy, vol. 135, 16–23, 2013.

[Yang 2012] P. Yang, and J.M. Tarascon. *Towards systems materials engineering*. Nature Materials, vol. 11, 560–563, 2012.

[Yang 2015] H. Yang, T.J. Pennycook, and P.D. Nellist. *Efficient phase contrast imaging in STEM using a pixelated detector. Part II: Optimisation of imaging conditions*. Ultramicroscopy, vol. 151, 232–239, 2015.

[Yang 2021] Y. Yang, J. Zhou, F. Zhu, Y. Yuan, D.J. Chang, D.S. Kim, M. Pham, A. Rana, X. Tian, Y. Yao, S.J. Osher, A.K. Schmid, L. Hu, P. Ercius, and J. Miao. *Determining the three-dimensional atomic structure of an amorphous solid*. Nature, vol. 592, 60–64, 2021.

[Yankovich 2014] A.B. Yankovich, B. Berkels, W. Dahmen, P. Binev, S.I. Sanchez, S.A. Bradley, A. Li, I. Szlufarska, and P.M. Voyles. *Picometre-precision analysis of scanning transmission electron microscopy images of platinum nanocatalysts*. Nature Communications, vol. 5, 4155, 2014.

[Yoshida 2012] H. Yoshida, Y. Kuwauchi, J. Jinschek, K. Sun, S. Tanaka, M. Kohyama, S. Shimada, M. Haruta, and S. Takeda. *Visualizing Gas Molecules Interacting with Supported Nanoparticulate Catalysts at Reaction Conditions*. Science, vol. 335, 317–319, 2012.

[Yu 2008] Z. Yu, D.A. Muller, and J. Silcox. *Effects of specimen tilt in ADF-STEM imaging of a-Si/c-Si interfaces*. Ultramicroscopy, vol. 108, 494–501, 2008.

[Yu 2019] J. Yu, X. Li, J. Miao, W. Yuan, S. Zhou, B. Zhu, Y. Gao, H. Yang, Z. Zhang, and Y. Wang. *Atomic Mechanism in Layer-by-Layer Growth via Surface Reconstruction*. Nano Letters, vol. 19, 4205–4210, 2019.

[Zanchet 2000] D. Zanchet, B.D. Hall, and D. Ugarte. *Characterization of Nanophase Materials - Chapter 2 X-ray Characterization of Nanoparticles*. Weinheim: Wiley-VCH, 2000.

[Zewail 2006] A.H. Zewail. *4D Ultrafast Electron Diffraction, Crystallography, and Microscopy*. Annu. Rev. Phys. Chem., vol. 57, 65–103, 2006.

[Zhang 2011] C. Zhang, A. Michaelides, and S.J. Jenkins. *Theory of gold on ceria*. Physical Chemistry Chemical Physics, vol. 13, 22–33, 2011.

[Zhou 2016] D. Zhou, K. Müller-Caspary, W. Sigle, F.F. Krause, A. Rosenauer, and P.A. van Aken. *Sample tilt effects on atom column position determination in ABF-STEM imaging*. Ultramicroscopy, vol. 160, 110–117, 2016.

[Zhou 2019] J. Zhou, Y. Yang, Y. Yang, D. S. Kim, A. Yuan, X. Tian, C. Ophus, F. Sun, A. K. Schmid, M. Nathanson, H. Heinz, Q. An, H. Zeng, P. Ercius, and J. Miao. *Observing crystal nucleation in four dimensions using atomic electron tomography*. Nature, vol. 570, 500–503, 2019.

[Zhu 2020] N. Zhu, D. Zhang, W. Wang, X. Li, B. Yang, J. Song, X. Zhao, B. Huang, W. Shi, R. Lu, P. Niu, P. Zhan, Z. Ma, D. Wang, W. Xu, G. Wu, G.F. Gao, and W. Tan. *A Novel Coronavirus from Patients with Pneumonia in China, 2019*. The New England Journal of Medicine, vol. 382, 727–733, 2020.

List of Symbols and Abbreviations

Roman characters

Character	Page	Explanation
a	40	linear scaling parameter
A_{jg}	61	transition probabilities for the number of atoms in an atomic column to go from j to g atoms from one frame to the next
$\mathbf{A}$	61	transition matrix
c	20	crystal lattice parameter in the z-direction
$c_t^{(n)}$	76	scaling factor
d	23	number of parameters of the model
	85	electron dose
$\mathbb{E}$	16	expectation value
f_{kl}	28	expectation model for the ADF STEM image intensity at pixel (k, l)
f_{mix}	22	Gaussian mixture model
$F_{\boldsymbol{\theta}}$	17	Fisher information matrix for parameters $\boldsymbol{\theta}$
g	21	component index of the Gaussian mixture model
	40	number of atoms in an atomic column
$g_t^{(n)}$	62	effective number of atoms in a column n at a given time t
G	22	number of components of the Gaussian mixture model
	40	maximum number of atoms in an atomic column
$\mathbf{h}_t$	58	hidden state at time t
$\mathbf{h}_t^{(n)}$	59	hidden state (number of atoms) at time t for atomic column n
$h_{tg}^{(n)}$	59	binary hidden state index: equal to 1 if the number of atoms in atomic column n in frame t equals g, otherwise equal to 0
$h_g^{(n)}$	60	binary hidden state index: equal to 1 if the number of atoms in atomic column n in the single frame equals g, otherwise equal to 0
$\mathbf{H}$	58	hidden state sequence
k	18	pixel index in x-direction
	41	iteration index
K	18	number of image pixels in x-direction
l	18	pixel index in y-direction
$L(\boldsymbol{t})$	17	likelihood function
L	18	number of image pixels in y-direction
$\mathcal{M}_g$	40	library value corresponding to an atomic column with g atoms
n	18	atomic column index
N	18	total number of atomic columns in the image
$\mathcal{N}$	22	Gaussian distribution
N_{ad}	88	number of adatoms

o_n	60	stochastic variable related to the scattering cross section of atomic column n in a single frame
$\mathbf{o}_t$	58	observation at time t
$o_t^{(n)}$	60	stochastic variable related to the scattering cross section of atomic column n in frame t
$\hat{o}_t^{(n)}$	59	observed scattering cross section for atomic column n in frame t
$\mathbf{O}$	58	(stochastic variable relate to) observed sequence
$\hat{\mathbf{O}}$	63	sequence of observed scattering cross sections
$\mathbf{O}^{(n)}$	79	observed sequence for atomic column n
$p(\boldsymbol{x})$	16	joint probability (density) function
P	84	probability of structural changes
P_{sd}	87	probability of surface diffusion
$q_t^{(n)}$	64	number of atoms in atomic column n at time t
$Q(\mathbf{\Omega}, \mathbf{\Omega}^{\mathrm{old}})$	74	auxiliary function for Baum-Welch algorithm
t	58	time series frame index
$\boldsymbol{t}$	17	independent variables
T	58	number of frames in a time series
$^{\mathsf{T}}$	17	transposed vector
$\hat{V}_n$	19	estimated scattering cross section of atomic column n
V_n	22	stochastic variable related to the n^{th} scattering cross section
$\mathbf{V}$	22	vector summarising the stochastic variables for all scattering cross sections
w_{kl}	18	pixel values for pixel (k, l)
$\mathbf{w}$	18	vector summarising all pixel values
X_m	16	stochastic variable
$\boldsymbol{X}$	16	vector summarising stochastic variables
x_k	18	x-coordinate corresponding to pixel index k in the image
x_m	16	independent variable related to the observed data
$\boldsymbol{x}$	16	vector summarising the independent variables related to the observed data
$\mathbf{x}$	17	vector summarising the observed data points
y_k	18	y-coordinate corresponding to pixel index l in the image

Greek characters

Character	Page	Explanation
α	12	probe convergence angle
	29	angle that describes the orientation of the elliptical Gaussian peaks
$\alpha(h_{tg}^{(n)})$	75	forward variable
$\hat{\alpha}(h_{tg}^{(n)})$	76	scaled forward variable
β_1	12	inner angle of the annular detector
β_{x_n}	18	x-coordinate of the n^{th} atomic column
β_{y_n}	18	y-coordinate of the n^{th} atomic column
$\beta(h_{tg}^{(n)})$	75	backward variable
$\hat{\beta}(h_{tg}^{(n)})$	76	scaled backward variable
$\gamma(h_{tg}^{(n)})$	74	posterior probability that atomic column n contains g atoms at time t

δ	38	(average) distance between the locations of a Gaussian mixture model
	65	(average) difference between the mean values of the Gaussian emission probabilities
ϵ	32	aspect ratio of an elliptical Gaussian
ζ	18	constant background present in the image
η_n	18	height of the n^{th} Gaussian peak
θ_k	17	parameter
$\hat{\theta}_k$	17	parameter estimator
$\boldsymbol{\theta}$	17	parameter vector
	18	parameter vector of the parametric imaging model
$\boldsymbol{\Theta}$	28	parameter vector of the elliptical parametric imaging model
ι_g	60	initial probability for an atomic column to have g atoms
μ_g	22	location of the g^{th} component in the Gaussian mixture model
	60	mean of the Gaussian emission probability
$\xi(h^{(n)}_{t-1,j} h^{(n)}_{tg})$	75	joint posterior probability that atomic column n contains j atoms at time $t-1$ and g atoms at time t
π_g	22	mixing proportion of the g^{th} component
	40	equal to the probability for an atomic column to have g atoms in the hybrid approach
$\pi^{(t)}_g$	61	probability for an atomic column to have g atoms at time t
ρ	18	width of 2D Gaussian peaks
ρ_x	29	width of 2D elliptical Gaussian peaks in the x-direction
ρ_{x_n}	29	width of the n^{th} 2D elliptical Gaussian peak in the x-direction
ρ_y	29	width of 2D elliptical Gaussian peaks in the y-direction
ρ_{y_n}	29	width of the n^{th} 2D elliptical Gaussian peak in the y-direction
σ	22	width of Gaussian components
	60	width of the Gaussian emission probability
σ/δ	38	relative width of the components of a mixture model
	65	relative width of the Gaussian emission probabilities for different thicknesses
σ_{sd}	87	cross section related to surface diffusion
$\tau_g\left(\hat{V}_n \vert \hat{\boldsymbol{\Psi}}_G\right)$	44	posterior probability function
$\boldsymbol{\Psi}^{\text{stat}}_G$	22	parameter vector of the Gaussian mixture model with G components in the statistics-based method
$\boldsymbol{\Psi}_G$	40	parameter vector of the Gaussian mixture model with G components in the hybrid method
$\boldsymbol{\Omega}$	61	parameter vector of the hidden Markov model

Abbreviations

Character	Page	Explanation
2D	4	two-dimensional
3D	5	three-dimensional
4D	12	four-dimensional
Å	16	angstrom, 10^{-10} meter
ABF	12	annular bright field

ADF	12	annular dark field
arg max	17	argument that maximises a function
BF	12	bright field
CBED	12	convergent beam electron diffraction
cov	17	covariance matrix
CNN	91	convolutional neural network
EDX	13	energy-dispersive X-ray spectroscopy
EELS	13	electron energy loss spectroscopy
EM	22	Expectation-Maximisation
e^-	50	electrons
eV	88	electron volt
FWHM	69	full width at half maximum
HAADF	12	high angle annular dark field
ICL	23	Integrated Classification Likelihood
kV	45	kilovolt
keV	65	kiloelectron volt
LAADF	12	low angle annular dark field
MAADF	12	medium angle annular dark field
MAP	6	maximum *a posteriori*
MD	90	molecular dynamics
MLE	17	maximum likelihood estimator
μm	1	micrometer, 10^{-6} meter
mrad	30	milliradian
nm	1	nanometer, 10^{-9} meter
pm	2	picometer, 10^{-12} meter
TDS	13	thermal diffuse scattering
TEM	4	transmission electron microscopy
STEM	4	scanning transmission electron microscopy
var	16	variance
Z	13	atomic mass number

List of Publications

Contributions to scientific journals

- A. De wael, A. De Backer, I. Lobato, S. Van Aert, *Modelling ADF STEM images using elliptical Gaussian peaks and its effects on the quantification of structure parameters in the presence of sample tilt*, Submitted.
- P. Liu, E. Arslan Irmak, A. De Backer, A. De wael, I. Lobato, A. Béché, S. Van Aert, S. Bals, *Three-dimensional atomic structure of supported Au nanoparticles at high temperature*, Nanoscale 13 (2021), 1770-1776.
- A. De wael, A. De Backer, S. Van Aert, *Hidden Markov model for atom-counting from sequential ADF STEM images: Methodology, possibilities and limitations*, Ultramicroscopy 219 (2020), 113131.
- A. De wael, A. De Backer, A. Varambhia, L. Jones, P.D. Nellist, S. Van Aert, *Measuring dynamic structural changes of nanoparticles at the atomic scale using scanning transmission electron microscopy*, Physical Review Letters 124 (2020), 106105.
- A. De wael, A. De Backer, L. Jones, P.D. Nellist, S. Van Aert, *Hybrid statistics-simulations based method for atom-counting using scanning transmission electron microscopy*, Ultramicroscopy 177 (2017), 69-77.
- A. De Backer, A. De wael, J. Gonnissen, G.T. Martinez, A. Béché, K.E. MacArthur, L. Jones, P.D. Nellist, S. Van Aert, *Quantitative annular dark field scanning transmission electron microscopy for nanoparticle atom-counting: What are the limits?*, Journal of Physics: Conference Series 644 (2015) 012034.
- A. De Backer, A. De wael, J. Gonnissen, S. Van Aert, *Optimal experimental design for nano-particle atom-counting from high-resolution STEM images*, Ultramicroscopy 151 (2015) 46-55.

Conference abstracts

- A. De wael, A. De Backer, L. Jones, A. Varambhia, P.D. Nellist, *Measuring dynamic structural changes of nanoparticles at the atomic scale using scanning transmission electron microscopy*, MC 2021, Microscopy Conference 2021, Online, August 22-26, 2021, Submitted.
- A. De wael, A. De Backer, L. Jones, A. Varambhia, P.D. Nellist, *Quantification of dynamic structural changes of nanomaterials via atom-counting from sequential ADF STEM images*, MMC 2021 incorporating EMAG 2021, Microscience Microscopy Congress, Online, July 5-9, 2021, Submitted.

- S. Van Aert, A. De Backer, A. De wael, J. Fatermans, E. Arslan Irmak, T. Friedrich, I. Lobato, L. Jones, A.J. den Dekker, P.D. Nellist, S. Bals, *Strategies for quantifying the 3D atomic structure and the dynamics of nanomaterials using model-based STEM*, 2020 Virtual MRS Spring/Fall Meeting, Online, November 27 – December 4, 2020.

- A. De wael, A. De Backer, L. Jones, A. Varambhia, P.D. Nellist, S. Van Aert, *Measuring dynamic structural changes of nanoparticles at the atomic scale using scanning transmission electron microscopy*, Virtual Early Career European Microscopy Congress, Online, November 24-26, 2020.

- S. Van Aert, A. De Backer, A. De wael, J. Fatermans, T. Friedrich, I. Lobato, C. O'Leary, A. Varambhia, T. Altantzis, L. Jones, A.J. den Dekker, P.D. Nellist, S. Bals, *3D atomic scale quantification of nanostructures and their dynamics using model-based STEM*, M&M 2020, Microscopy & Microanalysis Virtual Meeting, Online, August 2-6, 2020.

- A. De Backer, A. De wael, I. Lobato, T. Altantzis, A. Béché, L. Jones, P.D. Nellist, S. Bals, S. Van Aert, *Quantification of 3D Atomic Structures and Their Dynamics by Atom-Counting from an ADF STEM Image*, M&M 2019, Microscopy & Microanalysis 2019 Meeting, Portland, Oregon, US, August 4-8, 2019.

- S. Van Aert, A. De wael, J. Fatermans, I. Lobato, A. De Backer, L. Jones, A.J. den Dekker, P.D. Nellist, *Quantifying 3D atomic structures of nanomaterials and their dynamics using model-based scanning transmission electron microscopy*, EMRS Spring Meeting 2019, Nice, France, May 27-31, 2019.

- A. De wael, A. De Backer, A. Varambhia, L. Jones, P.D. Nellist, S. Van Aert, *How to count atoms from an ADF STEM time series of dynamically changing nanostructures with high reliability*, PICO 2019, 5th Conference on Frontiers of Aberration Corrected Electron Microsopy, Kasteel Vaalsbroek, The Netherlands, May 6-10, 2019.

- S. Van Aert, A. De wael, J. Fatermans, I. Lobato, A. De Backer, L. Jones, A.J. den Dekker, P.D. Nellist, *Strategies for quantifying 3D atomic structures of nanomaterials and their dynamics using dose-efficient ADF STEM, PICO 2019*, 5th Conference on Frontiers of Aberration Corrected Electron Microsopy, Kasteel Vaalsbroek, The Netherlands, May 6-10, 2019.

- A. De wael, L. Janssens, A. De Backer, S. Van Aert, *Model-based quantification of ADF STEM images in the presence of crystal tilt*, EMAG 2018, Conference on Applications of Electron Microscopy to Beam Sensitive Materials, University of Warwick, Coventry, UK, July 4-6, 2018.

- A. De wael, A. De Backer, L. Jones, P.D. Nellist, S. Van Aert, *Hybrid statistics-simulations based method for atom-counting using scanning transmission electron microscopy*, MC 2017, Microscopy Conference 2017, Lausanne, Switzerland, August 21-25, 2017, IM1-24.

- S. Van Aert, A. De Backer, M. Alania, A. De wael, K.H.W. van den Bos, T. Altantzis, I. Lobato, L. Jones, G.T. Martinez, P.D. Nellist, S. Bals, *Towards 3D atomic structures through nanoparticle atom-counting: advances, challenges, and expectations*, MMC 2017 incorporating EMAG 2017, Microscience Microscopy Congress, Manchester, UK, July 3-6, 2017.

- S. Van Aert, K.H.W. van den Bos, A. De wael, M. Alania, A. De Backer, L. Jones, G.T. Martinez, S. Bals, P.D. Nellist, *Model-based ADF STEM: from images towards precise atomic structures in two and three dimensions*, MRS 2016, 2016 MRS Fall Meeting & Exhibit, Boston, Massachusetts, USA, November 27 - December 2, 2016.

- A. De wael, A. De Backer, L. Jones, P.D. Nellist, S. Van Aert, *Hybrid statistics-simulations based method for atom-counting using scanning transmission electron microscopy*, RBSM 2016, Golden Jubilee Meeting of the Royal Belgian Society for Microscopy, Brussels, Belgium, September 8-9, 2016.

- A. De Backer, A. De wael, J. Gonnissen, G.T. Martinez, A. Béché, K.E. MacArthur, L. Jones, P.D. Nellist, S. Van Aert, *Quantitative annular dark field scanning transmission electron microscopy for nanoparticle atom-counting: What are the limits?*, RBSM 2016, Golden Jubilee Meeting of the Royal Belgian Society for Microscopy, Brussels, Belgium, September 8-9 2016.

- S. Van Aert, A. De Backer, A. De wael, L. Jones, G.T. Martinez, B. Goris, T. Altantzis, A. Béché, S. Bals, P.D. Nellist, *Nondestructive nanoparticle characterisation using a minimum electron dose in quantitative ADF STEM: how low can one go?*, EMC 2016, The 16th European Microscopy Congress, Lyon, France, August 2 - September 2, 2016.

- S. Van Aert, A. De wael, K.H.W. van den Bos, J. Gonnissen, A. De Backer, L. Jones, M. Alania, G.T. Martinez, P.D. Nellist, *Minimum electron budget for maximum structural information of beam-sensitive nanoparticles using quantitative scanning transmission electron microscopy*, MRS 2016, Phoenix, USA, March 28 - April 1, 2016, 2408003.

- S. Van Aert, A. De wael, K.H.W. van den Bos, J. Gonnissen, A. De Backer, L. Jones, M. Alania, G.T. Martinez, P.D. Nellist, *Minimum electron budget for maximum structural information of beam-sensitive nanoparticles using quantitative scanning transmission electron microscopy*, ACMM 2016, Melbourne, Australia, January 31 - February 4, 2016, 69.

- S. Van Aert, A. De Backer, A. De wael, K.H.W. van den Bos, J. Gonnissen, G.T. Martinez, *Precise nanoparticle atom-counting using a mininum electron budget*, Microscopy Conference - MC2015, Göttingen, Germany, September 6-11, 2015, IM2.042.

- A. De Backer, A. De wael, J. Gonnissen, G.T. Martinez, A. Béché, K.E. MacArthur, L. Jones, P.D. Nellist, S. Van Aert, *Quantitative annular dark field scanning transmission electron microscopy for nanoparticle atom-counting: What are the limits?*, MMC 2015 incorporating EMAG 2015, Manchester, UK, June 29 - July 2, 2015, 4033.

- S. Van Aert, A. De Backer, A. De wael, J. Gonnissen, G.T. Martinez, A. Béché, K.E. MacArthur, L. Jones, P.D. Nellist, *Quantitative annular dark field scanning transmission electron microscopy for nanoparticle atom-counting: What are the limits?*, PICO 2015 - 3rd Conference on Frontiers of Aberration Corrected Electron Microscopy, Kasteel Vaalsbroek, The Netherlands, April 19-23, 2015.

- A. De Backer, A. De wael, S. Van Aert, *Probability of error for counting the number of atoms from high resolution HAADF STEM images*, 18th International Microscopy Congress IMC 2014, Prague, Czech Republic, September 7-12, 2014, IT-2-P-2255.

Dankwoord

In 2011 koos ik met veel overtuiging en enthousiasme voor de opleiding Fysica aan de Universiteit Antwerpen. Een abstract wetenschappelijke richting, en wat doet een fysicus eigenlijk als job? Ik besef inmiddels maar al te goed dat die keuze voor de meeste meisjes niet zo evident is als ze voor mij destijds was, en ik ben mijn ouders dan ook zeer dankbaar voor het creëren van een sfeer vol vertrouwen en motivatie rond onze studies. Dankjewel, mama en papa, om altijd in mijn capaciteiten te geloven en me alle kansen te geven om me verder te ontplooien. Dankjewel, mama en papa, en ook mijn broer en zus, Koen en Hanne, voor de interesse in mijn onderzoek en voor het zo goed mogelijk proberen begrijpen waar ik nu juist mee bezig ben! Een grote dankuwel is ook zeker op zijn plaats voor de gemotiveerde leerkrachten van de Middenschool Anton Bergmann en het Koninklijk Atheneum te Lier, die zich naast hun toffe lessen ook inzetten voor allerlei buitenschoolse wetenschaps- en wiskunde olympiades. In het bijzonder wil ik van de gelegenheid gebruik maken om mijn ontzettend lieve wiskunde leerkracht uit de laatste graad, mevrouw Geukens, uitdrukkelijk te bedanken voor al de leerrijke (levens-)lessen!

Aan het einde van het tweede bachelor Fysica werden enkele topics voorgesteld voor de bachelorthesissen. Het stukje parameterschattingstheorie tijdens de laatste lessen van prof. Sandra Van Aert had inmiddels mijn ogen geopend: wat kon statistiek boeiend zijn! Dat leek wel een goede keuze voor een theoretische bachelorproef. Het “toeval” wil dat ik zonder het te weten koos voor een experimentele bachelorproef bij Sandra’s echtgenoot, dr. Philippe Geuens, bij Atlas Copco. Ik herinner me nog heel goed dat ik dit enigszins verbaasd ontdekte op Sandra’s bureau, samen met Annick De Backer, die mijn co-promotor zou worden. De theoretische bachelorproef bleek me heel erg te liggen, en ik was dan ook zeer blij dat Sandra en Annick me graag ook wilden begeleiden voor mijn masterthesis. Ze stelden me een uitdagend en vernieuwend onderwerp voor en gaven me zelfs de kans om een stage in Oxford uit te voeren, in de onderzoeksgroep van prof. Pete Nellist. I would also like to take the opportunity to thank Pete for this opportunity. I really learned a lot during my internship at Oxford. I would also like to explicitly thank dr. Lewys Jones for helping me find my way around during my internship and for the never-ending enthousiasm during our meetings and collaborations.

Ik was dus tijdens mijn opleiding Fysica echt wel met mijn gat in de boter gevallen, met al die geweldige kansen die ik reeds gekregen had. Het was voor mij dan ook een makkelijke keuze om verder te gaan met een doctoraat onder de kundige en aangename begeleiding van Sandra en Annick. En wat ben ik blij dat ik dit gedaan heb! Ik krijg spontaan een grote glimlach op mijn gezicht als ik terugdenk aan onze vele gesprekken op Sandra’s kantoor, over werk, maar ook over het leven buiten het werk - destijds, toen dat nog mocht, in een wereld voordat de pandemie uitbrak, die ik me soms bijna niet meer kan voorstellen. De laatste tijd is dit iets minder evident geweest, maar zelfs in onze online gesprekken heb ik altijd het gevoel gehad dat we een fijne band hadden en dat jullie steeds voor me klaar stonden! Dankjewel, Sandra, om steeds tijd te maken voor vragen, problemen, ideeën en voorbereidingen voor presentaties. Je stond altijd klaar met opbeurende en aanmoedigende woorden als ik even niet meer wist in

welke richting verder te gaan. Dankjewel, Annick, voor al die keren dat ik onaangekondigd luidop kon komen nadenken in je kantoor. Van jou heb ik bovendien ook veel geleerd over het duidelijk presenteren van mijn onderzoek.

I would also like to thank all my EMAT colleagues, past and present. I really enjoyed our many walks in the beautiful park right outside the campus, going swimming or squashing, and the many lively discussions in the coffee room. I really hope we can get back to a completely safe environment quickly, such that we can for example pick up on our weekly coffee breaks and monthly melting pot lunches again! In het bijzonder wil ik Lydia en Miek bedanken om alle paperassen te regelen. Jullie doen organisatie en administratie op kinderspel lijken, zodat wij hier niet van moeten wakker liggen, dankjewel! Ik wil ook expliciet Liesbet bedanken voor alle grafische tovenarij en de mooie omslag van mijn thesis. Bij mijn doctoraat hoorde ook een lesopdracht. Ik vond het dan ook heel fijn om samen te werken met Sandra en Annick voor de lessen Kansrekenen en Statistiek, en met prof. Sara Bals voor de lessen Algemene Fysica. Dankjewel, Sara, om altijd zo lovend te zijn over mijn aanpak en organisatie van de lessen, dat heeft me heel erg veel vertrouwen gegeven! Bovendien wil ik je ook bedanken voor het verder uitbouwen van EMAT tot de succesvolle onderzoeksgroep die het tegenwoordig is, en waar het fijn is om aan onderzoek te doen. And then there are of course my office mates, Thomas and Ivan. I shared an office with Ivan from the start of my PhD, and I could always count on a lot of help, thank you! A few years later, we were joined by Thomas, a very nice addition to our office! I look forward to the day that we won't have to take turns coming to the office anymore. A big thank you goes out to all the PhD students and postdocs of "team Sandra", past and present, for all the nice discussions over the years. I am especially thankful for all your encouraging words during my preparation for the thesis and the defence via our online meetings. It's not the same as meeting in person, but I feel like we really made it work!

A big thank you is definitely also in place for my jury members, prof. Scott Findlay, dr. Rolf Erni, prof. Christel Faes, prof. Milorad Milosevic and prof. Pierre Van Mechelen. I consider it a great compliment that you have taken such an interest in my research, resulting in very interesting discussions.

En dan rest er nog de grootste dankuwel van allemaal. Livio, mijn lieve echtgenoot, wat een boeiende jaren hebben we samen al achter de rug! Je was (en bent) er altijd voor me, wanneer het goed ging en zeker ook wanneer het minder goed ging. Je bent samen met mij door formules en vele lijnen code gegaan. We werken ondertussen al een hele tijd samen thuis, wat vaak leuk, maar soms ook best uitdagend is geweest, vooral met een kruipende baby in huis tijdens de volledige lockdown. Ondertussen hebben we twee schatjes van kinderen! Lars en Margot, wat maken jullie me toch gelukkig, mijn kleine deugenietjes! Een lach of een knuffel van jullie beurt me instant op! Ik kijk er naar uit om jullie te zien opgroeien tot lieve, verstandige en vooral gelukkige mensen.

Annelies De wael
Juli 2021